

SEISMIC TOMOGRAPHY METHODS AND SUBSURFACE STUDIES OF THE KUMAON HIMALAYA

Ph.D. THESIS

by

CHINMOY KUMBHAKAR



**DEPARTMENT OF EARTH SCIENCES
INDIAN INSTITUTE OF TECHNOLOGY ROORKEE
ROORKEE-247 667 (INDIA)
DECEMBER, 2015**

SEISMIC TOMOGRAPHY METHODS AND SUBSURFACE STUDIES OF THE KUMAON HIMALAYA

A THESIS

*Submitted in partial fulfilment of the
requirements for the award of the degree*

of

DOCTOR OF PHILOSOPHY

in

EARTH SCIENCES

by

CHINMOY KUMBHAKAR



**DEPARTMENT OF EARTH SCIENCES
INDIAN INSTITUTE OF TECHNOLOGY ROORKEE
ROORKEE – 247 667 (INDIA)
DECEMBER, 2015**

**©INDIAN INSTITUTE OF TECHNOLOGY ROORKEE, ROORKEE- 2015
ALL RIGHTS RESERVED**



INDIAN INSTITUTE OF TECHNOLOGY ROORKEE ROORKEE

CANDIDATE'S DECLARATION

I hereby certify that the work which is being presented in the thesis entitled “**SEISMIC TOMOGRAPHY METHODS AND SUBSURFACE STUDIES OF THE KUMAON HIMALAYA** ” in partial fulfillment of the requirements for the award of the Degree of Doctor of Philosophy and submitted in the Department of Earth Sciences of the Indian Institute of Technology Roorkee, Roorkee is an authentic record of my own work carried out during a period from July, 2009 to December, 2015 under the supervision of **Dr. A. Joshi**, Professor, Department of Earth Sciences, Indian Institute of Technology Roorkee, Roorkee.

The matter presented in this thesis has not been submitted by me for the award of any other degree of this or any other Institute.

(**CHINMOY KUMBHAKAR**)

This is to certify that the above statement made by the candidate is correct to the best of my knowledge.

(A. Joshi)

Supervisor

Date:

The Ph.D. Viva-Voce Examination of **Mr. CHINMOY KUMBHAKAR**, Research Scholar, has been held on

Chairman, SRC


Signature of External Examiner

This is to certify that the student has made all the corrections in the thesis.

Signature of Supervisors

Head of the Department

ABSTRACT



Seismic tomography evolved as one of the most important tools for both quantitative and qualitative determination and investigation of the internal structure of Earth including subducted slabs, sources of hotspots, convection pattern in the mantle and detailed subsurface velocity structure. This tool has been extensively used by researchers and engineers for setting up parameters required in making different structures such as dams, reservoirs and buildings as well as, for search of ground water.

Mathematically tomography is an inverse technique which combines the idea of forward computation as well as inverse computation. Therefore the basis of tomography can be defined in terms of basics of inverse theory such as parameter representation, forward problem, inverse problem and analysis of robustness of solution.

One of the most challenging problems that are exclusively related to tomography is accurate and fast solution of forward problem. The problem arises because of nonlinear relationship between velocity and ray path geometry. Many methods have been given in past to solve out different problems in this field. One of the major problems in the forward problem is computation of first arrivals as these phases are very crucial particularly for determination accurate velocity models and for resolving thin layers of a structural feature. Fast Marching Method (FMM) is a method that gives mathematical guarantee to solve this problem. Similar to other methods, the numerical problems are associated with this method. The source neighborhood errors cause a great problem in accuracy. Many authors in past have given several methods. Multi-Stencils Fast Marching (MSFM) Method is a method that mathematically address the problem more closely. However, this method solves the basic problems to some limited extent. In this thesis a new method called Multistencils Pseudoanisotropic Fast Marching Method (MPFMM), by extending the concept of MSFM method, has been developed and discussed. The developed method improves significantly the numerical errors associated with FMM and MSFM method.

Conventional methods of ray path computations such as ray tracing are still used as these methods do not suffer from large numerical errors and provide better accuracy in computations. These are largely used in determination of preliminary 1D velocity models as well as 2D velocity models. One of the major problems associated with ray tracing is that this often fails to converge to true source-receiver ray paths and consumes time. This problem has been addressed in this thesis. A method has been developed for ray tracing which is parallel to shooting method of ray tracing. The method has been tied up with two techniques of ray path adjustments which have been named as Spiral Path Search Method

and Gradient Path Search method. Both these method works in series and computes ray path very efficiently.

Simultaneous inversion for the determination of a set of related parameters is always better than the inversion which considers only one parameter. There are many methods for computation of velocity and hypocenters with origin time. Determination of layered structure of earth is an important aspect of research because these are related with the earth's feature called discontinuities in velocity or quality factor. In that context inversion scheme and algorithms have been developed which simultaneously determine body wave velocities, hypocenters with origin times as well as layer interfaces. In that inversion scheme both P-and S-wave data are considered to increase the amount of information from data. This has been done because tomography problems often face one practical problem that is the problem of scarcity of data. To remove this to some extent both P-and S-wave are inverted simultaneously in the scheme. The developed method has been given the name multiparameter inversion method. The multiparameter inversion method has been used for determination of 1D velocity structures, hypocenter parameters beneath the Kumaon Himalaya.

The proposed MPFMM has been used to develop 2D and 3D traveltime tomography methods which have been applied successfully for the data of Kumaon. To study the attenuation structure of the same region, a methodology of 3D attenuation tomography using grid type of parameterization has been developed and discussed.

Data of the present study have been taken from strong motion network deployed in the Kumaon part of Himalaya. A total of 870 first arrival P- and S-phases from a total of 116 earthquakes have been used in the study. The observation times of first arrival phases have been used as data for traveltime inversions. A total of 373 phases of first arrival P-waves have been used for determination of 2D P-wave velocity structure while a total of 497 first arrival S-phases have been used for determination of 2D S-wave velocity structure. In determination of 3D shear wave velocity structure, a total of 405 first arrival S-phases from a total of 98 earthquakes have been used. To study the 3D attenuation tomography a total of 344 S-phase spectra recorded by 17 stations from a total of 82 events have been considered.

The located earthquakes form a shape that is oriented along Himalayan belt. Most of the epicenters form a group that lies between MCT and NAT in the areas of Baluakot, Dharchula and Joljibi. The number of earthquakes along MCT is fewer than that along MT. Most of the earthquakes are found to occur at shallow depths. Some of the earthquakes occurs at sub moho depth which support the idea that upper mantle deforms by brittle processes.

One dimensional velocity model shows the Indian moho beneath the Kumaon Himalayan region. The depth to the moho is ~50 km from mean sea level. This when tied up with other studies gives moho plane which has strike and dip respectively, N27E and 4.6° northeastern direction. At depth ~10 km P-wave velocity changes from ~5.7 km/s to ~6.1 km/s and S-wave velocity change from ~3.1 km/s to ~3.3 km/s. At depth ~50 km P-wave velocity changes from ~6.9 km/s to ~8.3 km/s and S-wave velocity change from ~4.1 km/s to ~3.7 km/s.

2D vertical body wave velocity images have been obtained from Lohaghat to northwestern side of Sobla, along a plane that strikes N26E. 2D Velocity models for body waves show the extensive disturbances of crust due to underthrusting of Indian plate beneath the Eurasian plate. The outcrops of crystalline complexes in Lesser Himalaya near Thal and Dharchula respectively are well resolved in 2D velocity sections especially in P-wave velocity section. The Conrad discontinuity lies around 12 km depth below mean sea level (msl). The P-wave velocity of upper crust in most of the portion in the section, vary from 4.2 km/s to 5.6 km/s and the same in lower crust vary from 5.6 km/s to slightly more than 7.8 km/s. The S-wave velocity in most of the upper crust in the section, vary from 2.9 km/s to 3.3 km/s and the same in lower crust vary from 3.3 km/s to slightly more than 4.4 km/s.

A 3D shear wave velocity structure up-to a depth of 33 km beneath the Kumaon region has been obtained using the data and developed methodology of tomography using MPFMM. The obtained velocity structure clearly resolves the outcrops of crystalline complexes present in the study region. Alternating zones of low and high velocities have been observed with increasing depth in the upper crust. This may be related to the overturning nature of the crustal layers beneath the Kumaon Himalaya.

Site amplification for all the station locations have been obtained and found some important characteristics. Askot and Didihat are the two areas which show gradual increase in site amplifications with the increases of frequencies, and Bageshwar and Muwani are two areas which show gradual decrease of site amplifications with the increase of frequency. Berinag and Kamedi Devi are the two areas which show almost frequency independent site amplification characteristics.

3D Attenuation tomography is performed up-to a depth of 33 km using the developed tomography method in the Kumaon Himalaya. The quality factor shows variation from near about 0 to 2300 beneath the study area. The crystalline complexes near Didihat and Dharchula are resolved and show quality factor (~650-700) against the background values of (~0-200). The variation of quality factor and wave velocity beneath the Kumaon Himalaya

favours that subsurface layers beneath this region are suffered from overturning and probably rotation.

ACKNOWLEDGEMENT



This thesis arose as a concluding part of my journey in pursuing Ph. D degree in IIT Roorkee. The work out of years of research has been kept on track in form of thesis which has been seen through to completion with the contribution, support and encouragement of numerous people. It is pleasure to convey my gratitude to them in my humble acknowledgement.

First and foremost I thank the incessant source of divine blessings, the almighty God, who always motivates me to move forward with his omens and love.

I would like to acknowledge and extend my heartfelt gratitude to my supervisor Dr. Anand Joshi, Professor, Department of Earth Sciences, Indian Institute of Technology Roorkee. I feel privilege to express my sincere regards to my guide for his valuable guidance, support and constant encouragement throughout the course of my research work. His truly scientific intuition and broad vision inspired and enriched my growth as a student and researcher. The critical suggestions and valuable comments, rendered by him during the discussions are deeply acknowledged. This work would not have been possible without his guidance, support and encouragement. Under his guidance I successfully overcame many difficulties and learned a lot. I humbly acknowledge a lifetime's gratitude to him.

I express my gratitude to the research committee members Prof. M. Israil, SRC Chairman, Dr. Kamal, Internal Expert, Department of Earth Sciences and Prof. J. P. Narayan, External Expert, Department of Earthquake Engineering, for their valuable suggestions throughout the research work. I also express my thanks to Head of the Department Prof. D. C. Srivastava, Prof. A. K. Saraf (former Head), Prof. R. P. Gupta (former Head), Prof. P. K. Gupta (former Head) and Prof. G. J. Chakrapani (former SRC Chairman), Prof. Sandeep Singh, Dean of Alumni Affairs and International Relations, for their academic support and encouragement and for departmental facilities for carrying out my research work.

My special thanks to Nair Ji and other staff of Department of Earth Sciences for their help in dealing with administrative and bureaucratic matters during my research work at IIT Roorkee.

I am also thankful to the Ministry of Earth Sciences (MoES), Government of India supported project (grant no. MoES/P.O.(Seismo)/1(42)/2009) and the Department of Science and Technology (DST), Government of India supported project (grant no. DST/23(483)/SU/2004) for providing strong motion data that have been used practical aspects of research presented in this thesis.

Collective and individual acknowledgements are also owed to my colleagues and friends Ashwani, Parveen, Pushpa, Piu for providing their cooperation, support, healthy and progressive research environment. I consider myself truly blessed as I have always been in a good company of friends. Their love, inspiration, supports and cooperation is beyond the scope of my acknowledgement, yet I would like to express my heartfelt gratitude here to Mandira, Asmita, Sujata, Kamlesh, Sudhakar, Rabin, Alok, Naresh, Pawan, Vivekanand, Tapas and many others for their unflinching support and encouragement and giving me such a memorable and pleasant time in Roorkee.

I express my love and gratitude to my family members for their continuous encouragement and support since my childhood. My parents deserve a special mention for their caring and unconditional support since my childhood. I express my thanks to my elder sister who is the source of inspiration for me since my childhood. Thanks to my brother for being supportive and caring sibling.

Yes, one most important need to survive a person in this physical world which is financial requirements. For this, I want to acknowledge to the Ministry of Human Resources Development (MHRD), Government of India for providing me financial support in form of JRF and SRF, and contingency grants for my research work.

With profound gratitude, love and devotion, I dedicate this thesis to my parents.

Roorkee

December, 2015

(CHINMOY KUMBHAKAR)

TABLE OF CONTENTS

TITLE	PAGE NO.
CANDIDATE'S DECLARATION	i
ABSTRACT	iii
ACKNOWLEDGEMENTS	vii
TABLE OF CONTENTS	ix
LIST OF FIGURES	xiii
LIST OF TABLES	xxi
LIST OF ABBREVIATIONS	xxiii
CHAPTER 1: INTRODUCTION	1
1.1 MOTIVATION AND LITERATURES REVIEW	1
1.2 SEISMIC TOMOGRAPHY AS AN INVERSION	6
1.2.1 Model Parameterization	7
1.2.1.1 Velocity Parameterization	8
1.2.1.2 Interface Parameterization	10
1.2.1.3 Quality Factor Parameterization	12
1.2.2 Traveltime Determination	12
1.2.2.1 Ray Tracing	13
1.2.2.1.1 Shooting Method	13
1.2.2.1.2 Bending Method	16
1.2.2.2 Wavefront Tracking	19
1.2.2.2.1 Finite Difference Schemes	19
1.2.2.2.2 Fast Marching Method	21
1.2.2.3 Review on Improved Fast Marching Methods	22
1.2.2.3.1 The Shifted Grid Fast Marching Method	22
1.2.2.3.2 The Group Marching Method	23
1.2.2.3.3 The FMM on Spherical Domain	23
1.2.2.3.4 The FMM Based on Source Neighbourhood Refinement	24
1.2.2.3.5 The Untidy Fast Marching Method	24
1.2.3 Determination of Spectral Acceleration	24
1.2.4 Inverse Step of Tomography	26
1.2.4.1 Objective Function of an Inverse Problem	26
1.2.4.2 Gauss-Newton Method and Damped Least Square Method	29
1.2.5 Analysis of Solution Quality	31
1.2.5.1 Resolution and Covariance matrices	31
1.2.5.2 Synthetic Tests	32
1.3 A BRIEF REVIEW OF TOMOGRAPHY METHODS IN PRACTICES	33
1.4 REGIONAL GEOLOGICAL SETUP	34
1.5 REGIONAL TECTONIC SETTINGS AND SEISMICITY OF STUDY REGION	38
1.6 A BRIEF REVIEW ON UNDERLYING VELOCITY STRUCTURE OF THE HIMALAYAN TERRAIN	41
1.7 A BRIEF REVIEW ON UNDERLYING ATTENUATION STRUCTURE OF THE HIMALAYAN TERRAIN	44
1.8 SYNTHESIS OF THE PROBLEMS AND OBJECTIVES THE PRESENT WORK	47

1.9	THE WORKS PRESENTED IN THE THESIS	50
1.10	OVERVIEW OF THE THESIS	51
CHAPTER 2:	RAY TRACING	53
2.1	INTRODUCTION	53
2.2	MODEL PARAMETERIZATION: TYPE-A AND TYPE-B	54
2.3	VECTOR EQUATIONS FROM SNELL'S LAW	55
2.3.1	The Equation of a Refracted Ray for a given Incident Ray on a given Surface	55
2.3.2	The Equation of a Reflected Ray for a given Incident Ray on a given Surface	59
2.3.3	The Intersection Point of a Plan and a Line	60
2.4	BASIC ALGORITHM OF RAY-TRACING USING TYPE-A PARAMETERIZATION	61
2.5	ALGORITHM OF RAY TRACING USING TYPE-B PARAMETERIZATION	65
2.6	THE SPIRAL PATH SEARCH METHOD (SPSM)	67
2.6.1	Equation of Spiral	67
2.6.2	Equation of Discrete Take off Vector	68
2.7	AN ALGORITHM TO COMPUTE TWO POINT RAY TRACING	71
2.8	NUMERICAL EXPERIMENTS	72
2.8.1	Experiment 1	72
2.8.2	Experiment 2	74
2.8.3	Experiment 3	75
2.8.4	Experiment 4	77
2.8.5	Experiment 5	78
2.8.6	Experiment 6	80
2.9	CONCLUSIONS	81
CHAPTER 3:	NUMERICAL EXPERIMENTS ON FAST MARCHING METHOD	83
3.1	INTRODUCTION	83
3.2	GENERAL SOLUTION OF UPWIND DIFFERENCE SCHEME	84
3.3	IMPLEMENTATION OF NARROW BAND TECHNIQUE	85
3.4	INCORPORATION OF HEAP SORTING IN NARROW BAND	87
3.5	NUMERICAL CASE STUDIES	88
3.5.1	Experiment 1	89
3.5.2	Experiment 2	94
3.5.3	Experiment 3	96
3.5.4	Experiment 4	98
3.5.5	Experiment 5	101
3.5.6	Experiment 6	102
3.5.7	Experiment 7	104
3.5.8	Experiment 8	105
3.5.9	Experiment 9	106
3.5.10	Experiment 10	108
3.6	CONCLUSIONS	109
CHAPTER 4:	MULTISTENCILS PSEUDOANISOTROPIC FAST MARCHING METHOD	111
4.1	INTRODUCTION	111
4.2	MULTISTENCILS FAST MARCHING (MSFM) METHOD	112

4.3	CONCEPT OF PSEUDOANISOTROPIC GRADIENT	112
4.4	ANGULAR WEIGHTED INTERPOLATION	113
4.5	MULTISTENCILS PSEUDOANISOTROPIC FAST MARCHING METHOD (MPFMM)	115
4.5.1	2D Multistencils Pseudoanisotropic Fast Marching Method	115
4.5.1.1	Interpolation of Directional Derivatives in 2D Stencils	115
4.5.1.2	The Upwind Equation	119
4.5.1.3	Upwind Condition	120
4.5.2	3D Multistencils Pseudoanisotropic Fast Marching Method	121
4.5.2.1	Interpolation of Directional Derivatives in 3D Stencils	121
4.5.2.2	The Upwind Equation	123
4.5.2.3	Upwind Condition	127
4.6	COMPUTATIONAL COMPLEXITIES	127
4.7	NUMERICAL EXPERIMENTS	127
4.7.1	Accuracy	128
4.7.1.1	Experiment 1	129
4.7.1.2	Experiment 2	131
4.7.1.3	Experiment 3	132
4.7.1.4	Experiment 4	133
4.7.1.5	Experiment 5	135
4.7.1.6	Experiment 6	136
4.7.2	Effects of Multistencils in Accuracy	137
4.8	CONCLUSIONS	138
CHAPTER 5: SEISMIC TOMOGRAPHY OF NATURAL LATERED EARTH: MULTIPARAMETER INVERSION		139
5.1	INTRODUCTION	139
5.2	MODEL CONSIDERATION	140
5.3	REPRESENTATION OF MODEL VECTOR AND DATA VECTOR	141
5.4	FORMULATION OF THE INVERSE PROBLEM	144
5.5	DERIVATION OF FRÉCHET DERIVATIVES	149
5.6	ALGORITHM TO COMPUTE FRÉCHET DERIVATIVES	157
5.7	ALGORITHM TO INVERSION	161
5.8	GRADIENT PATH SEARCH METHOD	163
5.9	JOINT WORKING OF GPSM AND SPSM	165
5.10	CONCLUSIONS	167
CHAPTER 6: SEISMICITY AND SUBSURFACE STRUCTURES OF THE KUMAON HIMALAYA		169
6.1	INTRODUCTION	169
6.2	STRONG MOTION NETWORK AND DATA	171
6.3	SEISMICITY AND 1D VELOCITY MODELS OF KUMAON HIMALAYA	173
6.3.1	Practical Consideration and Method	173
6.3.2	Results	174
6.4	2D AND 3D VELOCITY MODELS OF KUMAON LESSER HIMALAYA	177
6.4.1	Methodology	178
6.4.2	2D Results	180
6.4.3	3D Results	181
6.5	DISCUSSIONS	181
6.5.1	Seismicity	183

6.5.2	Velocity models	184
6.6	CONCLUSIONS	186
CHAPTER 7:	3D ATTENUATION STRUCTURES OF THE KUMAON HIMALAYA	187
7.1	INTRODUCTION	187
7.2	TOMOGRAPHY METHOD	188
7.3	SITE AMPLIFICATION	190
7.4	STUDY REGION, STRONG MOTION NETWORK AND DATA	190
7.5	COMPUTATION OF SITE AMPLIFICATION AND RESULTS	191
7.6	COMPUTATION OF ATTENUATION TOMOGRAPHY AND RESULTS	191
7.7	DISCUSSIONS	191
7.7.1	Site Amplification	191
7.7.2	Attenuation Tomography	195
7.8	CONCLUSIONS	196
CHAPTER 8:	CONCLUSIONS	197
	LIST OF PUBLICATIONS FROM THE RESEARCH WORK	203
	BIBLIOGRAPHY	205

Figure No.	LIST OF FIGURES	Page No.
1.1	Different types of velocity parameterization: (a) constant velocity blocks, (b) a grid of velocity nodes, and (c) triangulated velocity grid (after White, 1989).	8
1.2	Schematic representation of a typical layered velocity structure that is imaged in traveltimes tomography. The velocity functions describe the velocity variations for different layers.	10
1.3	Types of interface parameterization used in 2D (a, b) and 3D (c, d) models. (a) Piecewise linear segments, (b) piecewise cubic B-spline curve, (c) surface defined by mosaic of triangular patches, (d) surface defined by mosaic of bicubic B-spline patches.	11
1.4	Principle of the shooting method. The initial take-off angle of ray 1 is iteratively adjusted until the final ray (4) passes sufficiently close to the receiver.	14
1.5	Principle of the bending method. The initial ray path (ray 1) is adjusted until it satisfies Fermat's principle (ray 4).	17
1.6	Principle of the pseudo-bending method of Um and Thurber (1987). An initial guess ray path defined by three points is provided. The center point is perturbed to best satisfy the ray equation. Then the number of segments is doubled and the process is repeated.	18
1.7	The procedure of finite difference method (a) and expanding square method (b) to obtain traveltimes field as introduced by Vidale (1988). Traveltimes to the filled circles are calculated from the open circles. The filled square is the source.	20
1.8	Schematic illustration showing how the expanding square method can fail to find first arrival ray path. The traveltimes along path 1 is determined by the expanding square but path 2 has a shorter traveltimes due to the high velocity zone.	21
1.9	Figure 1.9: Figure showing the geology and tectonic settings of Himalayan belt (a) and of a magnified portion of the study area (b), modified after Valdia (1980).	37
1.10	Schematic cross section through the Kumaun Himalaya modified after C��lerier et al. (2009).	39
2.1	Model parameterization; Type-A, a; Type-B, b.	54
2.2	Geometry of refracted ray and reflected ray for a incident ray on a plane having normal vector, \mathbf{n} . In the diagram θ_i , θ_r and θ_l are respectively incident angle, refracted angle and reflected angle.	55
2.3	Geometry of refracted ray paths, for case 1, (a) and case 2, (b), redrawn from Figure 2.2 in two dimensions.	56

2.4	Geometry of reflected ray paths redrawn from Figure 2.2 in two dimensions.	59
2.5	An algorithm to find intersection point between a straight line formed by a given vector point, ps_o and a given tangent, m and a plane out of three planes with weight, w .	62
2.6	The basic ray tracing algorithm. All the shapes in the Figure have standard meanings.	64
2.7	The replacement units of IL-B to convert the same into IL-C. The sub-process A is added in IL-A to convert the same into MIL-A (a) which is added in IL-B to convert the same into IL-C (b).	66
2.8	Equispaced discrete points on a spiral.	68
2.9	Geometry of spiral and its location with respect to source position at origin, O.	69
2.10	Geometry of nine nodes used to define parameters for next iteration in spiral search. Grid point n_m and 8 corresponds to the first and second least errors respectively in first iteration.	70
2.11	A two point ray tracing algorithm is shown.	72
2.12	A model of uniform velocity medium.	73
2.13	Ray path obtained for the model considered in Figure 2.12.	73
2.14	A model with two media having different velocities.	74
1.15	Ray path obtained for the model considered in figure 2.14.	75
2.16	A model of uniform high velocity burried body in a uniform medium.	76
2.17	Ray path obtained for the model considered in Figure 2.16.	76
2.18	A Model having constant gradient of velocity along Z axis.	77
2.19	Ray paths obtained for two station locations for the model considered in Figure 2.18.	78
2.20	A model whose velocity varies in two directions according to the velocity function shown in the same figure.	79
2.21	Ray paths for two type of velocity function for the model considered in Figure 2.20. Red ray path is obtained for the velocity function shown in the model but black ray path is obtained when the variation of velocity along z axis is not allowed.	80
2.22	The ray path in three dimensions for a model having same positive constant velocity gradient along X and Y axis but along the Z axis gradient is constant	81

but negative.

- 3.1 Narrow band or wavefront evolution technique. Gray points are the Alive points, black points and red point are Close points in which red point is having minimum traveltimes and white points are Far points. The upwind side contains all the Alive grid points and downwind side contains all the Far grid points. 86
- 3.2 An algorithm to compute traveltimes to a set of grid points. 86
- 3.3 Schematic diagram showing two types of binary tree; a complete binary tree (a) and a incomplete binary tree (b). 87
- 3.4 Schematic diagram showing three dimensional homogenous model. 89
- 3.5 A depth slice of the wavefronts through source, showing that at equal interval of time wavefronts propagate equal distance in a homogenous medium (the results obtained for model in Figure 3.4). The time interval between two successive wavefronts is two seconds, which is also shown on the colour scale for the contour. 90
- 3.6 Position of the wavefront above the source or $Z=50$ km at 20 s within the model in figure 2.1 (After plotting the results obtained for model in Figure 3.4) (A) A view from above (0,0,0) coordinates (B) a view from above (300,300,0) coordinates. 91
- 3.7 Position of the wavefront above the source or $Z=50$ km at 30 s within the model in Figure 3.4 (After plotting the results obtained for model in Figure 3.4) (A) A view from above (0,0,0) coordinates (B) a view from above (300,300,0) coordinates. 92
- 3.8 Position of the wavefront above the source or $Z=50$ km at 45 s within the model in Figure 3.4 (After plotting the results obtained for model in Figure 3.4) (A) A view from above (0,0,0) coordinates (B) a view from above (300,300,0) coordinates. 93
- 3.9 A three dimensional model having two media of different velocities (After sketching). The velocity of upper medium is 4.0 km/s and that of lower is 7.0 km/s. 94
- 3.10 A portion of vertical slice of the wavefronts through the source, illustrating the Snell's law (After plotting the results obtained for model in Figure 3.6). A ray path (red line in the above figure) has been drawn for offset verification by Snell's law. The offsets at the boundary and at $Z=100$ km along the X axis travelled by the sketched ray obey the Snell's law of refraction. The blue line shows the critical offset along the X axis beyond which head waves starts generating. The yellow line shows a normal at the boundary at which refraction of red line (red ray) takes place. The time interval between two successive wavefronts is 5 seconds. 95
- 3.11 A portion of vertical slice of the wavefronts through the source; illustrating that beyond the crossover distance it is the critically refracted head waves that are the first arrivals (After plotting the results obtained for model parameter in 97

Table 3.3). The red lines in the figure are the ray paths for critically refracted head waves. The white line indicates the boundary separating two media and the yellow lines are normals at the boundary at different position shown in the figure. The longest yellow line marks the critical offset along X axis. The time interval between two successive wavefronts is three seconds.

- 3.12 A three dimensional model showing a high velocity vertical slab parallel to Y-Z plane of the model; cutting a three dimensional homogeneous medium (After drawing). 98
- 3.13 A vertical section of the wavefronts through the source showing that the disturbance of wavefronts propagating in a uniform low velocity medium by a high velocity uniform slab happens in such a way that the wavefronts after crossing the slab remains parallel to the wavefronts what would have existed if the slab were not present (After plotting the results obtained for model in Figure 3.9). The blue line marks, at the surface of the slab, the critical offset along Z axis. The ray path (yellow line) after crossing the boundary makes an offset from its original path indicated by white line. The velocities are shown on the colour scale on the right side of the figure. The time interval between two successive wavefronts is two seconds. 99
- 3.14 A three dimensional view of the wavefront within the model at 36s and above the source or $Z=20$ km (After plotting the results obtained for model in figure 3.12). (A) A view from above (0,0,0) coordinates; (B) a view from above (250,200,20) coordinates. 100
- 3.15 A three dimensional heterogeneous model whose velocity function is given in the Table 3.5. 101
- 3.16 A vertical slice of the wavefronts through the source; showing how the spacing between two consecutive wavefronts depends upon time and position of the wavefronts (After plotting the results obtained for the model in figure 3.12). The time interval between two successive wavefronts is two seconds. The velocities of the medium are shown on the colour scale on the right side of the figure and the red star indicates the source position. 102
- 3.17 A three dimensional model showing a heterogeneous buried body within a heterogeneous medium. 103
- 3.18 A vertical slice of the wavefronts through the source; showing the behavior of the wavefronts within the heterogeneous model (After plotting the results obtained for model the in Figure 3.14). The deep green line shows the path along which there is no change of velocity (except within the buried body where it becomes 0.3 times more than the surrounding medium) and hence along this direction at any point the relation of distance, time and velocity can be easily verified. The yellow lines are drawn for verification of the latter statement. The time interval between two successive wavefronts is two seconds. The velocities of the medium are shown on the colour scale on the right side of the figure and the red star indicates the source position. 103
- 3.19 A simplistic three dimensional subduction model (After drawing). 104

3.20	A portion of vertical section of the wavefronts through the source; showing that only head waves are first arrivals on the exposed surface of subducted plate for the model under consideration (After plotting the results obtained for the model in Figure 3.19). The time interval between two successive wavefronts is one second. The velocities of different plates are shown on color scale below the figure and the red star indicates the source position.	105
3.21	A vertical section of the wavefronts through the source; showing the behavior of waves through the plumbing system (After plotting the results for the model considered in section 3.21) The medium velocities and the velocities of the plumes are shown on the color scale on right side of the figure. (A) A vertical section for the source position at (150,10,10) km; (B) a vertical section for the source position at (10,10,100) km. The time interval between two successive wavefronts is two seconds and the source position are indicated by red star.	106
3.22	Anticline and syncline model; in one case the Y-direction is considered without dip and in another case the Y-direction is considered with a dip of 6.7° . Direction of strike is along Y-axis in the model.	107
3.23	The computed traveltimes contours; (a) when source is at (50,50,1) km and (b) when source is at (100,50,1) km obtained using the model in Figure. 3.22 without applying dip in the Y-direction. The computed traveltimes contours; (c) when source is at (50,50,1) km and (d) when source is at (100,50,1) km obtained using the model in Figure. 3.22 after applying dip of 6.7° in the Y-direction.	108
3.24	Vertical section of the normal fault model in the X-Z plane, with X-axis as dip direction, (a); Contours of traveltimes for the normal fault considered in case study, (b); Vertical section of Horst and Graben type of fault model in the X-Z plane, (c); Contours of traveltimes for Gaben and Horst type fault considered in case study, (d).	109
4.1	Schematic diagram showing angular interpolation in 2D (a) and 3D (b).	114
4.2	The stencil S_v centered at point (x, y) that intersects the 2D lattice at diagonal grid points p_5, p_6, p_7 and p_8 . The natural stencil intersects the 2D lattice at grid points p_1, p_2, p_3 and p_4 . q_5 and q_7 are two hypothetical grid points.	116
4.3	Stencil S_w centered at point (x, y, z) that intersects the 3D lattice at the grid points $p_{11}, p_{12}, p_{19}, p_{20}, p_{21}$ and p_{22} . OA, OB and OC are three straight line depicting direction along which interpolation scheme is applied.	121
4.4	The proposed stencils for the 3D Cartesian domain. T_1 , T_2 and T_3 are minimum traveltimes along each arm of the stencil. (a) S_1 . (b) S_2 . (c) S_3 . (d) S_4 . (e) S_5 . (f) S_6 . (g) S_7 . (h) S_8 . (i) S_9 . (j) S_{10} .	125
4.5	Contours of T_1 , (a); T_2 , (b); T_3 , (c) and T_4 , (d).	129
4.6	Contours of error norm L_1 computed from FMM (a, c) and MPFMM (b, d)	130

using grids of size 81×81 and isotropic spacing 0.5×0.5 (a, b) and anisotropic spacing 0.4×0.8 (c, d). The source position in all the cases is at the center of the grid structure.

- 4.7 Cross sections in the travelttime field of a 3D unit speed wave that propagate from the center of a coarse grid of size $81 \times 81 \times 25$ and spacing $0.4 \times 0.8 \times 0.5$ using (a) FMM and (b) the proposed MPFMM. It is seen that the proposed MPFMM provides better high-curvature solution that the FMM. 137
- 5.1 A schematic 3D layered structural model where q indicate layer number as well as upper discontinuity-surface bounding the same layer. N_L is the total number of layers considered in the model. 140
- 5.2 A special configuration of three adjacent layers in the model in Figure 5.1 in which the left side of middle layer of upper figure is very thin and can be approximated to a realistic situation shown in lower figure, where middle layer have sharp end. 141
- 5.3 Schematic diagrams showing 16 nodes of a bicubic Surface (a) and a typical bicubic surface (b) given by 16 nodes. 142
- 5.4 Phenomena of internal reflection by discontinuity surface by a segment of arbitrary ray path. The numbering of elementary points, starting from r^{th} point is shown. The layer number between r and $r+1$ is r . The false layer or pseudo layer, $r+1$ lies between elementary point $r+1$ and $r+2$ in the figure. 149
- 5.5 A unit of algorithm to compute coefficients B in Equation (5.57) for a source station ray path. 158
- 5.6 A unit of algorithm to compute coefficients C in Equation (5.64) for a source station ray path. 159
- 5.7 A unit of algorithm, DEVL to compute length derivatives in Equation (5.33). 160
- 5.8 Integrated algorithm to compute Fréchet derivatives for a source-station ray path. 161
- 5.9 The work flow tomographic inversion using DLS inversion. 163
- 5.10 An algorithm (IL-Q) to update the take off vector at the position of a hypocenter using GPSM. 165
- 5.11 A part of an algorithm to solve forward problem using Gradient Path Search Method. 166
- 6.1 Overview map with the topography and major tectonic settings of the Himalayan terrain covering the Kumaon Lesser Himalaya. The strong motion stations of local network are marked by red solid triangles. 172
- 6.2 The geology and tectonic setting of the region after GSI (2000). The study region is marked by rectangle SPQR. Direction from A to B, marked by white 172

line dividing the rectangle SPQR into two equal halves and making an angle of 26° with respect to north, is the direction along which vertical section of velocity structure is investigated. Locations of seismographs are denoted by solid black triangles.

- 6.3 The above figures depict epicentral distribution of relocated earthquakes, a; an enlarge view of figure a, b; depth wise distribution along constant longitudes, c; depth wise distribution along constant latitudes, d; initial rmstraveltime residuals, e; final rmstraveltime residuals, f. 175
- 6.4 Map showing the positions of relocated events. 176
- 6.5 The above figures show the 1D velocity models of the Himalayn terrain. With the obtained velocity models shown by red line plot, two other velocity models for P-waves and S-waves given by Mukhopadyay and Sharma (2010) and Monsalve et al. (2006) are also shown to study the depth variation of Moho. 176
- 6.6 A cell of grid showing inversion and interpolated non-inversion nodes. The inversion nodes are shown with brown spheres and non-inversion nodes are shown by red stars. The primary velocities are figured. 178
- 6.7 Vertical section of P-wave velocity structure (a) and S-wave velocity structure (b) of the Kumaon Himalaya along line AB in map (Figure 6.2). The distribution of absolute values of standard errors for P-wave and S-wave velocity structures are shown in (c) and (d) respectively. 181
- 6.8 Depth slices of velocity structure (a) and resolution matrix (b) at different depths from about 1.5 km above msl to 31.5 km below msl. The velocity structure is obtained beneath the Kumaon Himalaya in the region marked by SPQR in Figure 6.2. 182
- 6.9 Depth slices of absolute values of standard errors at different depths from about 1.5 km above msl to 31.5 km below msl. Standard errors correspond to 3D velocity variation in Figure 6.8 (a). 183
- 7.1 The obtained value of site amplification factors at each station (a-r) using strong motion data. The factors are shown in scatter plot by cross. The mean standard errors in computed factors for different stations are shown on right sides of station names in parentheses. 193
- 7.2 Depth slices of quality factor contours at an interval of 3 km in the study region (Figure 6.2) marked by rectangle SPQR. 194
- 7.3 A vertical section of quality factor variation along the white line in Figure 6.2. The color scale is same as that of Figure 7.2. 194

Table No.	LIST OF TABLES	Page No.
2.1	The parameters taken for the model in Figure 2.12	73
2.2	The parameters taken for the model in Figure 2.14	74
2.3	Parameters taken for the model in Figure 2.16	76
2.4	Parameters taken for the model in Figure 2.18	77
2.5	Parameters taken for the model in Figure 2.20	79
2.6	Parameters for the model considered in Figure 2.22	80
3.1	Parameters for the model considered in Figure 3.1	89
3.2	Parameters for the model considered in Figure 3.9	95
3.3	Modified parameters for the model considered in Figure 3.9	97
3.4	Parameters for the model considered in Figure 3.9	98
3.5	Parameters for the model considered in Figure 3.15	101
3.6	parameters for the model considered in figure 3.16	104
3.7	Parameters of a model to study anticline and syncline	107
4.1	Proposed Unit vectors	126
4.2	Traveltime Functions for both 2D and 3D Cartesian Domains	128
4.3	Error Norms of the Computed T_1 from Different Source Points in an Isotropic Grid of Size 81×81 and Grid Spacing 0.5×0.5	131
4.4	Error Norms of the Computed T_1 from Different Source Points in an anisotropic Grid of Size 81×81 and Grid Spacing 0.4×0.8	131
4.5	Error Norms of the Computed T_2 from Different Source Points in an Isotropic Grid of Size 81×81 and Grid Spacing 0.5×0.5	132
4.6	Error Norms of the Computed T_2 from Different Source Points in an anisotropic Grid of Size 81×81 and Grid Spacing 0.4×0.8	132
4.7	Error Norms of the Computed T_3 from Different Source Points in an Isotropic Grid of Size 71×71 and Grid Spacing 0.5×0.5	133
4.8	Error Norms of the Computed T_3 from Different Source Points in an	133

	anisotropic Grid of Size 71×71 and Grid Spacing 0.4×0.8	
4.9	Error Norms of the Computed T_4 from Different Source Points in an Isotropic Grid of Size 51×51 and Grid Spacing 0.4×0.4	134
4.10	Error Norms of the Computed T_1 from Different Source Points in an anisotropic Grid of Size 51×51 and Grid Spacing 0.4×0.6	134
4.11	Error Norms of the Computed T_5 from Different Source Points in an Isotropic Grid of Size $41 \times 41 \times 41$ and Grid Spacing $0.5 \times 0.5 \times 0.5$	135
4.12	E Error Norms of the Computed T_5 from Different Source Points in an Isotropic Grid of Size $41 \times 41 \times 41$ and Grid Spacing $0.4 \times 0.8 \times 0.6$	135
4.13	Error Norms of the Computed T_6 from Different Source Points in an Isotropic Grid of Size $51 \times 51 \times 31$ and Grid Spacing $0.5 \times 0.5 \times 0.5$	136
4.14	Error Norms of the Computed T_6 from Different Source Points in an anisotropic Grid of Size $51 \times 51 \times 31$ and Grid Spacing $0.4 \times 0.5 \times 0.6$	136
4.15	Error Norms of the Computed T_1 for different set of stencils incorporated in MSFM and MPFMM	137
5.1	Coefficients in Equation set (5.62)	155
6.1	Strong Motion Network	171
6.2	1D Velocity Models in the Himalayan Terrain	174
6.3	Obtained 1D velocity models	177
7.1	Initial model of shear wave quality factor considered	191

LIST OF ABBREVIATIONS

The following table describes the meanings of various abbreviations and acronyms used throughout the thesis. The page number on which each one is defined or first used is also given.

Abbreviation	Meaning	Page No.
No.	Number	vii
MoES	Ministry of Earth Sciences	Vii
msl	mean sea level	v
CSW	Continuous Surface Wave	2
MASW	Multichannel Analysis of Surface Wave	2
NORSAR	Norwegian Seismic Array	2
FFT	Fast Fourier Transform	3
3D	Three Dimensional	4
2D	Two Dimensional	5
PREM	Preliminary Reference Earth Model	5
1D	One Dimensional	5
FMM	Fast Marching Method	6
CVB	Constant Velocity Block	8
CVV	Constant Velocity Voxel	8
CQFB	Constant Quality Factor Block	12
SGFM	Shifted Grid Fast Marching	22
GMM	Group Marching Method	23
CPU	Central Processing Unit	24
UFMM	Untidy Fast Marching Method	24
DLS	Damped Least Square	31
LET	Local Earthquake Tomography	33
km	Kilometer	33
ITSZ	Indus-Tsangpo Suture Zone	35
THS	Tethyan Himalayan Sequence	36
GHC	Great Himalayan Crystalline	36
LHS	Lesser Himalayan Sequence	36

NW	North West	36
STD	South Tibetan Detachment	38
MCT	Main Central Thrust	38
MBT	Main Boundary Thrust	38
HFT	Himalayan Frontal Thrust	38
MF	Martoli Fault	39
PT	Panjaj Thrust	39
mm	millimeter	39
yr	year	39
mb	body-wave magnitude	39
NAT	North Almora Thrust	40
SAT	South Almora Thrust	40
s	Second	41
NS	North South	42
NW	North West	42
NE	North East	43
SW	South West	43
E	East	43
Hz	Hertz	45
MSFM	Multistencils Fast Marching	48
MPFMM	Multistencils Pseudoanisotropic Fast Marching Method	50
IL	Integrated Algorithm	65
MIL	Modified Integrated Algorithm	65
SPSM	Spiral Path Search Method	67
MSFMM	Multistencils Fast Marching Method	127
GPSM	Gradient Path Search Method	163
USA	United States of America	171
MHT	Main Himalayan Thrust	174



INTRODUCTION

1.1 MOTIVATION AND LITERATURES REVIEW

Seismic data are among the most common and valuable resources for investigating the internal structure of Earth. One of the first people to deduce the deep interior structure of Earth from seismic records was Richard Dixon Oldham. In 1906, he identified the separate arrivals of P-waves, S-waves and surface waves on seismograms and found the clear evidence of the presence of Earth's core from the absence of direct P and S arrivals at source receiver distances beyond about 100° . In 1909, Andrija Mohorovičić, a Serbian seismologist observed two distinct traveltimes curves from a regional earthquake. He concluded that one curve corresponded to a direct wave through the crust and other to a wave refracted by a discontinuity in elastic properties between crust and mantle. This worldwide discontinuity is now known as the Mohorovičić discontinuity or Moho in short. The method of Herglotz and Wiechart as described in Gubbins (1992) was used in a wide scale in 1910 to determine one dimensional whole earth model. The method uses relationship between ray parameter and angular distance to determine velocity as a function of radius within the earth. Rapid improvement of seismographs in the late 19th and early 20th century allow the scientist to construct travel time table (arrival times of seismic waves as a function of distance from the earthquakes) and the first widely used tables were produced by Zoeppritz in 1907. Beno Gutenberg reported the accurate estimate of depth of Earth's core using the travel time tables published by him in 1914. Harold Jeffreys was the first to claim in 1926 that the material state of the Earth's core is liquid. Later on in 1936, Inge Lehmann discovered that the earth has a solid inner core inside a molten outer core.

Travel time curves were widely used in the early and mid 20th century to determine Earth's average velocity versus depth structure. In the beginning of 1960s, a new type of tool

called seismological arrays helped to lower the detection threshold of global earthquakes and specially of nuclear explosions and provided a possibility of resolving the fine structure of the Earth's interior (Birtill and Whiteway, 1965; Whiteway, 1966; Wright, 1972; Doornboos and Husebye, 1972; Weber et al., 1996). These seismological instruments consist of numerous seismometers placed at discrete points in a well-defined configuration (Husebye and Ruud, 1989). One of the best examples of earliest and largest array is NORSAR (Norwegian Seismic Array). This was initially established to provide data for research on seismological detection and classification problems, and to provide event monitoring functions in the possible advent of a comprehensive test ban treaty (Bungum et al., 1971). Later on, NORSAR has broadened its research activities which include subjects like earthquake hazard, risk assessment, micro-seismicity, and seismic modelling for the petroleum exploration purpose.

Advancement of digital innovation in seismographs took place around 1970s and 1980s. The digital seismographs have a wider range of frequencies and high level of signal to noise ratio. Recording with these instruments facilitates the study of microearthquakes (Gupta et al., 1996; Paul et al., 2010). The array measurement techniques have been boosted up by these instruments. Many authors including Kuo et al. (2009) and Lin et al. (2009) have used recordings of microearthquakes from seismological array to study the subsurface features. Gibbons et al. (2007) have given an insight to the use of multichannel waveform correlation over network and array to improve the low magnitude event detection capabilities.

Today, an abundance of methods is available for determination of Earth's internal structure where different components of seismic records like traveltime, amplitude, waveform spectra, full waveform or entire wave-field may be used. The configurations of source-receiver array also differ. The array may be inline or cross line. Sources may be natural or artificial, location of sources may be close or distant to the receiver, and the scale of study may be tens of meters to the whole earth.

Surface waves usually dominate the seismogram and show dispersive characteristics (frequency dependence of velocity). The use of surface waves for investigation of subsurface structure started in mid 20th century when the early pioneering work of Van der Pol (1951), Jones (1955) lead to the birth of Continuous Surface Wave (CSW) method (Matthews et al., 1996). Later on, other parallel methods like spectral analysis of surface waves (SASW) and multichannel analysis of surface waves (MASW) methods were developed. An approximate chronological order of historical developments of these methods can be found in Park and Ryden (2007).

The surface wave method makes use of dispersive property (frequency dependence of velocity) of Rayleigh and Love waves to derive shear wave velocity versus depth profile. Briefly, a Fast Fourier Transform (FFT) is applied to a time domain record to convert the same into frequency domain from which phase shifts of different frequencies are obtained. The phase shifts are then used to compute variation of phase velocity with frequency or time period. The phase velocity curves are then applied in an inversion scheme to obtain shear wave velocity model of subsurface (Mohan et al., 1992; Chauhan and Singh, 1996; Mohan et al., 1997; Singh et al., 1999; Xia et al., 1999; Rahimi et al., 2014). There are some other applications of surface wave dispersion method such as anomaly detection (Park et al., 1998; Phillips et al., 2004; Nasser-Moghaddam, 2006) and soil damping evaluation (Rix and Lai, 1998; Rix et al., 2001).

An alternative method which is comparatively new for determination of subsurface velocity structure is one that uses receiver function. The receiver function technique was originally developed by Langston (1979) and was then improved by various authors including Ammon et al. (1990), Cassidy (1992), Shibutani et al. (1996), Sambridge (1999) and Park and Levin (2000), for different aspects such as spectral estimation, inversion etc. The receiver functions rely on teleseismic earthquakes which contain the information of the earth's features along long travel paths. One can obtain the partial impulse response of the earth just beneath the station by removing the common feature from the source and most of the paths which are recorded on different components. The resultant estimated function is then inverted using some inversion schemes to obtain velocity-depth model in the vicinity of the station. The receiver function methods are very sensitive to the velocity discontinuities and hence these are useful to insight the earth's heterogeneities beneath the stations. However, the information provided by this method is limited to a volume beneath a single station and the obtained velocities are insensitive to the absolute velocity unless surface waves are added. Further, limitations come from the simplified assumptions which cannot explain real earth features including dipping layers, anisotropy and two or three dimensional velocity distributions. Many authors in the recent past have used receiver function techniques to obtain the earth's subsurface velocity structures. Some of them are Cruz-Atienza et al. (2001), Rai et al. (2006), Hazarika et al. (2013) and Kumar and Mohan (2014).

The receiver functions are mostly sensitive to sharp velocity changes and relatively insensitive to the average velocity and smooth velocity changes whereas surface wave dispersion techniques are sensitive to average shear velocity and largely insensitive to sharp velocity contrasts (Lawrence and Wiens, 2004). Combining these complimentary tools in a single inversion scheme allows for more unique analyses of subsurface structure (Julia et al.,

2000). Several workers (Last et al., 1997; Lawrence and Wiens, 2004) have combined successfully analyses of receiver functions and surface wave techniques to derive more unique solutions than either of the techniques in isolation.

Besides the studies of Earth's internal velocity structure, the studies of seismic attenuation play a very significant role in mapping the subsurface heterogeneities. The seismic attenuation is the decay of seismic wave energy due to spherical and inelastic propagation of seismic waves through the earth from the source. The attenuation is quantified using the inverse of a dimensionless quantity known as quality factor (Q). The quality factor is sensitive to temperature, fluids, compositional differences, and other rock properties which are distinct from that provided by P and S wave velocities. Therefore, the study of seismic attenuation is very important for material identification, tectonic interpretation, quantification of ground motion (Hoshiya, 1993; Akinci et al., 1995; Del Pezzo et al., 1995; Bianco et al., 1999, 2002), which are related to the estimation of seismic hazard of an area (Pulli, 1984; Herraiz and Espinosa, 1987; Havskov et al., 1989; Sato and Fehler, 1998; Paul et al., 2003; Mukhopadhyay and Tyagi, 2007; Allen et al., 2007). Most commonly, the attenuation is estimated either from body waves (Joshi, 2010), surface waves (Xia, 2014) or coda waves (Ma'hood et al., 2009, 2011).

One of the most common and widely used methods to estimate quality factor is coda normalization method. In this method, the coda waves are used as a proxy for the source and remove it from the S wave spectrum as described by Aki (1980a, b), Yoshimoto et al. (1993). Least square fit is then made to the amplitude as a function of distance in small frequency band. The slope of the obtained fit function is related to the path attenuation Q^{-1} at central frequency of each band and hence it is converted to power-law Q model for each station. The estimation of quality factor using coda waves gives its volumetric average of value around the station network.

So far the methods have been outlined which give depth wise variation of earth's subsurface velocity or average estimation of quality factor. Recent developments in solid earth geophysics, such as plate tectonics, earthquake prediction, and exploration for geothermal energy demand increasingly detailed information about three dimensional (3D) earth's internal structure. In that context, seismic tomography is a very important tool for imaging the earth's internal structures using seismic data. It is not a single method rather a class of methods specially differing from each other by the type of data that are used in different methods. The data type may be traveltime when the method is called traveltime tomography, it may be amplitude when the method is called attenuation tomography or it

may be full waveform or a portion of spectra with their own nomenclatures. The word *tomography* literally means *picture of a slice* (from the Greek word *tomos* meaning *slice*). The terminology was first used in medical imaging to describe the process of imaging the internal density distribution of human body using X-ray (Lee and Pereyra, 1993). The term was later appropriated by the almost all branches of sciences including seismology.

The first breakthrough two dimensional (2D) seismic tomographic regional map was produced by Aki and Lee (1976) using the data from NORSAR. The method implemented functional derivatives of seismic measurement with respect to structural model parameters (Backus and Gilbert, 1967; Fréchet, 1941; Woodhouse, 1974), which is most commonly known as Fréchet derivatives, Fréchet kernels or sensitivity kernels. Later on the use of the functional derivatives became so popular that these became backbone of subsequent tomography studies (Woodhouse, 1974, 1981; Dziewonski and Anderson, 1981; Woodhouse and Dziewonski, 1984). Soon after the publication of Preliminary Reference Earth Model (PREM, the first well-accepted one dimensional radially anisotropic model of the Earth) by Dziewonski and Anderson (1981), the seismic tomography officially opens a new era of global imaging. Their study includes observations of traveltimes, normal mode and attenuation and consideration of physical parameters such as Earth's mass and moment of inertia. The established reference frame has typical error less than 1% between predicted and observed traveltimes for teleseismic arrivals which became useful for 3D surveys. This seminal study eventually earned the two original authors well deserved Crawford Award (the Nobel Prize equivalence for all of geosciences). Many pioneering studies have been done in the field of tomography both in linear (Nakanishi and Anderson, 1982; Dziewonski, 1984; Woodhouse and Dziewonski, 1984) and non-linear (Tarantola and Valette, 1982; Snieder and Romanowicz, 1988) inversion schemes. Their studies have propelled the seismic tomography to the forefront of the earth sciences.

The Kumaon region of Himalaya is tectonically active and prone to frequent earthquakes. The tectonic settings of this region are very complex as described in Célérier et al. (2009). In context of delineating subsurface structure and hazard mapping an accurate three dimensional velocity tomography is not available in this part. One of the reasons may be the scarcity of digital data in this complex terrain. Inspired from the applicability of seismic data and tomography methods, it was desired to obtain seismic structure beneath the Kumaon Himalaya.

The three dimensional tomography require a precise estimation of 1D velocity as well as location of earthquakes. As the region is very complex therefore a method for joint inversion of P- and S-wave traveltimes to obtain body wave velocities, hypocenter

parameters and geometry of subsurface structures were imagined to formulate. The method has been developed and presented in Chapter 5. 1D velocity models has been estimated in the Kumaon region using the same.

Different types of waves including head waves and first arrival waves, and complex phenomenon such as ray triplications are common to aspect from a complex region. Therefore the forward problem of tomography as described in §1.2 is required to respect the above wave related phenomena. In this context several forward problems have been considered and it has been found that the Fast Marching Method (FMM) (§1.2.2.2.2) is one of the methods that respects the above wave related phenomena. However the FMM suffers from logical source neighborhood errors as described in Rawlinson (2003) and hence it is very difficult to use the same method in Local Earthquake Tomography (Rawlinson and Sambridge, 2003) without removal of the same. Working with the improvement of this method leads to the development of a parallel method presented in Chapter 4. The developed method has been combined with the inverse theory to further develop a tomography algorithm, which has been applied successfully to obtain the subsurface seismic structures of the Kumaon region.

The study of attenuation combined with the velocity is very helpful in hazard estimation. Many studies have been done in context of average estimation of attenuation as described in §1.7. Three dimensional attenuation tomography studies are rare in the Kumaon part of the Himalaya. An accurate three dimensional attenuation tomography requires proper velocity information. Inspired from the method of attenuation tomography given in Joshi et al. (2010), three dimensional attenuation tomography of the Kumaon region has been studied using the developed 3D velocity models of the Kumaon region.

1.2 SEISMIC TOMOGRAPHY AS A METHOD OF INVERSION

Though, tomography is a class of methods, at the roots of all methods it is basically an inversion technique based on inverse theory that is used to constrain 1D, 2D or 3D models of the earth's subsurface-structures with various significant model parameters. The model parameters can be body wave velocities in traveltimes tomography, quality factors in attenuation tomography, or can be some other parameters like coefficients defining surface of discontinuities separating two adjacent layers in media when the tomography can be termed as layered tomography.

If some property of subsurface structure of the earth, such as velocity (or quality factor) is represented by a set of model parameters \mathbf{m} , then a set of data \mathbf{d} , traveltimes (or spectral acceleration) can be predicted for a given array of source and receiver by line

integration through the model. The functional relationship, $\mathbf{d} = \mathbf{g}(\mathbf{m})$ between model parameters and data is the basis of any tomography approach. For a given set of observed dataset \mathbf{d}_o and an initial model \mathbf{m}_0 , the difference between \mathbf{d}_o and $\mathbf{g}(\mathbf{m}_0)$ gives an indication about the fitness of current model to predict the observed data. The inverse problem is then to adjust the initial model in order to minimize the difference between observed and computed or predicted data. This may be subjected to any regularization that may be required. The final result after inversion will be a mathematical representation of true subsurface structure. The accuracy of final results will depend on various factors including how well the initial model satisfy the observed data, assumptions made in model parameterization, errors in observed data and accuracy of inversion schemes. The tomography method therefore relies on general governing principles of inverse theory as described by Tarantola (1987) and Menke (1989).

As the seismic tomography is basically an inversion technique based on inverse theory, so the basic steps required to obtain a tomographic image can be defined as *model parameterization, forward problem, inverse problem, and analysis of robustness of solution*. In *model parameterization*, the seismic structure is defined in terms of a set of unknown model parameters. Tomography methods generally require an initial estimate of model parameter values to be specified. The next step after model parameterization is the *forward problem*, where the response of a model defined by suitable model parameters is obtained. The forward problem is called as the backbone of all tomographic approach, in which almost all of the accuracy and stability of tomography-methods depends. The *inverse problem* is defined as automated adjustment of model parameter values with the object of better matching the model data or computed data to the observed data subject to any regularization that may be required. Finally, the *analysis of solution robustness* is done by using the estimates of covariance and resolution (Tarantola, 1987) or by reconstructing the test models from synthetic data set.

1.2.1 Model Parameterization

Tomography is performed using data resulting from penetrating waves that originate at the source point and travel to the station point. Therefore, data or the responses of a medium are primarily dependent on the medium properties through which waves propagate. The data are required to be computed in the forward part of any tomography, therefore it is essential to quantify the medium properties in terms of some parameters. The type of parameters used in a particular problem depends on the type of a tomography; for example it

is velocity in travelttime tomography and the same is quality factor in attenuation tomography. To define the discontinuities in a medium, a set of interfaces whose geometry is constrained to satisfy data is often used.

Seismic structures is defined by a set of surface functions representing interfaces or a set of rectangular blocks, each having constant medium properties or nodes with a suitable interpolation function or a suitable combination of these. The most appropriate choice will depend on the *a priori* information such as known faults or discontinuities, whether data indicates the presence of interfaces such as presence of reflection or mode conversion, whether data coverage is adequate to resolve more than one parameter, and finally the capabilities of inversion algorithms used.

1.2.1.1 Velocity Parameterization

When the variation of velocity is defined using a set of rectangular blocks, each having constant velocity then this parameterization is simply termed as Constant Velocity Blocks (CVB) or Constant Velocity Voxels (CVV) as shown in Figure 1.1(a). This type of parameterization is simple to define and results in linear ray paths within each block. On the other hand, this type of parameterization is not a natural choice for representing smooth velocity variation in subsurface structure because of velocity discontinuities between adjacent blocks. These artificial velocity discontinuities often cause unwanted ray triplexion and shadow zones due to different critical angles presented by different block walls. However, if a large number of CVV are used and velocity changes between adjacent blocks are given restriction to a suitable degree, then a reasonable approximation to a continuous velocity field is possible.

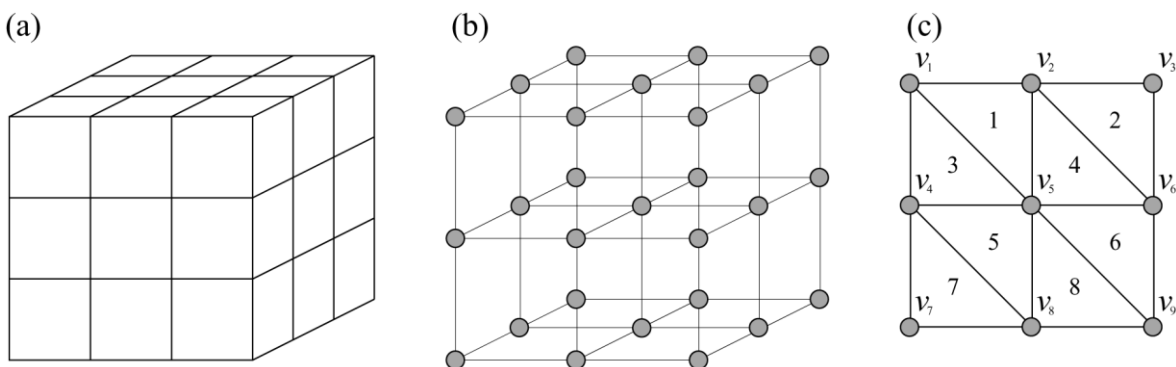


Figure 1.1: Different types of velocity parameterization: (a) constant velocity blocks, (b) a grid of velocity nodes, and (c) triangulated velocity grid (after White, 1989).

In teleseismic tomography, this type of parameterization has been used by many authors including Aki et al. (1977), Oncescu et al. (1984), Humphreys and Clayton (1988, 1990), Benz et al. (1992), and Saltzer and Humphreys (1997). Hildebrand et al. (1989) and Zhu and Ebel (1994) used CVV in their 3D refraction traveltime tomography while Williamson (1990) and Blundell (1993) used CVV in their reflection traveltime tomography. In local earthquake tomography, this type of parameterization has been used by many authors including Aki and Lee (1976) and Nakanishi (1985). The CVVs are not as common in wide angle tomography and are often avoided when strong ray curvature is expected.

An alternative to the above parameterization is to define the velocity at the nodes of a regular grid as shown in Figure 1.1(b), with a specified interpolation function. One of the first people to use this kind of parameterization is Thurber (1983). Thurber in his local earthquake tomography used a tri-linear interpolation function to describe the velocity at any point within a regular rectangular grid. The tri-linear function can be written as:

$$v(x, y, z) = \sum_{i,j,k=1}^2 V(x_i, y_j, z_k) \left(1 - \left|\frac{x-x_i}{x_2-x_1}\right|\right) \left(1 - \left|\frac{y-y_j}{y_2-y_1}\right|\right) \left(1 - \left|\frac{z-z_k}{z_2-z_1}\right|\right) \quad (1.1)$$

Where, $V(x_i, y_j, z_k)$ are velocity values of eight grid nodes surrounding point (x, y, z) . The Equation (1.1) represents a continuous velocity field with a discontinuous gradient. This type of parameterization has been used by many authors including Zhao et al. (1992), Scott et al. (1994) and Haslinger et al. (1999). Some ray tracing methods require velocity field to be continuous to some higher degree as described by Thomson and Gubbins (1982). In such case, a higher order interpolation function is required to be used in the parameterization. In this context, Cubic spline interpolation (Thomson and Gubbins, 1982; Lutter et al., 1990), Cubic B-splines (Farra and Madariaga, 1988; McCaughey and Singh, 1997) remained useful choices.

White (1989) describes a different type of model parameterization which somewhat bridges the gap between block and grid approaches. He used rectangular grid of nodes to define triangular region of constant velocity gradient as shown in Figure 1.1(c). The velocity within each cell is defined by:

$$v(x, y) = v_0 + (x - x_0) \nabla_x v + (y - y_0) \nabla_y v \quad (1.2)$$

Where, v_0 , $\nabla_x v$ and $\nabla_y v$ are determined at the nodes of the triangles such that $v_0 = v_1$, $\nabla_x v = (v_2 - v_1) / \Delta x$, $\nabla_y v = (v_2 - v_1) / \Delta y$ in cell 1 of Figure 1.1(c). The advantage of this parameterization is that the velocity remains continuous through the medium and because of this ray can be traced analytically within each cell. However, the gradient of velocity is

discontinuous in this approach and because of triangular shape source receiver ray tracing is difficult. This type of parameterization has also been used by Chapman and Drummond (1982). Cervený (1987) used a similar approach but considered constant gradient of square of slowness instead of constant gradient of velocity. This method of parameterization can be extended to three dimensions by using tetrahedral cell and with a linear interpolation function described in terms of velocities of four vertices of the tetrahedron. It is important to note that these types of parameterization are used mainly for analytical ray tracing and for adequate approximation to the subsurface velocity distribution.

1.2.1.2 Interface parameterization

One of the most common structural features that are often required to include in the velocity model is the velocity discontinuities of subsurface structures having sub horizontal layers as shown in Figure 1.2. These layers or similar to these type artifacts are responsible for reflected and refracted phases respectively in the reflection sections and refraction sections of seismic data. The reflection and refraction sections of seismic data are used in reflection tomography and refraction tomography respectively. The reflection sections of seismic data image only the reflectors and the refractions sections of seismic data contain various phases associated with velocity discontinuities.

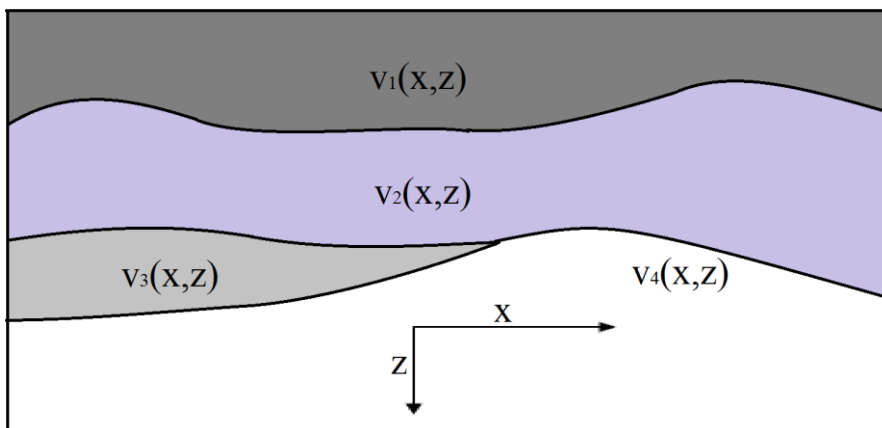


Figure 1.2: Schematic representation of a typical layered velocity structure that is imaged in travelt ime tomography. The velocity functions $v_i(x, z); i = [1, 4]$ describe the velocity variations for different layers.

The junction of two adjacent layers or interface can be imagined by piecewise continuous (Figure 1.3(a)) or continuous curves (Figure 1.3(b)) defined by appropriate functions in 2D parameterization. Zelt and Smith (1992) and Williamson (1990) used piecewise curves in their 2D tomography methods. The piecewise curves are useful to define complex multivalued interface. On the other hand the discontinuities given by such curves

may not be geologically realistic as the junction of two adjacent curve results in artificial shadow zones. However, this problem has been avoided by Zelt and Smith (1992) in their 2D wide angle travelttime tomography by using the technique of average filtering. The use of continuous curves will not create artificial shadow zones. On obvious problem with this type of curves is that it is very difficult to represent a complex surface using analytical function because of overturning nature of subsurface layers that may be associated with the structure.

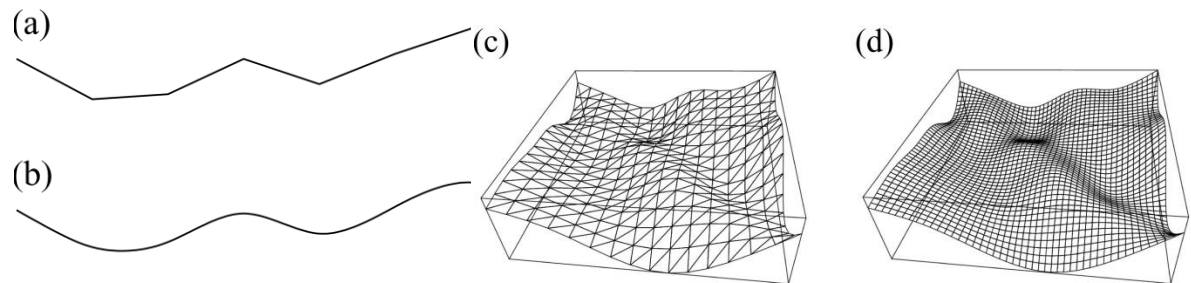


Figure 1.3: Types of interface parameterization used in 2D (a, b) and 3D (c, d) models. (a) Piecewise linear segments, (b) piecewise cubic B-spline curve, (c) surface defined by mosaic of triangular patches, (d) surface defined by mosaic of bicubic B-spline patches.

The interface parameterization in 3D can be imagined by a continuous or piecewise continuous surface defined by appropriate functions. The use of continuous surfaces and piecewise continuous surfaces in the interface parameterization will result in similar advantages and disadvantages as that of given by continuous or a piecewise continuous curves in 2D case. In other words, it is easy to represent a complex multivalued surface using piecewise continuous surfaces. However, these may create unnecessary shadow zones due to discontinuous junction between two adjacent surfaces. On the other hand, the use of continuous surface will not create shadow zones however a multivalued complex surface is very difficult to define using this type of parameterization. Many authors including Sambridge (1990) and Guiziou et al. (1996) used triangulated piecewise surface defined by piecewise triangular area segments (Figure 1.3(c)) in their tomographic methods.

Grid of depth nodes with appropriate interpolation functions can also be used to define interfaces. In 2D, conventional piecewise cubic spline functions with second degree continuity as shown in Figure 1.3(b) are often used in tomography (White, 1989; Rawlinson and Houseman, 1998). In 3D tomography, many authors including Gjøystdal et al. (1984) and Chiu et al. (1986) used smooth interfaces (Figure 1.3(d)) defined by appropriate functions. Cubic spline interpolation functions (Gjøystdal et al., 1984) and higher degree polynomials (Chiu et al., 1986; Davis, 1991; Kohler and Davis, 1997) remained good choices in that context. Davis (1991) used polynomial expansion to define the interfaces in his

teleseismic tomography and obtained the structure of lithosphere-asthenosphere boundary in East Africa. Kohler and Davis (1997) used a similar approach to determine two dimensional crustal thickness variations in California. There are other types of interface parameterization such as irregular parameterization, spectral parameterization which are beyond the scope of present study. A detailed description of such parameterizations can be found in Zelt and Smith (1992) and Wang and Houseman (1994).

1.2.1.3 Quality Factor Parameterization

Constant Quality Factor Blocks (CQFB) are the most common type of parameterization used in attenuation tomography. In this type of parameterization, the earth's subsurface structure is divided into a set of rectangular blocks and within each block the value of quality factor is kept constant. Many authors including Joshi et al. (2010) have used this type of parameterization in their attenuation tomography.

An alternative to the CQFB parameterization is to use of grid of nodes where quality factor is defined with suitable interpolation function. This is similar to velocity parameterization using grid of nodes. The other type of parameterization discussed in velocity parameterization can also be used in quality factor parameterization. However if the attenuation tomography is performed using the ray paths obtained in the traveltime tomography, then it is very essential to choose a parameterization which would give least amount of computational error in traveltime. This is because, the computation of attenuation is very sensitive to the traveltime error as described by Buske (1996).

1.2.2 Traveltime Determination

Determination of traveltime is the most crucial step in the traveltime inversion and this is done in the forward part of tomography. The equation governing the traveltime t of seismic wave from source S to receiver R is given as:

$$t = \int_S^R \frac{1}{v(\mathbf{x})} dl \quad (1.3)$$

Where, dl is the differential length of ray path, \mathbf{x} is the position vector and v is the velocity. It is clear from Equation (1.3) that, for a given velocity distribution, ray path must be known before evaluating the integral for traveltime. The propagation of wavefronts in elastic media is described by the eikonal equation which is given as (Shearer, 2009):

$$|\nabla T| = s(\mathbf{x}) \quad (1.4)$$

Where, T is the travelttime of the propagating wavefront and s is the local slowness. The Eikonal equation is subjected to the high frequency assumption; either, the wavelengths of seismic waves are considered to be much less than the length scale of velocity variations of the medium through which the waves pass. The equation for ray path is directly derived from eikonal equation and is given as (Aki and Richards, 1980):

$$\frac{d}{dl} \left(s(\mathbf{x}) \frac{d\mathbf{x}}{dl} \right) = \nabla s(\mathbf{x}) \quad (1.5)$$

This equation can be solved for ray path geometry for any given slowness field. The Equation (1.5) states that the ray path is time independent therefore it also describes the Fermat's principle which says that among all ray paths true ray path is one which is stationary with respect to time.

The traditional methods for computation of source-receiver traveltimes is ray tracing in which ray path is determined first then integration in Equation (1.3) is solved to obtain travelttime. An alternative way to obtain the travelttime is to solve the eikonal equation directly through the entire domain of computation which is achieved by using numerical schemes such as finite difference methods (Vidale, 1988, 1990; Qin et al., 1992). More recent methods in this context are Fast Marching Method (Sethian and Popovici, 1999) and its variants which use the property of entropy and viscosity in combination with numerical schemes to solve the eikonal equation directly. All such methods which aim to compute travelttime field in entire medium are termed as Wavefront Tracking.

1.2.2.1 Ray Tracing

Determination of a ray path between a source and receiver is a two point boundary value problem. To solve this problem there are two basic methods namely shooting and bending methods which are conventionally used.

1.2.2.1.1 Shooting Method

Under the shooting method of ray tracing, the Equation (1.5) is formulated as an initial value problem in which a known source coordinates and known initial ray direction is used to determine a complete ray path. The boundary value problem is solved by shooting rays from the source in the medium and adjusting the ray trajectories using the information from the computed paths, so that the rays more accurately target the receiver as shown in Figure 1.4. The ease with which the shooting method is solved depends on the model parameterization technique used. The velocity parameterization using constant velocity

blocks results in linear ray paths within every blocks. At the boundary of the blocks the ray trajectories are computed using Snell's Law:

$$\frac{\sin \theta_i}{v_i} = \frac{\sin \theta_r}{v_r} \quad (1.6)$$

Where, θ_i and θ_r denote incident and refracted angles of the propagating ray relative to normal vector to the interface or cell boundary. v_i and v_r are the velocities of adjacent blocks containing incident and refracted rays respectively.

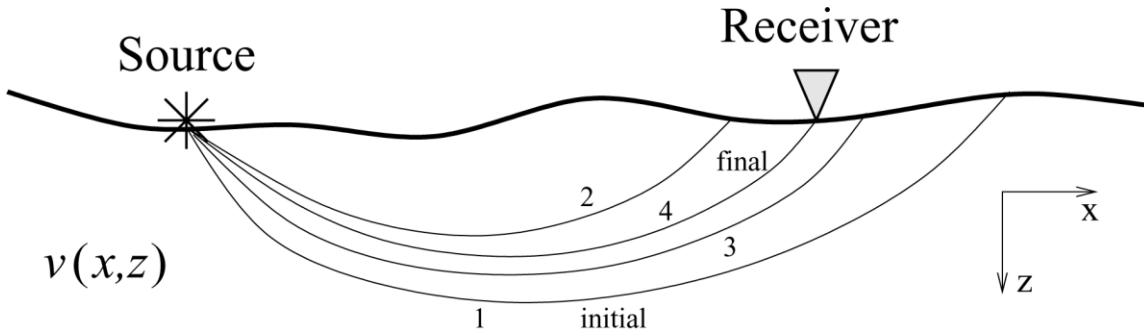


Figure 1.4: Principle of the shooting method. The initial take-off angle of ray 1 is iteratively adjusted until the final ray (4) passes sufficiently close to the receiver.

Analytical ray tracing as described by Telford et al. (1976) is also possible using constant velocity gradient. However the analytical solution of the initial value problem is possible only with simple velocity functions. For velocity functions with arbitrary complexity the numerical solution is required. Zelt and Smith (1992) in their 2D wide angle tomography have solved the following pair of differential equations:

$$\frac{dz}{dx} = \cot \theta \quad \frac{d\theta}{dx} = \frac{v_z - v_x \cot \theta}{v} \quad (1.7)$$

Or

$$\frac{dx}{dz} = \tan \theta \quad \frac{d\theta}{dz} = \frac{v_z \tan \theta - v_x}{v} \quad (1.8)$$

Where, θ is the incident angle relative to z axis and, v_x and v_z are derivative of v with respect to x and z respectively. Runge-Kutta method with error control is used to solve both system of equations. To solve the initial value problem in three dimensions, Sambridge and Kennet (1990) used the following equations:

$$\left. \begin{aligned}
\frac{\partial x}{\partial \tau} &= v \sin i \cos j \\
\frac{\partial y}{\partial \tau} &= v \sin i \sin j \\
\frac{\partial z}{\partial \tau} &= v \cos i \\
\frac{\partial i}{\partial \tau} &= -\cos i \left(\frac{\partial v}{\partial x} \cos j + \frac{\partial v}{\partial y} \sin j \right) + \frac{\partial v}{\partial z} \sin i \\
\frac{\partial j}{\partial \tau} &= \frac{1}{\sin i} \left(\frac{\partial v}{\partial x} \sin j - \frac{\partial v}{\partial y} \cos j \right)
\end{aligned} \right\} \quad (1.9)$$

Where, i and j denote respectively the incidence angle and azimuth of the ray trajectories. Establishing an initial value problem and obtaining its solution is the first step in determination of ray path. The next step is more difficult where two point boundary value problems are solved. In that context, Julian and Gubbins (1977) suggested two iterative methods. The one of these methods is the Newton's method. The basic equation behind this method is given as:

$$\begin{bmatrix} \frac{\partial h}{\partial i_0} & \frac{\partial h}{\partial j_0} \\ \frac{\partial g}{\partial i_0} & \frac{\partial g}{\partial j_0} \end{bmatrix} \begin{bmatrix} i_0^{n+1} - i_0^n \\ j_0^{n+1} - j_0^n \end{bmatrix} = \begin{bmatrix} H - h(i_0^n, j_0^n) \\ G - g(i_0^n, j_0^n) \end{bmatrix} \quad (1.10)$$

Where, h, g are computed horizontal coordinates of endpoint of ray, H, G are desired destination points of ray such as station point or receiver point and i_0, j_0 are respectively the inclination and azimuth of the ray tangent at the source point. The n value represents number of iteration. One obvious difficulty with this method is accurate computation of partial derivatives appeared in Equation (1.10). The second method involves fitting a plane to the points (h, g) using three known ray paths. An improved estimate of i_0 and j_0 are those in which the computed plane contains the desired point (H, G) . This method is faster than Newton's method at each iteration but it converges more slowly.

Shooting a fan of rays from the source in a medium is an effective way for determination of nearby ray paths to all targets in two dimensional problems. Zelt and Smith (1992) used bisection method to confine the required phases that reflects back from a particular interface. The boundary value problem is then solved by shooting a fan of rays into each defined region and thereafter interpolating required rays between two closest rays that confine the receiver. A similar approach is used by Blundell (1993), Cassell (1982) and Langan et al. (1985) to determine 2D reflection arrivals. Shooting method in 2D has also

been applied by other authors including Farra and Madariaga (1988), White (1989), Lutter et al. (1990), Williamson (1990), McCaughey and Singh (1997).

The use of Shooting method in 3D is not as common as 2D. The authors who have used this in their 3D local earthquake tomography are Benz and Smith (1984), Ankeny et al. (1986), Sambridge (1990). In 3D teleseismic tomography study Neel et al. (1993) and VanDecar et al. (1995) have used Shooting method of ray tracing. Shooting method can also be applied to layered media as describe by Rawlinson et al. (2001), where the analytical ray tracing is implemented and boundary value problem is solved by Newton's method. The resultant ray paths are shown in Figure 1.4.

1.2.2.1.2 Bending Method

Bending method, as the name implies, is the method in which a ray path between source and receiver is bended or adjusted until it becomes a true ray path that satisfies Fermat's principle (Figure 1.5). This was originally proposed by Julian and Gubbins (1977) for a continuous 3D velocity medium. Their method uses the first order differential equations for determination of ray path and associated travelttime. They described the ray path parametrically as $\mathbf{x} = \mathbf{x}(q)$ with the parameter $q = l/L$, in which L is the total length of ray path between source and receiver and l is the length segment of ray path which is limited as $0 \leq l \leq L$. The Euler-Lagrange equations as given by Julian and Gubbins (1977) are:

$$\left. \begin{aligned} \frac{d}{dq} \frac{\partial}{\partial \dot{x}} (sF) &= \frac{\partial}{\partial x} (sF) \\ \frac{d}{dq} \frac{\partial}{\partial \dot{y}} (sF) &= \frac{\partial}{\partial y} (sF) \\ \frac{\partial F}{\partial q} &= 0 \end{aligned} \right\} \quad (1.11)$$

Where, s is slowness and expression for F is:

$$F = \frac{dl}{dq} = \sqrt{\dot{x}^2 + \dot{y}^2 + \dot{z}^2} \quad (1.12)$$

In Equation (1.12) the derivatives \dot{x} , \dot{y} and \dot{z} are taken with respect to q . The boundary conditions are set such as $\mathbf{x}(0) = \mathbf{x}_s$ and $\mathbf{x}(1) = \mathbf{x}_r$ where \mathbf{x}_s and \mathbf{x}_r are the coordinates of source and receiver point. The equation set (1.11) is non-linear and cannot be solved directly. However, if it is assumed that $x^0(q)$ passes through source and receiver then an improved estimate is given by:

$$\mathbf{x}^1(q) = \mathbf{x}^0(q) + \mathbf{x}_p^0(q) \quad (1.13)$$

Where, \mathbf{x}_p^0 denotes perturbation to the initial ray path. If Equation (1.13) is substituted in the Equation set (1.11) then resulting equation can be linearised in terms of \mathbf{x}_p^0 and can be solved which gives \mathbf{x}^1 from Equation (1.13) as described by Julian and Gubbins (1977). This process is repeated until the solutions converge. Once the ray path is determined the following equation is used to compute traveltime (Julian and Gubbins, 1977):

$$\tau = \int_{q|_s}^{q|_R} sF dq \quad (1.14)$$

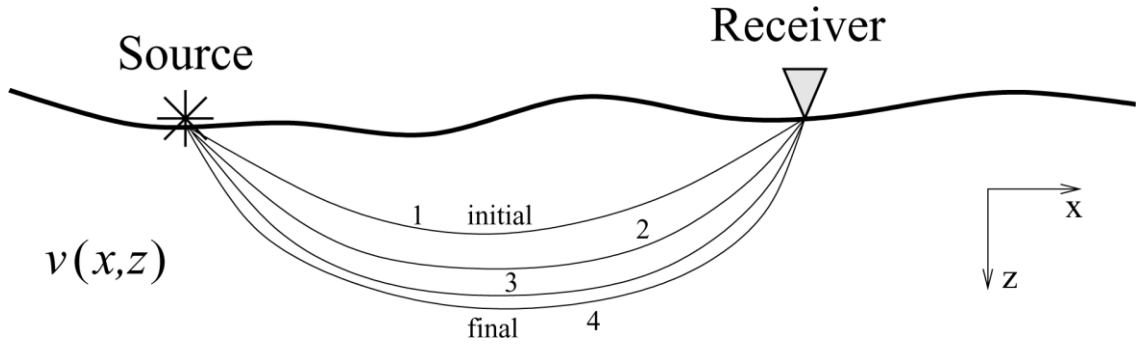


Figure 1.5: Principle of the bending method. The initial ray path (ray 1) is adjusted until it satisfies Fermat's principle (ray 4).

Pereyra et al. (1980) extended the concept of the method given by Julian and Gubbins (1977) to include interfaces in media. For a medium with different velocity variations separated by interfaces, the bending method is solved by using separate system of differential equations in each region. Thereafter, the condition of discontinuity at each interface that is traversed by computed ray can be imposed to couple the separate systems. The disadvantage with this method is that the order of the interfaces traversed by ray path is required to be known in advance.

A method similar to bending method is pseudo-bending method developed by Um and Thurber (1987) for solving two point boundary value problems in 3D continuous media. Their method uses a perturbation scheme in which the step size of integration is progressively halved. This can be explained using Figure 1.6. In the beginning, the initial path is linearly interpolated using three points including source, receiver and expected one point in the medium. To properly relocate this expected point, it is iteratively perturbed using geometric interpretation of equation of ray path to obtain a point at which the ray equation is approximately satisfied and the traveltime extremum converges within a specified limit. Once the relocation of expected point is done, the path segments are doubled and the three-

point perturbation technique is repeated from both the endpoints to the middle or relocated point. The total number of three-point perturbation steps is now becomes three. Segments are again divided to make them double in number and the procedure is repeated until the step change in travelt ime between two successive iteration satisfies a suitable convergence criterion. Pseudo-bending method is much faster than earlier methods as described by Um and Thurber (1987).

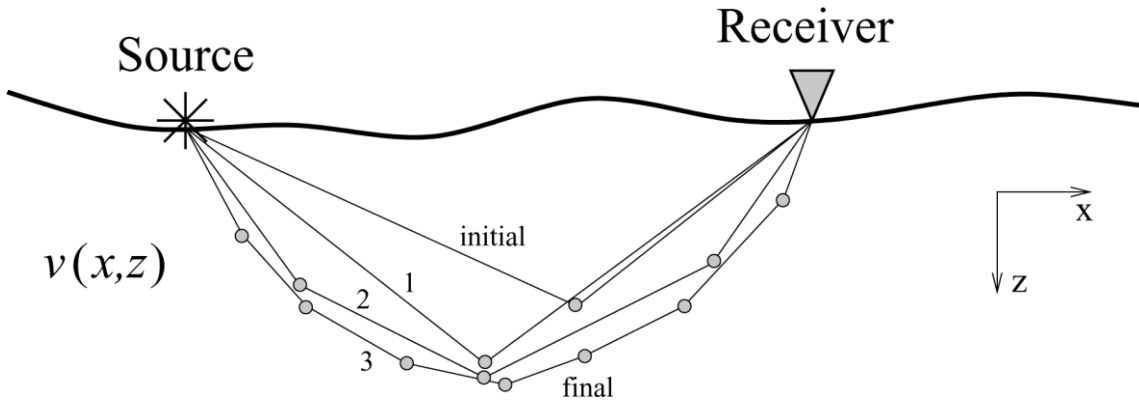


Figure 1.6: Principle of the pseudo-bending method of Um and Thurber (1987). An initial guess ray path defined by three points is provided. The center point is perturbed to best satisfy the ray equation. Then the number of segments is doubled and the process is repeated.

Bending methods of ray tracing have been implemented by many authors including Thomson and Gubbins (1982), Zhao et al. (1994, 1996) and Steck et al. (1998) in their teleseismic data. Chiu et al. (1986) used bending method in their inversion of 3D reflection data while Zhao et al. (1992) used pseudo bending method in their tomography to obtain 2D crustal structure. Many authors including Eberhart-Phillips (1990), Zhao et al. (1992), Scott et al. (1994), Eberhart-Phillips and Reyners (1997) and Graeber and Asch (1999) have used the bending methods in their works in tomography. Julian and Gubbins have suggested that, in media with continuous velocity variations, the bending method is faster than the shooting method by a factor of 10 or more. However, when discontinuities are present this method become very complex. Therefore, shooting method is preferred in media with complex velocity variation and bending method in comparatively less complex media (Červený, 1987).

Ray tracing methods are simple and provide high degree of accuracy in ray path computation. However, there are some disadvantages. In velocity models defined CVV parameterization, the ray tracing often fail to converge the final ray point to its destination. This happen frequently in complex velocity media and sometime even in simple

heterogeneous media. Failure of convergence of final ray path to its destination occurs because each contrasting block in CVV has its own critical angle with respect to normal to the block wall. When a ray strike on the wall at an angle greater than the critical angle provided by the wall, then it gets reflected and deviated from its actual path predicted.

First arrival phases are widely used in tomography methods because these are easy to identify in seismograms with high degree of confident comparative to others arrivals. First arrivals ray paths are also used for determination of earthquake hypocenters and precise 1D velocity models. One of the major disadvantages of ray tracing is that it does not give guarantee to the first arrivals.

1.2.2.2 Wavefront Tracking

Computation of ray paths and then solving integration for traveltimes lead to several problems as described in §1.2.2.1.2. An alternative way is to determine traveltimes to all defined points in a medium by solving the eikonal equation directly. This is called wavefront tracking and most commonly done using finite difference schemes described below.

1.2.2.2.1 Finite Difference Schemes

Vidale (1988) proposed a 2D finite difference scheme that computes traveltimes to all grid points in a 2D grid, from the source along an expanding square. The eikonal equation (Equation 1.4) in 2D can be written as:

$$\left(\frac{\partial T}{\partial x}\right)^2 + \left(\frac{\partial T}{\partial y}\right)^2 = s^2(x, y) \quad (1.15)$$

Where, $s(x, y)$ is the slowness and $T(x, y)$ is the traveltime of any phase of a propagating wave. Formulation of Vidale's method is based on square grid of velocity nodes. Consider grid points as shown in Figure 1.7(a) in which source grid point A is surrounded 8 neighboring grid points. Considering traveltime to point A is T_0 the traveltime to the points $B_i; i = [1, 4]$ are given by:

$$T_{B_i} = T_0 + \frac{h}{2}(s_{B_i} + s_A) \quad (1.16)$$

Where, h is the grid spacing and s_A and s_{B_i} are the slowness at the nodes A and B_i respectively. To compute traveltime to corner points; for example C_1 , consider the finite difference schemes as:

$$\left. \begin{aligned} \frac{\partial T}{\partial x} &= \frac{1}{2h}(T_{B_1} + T_{C_1} - T_A - T_{B_2}) \\ \frac{\partial T}{\partial y} &= \frac{1}{2h}(T_{B_2} + T_{C_1} - T_A - T_{B_1}) \end{aligned} \right\} \quad (1.17)$$

This set of derivatives, when substituted in Equation (1.15), gives:

$$T_{C_1} = T_A + \sqrt{2(h\bar{s}_{AB_1B_2C_1})^2 - (T_{B_2} - T_{B_1})^2} \quad (1.18)$$

Where, $\bar{s}_{AB_1B_2C_1}$ is the average velocity of all four points A , B_1 , B_2 and C_1 which are under consideration for the evaluation of traveltimes to point C_1 . This procedure can be used to calculate traveltimes to all C_i . The next computation is done on an expanded square as shown in Figure 1.7(b). The computation of traveltimes on this new square is not arbitrary rather a scheme as given by Vidale (1988) is required to make the traveltimes in order, which will only be the valid seismic traveltimes.

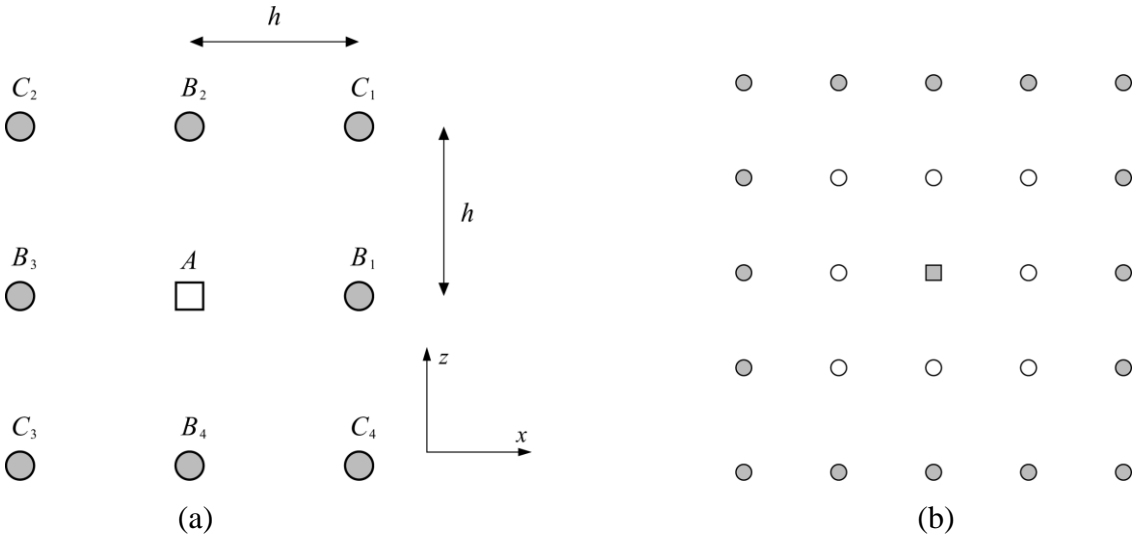


Figure 1.7: The procedure of finite difference method (a) and expanding square method (b) to obtain traveltime field as introduced by Vidale (1988). Traveltimes to the filled circles are calculated from the open circles. The filled square is the source.

Vidale's method does not track any wavefronts truly, rather it represents a precursor to the class of scheme that do so. Vidale (1988) also proposed a scheme that gives locally circular wavefronts which are useful for the evaluation of strongly curved wavefronts. Vidale (1990) extended his methodology from 2D to 3D.

The wavefront tracking methods do not explicitly find source receiver ray path directly. However, the ray paths from a receiver to source can be tracked by following the negative direction given by gradient of traveltime field. Unlike ray tracing method, the wavefront tracking methods do not show convergence problems as these methods do not

compute ray paths directly. The problem of obtaining first arrivals are solved to some extent by this method, however the same may be failed in a zone of large velocity contrasts as described in Figure 1.8. Path 1 in Figure 1.8 corresponds to one determined by expanding square method whereas path 2 is the least traveltime path by virtue of the high velocity zone. This happens because the way expanding square method progressively computes traveltimes field does not simulate actual geometry of a propagating wavefront. A number of authors including van Trier and Symes (1991), Podvin and Lecomte (1991) and Qin et al. (1992) have used the basic idea of Vidale (1988) to develop their own schemes. However the problems for determination of first arrivals with certainty survived.

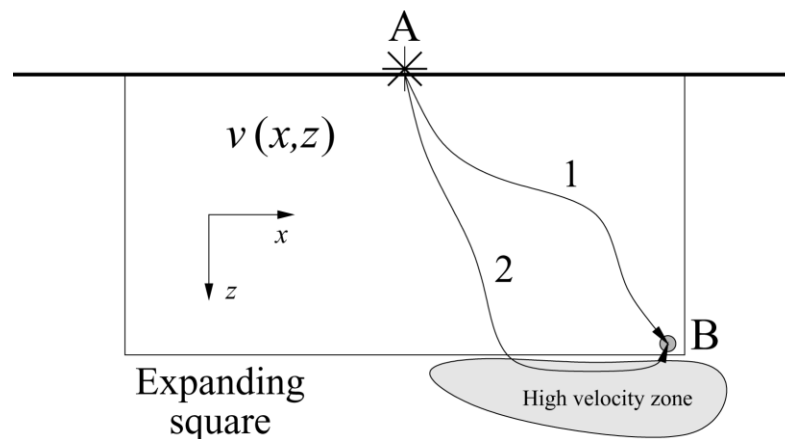


Figure 1.8: Schematic illustration showing how the expanding square method can fail to find first arrival ray path (after Rawlinson and Sambridge, 2003). The traveltime along path 1 is determined by the expanding square but path 2 has a shorter traveltime due to the high velocity zone.

1.2.2.2.2 Fast Marching Method

One of the major problems with eikonal grid based methods (Vidale, 1988, 1990; Qin et al., 1992) arises when the true wavefront is not differentiable. In other words, first arrival wavefront contains kinks or discontinuities in gradient. This is particularly the case in complex velocity media in which multi-pathing (wavefront crossing itself) is common phenomena. This problem can be addressed by searching weak solution to proceed through these discontinuities. A weak solution to a differential equation is entropy-satisfying viscosity solutions that is not differentiable everywhere but the same satisfies the integral equation formed from the differential equation. One of the major advantages of this is that more general solution is permitted as the demand of differentiability of the original equation vanishes. These types of solutions have been analysed by Sethian (1982, 1987) in his initial work which lead to the birth of level set method (Osher and Sethian, 1988) and finally to

Fast Marching Method (Sethian, 1996; Sethian and Popovici, 1999). The basic equation of this method in 3D grid can be written in its simplest form as:

$$\left[\begin{array}{l} \max(D_{ijk}^{-x}T, -D_{ijk}^{+x}, 0)^2 + \\ \max(D_{ijk}^{-y}T, -D_{ijk}^{+y}, 0)^2 + \\ \max(D_{ijk}^{-z}T, -D_{ijk}^{+z}, 0)^2 \end{array} \right]^{\frac{1}{2}} = s_{ijk} \quad (1.19)$$

Where, D denotes differential operator notation which are given as:

$$D^{+x}T = \frac{T(x + \delta x) - T(x)}{\delta x} \quad (1.20)$$

$$D^{-x}T = \frac{T(x) - T(x - \delta x)}{\delta x} \quad (1.21)$$

The parameter s_{ijk} is the local slowness at the grid point (i, j, k) . Equation (1.19) is non-linear and quadratic. Out of two solutions, the larger is always correct value. The exact procedure to obtain solution is described in detail in Chapter 3.

The Fast Marching Method is the first unconditionally stable scheme to solve eikonal equation. This is highly efficient and accurate technique that deals with the problem of evolution of interfaces in heterogeneous media. The algorithm based on this method accurately and robustly deals with the heterogeneity of a medium with the formation of cusp, corner and topological changes in the propagating interfaces. The condition of entropy controls the solutions to give first arrivals and the condition of viscosity makes the algorithm stable in a medium with steep velocity gradients. Further the application of narrow band makes the algorithms very fast in computation.

The error in FMM is of two types: one is pure numerical error and another is mapping error and both those error originate due to finite size of grid spacing. Mapping error is related to the fact that how well the grid nodes map the strong curvature in the neighbourhood of source.

1.2.2.3 Review on Improved Fast Marching Methods

Many authors in the recent past have documented various methods to improve the basic fast marching method. Some of these are discussed below.

1.2.2.3.1 The Shifted Grid Fast Marching Method

The SGFM technique introduced by Danielsson and Lin (2003) improved the accuracy of the FMM to a limited degree. The central idea of the technique is to define the

objective function at half-grid positions; therefore, the objective is dependent on marching direction. The strategy for updating or computing arrival time in the neighborhood of a known grid point under the scheme is inferred from optimal control theory in a fashion similar to Tsitsiklis (1995). Therefore, the solution is restricted to take advantage of higher order finite difference schemes. In SGFM method, two solution models based on whether the method uses 4-connected neighbor or 8-connected neighbors are proposed in 2D scheme. The scheme with 4-connected neighbor has no advantages over FMM, whereas the scheme with 8-connected neighbors is better than FMM (Hassouna and Farag, 2007). In both the schemes the idea is same. The scheme with 4-connected neighbor divides the 2D space around the unknown grid point into quadrants and obtains a maximum of four solutions from the available known points whereas the scheme with 8-connected neighbor divides the 2D space around the unknown grid point into octants and obtains a maximum of eight solutions from the available known points. Out of all the solutions the minimum solution is assigned to the unknown point. The advantage of SGFM method is limited to 2D only as in 3D no improvements over FMM has been reported.

1.2.2.3.2 The Group Marching Method (GMM)

The GMM is a modified FMM where a group of points simultaneously advances unlike a single point from the narrow band as in FMM. The new procedure reduces the computational complexity from $O(n \log n)$ to $O(\log n)$, where n is the total number of grid nodes, while maintaining the same accuracy. The scheme works as follows: a group of points, G is selected from the narrow band and traveltime is recomputed to the neighboring points to the G and then registered the updated traveltime in the narrow band and finally G is tagged as known point.

1.2.2.3.3 The FMM on Spherical Domain

FMM on Cartesian coordinate system gives minimum error along the axial direction and maximum error along the diagonal direction in constant velocity medium. This is because the gradient term in the Eikonal equation is precisely computed along the axial direction whereas the same is most inaccurately computed along the diagonal direction, particularly in the source neighborhood due to high wavefront curvature. Alkhalifah and Fomel (2001) remove the biasness of directivity in the computational domain by introducing the spherical grid centered on source point. The new method completely reduces the error to zero in constant velocity media but in complex velocity models as the errors are aligned

randomly in the Cartesian domain so the use of spherical domain does not offer any advantages to Cartesian.

1.2.2.3.4 The FMM Based on Source Neighborhood Refinement

Kim and Cook (1999) admit the grid refinement strategy in their methodology. In their technique the grid spacing increases progressively away from the source. This technique allows the better mapping of high wavefront curvature in the source neighborhood. Rawlinson and Sambridge (2004) proposed a parallel technique where they have used a single level of grid refinement in the neighborhood of source instead of variable grid. Both the methods reduce the errors except at the cost of CPU time which is huge in 3D computational space.

1.2.2.3.5 The Untidy Fast Marching Method (UFMM)

Yatziv et al. (2006) proposed this method to reduce the run-time of FMM from $nO(n)$ to $O(n)$ by introducing a dynamic circular array in the narrow band. The dynamic circular array maintains a special data structure called untidy priority queue whose maintenance cost is $O(1)$. In this method each computed traveltimes is quantized and the same quantization is used to place the grid point in the priority queue, whereas actual traveltimes is used to solve the eikonal equation for a selected grid point. Therefore, the errors in this method originate due to wrong selection order. Authors have shown that the magnitude of error due to wrong selection is of same order as that of FMM.

1.2.3 Determination of Spectral Acceleration

The forward problem in attenuation tomography is to compute spectral acceleration for a given distribution of quality factor. This problem can be solved by incorporating the quality factor into the transport equation (Shearer, 2009) and solving the same as described in Shearer (2009). The transport equation contains second derivative of traveltimes and its evaluation lead to high degree of numerical error as described by Buske (1996). Therefore solution of forward problem using transport equation is almost impractical to use in real earth.

An alternative method to solve the forward problem is to use an observed empirical relationship between spectral acceleration and quality factor. Some of the useful relationships are those given by Boore (1983), Boore and Atkinson (1987), Beresnev and Atkinson (1997),

and Chopra et al. (2011, 2013b). A modified version of these relationships which can be used in block type of model parameterization is given by Hashida and Shimazaki (1984) as:

$$A(f) = S(f) G g \exp\left(-\pi f \sum_{i,j,k} T_{ijk} Q_{ijk}^{-1}\right) \quad (1.22)$$

In Equation (1.22), $A(f)$ and $S(f)$ represent observed spectral value and source spectral value at frequency f . G is the geometrical factor which is assumed to be inverse of hypocentral distance between source and observation point. g is a factor accounting for amplifying effects at the surface at observation point. The parameter Q_{ijk} and T_{ijk} denote quality factor and time spent in i^{th} , j^{th} and k^{th} block in CVV type of parameterization.

The basic form of the attenuation as a function of distance is (modified after Shearer, 2009):

$$A(x) = A_0 \exp\left(-\pi f x / c Q\right) \quad (1.23)$$

Where, A_0 and $A(x)$ are the amplitudes of seismic waves at the position of source and at x distance away from source. The parameter c represents velocity of seismic waves. The form of relationship given in Equation (1.22) can be derived from Equation (1.23). Consider a block 1, in which a seismic ray enters and assume the quality factor to be Q_1 . Since velocity does not alter within a CVV, therefore quantity x/c can be replaced with total traveltimes spent T_1 by seismic ray in that block. Since, quality factor does not vary in a block, so the only variable is frequency f . Hence, elementary attenuation A_1 within a block can be written as:

$$A_1(f) = A_0 \exp\left(-\pi f T_1 Q_1^{-1}\right) \quad (1.24)$$

Where, A_0 is the initial amplitude of seismic wave. Consider a second block 2, adjacent to the first one where the ray enters after emerging from first block. For the block 2 the attenuated amplitude from the block 1 will be the initial amplitude, then applying the Equation (1.24), the total attenuation in amplitude of a wave in the two blocks can be written as:

$$A_2(f) = A_0 \exp\left(-\pi f \sum_{i=1}^2 T_i Q_i^{-1}\right) \quad (1.25)$$

Applying the above procedure total attenuation through all the blocks through which the ray passes can be written as:

$$A(f) = A_0 \exp\left(-\pi f \sum_i T_i Q_i^{-1}\right) \quad (1.26)$$

Equation (1.26) can be extended to three dimensions as follows:

$$A(f) = A_0 \exp\left(-\pi f \sum_{ijk} T_{ijk} Q_{ijk}^{-1}\right) \quad (1.27)$$

Where, all the parameters in parenthesis in Equation (1.27) are same as those in the parenthesis of Equation (1.22). Equation (1.27) is derived assuming only inelastic attenuation. To account for loss of amplitude due to spherical divergence along the path, the hypocentral distance between source and observation point is generally used in accordance with the analytical formula (Shearer, 2009) of amplitude in spherical domain. Further, to account for surface amplification effects, an empirical factor is added to the formula. When these are considered Equation (1.27) readily takes the form of Equation (1.22). It is to be noted that, all the relationships between quality factor and spectral acceleration require the knowledge of ray paths. Therefore ray paths for a given source-receiver array is required be computed in advance.

1.2.4 The Inverse Step of Tomography

The inverse step of tomography automatically adjusts the model parameter values to minimize the difference between observed data \mathbf{d}_o and computed data $\mathbf{g}(\mathbf{m})$, under some regularization norms. In most of the cases in seismic tomography the functional \mathbf{g} is nonlinear and a suitable non-linear scheme accounts for this nonlinearity. There exist many methods of inversion; however we are restricted our study to gradient method and damped least square method only.

1.2.4.1 Objective Function of an Inverse Problem

The inverse problem is formulated by defining an objective function that consists of data residual term and few regularization terms. The misfit between observed data and predicted data is the essential component of an objective function. If the error in relationship $\mathbf{d}_o = \mathbf{g}(\mathbf{m}_{true})$ is of Gaussian type, then least square or L_2 measure is used to quantify the misfit as (Rawlinson and Sambridge, 2003):

$$\Psi(\mathbf{m}) = \|\mathbf{g}(\mathbf{m}) - \mathbf{d}_o\|^2 \quad (1.28)$$

To give more weight to the accurate data against the data with high uncertainty, the Equation (1.28) is written statistically as (Rawlinson and Sambridge, 2003):

$$\Psi(\mathbf{m}) = (\mathbf{g}(\mathbf{m}) - \mathbf{d}_o)^T \mathbf{C}_d^{-1} (\mathbf{g}(\mathbf{m}) - \mathbf{d}_o) \quad (1.29)$$

Where, \mathbf{C}_d is a data covariance matrix consisting of weights of data. If errors are uncorrelated the $\mathbf{C}_d = \left[\delta_{ij} (\sigma_d^j)^2 \right]$ where σ_d^j is uncertainty of j^{th} data. One of the major problems with this definition of data misfit is that the L_2 measure is sensitive to outliers. This means that the component of data having spurious values will have a significant effect on the size of Ψ since each residual is squared in L_2 norm. Therefore, sometime solution produced by this norm is less reliable compared to L_1 norm (Claerbout and Muir, 1973; Menke, 1989). Despite this weakness, most inversion schemes adopt L_2 norm under Gaussian statistics.

In most of the geophysical problems, the inverse problem are either under-determined or mixed-determined. These constraints are not addressed into the model parameters by data alone. Therefore a regularization term $\Phi(\mathbf{m})$ is included in the objective function to reduce the non-uniqueness of the problems. The function $\Phi(\mathbf{m})$ is generally defined as (Rawlinson and Sambridge, 2003):

$$\Phi(\mathbf{m}) = (\mathbf{m} - \mathbf{m}_o)^T \mathbf{C}_m^{-1} (\mathbf{m} - \mathbf{m}_o) \quad (1.30)$$

Where, \mathbf{C}_m is an a priori model covariance matrix (Tarantola, 2005). If the model parameters are uncorrelated then $\mathbf{C}_m = \left[\delta_{ij} (\sigma_m^j)^2 \right]$ where σ_m^j is uncertainty associated with j^{th} model parameters. The values considered in \mathbf{C}_m are usually taken from prior information. The effect of the model covariance matrix is to encourage the solution models that are more nearer to the initial reference model \mathbf{m}_o .

One more regularization term often considered in inversion problem is one that attempts to find an acceptable trade-off between predicted data satisfying the observed data and computed model with minimum structural variations (Constable et al., 1987). This regularization term is introduced in the objective function by defining the same as (Sambridge, 1990):

$$\Omega(\mathbf{m}) = \mathbf{m}^T \mathbf{D}^T \mathbf{D} \mathbf{m} \quad (1.31)$$

Where, $\mathbf{D}\mathbf{m}$ is matrix of finite difference estimate of a specified special derivative (Sambridge, 1990). Combining $\Psi(\mathbf{m})$, $\Phi(\mathbf{m})$ and $\Omega(\mathbf{m})$ the objective function is written as (Rawlinson and Sambridge, 2003):

$$S(\mathbf{m}) = \frac{1}{2} [\Psi(\mathbf{m}) + \varepsilon \Phi(\mathbf{m}) + \eta \Omega(\mathbf{m})] \quad (1.32)$$

Where, ε is referred to as the *damping factor* and η as the *smoothing factor*. The values of ε and η govern the trade-off between how well the solution model \mathbf{m}_{est} will satisfy the observed data \mathbf{d}_o , how closely \mathbf{m}_{est} is to \mathbf{m}_o and the degree of smoothness of \mathbf{m}_{est} . There are several means for selecting appropriate values of ε and η . One approach is to inspect the trade-off curves between model perturbation (or roughness) for different values of ε (η). For different non-zero values of ε and η the combine contour plot of model perturbation versus model roughness could be used. This process requires considerable computational efforts. An alternative ways of doing this is to perform a synthetic reconstruction of synthetic model using the real source receiver geometry. The appropriate values of ε and η would be those that provide most accurate reconstruction of synthetic model. Many authors (Oncescu et al., 1984; White, 1989; Steck et al., 1998; Rawlinson et al., 2001) uses semi-quantitative approach to choose the values of ε and η . In a Bayesian formulation of inversion, the knowledge of *a priori* information is of paramount importance. To properly respect this approach the smoothing term is required to be ignored which is done by setting $\eta = 0$. Under this setting, the covariance matrix would reflect the actual statistical properties of data. Since in this formulation, a priori model covariance matrix reflect the uncertainty associated with the a priori information. Minimizing the objective function results in an *a posteriori* model distribution in which associated uncertainty would be less than the prior uncertainty. This is the desired outcome and depends upon the quality of data that how good data are. The major difficulty with this method is that it is very difficult in practical scenario to obtain meaningful a priori information concerning the data and model errors. Nevertheless, the Bayesian formulation has been used by a number of authors including Aki et al. (1977), Lutter and Nowack (1990), Scales and Snieder (1997).

Gradient based method use the derivative of objective function $S(\mathbf{m})$ at a specific point in model space (Tarantola, 2005). One basic assumption that is shared by all gradient based method is that the objective function is sufficiently smooth such that it allows a local quadratic approximation about some current model as (Rawlinson and Sambridge, 2003):

$$S(\mathbf{m} + \delta\mathbf{m}) = S(\mathbf{m}) + \hat{\gamma}\delta\mathbf{m} + \frac{1}{2}\delta\mathbf{m}^T \hat{H} \delta\mathbf{m} \quad (1.33)$$

Where, $\delta \mathbf{m}$ is a perturbation to the current model and $\hat{\boldsymbol{\gamma}} = \partial S / \partial \mathbf{m}$ and $\hat{\mathbf{H}} = \partial^2 S / \partial \mathbf{m}^2$ are the gradient vector and the Hessian matrix respectively. These partial derivatives are given as:

$$\hat{\boldsymbol{\gamma}} = \mathbf{G}^T \mathbf{C}_d^{-1} [\mathbf{g}(\mathbf{m}) - \mathbf{d}_o] + \varepsilon \mathbf{C}_m^{-1} (\mathbf{m} - \mathbf{m}_0) + \eta \mathbf{D}^T \mathbf{D} \mathbf{m} \quad (1.34)$$

$$\hat{\mathbf{H}} = \mathbf{G}^T \mathbf{C}_d^{-1} \mathbf{G} + \nabla_m \mathbf{G}^T \mathbf{C}_d^{-1} [\mathbf{g}(\mathbf{m}) - \mathbf{d}_o] + \varepsilon \mathbf{C}_m^{-1} + \eta \mathbf{D}^T \mathbf{D} \quad (1.35)$$

Where, $\mathbf{G} = \partial \mathbf{g} / \partial \mathbf{m}$ is the Frechet matrix of partial derivatives which are computed during the solution step of forward problem. The computation of $\hat{\mathbf{H}}$ is a time consuming process and is practically avoided particularly in the situation where $\mathbf{g}(\mathbf{m}) - \mathbf{d}_o$ is small or if the functional \mathbf{g} is quasi linear in which term $\nabla_m \mathbf{G}^T$ can be neglected (Tarantola, 1987). Both the matrices do not lie in the model space, but in the dual of model space (Tarantola, 1987). Since \mathbf{g} in most of the cases is non-linear, the minimization of objective function (Equation 1.33) requires an iterative approach:

$$\mathbf{m}_{n+1} = \mathbf{m}_n + \delta \mathbf{m}_n \quad (1.36)$$

Where, \mathbf{m}_0 is the initial model. The objective function is minimized for the current estimated ray paths at each step to obtain \mathbf{m}_{n+1} , after which new ray paths are calculated for the next iteration. The iteration procedure cease when either the observed data are satisfied by the predicted data or the change in $S(\mathbf{m})$ with increasing iteration gets sufficiently small.

1.2.4.2 Gauss-Newton Method and Damped Least Square Method

The Gauss-Newton method aims to locate the updated model \mathbf{m}_{n+1} by computing the minimum of the tangent paraboloid to $S(\mathbf{m})$ at \mathbf{m}_n . At the minimum value of S , gradient of it with respect to \mathbf{m} will vanish, therefore:

$$\mathbf{F}(\mathbf{m}) = \mathbf{G}^T \mathbf{C}_d^{-1} [\mathbf{g}(\mathbf{m}) - \mathbf{d}_o] + \varepsilon \mathbf{C}_m^{-1} (\mathbf{m} - \mathbf{m}_0) + \eta \mathbf{D}^T \mathbf{D} \mathbf{m} = 0 \quad (1.37)$$

Where, $\mathbf{F}(\mathbf{m}) = \hat{\boldsymbol{\gamma}}$. For a new model \mathbf{m}_{n+1} , the functional $\mathbf{F}(\mathbf{m})$ can be expanded using Taylor series around an old model \mathbf{m}_n as (Rawlinson and Sambridge, 2003):

$$F_i(m_{n+1}^1, \dots, m_{n+1}^M) = F_i(m_n^1, \dots, m_n^M) + \sum_{j=1}^M (m_{n+1}^j, \dots, m_n^j) \frac{\partial F_i}{\partial m^j} \Big|_{m_n} = 0 \quad (1.38)$$

In Equation (1.38), M indicate number of model parameters and F_i is component of the matrix \mathbf{F} . Equation (1.38) is written as (Rawlinson and Sambridge, 2003):

$$\mathbf{m}_{n+1} = \mathbf{m}_n - \left[\frac{\partial \mathbf{F}}{\partial \mathbf{m}} \right]_n^{-1} [\mathbf{F}_n] = \mathbf{m}_n - \left[\frac{\partial^2 \mathcal{S}}{\partial \mathbf{m}^2} \right]_n^{-1} \left[\frac{\partial \mathcal{S}}{\partial \mathbf{m}} \right]_n \quad (1.39)$$

Where, $[\partial \mathcal{S} / \partial \mathbf{m}]_n$ is the gradient vector and $[\partial^2 \mathcal{S} / \partial \mathbf{m}^2]_n$ is the Hessian matrix. Substitution of derivatives from Equation (1.34, 1.35) gives Gauss-Newton solution as (Rawlinson and Sambridge, 2003):

$$\begin{aligned} \delta \mathbf{m}_n = & - \left[\mathbf{G}_n^T \mathbf{C}_d^{-1} \mathbf{G}_n + \nabla_m \mathbf{G}_n^T \mathbf{C}_d^{-1} [\mathbf{g}(\mathbf{m}_n) - \mathbf{d}_o] + \varepsilon \mathbf{C}_m^{-1} + \eta \mathbf{D}^T \mathbf{D} \right]^{-1} \\ & \times \left[\mathbf{G}_n^T \mathbf{C}_d^{-1} [\mathbf{g}(\mathbf{m}_n) - \mathbf{d}_o] + \varepsilon \mathbf{C}_m^{-1} (\mathbf{m}_n - \mathbf{m}_0) + \eta \mathbf{D}^T \mathbf{D} \mathbf{m}_n \right] \end{aligned} \quad (1.40)$$

In quasi Newton method, the Hessian matrix is ignored as mentioned earlier, therefore quasi Newton form is (Rawlinson and Sambridge, 2003):

$$\begin{aligned} \delta \mathbf{m}_n = & - \left[\mathbf{G}_n^T \mathbf{C}_d^{-1} \mathbf{G}_n + \varepsilon \mathbf{C}_m^{-1} + \eta \mathbf{D}^T \mathbf{D} \right]^{-1} \\ & \times \left[\mathbf{G}_n^T \mathbf{C}_d^{-1} [\mathbf{g}(\mathbf{m}_n) - \mathbf{d}_o] + \varepsilon \mathbf{C}_m^{-1} (\mathbf{m}_n - \mathbf{m}_0) + \eta \mathbf{D}^T \mathbf{D} \mathbf{m}_n \right] \end{aligned} \quad (1.41)$$

An alternative formulation is commonly obtained when the functional \mathbf{g} is linearizable as:

$$\mathbf{d}_o \approx \mathbf{g}(\mathbf{m}_0) + \mathbf{G}(\mathbf{m} - \mathbf{m}_0) \quad (1.42)$$

Writing $\delta \mathbf{d} = \mathbf{d}_o - \mathbf{g}(\mathbf{m}_0)$ and $\delta \mathbf{m} = \mathbf{m} - \mathbf{m}_0$, the Equation (1.42) becomes:

$$\delta \mathbf{d} \approx \mathbf{G} \delta \mathbf{m} \quad (1.43)$$

One step solution is obtained by writing the objective function as (Rawlinson and Sambridge, 2003):

$$\mathcal{S}(\mathbf{m}) = \frac{1}{2} \left[(\mathbf{G} \delta \mathbf{m} - \delta \mathbf{d})^T \mathbf{C}_d^{-1} (\mathbf{G} \delta \mathbf{m} - \delta \mathbf{d}) + \varepsilon \delta \mathbf{m}^T \mathbf{C}_m^{-1} \delta \mathbf{m} + \eta \delta \mathbf{m}^T \mathbf{D}^T \mathbf{D} \delta \mathbf{m} \right] \quad (1.44)$$

The functional in this case is (Rawlinson and Sambridge, 2003):

$$\mathbf{F}(\mathbf{m}) = \mathbf{G}^T \mathbf{C}_d^{-1} (\mathbf{G} \delta \mathbf{m} - \delta \mathbf{d}) + \varepsilon \mathbf{C}_m^{-1} \delta \mathbf{m} + \eta \mathbf{D}^T \mathbf{D} \delta \mathbf{m} = 0 \quad (1.45)$$

Direct solution from Equation (1.45) can be written as (Rawlinson and Sambridge, 2003):

$$\delta \mathbf{m} = \left[\mathbf{G}^T \mathbf{C}_d^{-1} \mathbf{G} + \varepsilon \mathbf{C}_m^{-1} + \eta \mathbf{D}^T \mathbf{D} \right] \mathbf{G}^T \mathbf{C}_d^{-1} \delta \mathbf{d} \quad (1.46)$$

If smoothing term η is neglected then Equation (1.46) becomes:

$$\delta \mathbf{m} = \left[\mathbf{G}^T \mathbf{C}_d^{-1} \mathbf{G} + \varepsilon \mathbf{C}_m^{-1} \right] \mathbf{G}^T \mathbf{C}_d^{-1} \delta \mathbf{d} \quad (1.47)$$

The model solution in Equation (1.47) represents the maximum likelihood solution to the inverse problem or the stochastic inverse solution (Aki et al., 1977). When $\eta = 0$, the expressions in Equations (1.41) and (1.47) are called as damped least square solution to the inverse problem. To obtain the model solution using Equation (1.38), it is essential to have an *a priori* knowledge of \mathbf{C}_d and \mathbf{C}_m . An alternative expression for linearizable inverse

problem was given by Levenberg (1944) which do not require knowledge of C_d and C_m in advance. The solution is given as (modified after Joshi et al., 2010; Mohan and Rai, 1995):

$$\delta m = [G^T G + \lambda I]^{-1} G^T \delta d \quad (1.48)$$

Applying simple algebraic operation, it can be shown that both the Equations (1.47) and (1.48) are similar if data and model parameters are not correlated. The DLS method is the solution technique which is most commonly used in seismic tomography. Many authors have used this technique. Some of those are Aki et al. (1977), Thurber (1983), Zhao et al. (1994), Steck et al. (1998) and Joshi et al. (2010).

1.2.5 Analysis of Solution Quality

The whole process of tomography is incomplete unless some estimate of solution quality or robustness is made. It is inadequate to obtain the solution by simply minimizing objective function without any knowledge of resolution. In most of the cases in seismic tomography, generally two approaches are used to estimate solution robustness. First approach uses local linearity to obtain resolution and model covariance. Second approach uses tests of resolution of artificial synthetic models with realistic source receiver geometry.

1.2.5.1 Resolution and Covariance matrices

To derive the resolution and covariance matrices generally the smoothing parameter η is set to zero. This is because it is more common and straightforward to consider resolution and covariance matrices in Bayesian formulation where error statistics associated with the data and *a priori* model information are assumed to be well known. The true statistical knowledge of error then combines to produce a more accurate posterior model distribution. Under such circumstance ε is also set to zero to respect true *a priori* model covariance. In Bayesian formulation the resolution matrix \mathbf{R} and a posteriori covariance matrix C_M are given as (Tarantola, 1987):

$$\mathbf{R} = [G^T C_d^{-1} G + C_m^{-1}]^{-1} G^T C_d^{-1} G \quad (1.49)$$

$$C_M = [G^T C_d^{-1} G + C_m^{-1}]^{-1} \quad (1.50)$$

The relationship between \mathbf{R} and C_M is given by (Tarantola, 1987):

$$\mathbf{R} = \mathbf{I} - C_M C_m^{-1} \quad (1.51)$$

If parameter ε is kept to be variable, then the above relationships for \mathbf{R} and C_M becomes (Rawlinson and Sambridge, 2003):

$$\mathbf{R} = \left[\mathbf{G}^T \mathbf{C}_d^{-1} \mathbf{G} + \varepsilon \mathbf{C}_m^{-1} \right]^{-1} \mathbf{G}^T \mathbf{C}_d^{-1} \mathbf{G} \quad (1.52)$$

$$\mathbf{C}_M = \varepsilon \left[\mathbf{G}^T \mathbf{C}_d^{-1} \mathbf{G} + \varepsilon \mathbf{C}_m^{-1} \right]^{-1} \quad (1.53)$$

In Levenberg (1944) formulation these relationship becomes:

$$\mathbf{R} = \left[\mathbf{G}^T \mathbf{G} + \lambda \mathbf{I} \right]^{-1} \mathbf{G}^T \mathbf{G} \quad (1.54)$$

$$\mathbf{C}_M = \sigma_{ii}^2 \left[\mathbf{G}^T \mathbf{G} + \lambda \mathbf{I} \right]^{-1} \quad (1.55)$$

Where, σ_{ii}^2 ($i=1,2,3..$) indicate the diagonal elements of model covariance matrix. The diagonal elements represent the standard deviation of the model parameters. If the resolution matrix \mathbf{R} is close to the identity, the posterior covariance matrix is close to zero then the solution model is more close to the real earth (Tarantola, 1987). The resolution and covariance matrices have been used by numerous authors to qualify their solution. Some of those authors are Aki et al. (1977), Steck et al. (1998), Hole (1992), Zelt and Smith (1992), Graeber and Asch (1999), Zhang and Toksöz (1998) and Joshi et al. (2010).

1.2.5.2 Synthetic Tests

Parameterization with continuous field of model parameter such as velocity field often requires reconstruction of a synthetic model using the realistic source receiver geometry. The principle idea behind this approach is that if solution model recovers some known structure with similar length scales using similar ray paths, then the solution model is considered to be reliable. To perform this, the synthetic model is divided into alternating regions of high and low model parameters with length scale equal to or greater than the smallest wavelength structure recoverable in the solution model. This technique is commonly called as checkerboard test. The initial model used for the checkerboard test is same as that used for the real inversion. Regions in which the checkerboard pattern is recovered well are those regions in which structures within the solution model is considered to be well resolved. L  v  que et al. (1993) suggests that this approach is not necessarily as reliable as it appears. It is possible in the checkerboard test that some small structures are well resolved while large structures are poorly resolved. This is because a checkerboard reconstruction can account for the non-linearity of the data dependence on the checkerboard structure but the same cannot account for the non-linearity of the data dependence on the true structure. Therefore, it appears to be much better to use the ray paths produced by the inversion of the real data instead of performing iterative inversion of checkerboard structure. Seismic tomography studies that have used checkerboard resolution tests include Seber et al. (1996), Graeber and Asch (1999), Zelt et al. (1999, 2001), Day et al. (2001) and Mukhopadhyay et al. (2008).

1.3 A BRIEF REVIEW OF TOMOGRAPHY METHODS IN PRACTICES

The tomography method depends upon the class of data such as reflection, wide angle, teleseismic and local earthquake. Normal incident reflection data contain reflected phases so interfaces are required to include in the parameterization whereas teleseismic data do not contain useful reflected phases so model parameter representation is required to be continuous. Therefore different types of data types resolve different aspects of the earth structures. The seismic reflection tomography methods have been presented by various authors including Bishop et al. (1985), Chiu et al. (1986), Farra and Madariaga (1988), Williamson (1990) and Kosloff et al. (1996). Bishop et al. (1985) presented method for simultaneous determination of velocity and interfaces by defining the interfaces with cubic spline. The forward problem is solved by shooting method and the inverse problem is solved by Gauss-Newton method. Farra and Madariaga (1988) presented a method of reflection tomography in which layer parameterization is adopted where interfaces and lateral velocity variation within the layers are defined by cubic B-spline. Shooting method in forward problem and DLS method in inverse problem have been implemented in their method.

Wide angle data contain both refracted as well as reflected phases. One of the first methods for wide angle tomography is given by Zelt and Smith (1992). In their method the model parameterization is done using irregular blocks. Refractions, reflections and head waves are traced through the model by numerical method to solve initial value problem formulated in terms of a pair of first order ordinary differential equations. DLS method has been used for inversion. The method of Zelt and Smith (1992) has been adopted by several authors including Kanasevich et al. (1994), Staples et al. (1997) and Navin et al. (1998).

Teleseismic tomography has been used extensively to map the structure of the lithosphere and crust. The scale of study varies from 10s of km (Rawlinson and Houseman, 1998; Steck et al., 1998) to 100s of km (Mohan and Rai, 1995; Dorbath and Paul, 1996). One of the first papers that describe a method of seismic tomography using teleseismic data was that of Aki et al. (1977). In their method lithosphere is represented by layers of constant velocity blocks. The wavefronts that incident on the surface of model are considered to be planer. The task of ray tracing is straightforward. The inversion step is solved using DLS method.

Local earthquake tomography (LET) is a common tool to obtain structure in seismically active areas. Many studies have been carried out in different parts of the world including California (Aki and Lee, 1976; Thurber, 1983; Scott et al., 1994), Taiwan (Kao and Rau, 1999), Japan (Zhao et al., 1992), Mediterranean (Papazachos and Nolet, 1997;

Haslinger et al., 1999), India (Singh et al., 2011). Compared to other types of tomography one of the distinguishing features of LET is that the earthquake hypocenters (origin time and spatial location) need to be located as a part of image reconstruction.

One of the original studies was documented by Aki and Lee (1976). In their study, 3D crustal structure is parameterized by constant slowness blocks. The initial model was homogeneous and considered DLS inversion was linear, therefore rays consist of straight line paths connecting sources and receivers. The method was implemented to the data collected from a network of 60 stations in Bear Valley, California, from 32 local earthquakes. The robustness of the solution model was analysed using resolution and covariance matrices. The final obtained solution model contains a feature of narrow low velocity zone oriented along the San Andreas Fault zone.

The concept of Aki and Lee (1976) has been refined by many authors including Thurber (1983) and Eberhart-Phillips (1990). Thurber (1983) used velocity nodes of uniform grid and implemented linear interpolation to obtain continuous velocity field. Thereafter, he used approximate 3D ray tracing in his method. Eberhart-Phillips (1990) presented a pseudo bending scheme to more accurately locate the ray paths obtained from method of Thurber (1983). These kinds of refinements are common in most of the implementations of LET including the computer package SIMULPS12 (Evans et al., 1994) in recent times.

1.4 REGIONAL GEOLOGICAL SETUP

Surrounding to the north by Tibetan Plateau, to the south by Indo-Gangetic Plain, to the east by the Indian state of Assam, Arunachal Pradesh and to the west by the Karakoram, Hindu Kush ranges, the earth is occupied by its greatest and most spectacular mountain ranges, the Himalayas. These mountain ranges themselves stretch to form a 250 km wide and 2500 km long arc like shape from west to east between Nanga Parbat and Namcha Barwa which mark, respectively the western anchor and eastern anchor of Himalayas. The Himalayan arc is home of many of the highest peaks on Earth, including the highest, Mount Everest.

The immense mountain ranges, the Himalayas came into existence around 50 million years ago when the Indian plate, driven by plate-tectonic forces, collided with Eurasian plate. The two large landmasses being of equal density cannot under-thrust one completely below other and hence the huge tectonic forces force the upper layers of crustal parts of two landmasses in and around the collision zone skyward and thus formed the visible parts of the Himalayas. To the internal structure, it has been found out by several geophysical investigations that the Indian lithosphere is actually under-thrusting Eurasian lithosphere

along a gently northward dipping plane which is called as detachment plane. Many sub branches of this plane were also found.

The motion of one plate against other, just after the collision, does not come into rest as the studies say that the Indian plate is still moving northward. The relative movement of the two plates results into continuous development of stress in the collision zone which further results into frequent slips and faults in the form of earthquakes, mostly along the detachment plane and its sub branches. The high seismic activity has been reported along the strike of this plane (Monsalve et al., 2006).

The relative motion between the convergent plates produced a series of thrusts. Among these the major thrusts divide the Himalayan arc into four lithotectonic subdivision. These units from north to south are Tethyan Himalayan Sequence, Higher (Greater) Himalayan Sequence, Lesser (Lower) Himalayan Sequence, Siwalik Himalayan Sequence. Gently dipping major thrusts near the collision zone further divided the uplifting crust into two divisions which are: Indus Suture Zone and Trans-Himalayan batholiths. These two units lie to the north of Tethyan Himalayan sequence. The extent and composition of these units are not same in all parts of the Himalayan region. The geology and tectonic settings of the Himalayan belt is shown in Figure 1.9(a) and the area of interest (study) is magnified and shown in Figure 1.9(b). A brief geological description of different tectonic units as shown in Figure 1.9 is given below:

Trans-Himalayan Batholith: It is a complex plutonic unit partly covered by rocks of forearc and continental molasse. The complex is derived from upliftment of magmatic rocks followed by subsequent erosion. The major igneous rocks are gabbros, diorites, and granites. The formation of this complex is thought to have occurred in several phases of cooling of magmas resulted from partial melting of a subducting Neo-Tethyan slab beneath the Asian plate (Sorkhabi, 1999). The tectonic environment is not same along east west direction. The western igneous rocks in the Kohistan-Ladakh region represent an island arc environment whereas eastern igneous rocks represent an Andean-type environment as described by Windley (1995).

Indus-Tsangpo Suture Zone (ITSZ): It is the zone along which the Tethys Ocean was consumed by subduction processes. This zone includes areas of collision between the Indian plate and the Tibetan Lhasa block in the eastern Himalaya and the Kohistan-Ladakh arc in the western Himalayas as described by Windley (1995). This zone can be traced for more than 2000 km (Searle, 1991) and host various types of rocks from which a bit of formation history can be traced. The presence of complete successions of ophiolites containing diamonds suggests high pressure and rapid extrusion during subduction along this

zone. In the Ladakh region of Himalaya, the Spongtang Ophiolite consists of crustal rocks of oceanic floor and rocks of upper mantle. These rocks were obducted onto the northern passive continental margin of India during the Late Cretaceous (Pedersen et al., 2001). In the northwestern India, Olistoliths consist of sedimentary deposits of abyssal turbidite origin found in reefs and continental slopes. The major rocks include solidified lavas of mafic to felsic types as well as dunites, cherts, serpentinites. Red sandstones and limestones are associated with Tethys Ocean sediments and can be seen in Ladakh region (Windley, 1995).

Tethyan Himalayan Sequence (THS): Located to the south of ITSZ, it consists of 10-17 km thick marine sediments which were deposited before the collision on the shelf and slope of the Indian continent. These sediments are largely unmetamorphosed and occur in synclinal-type basins. These also formed the house of excellent preservation of fossils due to unmetamorphosed nature. The age fossiliferous rocks range from Late Precambrian to Cretaceous and some even Eocene age (Sinha, 1989). The sedimentary rocks are also interbedded with volcanic rocks of Paleozoic to Mesozoic origin (Brookfield, 1993; Steck et al., 1993; Critelli and Garzanti, 1994). Miller et al. (2001) used Rb-Sr dating method to obtain the age of mylonitic orthogenesis unit in the Kullu-Larji-Rampur Window and found to be ~1840 Ma. This Window is the part of Tethyan Himalayan Sequence (THS).

Greater Himalayan Crystalline (GHC) Complex: The higher or greater Himalayan crystalline complex lies on the lesser Himalayan sequence as a thrust sheet. It is also known as Central Crystalline Zone. It generally consists of high grade deformed metamorphic rocks of Paleoproterozoic to Ordovician age (1800-480 Ma). It forms a continuous belt to the south of THS and marks the existence of orogenic belt. The thrusting of HHC started around 20-23 Ma with the development of Main Central Thrust that brings the higher Himalaya on the top of lower Himalaya (Hubbard and Harrison, 1989). HHC also occur as isolated patches in the Zaskar and Tso-Morari strata of NW Himalaya where it is surrounded by THS (Honegger et al., 1982; Steck et al., 1998; DiPietro and Pogue, 2004).

Lesser Himalaya Sequence (LHS): This consists of sediments and low grade metasediments together with volcanic and granitic components. These may be shale, sandstone, conglomerate, slate, phyllite, schist, quartzite, limestone and dolomite. The age of these rocks ranges from Precambrian –Lower Paleozoic and Tertiary. Lithologically, the metasedimentary, metavolcanic and augen gneiss rocks are in the age group of 1870-1850 Ma (Yin, 2006) and these rocks are primarily from Indian origin. Low grade metasedimentary rocks are non-fossiliferous (Gansser, 1964; LeForte, 1975) and are overlain by Precambrian to Cretaceous sequence. The geology is complicated due to folding, faulting and thrusting. Tectonically, the entire Lesser Himalayas consists of two sequences of rocks:

allochthonous and autochthonous-paraautochthonous units with various nappes, klippes and tectonic windows. The para-autochthonous crystalline rocks are made up of low- to medium grade rocks. These lower Proterozoic clastic rocks (Parrish and Hodges, 1996) are subdivided into two groups. Argillo-arenaceous rocks dominate the lower half of the succession, whereas the upper half consists of both carbonate and siliciclastic rocks (Hagen, 1969; Le Forte, 1975; Stöcklin, 1980).

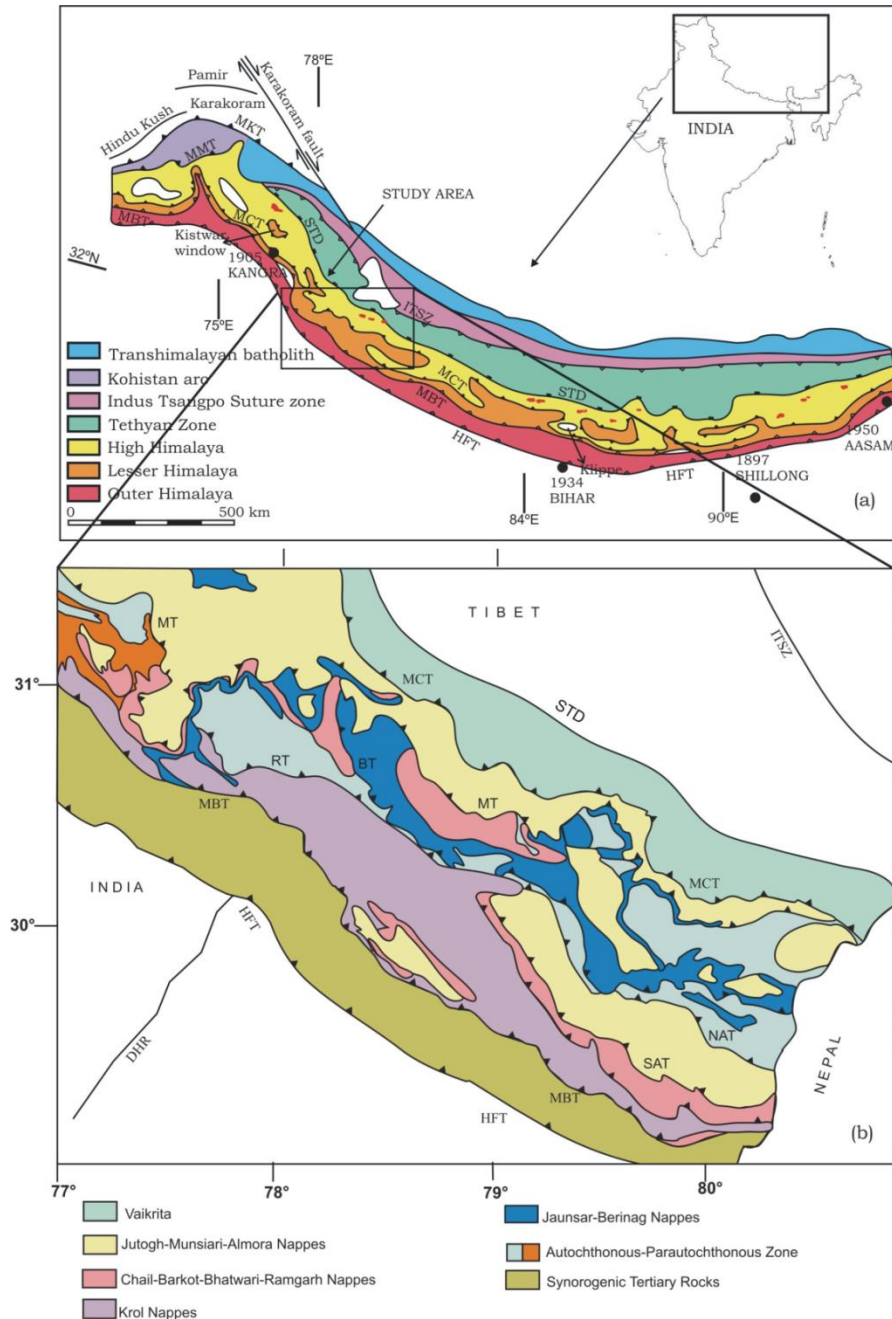


Figure 1.9: Figure showing the geology and tectonic settings of Himalayan belt (a) and of a magnified portion of the study area (b), modified after Valdiya (1980).

Valdiya (1978) is of the opinion that the metasedimentary sequence of the southern limb of the Almora synform is constituted of two thrust sheets, the upper one is called the Almora Nappe and the lower the Ramgarh Nappe (Pandey, 1950) overlying the Outer Sedimentary Belt. The Ramgarh Nappe is composed of mildly metamorphosed flyschoid rocks. The delimiting Ramgarh Thrust is not discernible in the northern flank, being overlapped by the rocks of the Almora Nappe with which the Ramgarh Nappe forms an imbricating pair. However, Raina and Dungrakoti (1975) deny the existence of the Raingarh Thrust.

Outer Himalayan Sequence: The outer or Siwalik Himalaya include the low altitude Siwalik Hills with flat-floored structural valleys. These valleys consist of 9500 m thick pile of Cenozoic sedimentary rocks characterized by folds and faults (Thakur, 1992). The basin comprised of eroded and denudated thick deposition of terrigenous sequence of Miocene age, which were produced by the upliftment, subsequent erosion of the Himalaya and deposition by rivers. Rock types are Siwalik Molasse conglomerates that extend southward to Gangatic basin. These rocks belong to Neogene Siwalik and Paleogene-early Miocene strata (Yin, 2006). The sedimentary basin has a good aspect of petroleum. Compared to Lesser Himalaya, the Outer Himalaya is wider in the western Himalaya.

The present study region covers in and around the Pithoragarh district which falls in the Lesser Himalaya zone. This region exposes extensive sedimentary belt which include the outer Krol Belt and inner Tejam-Pithoragarh Belt and few crystalline thrust sheets. In Pithoragarh, thick pile of argillo-calcareous and arenaceous sediments which constitutes the Garhwal Supergroup is exposed. This Supergroup is divisible into three groups namely: lower argillo-calcareous Tejam Group, middle predominantly arenaceous Berinag Group and the upper metamorphites of Didihat Group.

1.5 REGIONAL TECTONIC SETTINGS AND SEISMICITY OF STUDY REGION

The cross section of the Himalayan belt is divided into the South Tibetan Detachment (STD) and three principal thrusts, namely, the Main Central Thrust (MCT), the Main Boundary Thrust (MBT) and the Himalayan Frontal Thrust (HFT) (Thakur, 2004). A typical cross section of the Himalaya through Kumaon region is shown in Figure 1.10. The STD and principle thrusts are discussed below:

The South Tibetan Detachment (STD): This is defined by large scale, low angle, ductile shear zone-normal fault that bounds the top of GHC metamorphic sequence along the Higher Himalaya (Searle and Godin, 2003). This Detachment is also known as North Himalayan Normal Fault (Herren, 1987; Buchfiel et al., 1992). The system of STD separates

THS from GHS. In the region of Kumaon and Garhwal, this is also known as Dar-Martoli fault (MF).

The Main Central Thrust (MCT): it is the one of the major tectonic boundaries which divides two contrasting structures of GHC to the north and LHS to the south. The relative motion of the blocks across MCT has caused the development of buckles in which palaeogene and Neogene sediments were deposited. In the Kumaon and Garhwal Himalaya some researches also describe the MCT as Munsiri thrust which can be traced up to Kullu-Larji-Rampur window (Heim and Gansser, 1939), beyond which MCT is mission and replaced by Panjal Thrust (PT). The PT is described by many publications as MCT (Gansser, 1981). In the Kumaon region around Sobla, the MCT and STD are closer compared to their position in the western side. The MCT is largely inactive except in some reactivated segments showing lateral strike-slip movement as found in Central Nepal (Nakata, 1989).

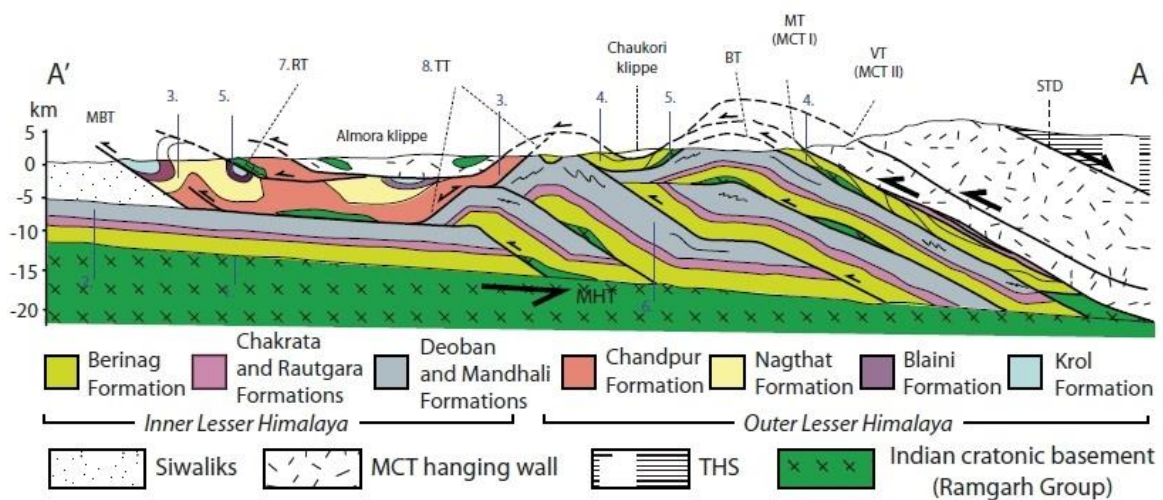


Figure 1.10: Schematic cross section through the Kumaun Himalaya modified after Célérier et al. (2009).

The Main Boundary Thrust (MBT): it is the one of the major tectonic boundaries between LHS to the north and Outer Himalayan foreland basin to its south (Gansser, 1964; Meigs et al., 1995; Decelles et al., 2001). Majorities of the earthquakes in the NW Himalaya are concentrated in the Lesser Himalayan zone confined between MCT and MBT and have shallow focus depths. The evolutionary history of Himalaya suggests MBT is younger than MCT and is more active currently (Le Forte, 1975). However, both these boundary have been treated as contemporaneous features in the steady state model of Seeber and Armbruster (1981).

The Himalayan Frontal Thrust (HFT): The HFT represents a zone of active deformation between the Outer Himalayan Sequence to the north and the Indian plain to the south. Compared to others this is the youngest, most active and have shallow depth. Some segments of HFT shows active faulting and neotectonic activity (Thakur, 2004). It currently demarcates tectonic displacement zone between the Himalaya and stable Indian continent with a convergence rate of 10–15 mm/yr (Thakur, 2004).

The model of Seeber and Armbruster (1981) suggests that all the above discontinuities converge with the plane of detachment which marks the interface between the subducting Indian slab beneath the Eurasian plate in the northern side and overlying sedimentary wedge in the southern side. The Kumaon Himalaya exposes all the above major discontinuities along with the thrust system found in the Almora Crystalline zone as discussed below.

The base of Almora Nappe demarcates tectonic base of Lesser Himalayan allochthonous unit which is characterized by two regional thrust systems (Heim and Gansser, 1939 and Valdiya, 1980). These thrusts are called as the North Almora Thrust (NAT) and South Almora Thrust (SAT). The rocks of the Almora Crystallines along with other lithologically correlatable units of the Baijnath, Askote, Chiplakot and Satpuli units, have been studied by many workers, including some pioneers in Himalayan geology, which suggests that the thrust sheets or nappes pushed over the younger rocks from the north with their roots in the Central Crystallines of the Higher Himalaya (Heim and Gansser, 1939 and Gansser, 1964). The NAT is an important fault system between the Inner and Outer Lesser Himalayas and with respect to Indian craton to the south, the former is more proximal than the latter (Valdiya, 1980; Srivastava and Mitra, 1994 and C  lerier et al., 2009).

The South Almora Thrust is a very low dipping thrust. The overlying and underlying formations converges and are made up of almost similar lithological units which has made its (SAT) quite difficult. Some workers including Saxena and Rao (1975) deny its very existence. Some detailed studies by Vashi and Merh (1974) and other workers have conclusively established the existence of the South Almora Thrust. They suggest that SAT joins up with the NAT at the northwestern closure of the vast plunging syncline in the western Nayar valley to the west of Dudhatoli massif.

The meizoseismal area of the 1905 Kangra earthquake extended well to the Garhwal Himalaya from the west (Khattri et al., 1989). The portion of Garhwal Himalayas immediately east of this is a part of nearly 700 km long seismic gap where earthquakes of magnitude 8 or greater have not happened in recorded history (Seeber and Armbruster, 1981; Khattri and Tyagi, 1983; Khattri, 1987). However the Garhwal Himalaya in the recent past

was rocked by two damaging earthquakes; the 20 October, 1991 Uttarkashi earthquake (mb 6.6) and the 28 March, 1999 Chamoli earthquake (mb 6.3). The Kumaon Lesser Himalaya falls in the seismic gap region in seismic zone IV and V of seismic zoning map of India. This region is prone to micro earthquakes to moderate earthquakes frequently. Most of the earthquakes in this region occur at shallow depths. The seismicity of the western Himalaya has been studied by several authors including Paul (2010), Paul et al. (2010) and Kumar (2012). One of the main characteristics is the trends of the location of hypocenters are along the Himalayan belt (Monsalve et al., 2006). This happens because most of the stress in the collision zone is released through seismic slip along the detachment plane.

1.6 A BRIEF REVIEW ON UNDERLYING VELOCITY STRUCTURE OF THE HIMALAYAN TERRAIN

An absolute and comparative study of structure and characteristics of lithosphere inferred from previous studies in and around the region concerned in the study area is very essential for setting up the problem of finding variation of velocity. This is because most of the geophysical problems are underdetermined and hence a prior knowledge of different parameter such as seismic velocities, crustal structure including depth to Moho is essential. This is not only to set up the problem, but it is also required to correlate same parameter from two different region and hence to give an effective trend of structure particularly those of same tectonic history such as different regions in the Himalayan arc system. In context of this I have studied the above works documented by the different authors and presented in this section in both absolute and comparative ways.

A number of authors (Kamble et al., 1974; Chander et al., 1986; Rai et al., 2006; Kumar et al., 2007; Oreshin et al., 2008; Caldwell et al., 2008, 2009; Mukhopadhyay and Sharma, 2010a; Kanaujia et al., 2012; Mahesh et al., 2013) have documented their studies related to design 1D velocity model of Western Himalaya using seismograms recorded from local and teleseismic earthquakes. In order to study the crustal structure beneath NW Himalaya, Rai et al. (2006) obtain several 1D shear wave velocity models using receiver function analysis of seismograms that were obtained from 15 broadband seismographs operated in a linear profile across NW Himalaya, from Gangetic plain in the north to the southwestern flank of the Karakoram in Ladakh. The study was primarily focused on the estimation of depth of Moho, which was reported to be progressively deepening, from ~40 km beneath Delhi in the south to ~75 km depth at Karakoram fault in the north. Kumar et al. (2007) obtained 1D velocity model using the 22 Hindu Kush earthquake data and reported upper mantle velocity along the north-west Himalaya to be 8.1 km/s. Oreshin et al. (2008)

performed integrated analysis of teleseismic body wave recordings to obtain several 1D velocity models for P and S waves in NW Himalaya including Ladakh and Western Tibet. The recordings were taken from a linear array of 16 portable broadband seismographs along an array running through the Himalaya to the Karakoram. The study shows low velocity mid crust only at stations around Indus Zangbo Suture. Caldwell et al. (2008) performed surface wave dispersion tomography to obtain 1D crustal shear wave velocity model using 15 broadband seismographs in a 500 km long NS array deployed in the NW Himalaya from the Indian plain in the south to Karakoram in the north through Tsangpo Suture and the Tso Moriri Dome. The model suggests a low velocity zone in the crust at a depth of 25-40 km that may be an indicative of fluid or partial melts. The same study was extended by Caldwell et al. (2009), but with 16 broadband seismometers along their previous profile and obtain several 1d velocity models that indicate again the partial melts in the mid crust in NW Himalaya.

Using the data from 42 stations in Garhwal and some part of Kumaon Himalaya, Mukhopadhyay and Sharma (2010) obtained both 1D and 2D velocity models of the area. They observed the P and S wave velocities that increase from ~5.47 km/s and ~3.05 km/s at the near surface to ~8.21 km/s and ~4.75 km/s at the moho depth, respectively. In the Garhwal Himalaya, Kanaujia et al. (2012) obtain 1D velocity model along with relocation of earthquakes that were recorded by 12-station seismological network deployed in the Garhwal Himalaya. The study reported four-layer velocity model and does not shows any low velocity layer in the crust. With the help of 50 digital broadband stations in the western Himalaya, Mahesh et al. (2013) obtained 1D velocity model to locate the local earthquakes. They reported that majority of the earthquakes are confined to the upper 20 km of the crust forming an ~10-km-wide band along the surface trace of the Munsiri Thrust.

As compared to number of studies for 1D velocity variation, the number of studies for 2D and 3D velocity variation in western Himalayas is fewer, with some of the notable studies are those contributed by Mukhopadhyay and Kayal (2003) and Malik (2009), Mukhopadhyay and Sharma (2010a), Hazarika et al. (2013). Using aftershock data of 1999 Chamoli earthquake (m_b 6.3), from 28 closely spaced temporary and permanent seismic stations, Mukhopadhyay and Kayal (2003) were successfully estimated 3-D seismic velocity variation in a $80 \text{ km} \times 60 \text{ km} \times 15 \text{ km}$ crustal volume. As their study remains limited up to a depth of 15 km and could not include the zone due north of MCT, the fact that crustal level folding and faulting involving the role of basement for deformation remains unclear (Mukhopadhyay and Sharma, 2010a). Mukhopadhyay and Sharma (2010a) show in their studies that shallow subsurface rocks indicate lower velocity in Tethys Sedimentary Zone,

Lesser Himalayas and in the sub-Himalayas whereas metamorphic rocks of Higher Himalayas indicate higher velocity. The moho depth was not resolved in their studies; however they noted that v_p/v_s ratio for most of the crust remain less than 1.78, indicating the poison solid. The distribution of hypocenter shows that most of the earthquakes occur along the tectonic trend of Western Himalaya, leaving a small seismic gap orienting NE–SW between 78.5°E and 79°E longitudes. The crustal level folding and faulting are shown in their results but the depth of moho remain unresolved. The observed 2D section of velocity do not show any northward dipping detachment plane as suggested by (Seeber and Armbruster, 1981; Baranowski et al., 1984; Ni and Barazangi, 1984; Molnar, 1990), that decouples upper crustal highly folded and faulted formations from underlying relatively deformation free basement of Indian crustal material. Using the data from 16 broadband stations, Hazarika et al. (2013) estimated the depth to moho in Western Himalaya and Ladakh using receiver function analysis. They have reported that depth to Indian Moho at this zone increases from ~ 50 km beneath the lesser and higher Himalaya to ~ 80 km beneath eastern Ladakh. They further notice the continuity of Indian Moho across across the Indus Tsangpo Suture zone, which suggest underthrusting Indian plate goes beyond the colison zone of India and Asia. They found that Poisson's ratio is comparatively high (0.280-0.303) beneath eastern Ladakh; intermediate (0.269-0.273) beneath the Tethyan Himalaya; and low (0.249-0.253) beneath the Lesser and Higher Himalaya.

Investigation of velocity variation of lithosphere in the Central part and Estern part of Himalayan belt has also been done by many authors (Monsalve et al., 2006, 2008; Li et al., 2008; Priestley et al., 2008; Acton et al., 2010; Kim et al., 2012). Using data from the HIMNT (Himalaya Nepal Tibet Seismic Experiment) broadband seismic station network, Monsalve et al. (2006) performed simultaneous inversion for hypocenter and velocity by applying the program VELEST as outlined by Kissling et al. (1994) to obtain 1D velocity models of eastern Nepal and the southern Tibetan Plateau. They found that accumulation of earthquakes occur along the Himalayan arc with a gap between longitude 87.3°E and 87.7°E . The vertical distribution of earthquakes shows bimodal depth distribution in the Himalayas of eastern Nepal and the southern Tibetan Plateau. They have also reported that some of the earthquakes occur at the upper mantle depths and from there they have reported the conclusion that the continental upper mantle deforms by brittle processes. The velocity profile shows the Moho depth of 55 km in the region of Nepal while the same is 70 km in the region of Tibet. Kim et al. (2012) also obtained a detailed 1D velocity model in the same region using the data from the same seismic station network as used by Monsalve et al.

(2006). They found contrasting low velocity zone between 50 km and 60 km beneath the High Himalaya.

Though numerous authors documented works on underlying velocity structure in the region of Himalayan belt, however the detailed 3D velocity structure are rare in that region. Some of the studies are those given by Mukhopadhyay and Kayal (2003), Li et al. (2008) and Malik (2009). One of the main reasons may be due to lack of seismic data in this terrain.

1.7 A BRIEF REVIEW ON UNDERLYING ATTENUATION STRUCTURE OF THE HIMALAYAN TERRAIN

Extensive works have been carried out in the recent past in the Himalayan belt to characterize the Himalayan lithosphere. In the Garhwal part of Himalaya, some of the studies are those documented by Gupta et al. (1995, 1996), Gupta and Kumar (1998), Mandal et al. (2001), Nath et al. (2008), Mukhopadhyay et al. (2008), Sharma et al. (2009), Mukhopadhyay and Sharma (2010b), Tripathi et al. (2014), Negi et al. (2015) and Kumar et al. (2015). In the adjoining southwestern part of Garhwal Himalaya, Gupta et al. (1995) analyzed the coda waves recorded from seven local earthquakes using single back scattering model in 30-60 sec windows. The results have shown the frequency dependence of coda Q_c as $Q_c = 126f^{0.95}$. This relationship says that the average attenuation in the Garhwal Himalaya is less pronounced at higher frequencies. Mandal et al. (2001) obtained a frequency dependent relation $Q_c = (30 \pm 0.8)f^{1.21 \pm 0.03}$ by analyzing coda wave in the window range 30-80 sec using data from Chamoli aftershocks recorded by National Geophysical Research Centre (NGRI). Nath et al. (2008) also obtained a frequency dependent shear wave attenuation relation as $Q_s = (78.38 \pm 19.2)f^{(0.74 \pm 0.09)}$ using weak motion near field data recorded from Chamoli Mukhopadhyay et al. (2008) used the Chamoli aftershocks data recorded by Geological Survey of India (GSI) to estimate different Q_c relations for separate window lengths. The estimated Q_c relationships are $Q_c = (33 \pm 2)f^{(1.17 \pm 0.03)}$, $Q_c = (55 \pm 6)f^{(1.16 \pm 0.05)}$, $Q_c = (78 \pm 15)f^{(1.12 \pm 0.08)}$, $Q_c = (93 \pm 18)f^{(1.07 \pm 0.08)}$ and $Q_c = (122 \pm 20)f^{(0.98 \pm 0.07)}$ for window lengths respectively 10, 20, 30, 40 and 50 sec. These results have shown that the value of Q_c systematically increase with the increasing value of window lengths. As with increasing window lengths deeper region show up, therefore it can be said that Q_c increase with increasing depths. Since, the Q_c is inversely proportional to attenuation, it means attenuation decrease with increasing depth. This facts states that

lithosphere becomes more homogenous with increasing depths (Mukhopadyay et al., 2008). At greater depths and at higher frequencies the value of Q_c becomes almost constant, which may be due to the decaying nature of turbidity with depth in the crust and transparent nature of mantle in this region (Gusev, 1995; Mukhopadyay et al., 2008). More or less similar conclusions have been drawn by Mukhopadhyay and Sharma (2010b) in their study. Sharma et al. (2009) have also investigated the Chamoli region using the aftershock data of the same 1999 Chamoli earthquake (M6.4). They have used 25 aftershocks from recorded by five stations to obtain P-wave and S-wave quality factors in the frequency range 1.5-24 Hz. They have estimated the relations $Q_p = (44 \pm 1) f^{(0.82 \pm 0.04)}$ and $Q_s = (87 \pm 3) f^{(0.71 \pm 0.03)}$ for P-wave and S-wave respectively. A comparison of this study with that of Mandal et al. (2001) shows clearly that $Q_c > Q_s$ for higher frequencies (>8 Hz) in that region.

Tripathi et al. (2014) studied attenuation characteristics using coda normalization method in the Garhwal Himalayan region. The data used were taken from portable broadband seismometers deployed at three locations namely New Tehri Town, Srikot and Narendra nagar of Garhwal Himalaya. The study reports strongly frequency dependent Q_p^{-1} and Q_s^{-1} values that decrease from $(15.86 \pm 0.90) \times 10^{-3}$ and $(5.35 \pm 0.51) \times 10^{-3}$ at 1.5Hz to $(0.54 \pm 0.11) \times 10^{-3}$ and $(0.34 \pm 0.06) \times 10^{-3}$ at 24 Hz, respectively following the power-law ($Q_p^{-1}(f) = (27.432 \pm 3.149) \times 10^{-3} f^{(-1.162 \pm 0.057)}$, $Q_s^{-1}(f) = (8.051 \pm 0.737) \times 10^{-3} f^{(-0.932 \pm 0.045)}$) showing P-wave attenuation is stronger than that for S-wave, suggesting high degree of heterogeneity in the crust of Garhwal Himalaya. They added further that such variation corresponds to seismically active region with tectonic complexity. Negi et al. (2015) also investigated the P-wave and S-wave attenuation characteristics in the Garhwal Himalaya using data recorded by eight stations operated by Wadia Institute of Himalayan Geology, Dehradun, India, from 2007 to 2012. They have estimated frequency dependent relations $Q_p = (56 \pm 8) f^{(0.91 \pm 0.002)}$ and $Q_s = (151 \pm 8) f^{(0.84 \pm 0.002)}$. Both the relations indicate strong attenuating crust of Garhwal Himalaya. Using strong motion data and single backscattering method, Kumar et al. (2015) have estimated the coda Q in Garhwal and Kumaon Himalaya as $Q_c = (65 \pm 2.4) f^{(1.07 \pm 0.04)}$ and $Q_c = (96 \pm 6.9) f^{(1.06 \pm 0.04)}$.

Compared to the number of studies in Garhwal Himalaya fewer studies have been done in Kumaon Himalaya. Some of those are Paul et al. (2003), Joshi (2006), Joshi et al. (2008, 2010), Paul et al. (2003) studied the attenuation of high frequency (1-25 Hz) seismic waves in the Kumaon part of Himalaya using single backscattering model given by Aki and

Chouet (1975). They have used the coda waves of 30 sec window length and obtained a frequency f dependent relationship for quality factor as $Q_c = (92 \pm 4.73) f^{(1.07 \pm 0.023)}$. They have attributed the low value of coda Q to the high tectonic activity of this region compared to stable region where coda Q is high. Joshi et al. (2006) studied the frequency dependent shear wave attenuation in the Pithoragarh region of Kumaon Himalaya using data from strong motion accelerographs deployed in the region. They have applied an inversion algorithm in their work and reported the frequency dependent variation of shear wave quality factor as $Q_s = 30 f^{1.45}$. The low value of Q_s supports the high level of tectonic activity in this region. Joshi et al. (2010) obtained three dimensional shear wave attenuation structures Q_s in the Pithoragarh region of Kumaon Himalaya using a modified version of attenuation tomography given by Hashida and Shimazaki (1984) using data from eight strong motion accelerographs deployed in this region. The study has reported the high value of Q_s in various places like Pithoragarh, Dharchula and Sobla, which indicates lesser attenuating subsurface and higher seismic hazard compared to other places like Thal and Didihat. Singh et al. (2015) have also estimated attenuation relations for P-wave and S-wave as $Q_p = (22 \pm 5) f^{(1.35 \pm 0.04)}$ and $Q_s = (104 \pm 10) f^{(1.3 \pm 0.03)}$ from 23 local earthquakes records. Both the relations indicate strong attenuating behavior of Kumaon Crust (Singh et al., 2015).

In the western part of Himalaya, several authors including Verma et al. (1998), Kumar et al. (2005), Mukhopadhyay et al. (2006), Mukhopadhyay and Tyagi (2007, 2008), Kumar (2010) and Parvez et al. (2012) have documented their works on attenuation quantification and characterization of the subsurface structures. Mukhopadhyay et al. (2006) obtained inverse of frequency dependent Q_c as $Q_c^{-1} = (113 \pm 7) f^{(1.01 \pm 0.05)}$ using data from 9 stations and 11 local earthquakes in the NW Himalaya. The stations were the part of 17 station northwestern Himalayan seismic network operated in the period July 2002-October 2003 (Rai et al., 2006). Their study has shown that the region is tectonically active and highly heterogeneous. Mukhopadhyay and Tyagi (2008) have performed a similar study and have concluded that the both coda and intrinsic attenuation decreases with depth. Kumar (2010) estimated the frequency independent shear wave attenuation in the NW Himalaya in the upper 15 km of the crust in this region. The estimated Q_s is 218 ± 56 which corresponds to the seismically active region. Parvez et al. (2012) have reported the frequency dependent characteristics of P-wave and S-wave attenuation in the upper crust of NW Himalaya for a frequency range 1.5 Hz to 18 Hz. They have estimated the quality factors Q_p and Q_s as

$Q_p = (97 \pm 3) f^{(1.06 \pm 0.06)}$ and $Q_s = (127 \pm 6) f^{(0.96 \pm 0.06)}$ respectively indicating strong frequency dependency. They have concluded from their results that the seismic energy of high frequency attenuates more in the upper lithosphere than in the lower lithosphere.

In the eastern part of Himalaya some of the studies are those give by Hazarika et al. (2009), Padhy and Subhadra (2010), Kumar et al. (2014). Hazarika et al. (2009) performed coda wave attenuation study in the northeastern India using 45 local earthquakes records. They have used single scattering model to analyze eight different time window durations (20, 30, 40, 50, 60, 70, 80, and 90 s) at ten frequency bands ranging from 1.0 to 18 Hz. They have obtained an average attenuation relation for this region as $Q_c = 52.315 \pm 1.07 f^{(1.32 \pm 0.036)}$.

The attenuation studies presented above have shown that the quality factor in the entire Himalayan belt can be defined to be the proportional of some power raised to frequency. Though entire belt is tectonically active, the Q_c value for Kumaon is higher than the Garhwal as described by Kumar et al. (2015). High level of heterogeneity in the upper part of crust compared to the lower part (Mukhopadhyay et al., 2008) has been reported.

Although a plenty of studies were documented on the quantitative estimation of attenuation in Western Himalaya to infer the seismic constraints on the behavior of the regional lithosphere; however, most of those were carried out either using coda wave normalization method or slop analysis of attenuation relation given by Aki and Richard (1980). These methods give average estimation of quality factor and do not provide any insight to the spatial variation in attenuation characteristics within the lithosphere. The detailed 3D estimation of quality factors were documented by Joshi et al. (2010) in the Kumaon part of Himalaya. The reason behind fewer studies on 2D or 3D attenuation characteristic may be attributed to the complex Himalayan terrain and lack of sufficient data required to perform 2D or 3D studies.

1.8 SYNTHESIS OF THE PROBLEMS AND OBJECTIVES THE PRESENT WORK

The roots of a seismic tomography method essentially consist of forward problem and inverse problem. There exist independent fields of research in both the problems. The forward problem has been considered in the present work as a subject of theoretical research whereas the study of inverse problem has been limited to the DLS method only. Reviews on the studies of forward problem in seismic travelttime tomography is given in §1.2.2 and §1.2.3, where the genesis of different methods have been discussed. We analyzed the following points before selecting a method of forward problem.

1) An accurate computation of true source-receiver ray paths in presence of lateral variation of wavespeed is always required in almost all tomography application. The ray paths are straight in a homogeneous medium or piecewise straight in a layered medium, but the same are complex in complex velocity zone where due to presence of sharp anomalous body ray triplication may occur.

2) Determination of first arrivals of seismic phases is very important particularly for precise estimation of the earth's velocity field and earthquake hypocenters.

3) The head waves dominate in the complex region or in the region of active orogeny like Himalayan belt. The computation of head waves is paramount importance for the structural evaluation of thin layers and low velocity zones. A method which does not properly respect the first arrivals will fail to compute the heads waves.

4) The fast computation is always required in practical application of a forward method. However, there always exists a trade-off between computation time and accuracy in numerical computation. A method is generally considered to be better which would permit a single step change in any of the two parameters subject to the requirements in practical applications.

All the above steps are fulfilled by the class of Fast Marching Methods only as these only give guarantee for the computation of first arrivals. The FMM is accurate and very fast as described in §1.2.2.2. Like other method it also has disadvantages that in the source neighborhood due to strong curvature of wavefronts, a numerical grid system with finite spacing fail to map the wavefronts properly, which produce an error that propagate throughout the medium. The maximum error is located in the neighborhood of source and gradually decreases away from the source. Many authors in the recent past have analyzed the problems and given several methods without changing the basis of FMM to remove the source neighborhood error. Multistencils Fast Marching (MSFM) method as described in Hassouna and Farag (2007) is comparatively new in the series of FMM which address the above issue without violating the general principle of the entropy concept imposed in the FMM. The method of MSFM is the only method which respects computation of traveltimes to a grid node from all the surrounding nodes in a 2D or 3D Cartesian domain. Therefore it removes the concept of axial direction directions and the source neighborhood error. The computation is of superior quality in the homogeneous or nearly homogeneous media with isotropic or nearly isotropic grid system. However, the computation error increases with the increases with the increase of anisotropy of grid system regardless of the medium.

The conventional ray tracings are still the important methods for the determination of earthquake hypocenters and preliminary velocity models of a region. For a little change in

take-off angle at source in a complex medium, both shooting and bending method suffers from high degree of fluctuation of ray paths, due to which convergence of final ray point to its destination become sometime difficult and time consuming.

The computation of interface geometry between two adjacent contrasting rock units is very important in proper structural evaluation. In reflection tomography many authors considered interfaces in their methods. However, in the refraction tomography the introduction of interfaces is rare. One of the major difficulties is that, due to minor change in the orientation or geometry of interfaces the ray paths changes to a greater degree, therefore computation of interface is required to include the computation of hypocenters as well as velocity simultaneously.

Besides the theoretical problems, the practical problem with the study region is that a proper velocity model is not available in this region. The region falls in the complex zone and the quantity of data is limited. Based on all the above problems, the objectives were divided into two folds as:

1) *Theoretical aspects:*

- a) To develop an algorithm parallel to shooting method, to speed up and to code the same.
- b) To study algorithm of FMM and to code the same and perform extensive numerical tests to analyze the derived results.
- c) To develop a method and algorithm that improves the results of MSFM method.
- d) To develop a multi-parameter inversion method and algorithm that performs simultaneous inversion of P and S waves to obtain hypocenters, origin times, body wave velocities, interface representing discontinuities.
- e) To develop a 3D traveltimes tomography algorithm and code based on derived and improved MSFM method.
- f) To write an algorithm for 3D attenuation tomography using parameterization of grid types.

2) *Practical aspects:*

- a) To study 1D, 2D, 3D velocity models and seismicity in the part of the Kumaon Lesser Himalaya using the developed algorithms and codes.
- b) To study 3D attenuation structure of the study region using a developed algorithm.

1.9 THE WORKS PRESENTED IN THE THESIS

To fulfill the objectives considered in §1.8, the forward problems are considered first. One ray tracing method and algorithm parallel to shooting method is developed first. One fast scanning method named as spiral search method is developed and implemented in the algorithm to compute two points ray paths. Later on, gradient method to automatically adjust the ray path is formulated and implemented in series with spiral search method. In the final algorithm, the spiral search method locates the ray path approximately where as gradient method gives the final location of the ray path between source and receiver. The self reflection within layers is considered so that the method would be useful even in complex geometry of interfaces that define discontinuities of a medium.

The marching equation is solved and algorithm is presented using binary tree for fast computation of traveltimes field. The traveltimes fields are tested for its validation using numerical models. The utility of traveltimes contours have also been discussed. To remove the source neighborhood error in FMM, a method is proposed in the direction of MSFM method. The algorithm to the method uses angular interpolation of directional derivatives from all possible direction and hence the biasness due to anisotropic grid system that appears in MSFM method is removed. Several numerical experiments have been performed, which have shown better results than the FMM and MSFM method.

To obtain simultaneously hypocenters, origin times, body wave velocities, interface representing discontinuities a multiparameter inversion method has been proposed and its algorithms are developed. The forward problem considering is solved by the use of developed ray tracing method and the inverse problem is solved using DLS method. The algorithm works both in 1D and 2D domain of computations. This algorithm has been used to obtain 1D, 2D velocity of the Kumaon Lesser Himalaya as well as to study the seismicity of the study region. The 3D velocity structure of Kumaon Himalaya is obtain by developing an tomography algorithm using developed MPFMM as a tool to solve forward problem and DLS method as a tool to solve inverse method.

A method of attenuation tomography is given by modifying the relation of spectral acceleration with quality factor Q to use the same in continuous field of Q . Data were processed and frequency shear wave dependent site amplification factors at all the stations were obtained using the method given in Joshi et al. (2010). Using the processed acceleration spectra, relocated hypocenters, computed velocity models and ray paths from traveltimes inversion, frequency dependent shear wave attenuation models were obtained and discussed.

1.10 OVERVIEW OF THE THESIS

The whole work of the present thesis is organized into 8 chapters including Chapter 1. This Chapter is devoted to the introduction and survey of literature relevant to the investigation compiled in the later chapters. Chapter 1 begins with the importance of seismic data which have been used from the very beginning in the field of seismology by different workers to investigate the internal structure of the earth using various methodologies including tomography. The seismic tomography method is then discussed in terms of inverse theory. Basic steps of tomography together with literature reviews have been presented. Later on, in this Chapter tectonic regional tectonic settings as well as seismicity of the Himalaya with special focus to the region which is considered in the thesis is discussed. Literature reviews related to velocity and attenuation structure of the study region are presented. The problems in tomography methods and the objective of this thesis are then discussed. The works presented in this thesis and organizations of this thesis are then given at the end of this Chapter.

In Chapter 2, the forward problem of tomography is considered using ray tracing similar to shooting method but with the help of spiral search technique. In the beginning of this Chapter, mathematical formulation of the Snell's law using simple vector algebra is given. For a given take off angle from a given source point in a medium, the same formulation is utilized to develop an algorithm to trace a ray path without destination (one point boundary value problem) using rectangular type of parameterization. This algorithm is presented in this Chapter. The one point boundary value problem is then converted into two point boundary value problem (complete ray tracing) with the help of spiral search technique. The spiral search technique was developed to complete the ray tracing as well as to speed up the algorithm. The mathematical basis of spiral search technique and complete mathematics of ray tracing is given later on. At the end, several numerical experiments which have been conducted to examine the algorithm are presented

In Chapter 3, the forward problem of tomography is considered using Fast Marching Method (FMM). The algorithm to the method was given with the help of binary tree for fast computation and then it was coded in FORTRAN and various numerical tests on numerical models have been done. This Chapter includes the algorithms and several numerical tests. The purpose of this Chapter was two ways: first, to tests the algorithm for common governing rules of wave propagation and second, to utilize the algorithm for analysis of travelttime contours of different geological structures of the earth..

In Chapter 4, an improved method of FMM is presented which removes significantly the source neighborhood problem encountered in FMM. The method is compared with other methods with the help of numerical experiments.

In Chapter 5, a multiparameter inversion method is developed, that allows to perform simultaneous inversion of P and S waves to obtain hypocenters, origin times, body wave velocities and interfaces representing discontinuities. Detailed mathematical formulations as well as developed algorithms are presented in parts.

In Chapter 6, the practical aspect of multiparameter inversion is presented. The study region with strong motion network is given. The seismicity is described in this region by locating several earthquakes using the developed algorithm. The known events were then utilized to obtain precise 1D velocity model as well as to improve the accuracy of event location with the help of same inversion algorithm. Both 1D velocity model as well as relocated events in terms of seismicity is discussed. Later on this Chapter, mathematical basis of 2D and 3D tomography using FMM is described. The obtained 1D velocity model has been utilized to obtain 2D velocity model of the region using the developed 2D tomography method. The same method with minor changes has been used to obtain 3D tomography of the study region. The results of tomography are then discussed with the help of resolution matrix.

In Chapter 7, 3D attenuation tomography is considered. An algorithm is presented for the attenuation tomography, which has been developed using the modified version of relation for spectral acceleration and quality factor. The method for computation of site amplification factor is also given. This has been utilized to obtain the site amplification at all the stations in the study region. The site amplification factor and the algorithm for 3D attenuation tomography are then utilized to obtain 3D attenuation structure of the study region. The obtained site amplifications at various stations and attenuation structures beneath the study region are discussed at the end.

In Chapter 8, overall conclusions and future direction of the works are given.





RAY TRACING

2.1 INTRODUCTION

Geometrical ray tracing between source and receiver has remained one of the most successful methods of forward problems in seismology to obtain hypocenters of earthquakes and preliminary subsurface structures of the earth. Since a source-receiver ray path in a medium depends on the velocity of the medium, therefore for a given take off angle from initial point (source location) if the ray path is traced through the medium then there is no guarantee that the ray will pass through the other destination point (station or receiver location). Therefore the basic problem of two point (complete ray) tracing is divided into two steps. The first step is to solve one point ray tracing for a given velocity model and for a given position of source. The next step is to consider destination point (receiver or station location) and to find a true take off angle at source position such that the ray passes through the destination point. First in this chapter, the model parameterization is considered by dividing a model into rectangular boxes and then defining the velocity in each box. One point ray tracing is then solved by developing an algorithm using vector algebra in three dimensions. The second step of ray tracing is solved by a method which has been called as spiral path search method. The spiral path search method when joined with gradient path search method gives fastest possible results. However, the gradient method and its joint working with spiral search method are discussed in Chapter 5. To include the interfaces, a model parameterization is also considered in the algorithm, where the horizontal envelopes of planes formed by different rectangular boxes are replaced by 3D surfaces to obtain a natural model parameterization that represents 3D layer geometry with 3D velocity variation. The natural model parameterization helps to solve the ray tracing in its most general form in three dimensions as it includes the reflected rays bounded by natural surfaces. The last part this chapter presents several numerical experiments using the developed algorithm.

2.2 MODEL PARAMETERIZATION: TYPE-A AND TYPE-B

The model parameterization is the platform of computational domain to solve the forward problem. It is decided based on the objective as well as scale of study of the forward problem. As for example, if the objective of forward problem is to know the effect of 1D variation of properties of the earth on wave propagation in small scale study then simple stack of rectangular boxes, each having separate physical properties (e.g. velocity or attenuation) are sufficient to define the model but if the same objective is oriented for large scale study then concentric spherical layers each having separate physical properties as used in the development of PREM (Dziewonski and Anderson, 1981) are to be considered. In the present work, two types of model parameterization namely Type-A and Type-B are considered. Under Type-A model parameterization, a medium is divided into rectangular boxes, as shown in Figure 2.1(a), and in each box the model parameter is defined separately. This type of model parameterization is known as called Constant Velocity Voxel (CVV) when the model parameter is velocity alone. This type of model parameter is simple to define 3D variation of medium properties and help to solve many of the tomographic problems.

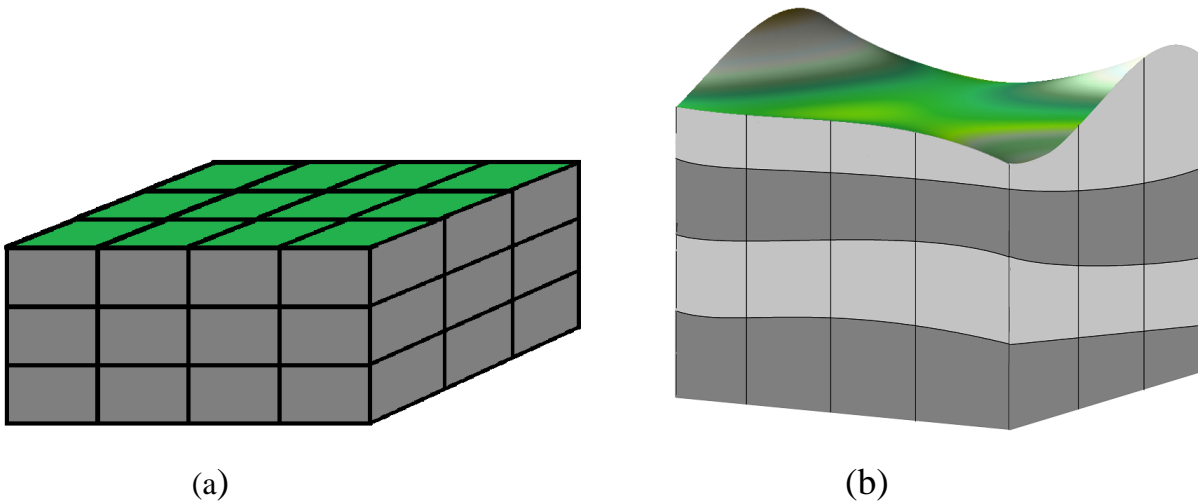


Figure 2.1: Model parameterization; Type-A, (a); Type-B, (b)

Although, Type-A parameterization is good to define straight layers of earth's subsurface; it does not define the natural layer boundary found inside the earth in the form of discontinuities, which may have 3D geometry. To consider the effect of such layers Type-B model parameterization is considered as shown in Figure 2.1(b). In type-B model parameterization the vertical definition is same as that of Type-A while the horizontal layers are replaced by 3D surfaces representing the discontinuity (interfaces) of the medium. Ray tracing algorithms are developed on the basis of both the types of model definition. The

Type-A model parameterization is implemented in Chapter 5 in the development of conventional tomographic algorithm which is used to solve the problem of earthquake location with origin time, and to find the body wave velocity structure of earth. The Type-B parameterization is implemented in the same tomographic algorithm which is used to find velocity structure, earthquake location with origin times as well as the natural 3D layer structure of earth.

2.3 VECTOR EQUATIONS FROM SNELL'S LAW

This section presents two basic vector equations which are derived using Snell's law. The first is for vector equation of refracted ray and second is for vector equation of reflected ray, for a given incident ray on a given plane. To obtain the geometry of refracted and reflected ray path, an elementary area of an arbitrary surface is considered and a ray is imagined to incident at a point where the surface has normal vector \mathbf{n} as shown in Figure 2.2. The vector equations for refracted and reflected ray are derived using vector algebra which are presented in § 3.2.1 and § 3.2.2. Later on in section 3.2.2 the basic vector equation for intersection of a straight line and plane is presented to make it use in the development of ray tracing algorithm.

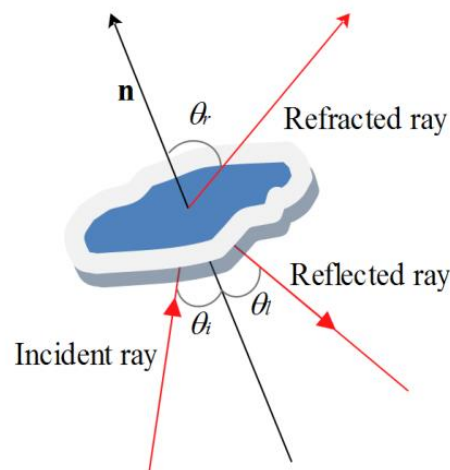


Figure 2.2: Geometry of refracted ray and reflected ray for a incident ray on a plane having normal vector, \mathbf{n} . In the diagram θ_i , θ_r , and θ_t are respectively incident angle, refracted angle and reflected angle.

2.3.1 THE EQUATION OF A REFRACTED RAY FOR A GIVEN INCIDENT RAY ON A GIVEN SURFACE

According to the Snell's first law, the incident ray, refracted ray and the normal to the plane lie in a single plane, so the Figure 2.2 can be redrawn as shown in Figure 2.3 in two

dimensions for refracted ray. Two types of cases are possible, depending upon velocity of two adjacent media as shown in Figure 2.3(a) and 2.3(b). In the Figure 2.3(a), KM is the incident ray and MT is the corresponding refracted ray and MN is the normal vector to the plane. θ_i and θ_r are the incident and refracted angles respectively. V_i and V_r are the velocities of the media in which incident ray and refracted ray lie respectively. In this case, the velocity of the medium containing refracted ray is lower than the velocity of the medium containing incident ray. The figure for opposite case is shown in Figure 2.3(b). Ray vectors parallel to the refracted ray have been drawn in both the cases which met the incident ray at K (in case 1) and at A (in case 2). These rays cut the normal vector at N (in case 1) and at D (in case 2). A plane parallel to the boundary plane was considered which passes through K (in case 1) and A (in case 2). This plane meets the normal at L (in case 1) and at B (in case 2). The aim is to find KN and AE vectors. For this case 1 has been considered first. The joint bold characters used in the equation are vectors and others are scalars.

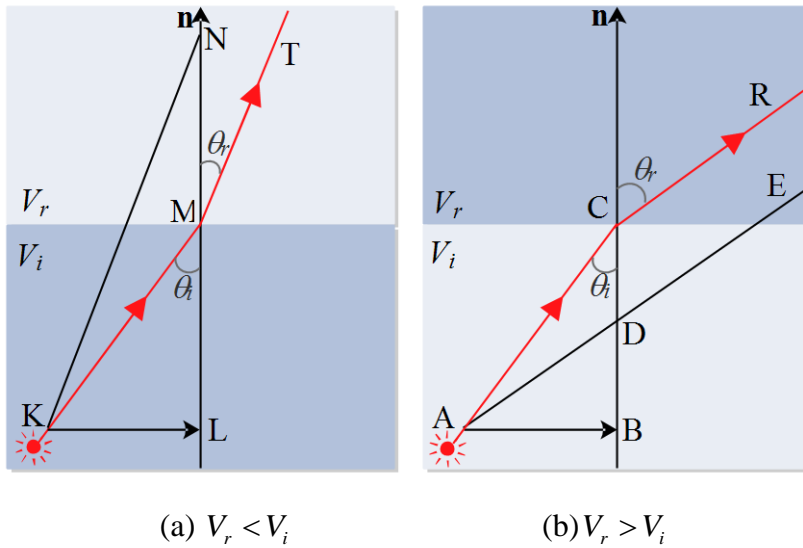


Figure 2.3: Geometry of refracted ray paths, for case 1, (a) and case 2, (b), redrawn from Figure 2.2 in two dimensions.

Since vector MT is parallel to the vector KN so,

$$\begin{aligned}
 \mathbf{KN} &= \mathbf{KM} + \mathbf{MN} \\
 &= \mathbf{KM} + |MN| \mathbf{n}
 \end{aligned}
 \tag{2.1}$$

From Figure 2.3(a),

$$\begin{aligned}
LN &= KL \tan(90 - \theta_r) \\
&= KL \cot \theta_r \\
&= \sqrt{KM^2 - ML^2} \cot \theta_r \\
&= \left[\left\{ KM^2 - (\mathbf{KM} \cdot \mathbf{n})^2 \right\} \cot^2 \theta_r \right] \\
&= \left[\left\{ KM^2 - (\mathbf{KM} \cdot \mathbf{n})^2 \right\} \left\{ \frac{V_i^2}{(V_r \sin \theta_i)^2} - 1 \right\} \right]^{\frac{1}{2}} \\
\therefore \frac{\sin \theta_i}{V_i} &= \frac{\sin \theta_r}{V_r} \text{ (from Snell's second law)}
\end{aligned}$$

$$\begin{aligned}
LN &= \left[\left\{ KM^2 - (\mathbf{KM} \cdot \mathbf{n})^2 \right\} \left\{ \left(\frac{V_i}{V_r} \right)^2 \frac{KM^2}{\left\{ KM^2 - (\mathbf{KM} \cdot \mathbf{n})^2 \right\}} - 1 \right\} \right]^{\frac{1}{2}} \\
&= \left[\left(\frac{V_i}{V_r} \right)^2 KM^2 - KM^2 + (\mathbf{KM} \cdot \mathbf{n})^2 \right]^{\frac{1}{2}} \\
&= \left[\left(\frac{V_i^2}{V_r^2} - 1 \right) KM^2 + (\mathbf{KM} \cdot \mathbf{n})^2 \right]^{\frac{1}{2}} \\
&= |\mathbf{KM}| \left[\left(\frac{V_i^2}{V_r^2} - 1 \right) + (\mathbf{I}_{KM} \cdot \mathbf{n})^2 \right]^{\frac{1}{2}} \\
\therefore LN &= |\mathbf{KM}| \left[\left(\frac{V_i^2}{V_r^2} - 1 \right) + (\mathbf{I}_{KM} \cdot \mathbf{n})^2 \right]^{\frac{1}{2}} \tag{2.2}
\end{aligned}$$

Where, \mathbf{I}_{KM} is the unit vector in the direction of \mathbf{KM} . Again from Figure 2.3(a) one can write:

$$\begin{aligned}
MN &= LN - LM \\
&= LN - \mathbf{KM} \cdot \mathbf{n}
\end{aligned} \tag{2.3}$$

Substituting the value of LN from Equation (2.2) in Equation (2.3), MN can be written as:

$$\begin{aligned}
MN &= |\mathbf{KM}| \left[\left(\frac{V_i^2}{V_r^2} - 1 \right) + (\mathbf{I}_{KM} \cdot \mathbf{n})^2 \right]^{\frac{1}{2}} - \mathbf{KM} \cdot \mathbf{n} \\
&= |\mathbf{KM}| \left[\left\{ \left(\frac{V_i^2}{V_r^2} - 1 \right) + (\mathbf{I}_{KM} \cdot \mathbf{n})^2 \right\}^{\frac{1}{2}} - (\mathbf{I}_{KM} \cdot \mathbf{n}) \right]
\end{aligned} \tag{2.4}$$

Substituting the expression of MN from Equation (2.4) in Equation (2.1), the vector \mathbf{KN} can be written as:

$$\mathbf{KN} = \mathbf{KM} + |\mathbf{KM}| \left[\left\{ \left(\frac{V_i^2}{V_r^2} - 1 \right) + (\mathbf{I}_{KM} \cdot \mathbf{n})^2 \right\}^{\frac{1}{2}} - (\mathbf{I}_{KM} \cdot \mathbf{n}) \right] \mathbf{n}$$

$$\frac{\mathbf{KN}}{|\mathbf{KM}|} = \mathbf{I}_{KM} + \left[\left\{ \left(\frac{V_i^2}{V_r^2} - 1 \right) + (\mathbf{I}_{KM} \cdot \mathbf{n})^2 \right\}^{\frac{1}{2}} - (\mathbf{I}_{KM} \cdot \mathbf{n}) \right] \mathbf{n} \quad (2.5)$$

If $|\mathbf{KM}|=1$, either if the incident vector is unit vector then Equation (2.5) becomes:

$$\mathbf{KN} = \mathbf{I}_{KM} + \left[\left\{ \left(\frac{V_i^2}{V_r^2} - 1 \right) + (\mathbf{I}_{KM} \cdot \mathbf{n})^2 \right\}^{\frac{1}{2}} - (\mathbf{I}_{KM} \cdot \mathbf{n}) \right] \mathbf{n} \quad (2.6)$$

Consider case 2 as shown in Figure 2.3(b), where we can write

$$\mathbf{AD} = \mathbf{AC} - \mathbf{CDn} \quad (2.7)$$

$$\begin{aligned} \mathbf{CD} &= \mathbf{BC} - \mathbf{BD} \\ &= \mathbf{AC} \cdot \mathbf{n} - \mathbf{BD} \end{aligned} \quad (2.8)$$

The expression for BD can be derived similar to LN as,

$$\mathbf{BD} = |\mathbf{AC}| \left[\left\{ \left(\frac{V_i^2}{V_r^2} - 1 \right) + (\mathbf{I}_{AC} \cdot \mathbf{n})^2 \right\}^{\frac{1}{2}} \right] \mathbf{n} \quad (2.9)$$

Where, \mathbf{I}_{AC} is unit vector parallel to incident ray AC. The expression for vector \mathbf{AD} in Equation (2.7), with the help of Equations (2.8) and (2.9) can be written as,

$$\frac{\mathbf{AD}}{|\mathbf{AC}|} = \mathbf{I}_{AC} + \left[\left\{ \left(\frac{V_i^2}{V_r^2} - 1 \right) + (\mathbf{I}_{AC} \cdot \mathbf{n})^2 \right\}^{\frac{1}{2}} - (\mathbf{I}_{AC} \cdot \mathbf{n}) \right] \mathbf{n} \quad (2.10)$$

If $|\mathbf{AC}|=1$, either if the incident vector is unit vector then Equation (2.10) becomes:

$$\mathbf{AD} = \mathbf{I}_{AC} + \left[\left\{ \left(\frac{V_i^2}{V_r^2} - 1 \right) + (\mathbf{I}_{AC} \cdot \mathbf{n})^2 \right\}^{\frac{1}{2}} - (\mathbf{I}_{AC} \cdot \mathbf{n}) \right] \mathbf{n} \quad (2.11)$$

It is clear from Equation (2.6) and (2.11) that refracted ray follows a similar expression for both the cases described through Figure 2.2. Therefore, if \mathbf{I}_i is an unit vector parallel to incident ray on a plane having normal \mathbf{n} , then the unit vector \mathbf{I}_r parallel to refracted ray can be written as:

$$\mathbf{I}_r = \varepsilon \left[\mathbf{I}_i + \left[\left\{ \left(\frac{V_i^2}{V_r^2} - 1 \right) + (\mathbf{I}_i \cdot \mathbf{n})^2 \right\}^{\frac{1}{2}} - (\mathbf{I}_i \cdot \mathbf{n}) \right] \mathbf{n} \right] \quad (2.12)$$

Where, ε is a scalar quantity. The value of ε is derived by taking modulus of Equation 2.12 from both sides, which is given as:

$$\varepsilon = \frac{V_r}{V_i} \quad (2.13)$$

Therefore, Equation (2.12) becomes

$$\mathbf{I}_r = \frac{V_r}{V_i} \left[\mathbf{I}_i + \left[\left\{ \left(\frac{V_i^2}{V_r^2} - 1 \right) + (\mathbf{I}_i \cdot \mathbf{n})^2 \right\}^{1/2} - (\mathbf{I}_i \cdot \mathbf{n}) \right] \mathbf{n} \right] \quad (2.14)$$

Equation (2.14) is the resultant expression for the unit vector, \mathbf{I}_r parallel to refracted ray for a unit vector, \mathbf{I}_i parallel to a given incident ray on a given plane having normal vector, \mathbf{n} at the point of incident.

2.3.2 THE EQUATION OF A REFLECTED RAY FOR A GIVEN INCIDENT RAY ON A GIVEN SURFACE

According to the Snell's first law, the incident ray, reflected ray and the normal to the plane lie in a single plane, so the Figure 2.2 can be redrawn as shown in Figure 2.4 in two dimensions for reflected ray. Let the ray in the direction of MB is incident at point B on a plane whose normal is \mathbf{n} . let the reflected ray is directed towards BN as shown in Figure 2.4. Lines MB, BN and DB parallel to normal vector must lie in a single plane due to Snell's first law, therefore a line is drawn parallel to BN which meets incident ray MB at A and normal line at D. A line parallel to MA is also drawn which meets reflected ray at C and normal line at D.

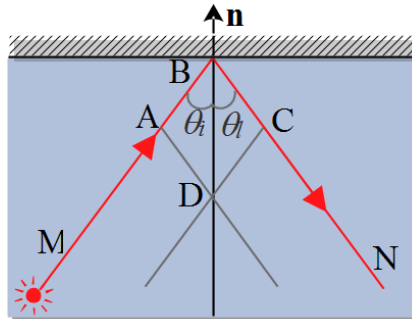


Figure 2.4: Geometry of reflected ray paths redrawn from Figure 2.2 in two dimensions.

Using the Snell's second law we have

$$\angle ABD = \angle DBC \quad (2.15)$$

Therefore,

$$AB = DC = BC = AD$$

$$\begin{aligned} BC &= AD = AB + BD \\ &= AB - BDn \end{aligned} \quad (2.16)$$

$$BD = 2AB \cdot n \quad (2.17)$$

$$BC = AB - 2(AB \cdot n)n \quad (2.18)$$

$$\frac{BC}{AB} = I_i - 2(I_i \cdot n)n$$

$$\therefore AB = BC$$

$$\therefore I_r = I_i - 2(I_i \cdot n)n \quad (2.19)$$

Where, I_i unit is vector parallel to incident ray and I_r is unit vector parallel to reflected ray. Equation (2.19) is the resultant equation of a reflected ray for a given incident ray on a given surface with normal vector n .

2.3.3 THE INTERSECTION POINT OF A PLANE AND A LINE

The vector equation of a plane in terms of a given normal vector, n to the plane and a given point, P_o on the plane is written as;

$$P \cdot n + d = 0 \quad (2.20)$$

Where, $d = -P_o \cdot n$ and P is any point in the plane.

The vector equation of a straight line parallel to a given line segment, M and passing through a point, I_o is written as;

$$I = I_o + Mt \quad (2.21)$$

Where, t is a scalar having real value. Intersection occur when $I=P$ so, from Equations (2.20) and (2.21), the value of t can be derived as;

$$t = -\frac{d + I_o \cdot n}{M \cdot n} \quad (2.22)$$

Intersection is possible only when $|n| \neq 0$. For this case, the point of intersection is given by substituting the value of t from Equation (2.22) into Equation (2.21) as:

$$I = I_o + \left(-\frac{d + I_o \cdot n}{M \cdot n} \right) M$$

or

$$\begin{aligned} I &= I_o + \left(\frac{I_o \cdot n - P_o \cdot n}{M \cdot n} \right) M \\ I &= I_o + \left\{ \frac{(I_o - P_o) \cdot n}{M \cdot n} \right\} M \end{aligned} \quad (2.23)$$

2.4 BASIC ALGORITHM OF RAY TRACING USING TYPE-A PARAMETERIZATION

For a given incident ray on one face of the voxel; the ray path across that voxel can be obtained only when two intersection points intersected by the ray in two faces out of six faces is known. The ray segment connecting these two intersection points will be the incident ray direction for the next adjacent voxel. So the main problem is to derive an iterative formula that can give the incident ray path for a voxel when the incident ray path for previous voxel is known. A voxel or box is made up of six faces. And hence there is huge number of faces even for a small number of voxels or boxes. If they are not define with respect to a single point it is very difficult to find out the intersection points between the ray and the faces which in turn because of difficulty in locating the faces and finding out their orientation. To handle this problem voxels parameterization has been imagined by considering three families of planes in all three X, Y, and Z direction. All the planes along an axis are perpendicular to the axis and hence these are parallel and the spacing between all the adjacent planes is constant. The intersections of such family of planes form the desired boxes. The spacing between the two adjacent planes defines the box size. In this way the all the faces of all the boxes have been located only by three families of planes mutually perpendicular to each other.

If a given line intersects a given plane out of three families of planes at a certain point then this line can be considered as incident ray on a face of the box whose other five faces are formed by a plane adjacent to the given plane in the direction of incident ray and four perpendicular planes closest to the intersection point. These planes can easily be defined with respect to the origin by appropriate spacing value between the two adjacent parallel planes. The refracted ray governed by Equation (2.14) will propagate within the box and finally it will intersect at one point on a particular face out of five faces or five planes adjacent to the initial face. To know that on which plane out of five planes ray intersects before emerging out from the box one plane has to be select out. It is not required to check all the five planes; only three planes lying in the direction of refracted ray is sufficient because the ray will intersects only on a plane out of three planes whose normal vectors lie in a particular quadrant decided by source and station position. This is because the curvature of refracted ray path through a medium is of first order therefore it is sufficient to obtain solution in a quadrant in which source and station lie. For checking the intersection between a ray and these three planes, the basic algorithm was defined as:

- 1) Select a plane and find out dot product between the refracted ray within the box and the normal to the selected plane.
- 2) If the dot product is zero then the intersection will not occur between the plane and the refracted vector, if this dot product is not zero then move to the next step.
- 3) Determine the intersection point and the length of the segment of the refracted vector lying between this intersection point and the previous intersection point and save these values. Until all planes are checked out go to step 1 again.
- 4) Find out the shortest line segment and save it as dist. The refracted ray will intersect the plane for which the length of this line segment is smallest.

Based on the above ideas, the detailed algorithm is developed as shown in Figure 2.5.

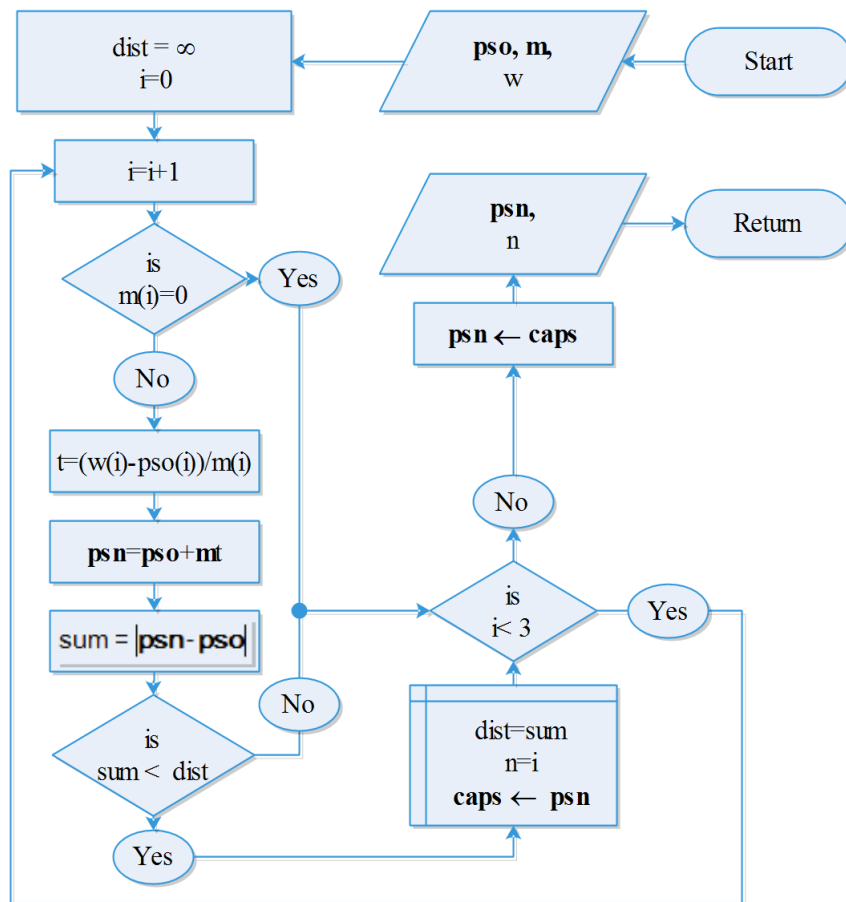


Figure 2.5: An algorithm to find intersection point between a straight line formed by a given vector point, ps_0 and a given tangent, m and a plane out of three planes with weight, w .

The input to the algorithm in Figure 2.5 is a vector point, \mathbf{pso} , vector tangent, \mathbf{m} and an three point array, w that defines the weight of the three planes with respect to corresponding axes. These parameters can be defined as:

$$\left. \begin{aligned} \mathbf{pso} &= (pso(1), pso(2), pso(3)) \\ \mathbf{m} &= (m(1), m(2), m(3)) \\ w &= \{w(1), w(2), w(3)\} \end{aligned} \right\} \quad (2.24)$$

The value n in the algorithm defines the intersected plane as for example its 1 or 2 or 3 value indicates x or y or z planes in a Cartesian domain. The output of the above algorithm is intersected point represented by vector, \mathbf{psn} where \mathbf{caps} is vector that store \mathbf{psn} temporarily. Similar to Equation (2.24) these can be defined as:

$$\left. \begin{aligned} \mathbf{psn} &= (psn(1), psn(2), psn(3)) \\ \mathbf{caps} &= (caps(1), caps(2), caps(3)) \end{aligned} \right\} \quad (2.25)$$

All other parameters in the algorithm are variable. The intersection point is calculated using Equation (2.23). The above unit of algorithm is named for further reference as ‘INTEGRATED ALGORITHM A’ abbreviated as IL-A.

Since a face of a box is common for two adjacent boxes so the refracted ray will be the incident ray for next adjacent box and the calculated intersection point will be the point on one face of the new box where the ray incidence take place. Now the same procedure can be applied to find out the refracted ray within this current box and the point of intersection on another face from which the ray will emerge out from the current box. In this way all the intersection point can be determined. The above ideas have been used to develop a basic unit of an algorithm called as IL-B and is shown in Figure 2.6 to solve two point ray tracing problem. This is called basic unit as it is basically do one point ray tracing, in other words for a given trial take off angle the ray is traced through the model. The algorithm perform two point (source and station) ray tracing under the condition that out of a number of trial take off angle which requires as input at least one take off angle must be the such angle that give acceptable error which measure the distance between final intersection point and station location. Once the final intersection point is determined on the outer boundary of a model surface for a given takeoff angle, the actual takeoff angle by which the ray comes to the station is determined by the following way after setting an error term having some low admissible value.

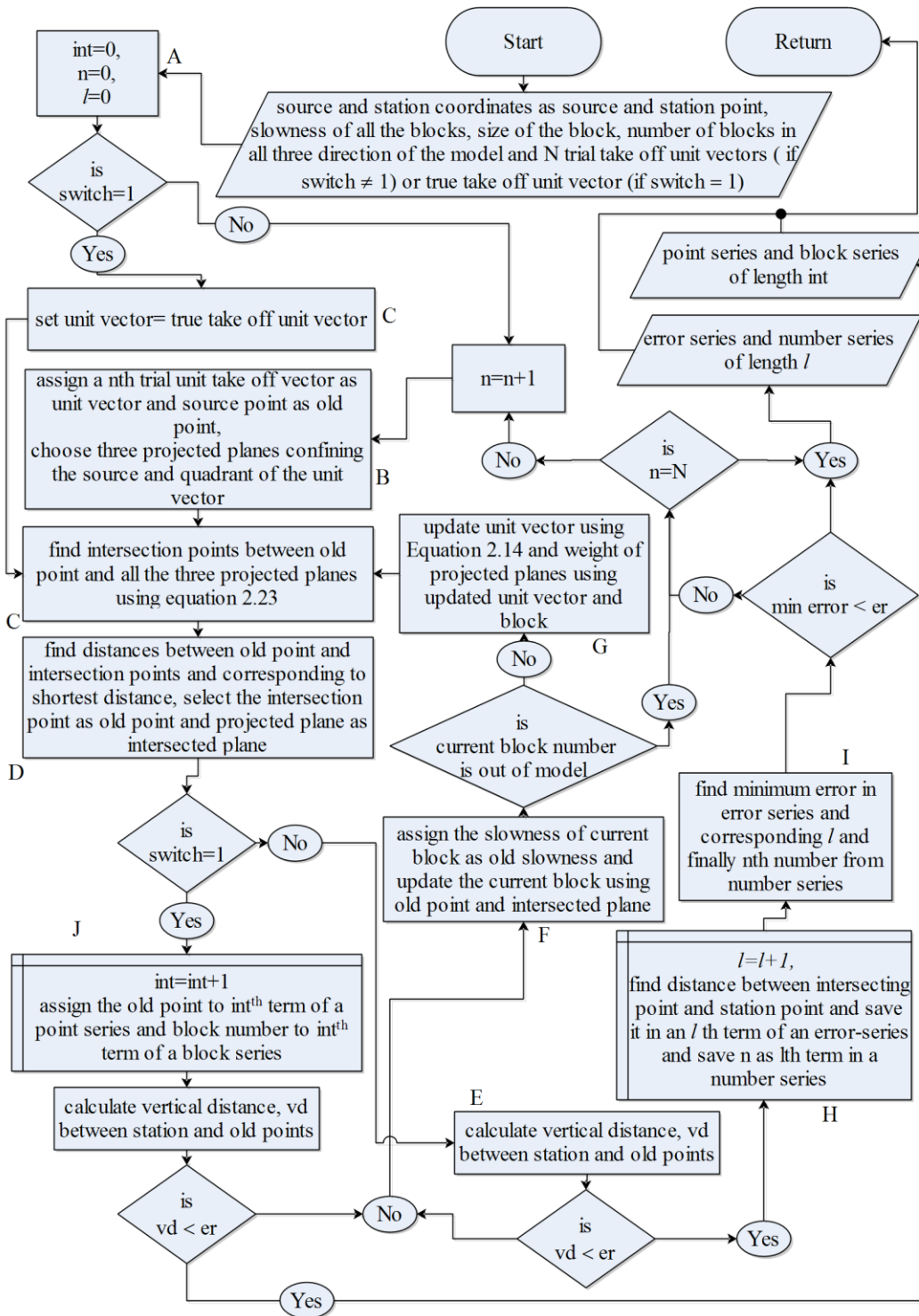


Figure 2.6: The basic ray tracing algorithm. All the shapes in the Figure have standard meanings.

The unit algorithm IL-B has two different types of output for two different values of switch. The switch with value 0 is run to obtain error series and number series, each of length l whereas the same switch with value 1 is required to obtain point series and block series of length int . The error here is defined as the distance between final intersected point and destination point, therefore for N trial angle there exists a maximum of N different values of

error which are stored in an array called as error series. The parameter er can be defined as an acceptable error. For each value of error the corresponding n value indicating n^{th} trial angle is stored in number series. The parameter point series store all the intersected points of true ray path or final ray path that intersects different unit cells (boxes) of the model. The number series parameter store sequentially the identity of all the unit cells through which the final (true) ray pass. The process path with switch value 0 is through ABCDEFGHI whereas the process path with switch value 1 is through ACDJ.

2.5 ALGORITHM OF RAY TRACING USING TYPE-B PARAMETERIZATION

This section presents ray tracing algorithm which is based on Type-B parameterization. The geometry of ray path in this model definition may show self reflection phenomenon because of bending of layers in Type-B model definition, therefore unlike IL-B, reflection cannot be neglected here. The first basic integrated algorithm, the IL-A is therefore modified to incorporate the reflection phenomenon and the modified version is shown in Figure 2.7(a) which is marked as MIL-A. All the basic steps are same as that of IL-A except initial input and one sub-process marked by shape A and final output. Two extra parameters nlp and scf are used in the input box which defined respectively interface number and interface coefficients. The output box has two extra parameters, rf and sn . If the value of n is neither 1 nor 2 then rf having value 1 indicate the phenomenon of refraction else reflection. The sn is a vector representing normal to the layer surface at the point of intersection, when the value of n is neither 1 nor 2.

The sub-process A is designed to perform the change in IL-A. This is aimed to check intersection with the interface above (when refraction takes place) and below (when self reflection takes place), bounding a unit voxel. After deciding intersection the lengths of line segments between intersected points and ps_0 are determined and corresponding to shortest length segment refraction or reflection is chosen temporarily. The shortest line segment within the unit cell is then compare with $dist$ and shortest of these two is chosen final $dist$. Corresponding to that $dist$ either refraction or reflection with above or below interfaces is chosen with n value 3 or with vertical wall with n value 1 or 2. The last step of this sub-process is to find the unit normal vector at the point of refraction or reflection if these phenomenon are chosen to occur. Therefore the general steps of sub-process A can be summarized as:

1. Compute intersection point between an interface (nlp) defined by coefficients (scf_{nlp}) and a line given by tangent m passing through point ps_0 and save it as intersected point, p_1 .

2. Compute intersection point between an interface ($nlp-1$) defined by coefficients (scf_{nlp-1}) and a line given by tangent m passing through point ps_0 and save it as intersected point, p_2 .
3. Compute two lengths as mod of ps_0-p_1 and ps_0-p_2 and select the minimum of these and $dist$.
4. Reflection occur only when the mod of ps_0-p_2 is smallest and for which set $rf=0$ else refraction occur and set $rf=1$.
5. If $rf=1$ and $dist$ is smallest then intersected point lies on the vertical wall of unit cell. For this case go to next adjacent process in the MIL-A.
6. If $rf=1$ and mod of ps_0-p_1 is smallest then intersected point lies on the interface segment bounding unit cell. For this case compute the normal vector sn at the point of intersection on the interface.

Once the MIL-A is defined a minor change is done in the IL-B between box B and C in Figure 2.6, as shown in Figure 2.7(b). The box B is split into two parts and this helps to update the unit vector for reflection using Equation 2.19.

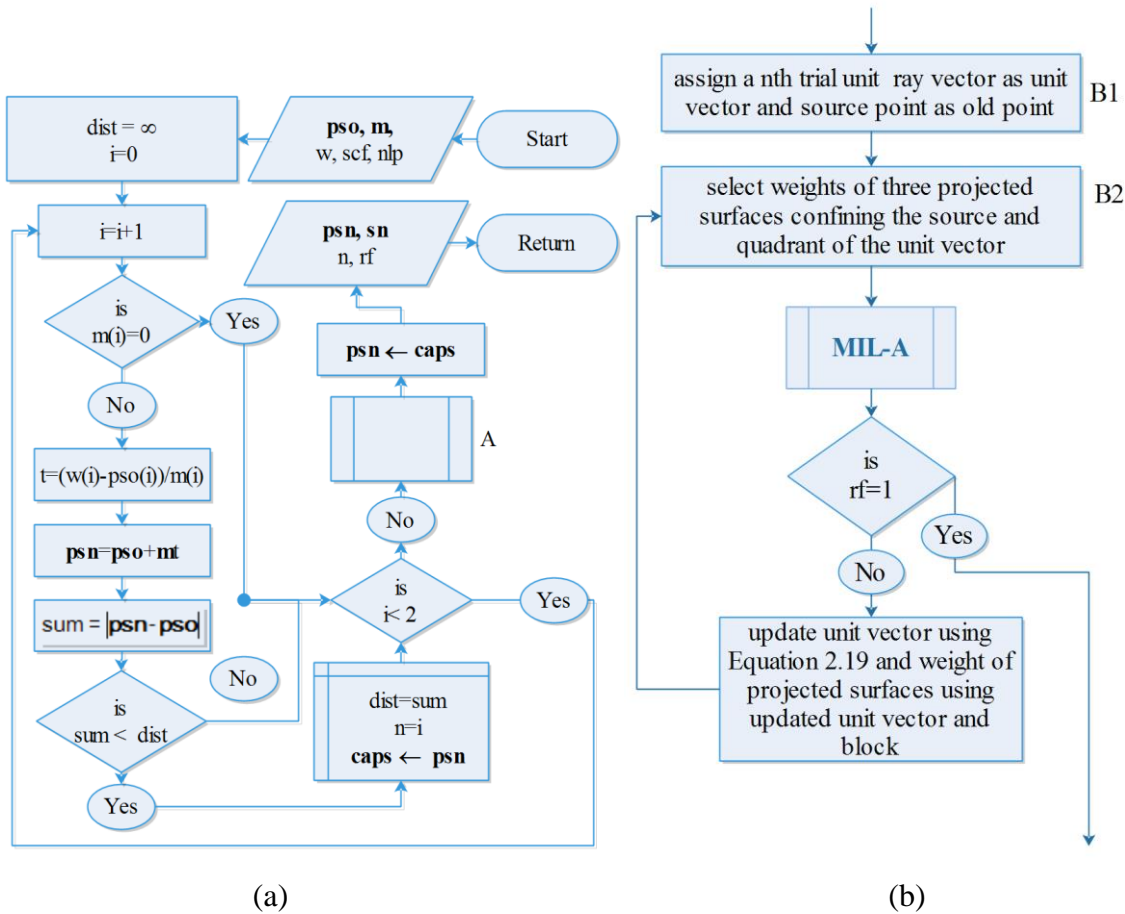


Figure 2.7: The replacement units of IL-B to convert the same into IL-C. The sub-process A is added in IL-A to convert the same into MIL-A (a) which is added in IL-B to convert the same into IL-C (b).

2.6 THE SPIRAL PATH SEARCH METHOD (SPSM)

The spiral search method is designed to find quickly the true unit take off vector in the IL-B or IL-C sub-process to complete the two point ray tracing. In the beginning, a circular search area is oriented at the position of destination point (receiver) of ray tracing in such a way that a normal to that area, passing through centre of the area pass through the origin at source. Continuous equispaced nodes are then created along the perimeter of a spiral constructed on the circular area with centre at the centre of circular area. All such nodes together with origin makes the trial takes off vectors. If switch is kept zero in the beginning in IL-B or IL-C, then the output of ILB or IL-C is error series measuring the distance of final intersected point and destination point for each take off unit vector. These set of takeoff vectors are analysed in a special fashion to create next set of take-off vectors which are used in next iteration of IL-B or IL-C. The complete mathematical theory is given in § 3.5.1 and § 3.5.2.

2.6.1 EQUATION OF SPIRAL

Consider the spiral motion of a point L^1 around a point L in such a way that the locus of the point L^1 is defined by a variable radius r_s and an angle Ω . Radius r_s measure the distance between points L and L^1 and angle Ω is the angle made by radius r_s at point L with respect to a reference axis. Further assume that one round of point L^1 around point L makes an increase of radius r_s by l , which leads to relate these parameters as:

$$r_s = \frac{l}{2\pi} \Omega \quad (2.26)$$

The perimeter C of the spiral is given by:

$$C = \int r d\Omega = \frac{l}{4\pi} \Omega^2 \quad (2.27)$$

Using Equation (2.26), the Equation (2.27) becomes:

$$C = \frac{\pi r_s^2}{l} \quad (2.28)$$

Consider that there exists equispaced n discrete points all through the perimeter and spacing between two adjacent point is l , then

$$n = \frac{C}{l} = \frac{\pi r_s^2}{l^2} \quad (2.29)$$

i.e.,

$$r_s = l \sqrt{\frac{n}{\pi}} \quad (2.30)$$

From Equations (2.26) and (2.30), it is possible to write:

$$\Omega = 2\sqrt{\pi n} \quad (2.31)$$

Equation (2.31) describe the equation of spiral motion of a point L^1 in terms of discrete number n and step length l . Equispaced discrete points along the perimeter of spiral are shown in Figure 2.8. This equation is used to define the initial take-off vector at the position of source.

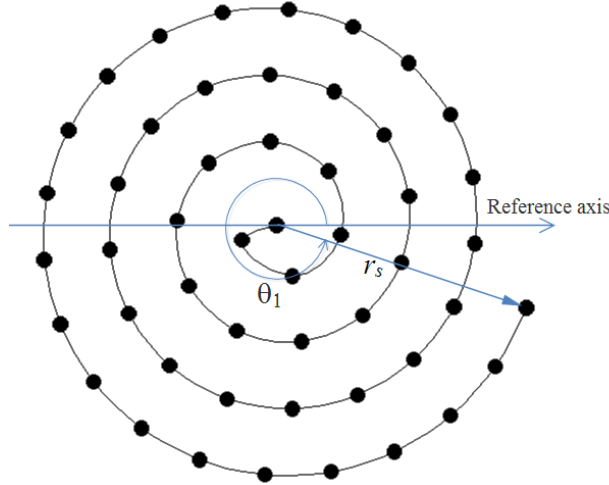


Figure 2.8: Equispaced discrete points on a spiral.

2.6.2 EQUATION OF DISCRETE TAKE OFF VECTOR

Consider a spherical coordinate system keeping the source at the centre, O and a spiral around a station A in such a way that a perpendicular through the point, A of spiral pass through the origin O of the coordinate system as shown in the Figure 2.9. Two perpendicular axes, CC and BB are drawn on the plane of spiral in such a way that BB lies in the xz plane and CC lies in the OAA plane. Let P is a trial point on the spiral, with radius r_s , then to find out the position P , two perpendicular lines from p are drawn on BB and CC as PM and PL . For simplicity of understanding the image of points M , A and axis CC are drawn on xy plane as M^1 , A^1 and M^1A^1 respectively.

It is clear from the geometry of Figure 2.9 that the approximate position P can be written as:

$$\left. \begin{aligned} R_p &= \sqrt{R^2 + r_s^2} \\ \theta_p &= \theta + \Delta\theta \\ \varphi_p &= \varphi + \Delta\varphi \end{aligned} \right\} \quad (2.32)$$

Where,

$$\left. \begin{aligned} \Delta\theta &\approx \angle AOL = \tan^{-1}\left(\frac{r_s \cos \Omega}{R}\right) \\ \Delta\varphi &\approx \angle AOM = \tan^{-1}\left(\frac{r_s \sin \Omega}{R}\right) \end{aligned} \right\} \quad (2.33)$$

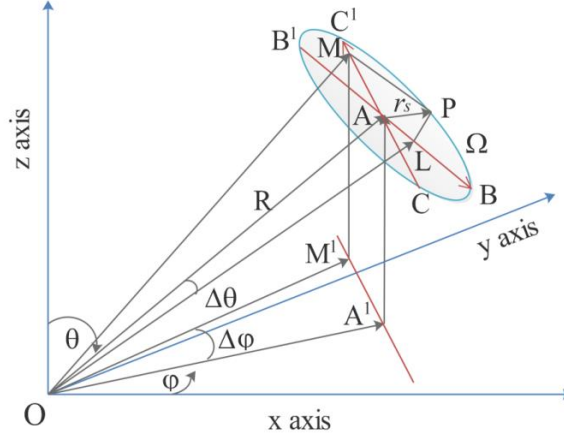


Figure 2.9: Geometry of spiral and its location with respect to source position at origin O.

Substitution of Equations (2.30) and (2.31) in set of Equations (2.33) gives:

$$\left. \begin{aligned} \Delta\theta &\approx \tan^{-1}\left(\frac{l}{R}\sqrt{\frac{n}{\pi}}\cos(2\sqrt{\pi n})\right) \\ \Delta\varphi &\approx \tan^{-1}\left(\frac{l}{R}\sqrt{\frac{n}{\pi}}\sin(2\sqrt{\pi n})\right) \end{aligned} \right\} \quad (2.34)$$

Equations (2.34) and (2.32) are utilized to determine an initial takeoff angle required in the algorithm IL-B. The initial take off angle corresponding to a particular value of n are chosen to be one that gives minimum error between observed and computed traveltime. Let n_m is the node in the spiral, corresponding to θ_m , φ_m and R_m that give minimum traveltime error. The next step is to shift the position of centre of spiral to this position and search by decreasing the value of step length l by some appropriate amount.

The new area of search is selected based on the fact that the new maximum radius of spiral must connect the grid point corresponding to least error and a grid point n_s corresponding to second least error.

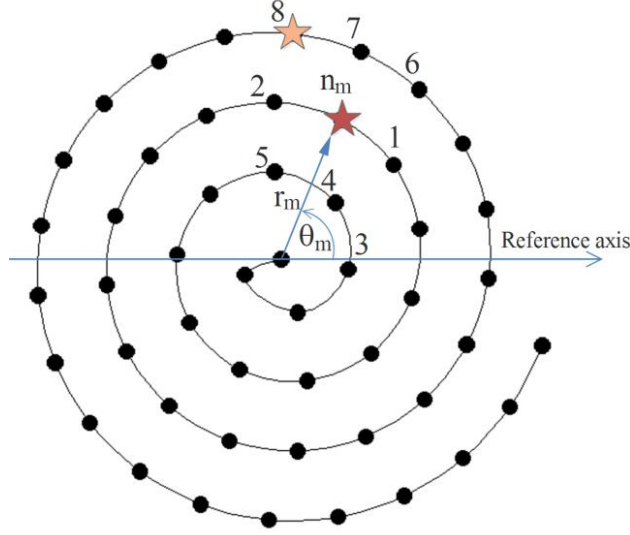


Figure 2.10: Geometry of nine nodes used to define parameters for next iteration in spiral search. Grid point n_m and 8 corresponds to the first and second least errors respectively in first iteration.

To determine n_s , 8 grid points are considered around n_m as shown in Figure 2.10. Grid point 1 and 2 are adjacent to n_m . Grid point 4 and 7 are the grid points which are respectively almost one turn lesser and one turn higher than the number of turn corresponding to n_m grid point. These grid points are computed as:

$$\left. \begin{aligned} (\Omega_m - 2\pi)^2 &= 4\pi n_4 + o_1 \\ (\Omega_m + 2\pi)^2 &= 4\pi n_7 + o_2 \end{aligned} \right\} \quad (2.35)$$

O_1 and O_2 represent error as excluding these right hand side is integer multiple of 4π while left hand side is fixed by n_m due to Equation (2.31), therefore

$$\left. \begin{aligned} n_4 &\approx (\sqrt{n_m} - \sqrt{\pi})^2 \\ n_7 &\approx (\sqrt{n_m} + \sqrt{\pi})^2 \end{aligned} \right\} \quad (2.36)$$

The point 3 and 5 are adjacent to point 4 and points 6 and 8 are adjacent to point 7. The trial take off angle corresponding to all these 8 grid points are computed and l -errors associated with these angles are registered during the computation of n_m . Here, l -error is the measure of distance between final intersected point and station location. Let us suppose that the second least l -error after what is given by n_m grid is determined to point 8 as shown in Figure 2.10,

and then it is sufficient to consider the maximum spiral area of second search with slightly larger than the radius which is a length of line segment connecting grid point n_m and 8.

2.7 AN ALGORITHM TO COMPUTE TWO POINT RAY TRACING

This section describes a complete two point ray tracing algorithm. In the preceding section, the algorithm solve the two point ray tracing only when a takeoff angle out of a number of trail takeoff angles given in form of unit vector gives minimum acceptable length error (*l-error*) measured in terms of length between final intersection point and destination point in the model. The problem of finding one true take off angle is solved using spiral path search method described in section 3.5. Therefore the condition of algorithm IL-B is removed by joining spiral search method as shown in Figure 2.11. The IL-C sub-process can also be used in place of IL-B sub-process.

The algorithm requires a circular search area lying perpendicular to a line passing through the origin of coordinate system in the model. This area with step size, l decides the maximum number of trail take off angles or unit vectors or maximum number of steps, *N-step* that is required to solve two point ray tracing. The N-step is given with the help of Equation (2.30) as:

$$N - step = \frac{\pi r_{\max}^2}{l} \quad (2.37)$$

Where, r_{\max} is the maximum radius of search area. The parameters R, θ and φ defines the initial position of spiral search area and are set initially using the coordinates of destination point (station) with respect to origin at initial point (source). The parameter *iter* is for iteration number and N-iter for maximum number of iteration. Setting switch=0 in the beginning, the operation begins with ‘block A’ which generate *N-step* unit take off vectors using Equations (2.33) and (2.35). As the parameter switch is set to zero in the beginning so the sub-process IL-B generates error series with nodes of the spiral that is checked in the further process to decide next iteration whether to begin.

After completion of sub-process IL-B, the node at which *l-error* is minimum is searched out by scanning the error series and it is termed as *first minimum l-error* node. The spiral is repositioned on the takeoff vector along the *first minimum l-error* node in the spiral. This operation is performed by block C. After operation block C *l-error* corresponding to *first minimum l-error* node is compared with acceptable error, N-error. At this position *iterr* is also compared with *N-iter*. After operation by block C followed by *No* decision, two nodes

in the spiral are obtained from the error series using Equation (2.37). Further extra six nodes are also selected which are adjacent to the previously selected nodes and lie along the perimeter of spiral. Out of 8 extra nodes selected one node is selected that have minimum error and called as second minimum *l-error*. The distance of this node from *first minimum l-error* node in spiral is the radius of search area for next iteration. The next iteration step *l* is set in block D by dividing the radius of search of next iteration by *N-step*.

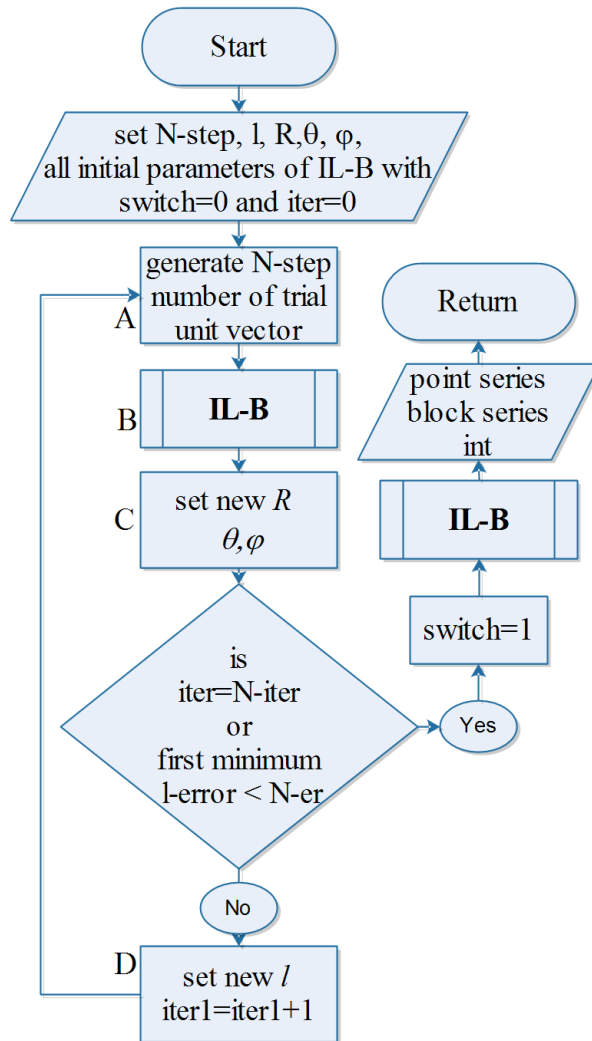


Figure 2.11: A two point ray tracing algorithm is shown.

2.8 NUMERICAL EXPERIMENTS

This section presents six numerical experiments that have been carried out using the developed algorithms to justify the snell's law and validity of wave propagation.

2.8.1 EXPERIMENT 1

This experiment is performed to show that ray path is straight in a uniform velocity medium. A three dimensional homogeneous model as shown in Figure 2.12 has been

considered. A point source has been placed at the bottom of the model and a station has been located at the surface of the model. The parameters for model, source and station co-ordinates are tabulated in Table 2.1.

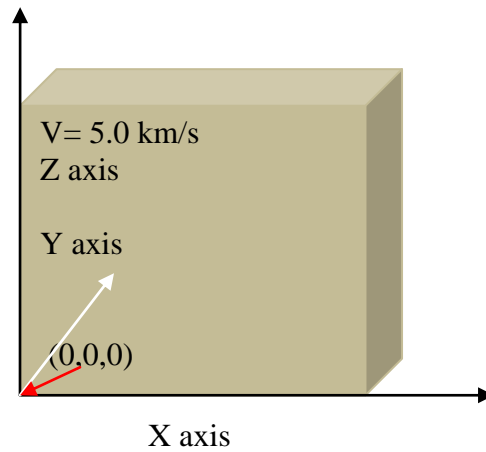


Figure 2.12: A model of uniform velocity medium.

Table 2.1: The parameters taken for the model in Figure 2.12

Parameters	Values
Model dimension	(100×10×100) km
Voxel size	(2.0×2.0×2.0) km
No of Voxels	50×5×50
Source co-ordinate	(0,0,0) km
Station co-ordinate	(80,0,100) km
Velocity	5 km/s

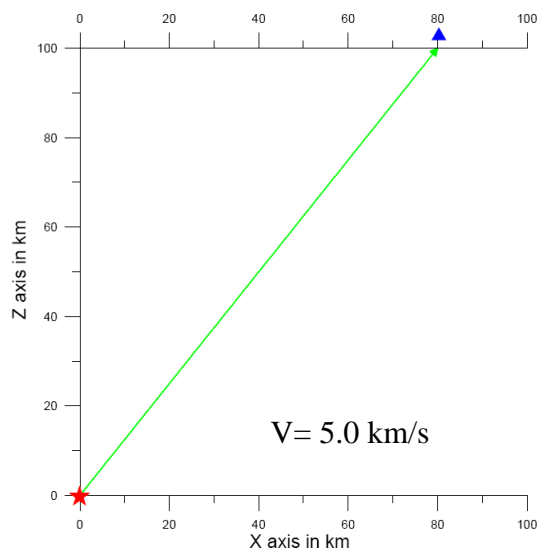


Figure 2.13: Ray path obtained for the model considered in Figure 2.12.

The ray path has been traced out and the result is shown in Figure 2.13. From the same figure it is clear that the ray path is a straight line joining source and station.

2.8.2 EXPERIMENT 2

This experiment is performed to show the validity of Snell's law. To show the validity of Snell's law by the solution, a model with two different velocities as shown in Figure 2.14 has been considered. The boundary separating two media is a plane at $Z=50.0$ km. The source has been placed at the bottom of the model and the station at the top of the model. The parameters for model, source and station co-ordinates are tabulated in Table 2.2.

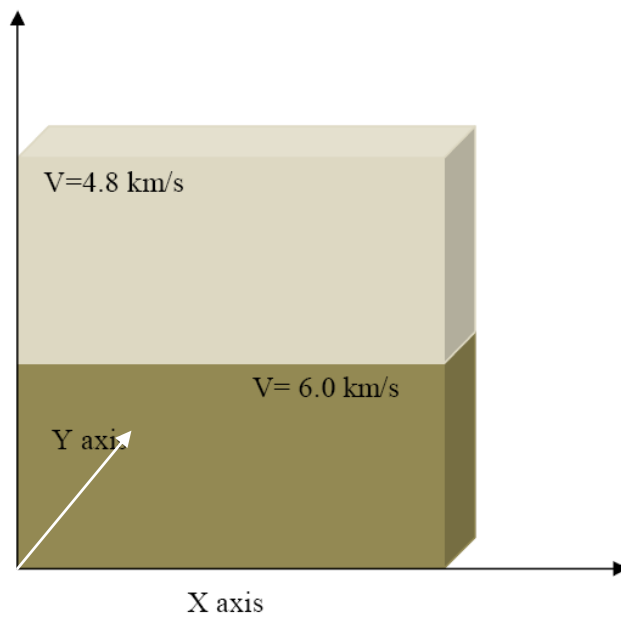


Figure 2.14: A model with two media having different velocities.

Table 2.2: The parameters taken for the model in Figure 2.14

Parameters	Values
Model dimension	(100×10×100) km
Voxel size	(2.0×2.0×2.0) km
No of Voxels	50×5×50
Source co-ordinate	(0,0,0) km
Station co-ordinate	(80,0,100) km
Velocities	4.8 km/s (upper medium) 6.0 km/s (lower medium)
Boundary plane	At $Z=50.0$ km

The solution was obtained and the result is shown in Figure 2.15.

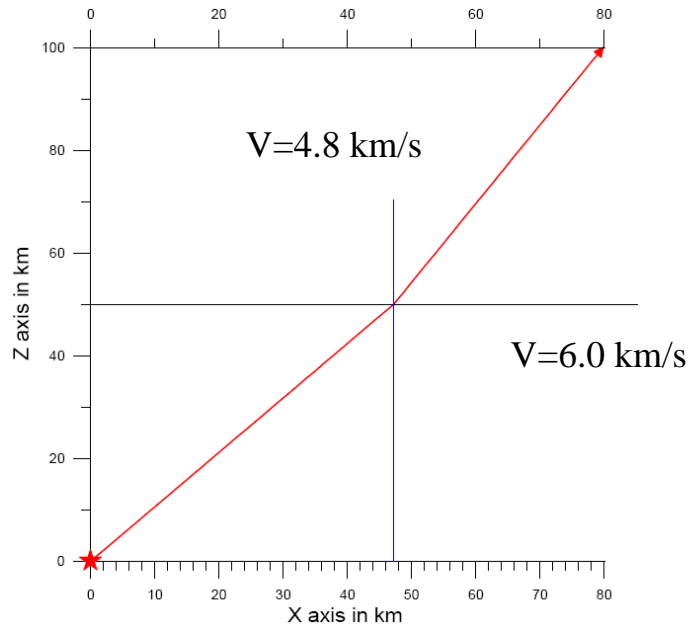


Figure 2.15: Ray path obtained for the model considered in Figure 2.14.

Since the ray covers a distance of 47 km up to the boundary so the incident angle θ_i at the lower boundary is given by

$$\theta_i = \tan^{-1}\left(\frac{47}{50}\right) = 43.2285^\circ$$

And the corresponding refracted angle θ_r is given by

$$\theta_r = \tan^{-1}\left(\frac{80 - 47}{50}\right) = 33.4248^\circ$$

From the Snell's law we have

$$\frac{\sin \theta_r}{\sin \theta_i} = 0.8 = \frac{V_2}{V_1}$$

Where, the ratio $\frac{V_2}{V_1}$ is the ratio of velocity of upper medium and that of lower medium and since this is also 0.80 so the Snell's law is justified.

2.8.3 EXPERIMENT 3

This experiment is performed to show that the solutions give the first arrivals in few cases. To show this a three dimensional uniform velocity model was considered and a high velocity rectangular body was kept inside the model as shown in the Figure 2.16. The parameters for source and station and model are given in Table 2.3.

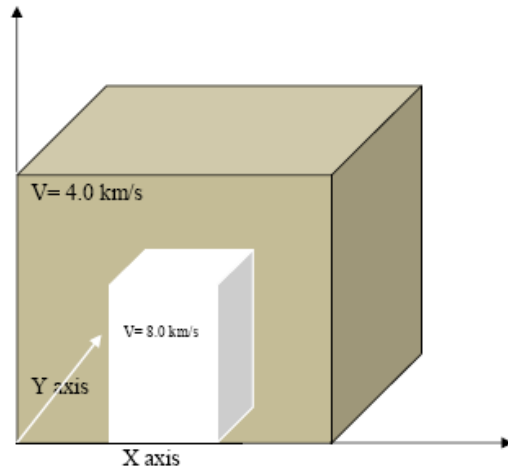


Figure 2.16: A model of uniform high velocity buried body in a uniform medium.

Table 2.3: Parameters taken for the model in Figure 2.16

PARAMETERS	VALUE
Model dimension	(300×20×300) km
Voxel size	(2.0×2.0×2.0) km
No of Voxels	150×10×150
Source co-ordinate	(0,0,0) km
Station co-ordinate	(150,0,300) km
Velocities	8.0 km/s (buried rectangular body) 4.0 km/s (medium)
Size of the buried body	(100×20×175) km
Location of the buried body	At X=100 km at the bottom of the model

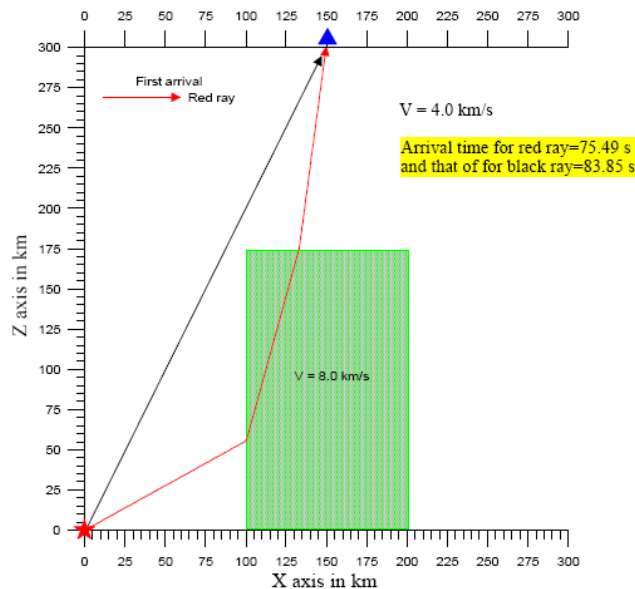


Figure 2.17: Ray path obtained for the model considered in Figure 2.16.

The solution was obtained which is shown in Figure 2.17. The red ray path is the solution obtained. The black ray path was drawn to show that it would have been the actual path if there were no high velocity buried body. The arrival time of black ray is more than the arrival time of red ray, so it justifies that the solution give the first arrivals.

2.8.4 EXPERIMENT 4

Experiment 4 is performed to show that if velocity in a medium increases continuously then the ray path becomes a curvature. To show this a three dimensional model as shown in Figure 2.18 was considered. The velocity of the medium was allowed to increase continuously along the positive Z axis only. The parameters for source, station and model are given in Table 2.4.

Table 2.4: parameters taken for the model in Figure 2.18

Parameters	Values
Model dimension	(100×10×100) km
Voxel size	(2.0×2.0×2.0) km
No of Voxels	50×5×50
Source co-ordinate	(0,0,0) km
Station co-ordinate	(70,0,100) and (80,0,100) km
Velocity function	3.0+0.04Z km/s

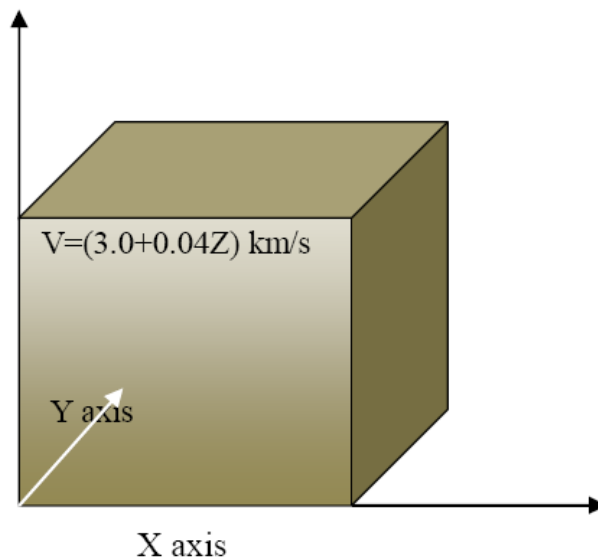


Figure 2.18: A Model having constant gradient of velocity along Z axis.

The solution was obtained for two station locations at the top surface of the model, one at $X=70$ km, $Y=0$ km and other at $X=80$, $Y=0$ km which is shown in Figure 2.19. The ray path is completely a curve with constant gradient. Further, it can be observed that as the station offset along X axis increases the pattern of the ray path does not changes which can be explained by Snell's law.

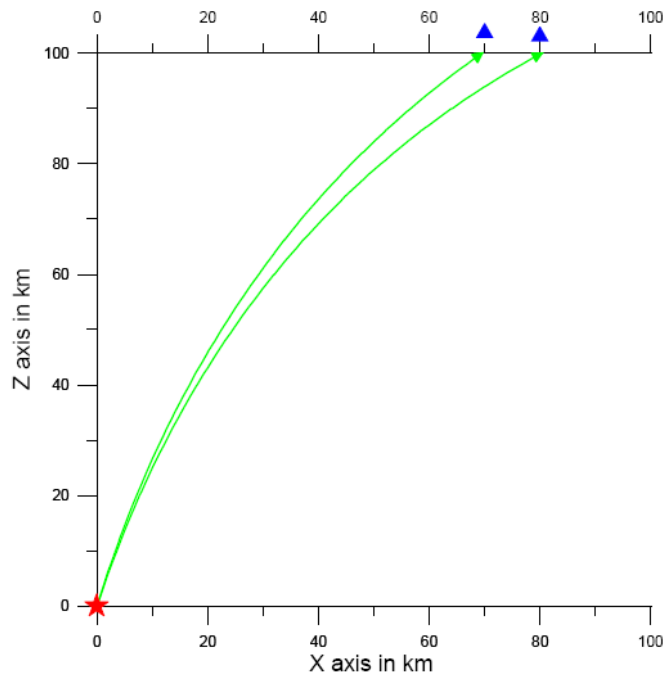


Figure 2.19: Ray paths obtained for two station locations for the model considered in Figure 2.18.

2.8.5 EXPERIMENT 5

Experiment 5 is performed to show that if velocity decreases in a medium continuously along a direction then the shape of the curvature for the ray path, for a particular source and station location, remains the same as that of when velocity increases continuously along that direction but the curve convexity align in opposite direction. Further to show that if velocity is allowed to increase along the perpendicular direction too then the gradient of the entire curve of ray path increases. To show this a three dimensional model shown in Figure 2.20 has been considered. First velocity allowed decreasing along positive Z axis and result was obtained and then velocity was allowed to increase along positive X axis, along with decrease along positive z axis. The model parameters and the source and station location are given in Table 2.5.

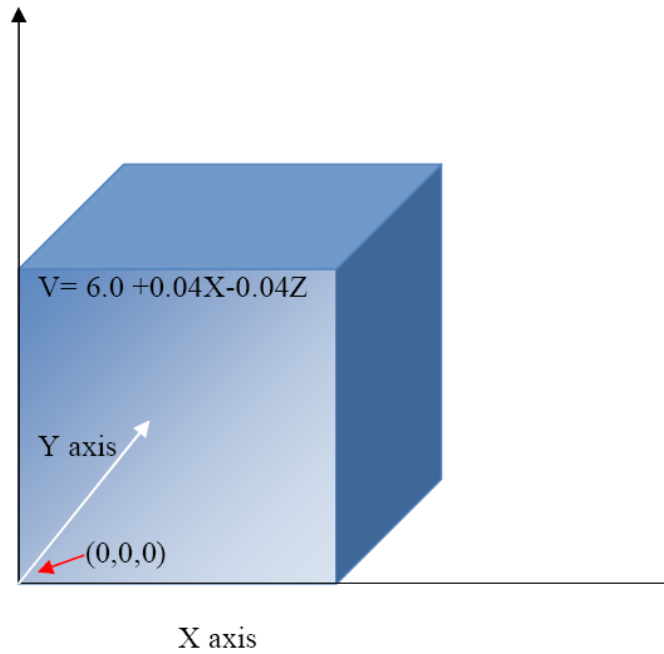


Figure 2.20: A model whose velocity varies in two directions according to the velocity function shown in the same figure.

Table 2.5: parameters taken for the model in Figure 2.20

Parameters	Values
Model dimension	(100×10×100) km
Voxel size	(2.0×2.0×2.0) km
No of Voxels	50×5×50
Source co-ordinate	(0,0,0) km
Station co-ordinate	(80,0,100) km
Velocity function	6.0+0.04X-0.04Z km/s

The solutions were obtained and are shown in Figure 2.21. The black curve in the Figure 2.21 is the solution for ray path when velocity decreases along only positive Z axis and green curve was obtained when velocity was allowed to increase along positive X axis along with decrease along positive Z axis. It is clear that the convexity of curve of the ray path align towards bottom-right side which is opposite alignment of the convexity with respect to the curves in Figure 2.19 of model shown in Figure 2.18, when velocity was allowed to increase along positive Z axis. Further, from the figure it is clear that the convexity of the ray path increases when velocity was allowed to increase in positive X axis along with decrease in positive z axis.

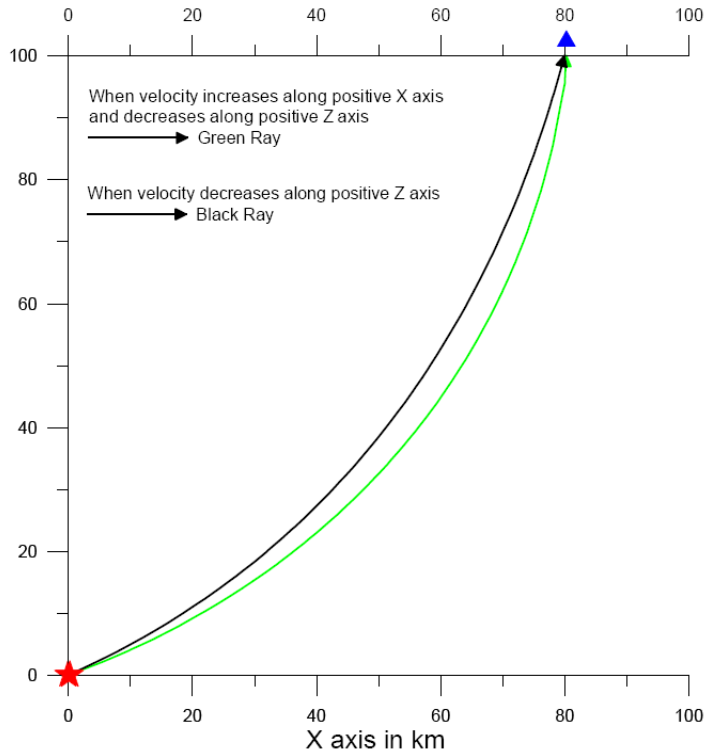


Figure 2.21: Ray paths for two type of velocity function for the model considered in Figure 2.20. Red ray path is obtained for the velocity function shown in the model but black ray path is obtained when the variation of velocity along z axis is not allowed.

2.8.6 EXPERIMENT 6

This experiment is performed to show that if velocity of a heterogeneous medium increases or decreases continuously along two mutually perpendicular direction then the ray path becomes symmetrical with respect to these two direction.

First a three dimensional homogeneous model was considered with dimension given in Table 2.6. Then velocity is allowed to increase continuously along positive X and Y axis and to decrease along positive Z axis with a function given in Table 2.6. The parameters for this model, source and station are also given in Table 2.6.

Table 2.6: Parameters for the model considered in Figure 2.22

Parameters	Values
Model dimension	(100×100×100) km
Voxel size	(2.0×2.0×2.0) km
No of Voxels	50×50×50
Source co-ordinate	(5,5,0) km
Station co-ordinate	(80,80,100) km
Velocity function	$V = 6.0 + 0.04x + 0.04y - 0.04z$ km/s

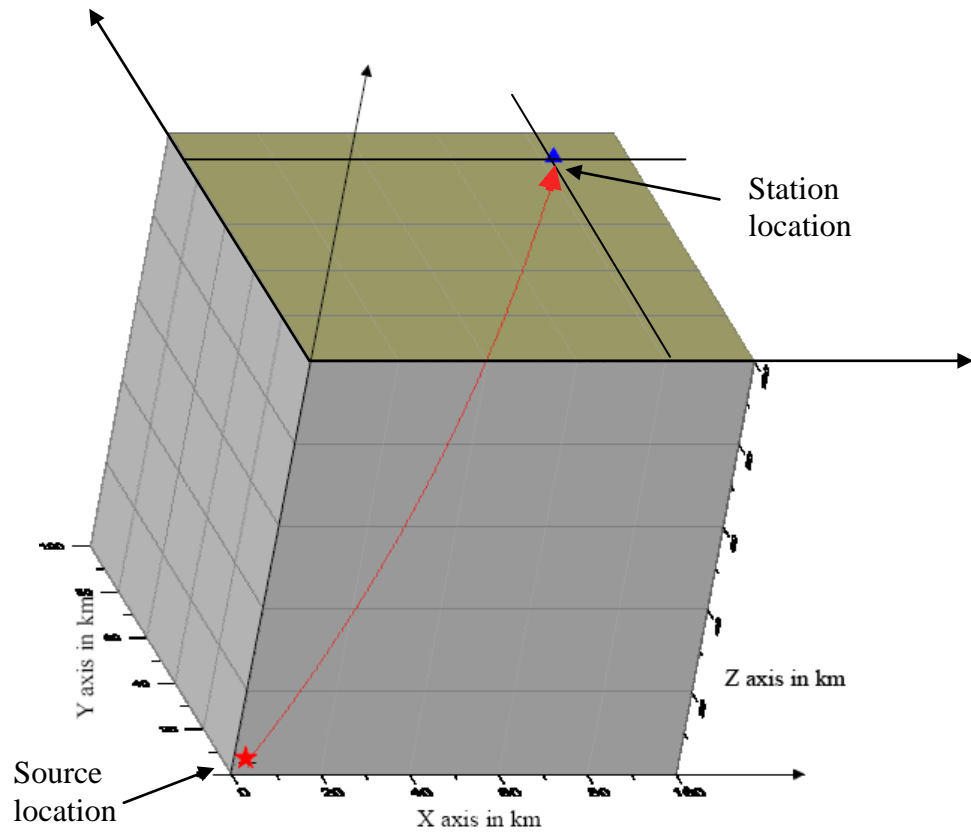


Figure 2.22: The ray path in three dimensions for a model having same positive constant velocity gradient along X and Y axis but along the Z axis gradient is constant but negative.

The resultant ray path is shown in the same Figure 2.22. It is clear from the same figure that the ray path is concave towards upward direction which is due to increment of velocity along downward direction. It is further observed that the ray path is symmetrical along a plane through the major diagonal of bottom and upper surface of the model. This is because of uniform velocity increment along positive X and Y direction.

2.9 CONCLUSIONS

Two types of model parameterizations are considered. In one type, model parameterization using Constant Velocity Voxels (CVV) is considered. This type of model parameterization is simple to define and solves many problems in tomography. Though CVV is simple it does not address smoothly 3D layer geometry of real earth. In that context, 3D interfaces defining discontinuities of media are incorporated in CVV parameterization to define smooth 3D layers of Earth. Appropriate vector equations for refracted, reflected rays and point of intersection between a line and a plane are derived. These are used in developing algorithm for one point (considering source without receiver) ray tracing using both types of parameterization considered. The phenomenon of self reflection that may take place in a 3D layer is also considered in the algorithm. Two point ray tracing (complete ray

tracing using source and receiver) is considered using a method which is called as spiral path search method. The formulation of spiral path search method and its use in the algorithm are discussed. The developed algorithm for two point ray tracing is tested using several numerical experiments which satisfy the normal wave propagation theory numerically.





NUMERICAL EXPERIMENTS ON FAST MARCHING METHOD

3.1 INTRODUCTION

Prediction of seismic ray paths between two points in a medium with lateral velocity variation is required in many application of seismology including body wave tomography, earthquake relocation and migration of reflection data. Accurate prediction of seismic ray paths between two points in heterogeneous media is one of the challenging problems in seismology. The difficulty of computing such ray paths arises from the non-linear relationship between velocity and ray path geometry.

Over the past few decades, the growing demand of accurate and fast computation of seismic ray paths has spawned a number of ray based and grid based techniques. The conventional method of predicting the source receiver ray path has been ray tracing as given by Julian and Gubbins (1977), Červený (1987, 2001), Virieux and Farra (1991). In this method trajectory of ray paths between two points are directly computed. This approach is highly accurate and efficient in homogeneous or mildly heterogeneous. However in a heterogeneous medium the ray tracing method often fail to converge to a true ray path and does not give guarantee as to whether ray path is for first arrival seismic energy or for multiples.

A number of methods based on grid base numerical techniques developed addressing the same problems in the early 90s. Some of these are three dimensional finite difference methods as given by Vidale (1990), two dimensional explicit finite difference method as given by Van Trier and Symes (1991), three dimensional explicit finite difference methods as given by Popovici (1991). Popovici showed the problem of instability in his method. Schneider (1995) reduces the problem of instability and devised a three dimensional robust finite difference technique, Podvin and Lecomte (1991) extended the work of Vidale's algorithm. However the use of finite difference methods solves the problem of locating ray paths for first arrival seismic energy often in heterogeneous media but again there is no guarantee that the solutions give the first arrivals in a medium with steep velocity gradients

as shown by Rawlinson and Sambridge (2004). Aside from the problem of computing first arrivals, the problem of stability of algorithms based on simple numerical schemes in highly heterogeneous media becomes a question as shown by Sethian (1996).

The problem of locating the first arrival seismic ray path is equivalent to tracking an interface propagating with a velocity normal to itself. Fast Marching Method originally developed in the field of computational mathematics is highly efficient and accurate technique that deals with the problem of evolution of interfaces in heterogeneous media. Initially the work of Sethian (1982, 1987) lead to the development of level set method as given by Osher and Sethian (1988), and finally to Fast Marching Method by Sethian (1996). This method is based on construction of entropy- satisfying viscosity solutions of appropriate partial differential equations by using numerical schemes. The algorithm based on this method accurately and robustly deals with the heterogeneity of a medium with the formation of cusp, corner and topological changes in the propagating interfaces. The condition of entropy controls the solutions to give first arrivals and the condition of viscosity makes the algorithm stable in a medium with steep velocity gradients. Further the application of narrow band makes the algorithms very fast in computation.

The knowledge of approximate model close to the actual model of subsurface of a region is a key to perform a precise seismic tomography of subsurface of that region. Choosing such model of subsurface of a region, particularly in a new region where no work related to subsurface structure has been done is another problem in field of seismic tomography. This Chapter presents the basics of Fast Marching Method and its utilization to obtain the traveltimes responses of various numerical models simulating different geological models and their studies. It is possible to obtain the contours of traveltimes from the data recorded in a network of seismographs installed in a region of earth. The contours of different artificial model then can be utilised to check for matching with that of observed responses. The matching of the observed response with the possible responses of different models may serves as a good idea to choose the approximate model of subsurface of a region.

3.2 GENERAL SOLUTION OF UPWIND DIFFERENCE SCHEME

The general solution of the marching Equation (1.19) in Cartesian co-ordinates with regular grids can be obtained by considering all the eight quadrants with respect to a grid point (unknown grid point) where the value is desired to be computed. The first order general solution to that grid point for traveltimes in any quadrant can be written as:

$$T = \frac{b + \sqrt{c}}{a} \quad (3.1)$$

Where,

$$\left. \begin{aligned} a &= \frac{C_x}{\Delta x^2} + \frac{C_y}{\Delta y^2} + \frac{C_z}{\Delta z^2} \\ b &= \frac{C_x T_x}{\Delta x^2} + \frac{C_y T_y}{\Delta y^2} + \frac{C_z T_z}{\Delta z^2} \\ c &= S^2 a - \frac{C_x C_y}{\Delta x^2 \Delta y^2} (T_x - T_y)^2 + \frac{C_y C_z}{\Delta y^2 \Delta z^2} (T_y - T_z)^2 + \frac{C_z C_x}{\Delta z^2 \Delta x^2} (T_z - T_x)^2 \end{aligned} \right\} \quad (3.2)$$

In the above equation C_x, C_y, C_z and T_x, T_y, T_z are respectively the coefficients of traveltimes and traveltimes, to the adjacent grid points in x, y , and z directions separated by $\Delta x, \Delta y$ and Δz with respect to the unknown grid point. The value of coefficients to any of the surrounding grid points will be one; if and only if the propagating wavefront has already passed through that point. Since there will be one traveltime value for the unknown grid point computed from one quadrant and there can be a maximum of eight quadrants so there will be a maximum of eight possible solutions for traveltime to the unknown grid point. Out of all possible solutions the smallest one would be the correct solution.

3.3 IMPLEMENTATION OF NARROW BAND TECHNIQUE

The upwind difference Equation (1.19) has the property of direction of flow of information or the property of entropy that it always computes the traveltime from smaller value to larger value and never from larger to smaller. To explain this two dimensional schematic diagram of grid points is shown in Figure 3.1, where at certain time of computation the position of wavefront is shown with red and black grid points. All the grid points in the wavefronts are called *Close* points, all the grid points (white grey points) through which wavefront has passed are called *Alive* points and all the grid points (white grid points) where traveltime has not been computed are called *Far* points. The narrow band evolved in downwind fashion by finding the *Close* point with minimum traveltime (which is true first-arrival traveltime), tagging it as *Alive*, updating any adjacent *Close* points and computing for the first time any adjacent *Far* points using Equation (3.1). If *Far* point is computed it is tagged as *Close*. Using this technique the shape of narrow band approximates the shape of first arrival wavefront. Choosing the *Close* point with minimum traveltime means that causality is satisfied. Use of binary mini heap sorting to locate the global minimum within narrow band decreases the computation time significantly and makes this method very fast. If there are N total grid points in the grids and NB is the maximum number

of points in the narrow band, then using the mini heap sorting the scheme solves the problem in $N \log(NB)$ steps as shown by Sethian and Popovici (1999). A simplified algorithm for computation of traveltimes to a set of grid points is given in Figure 3.2.

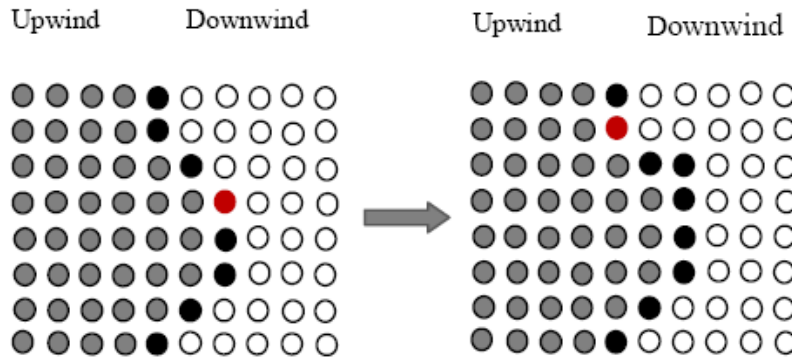


Figure 3.1: Narrow band or wavefront evolution technique. Gray points are the *Alive* points, black points and red point are *Close* points in which red point is having minimum traveltime and white points are *Far* points. The upwind side contains all the *Alive* grid points and downwind side contains all the *Far* grid points.

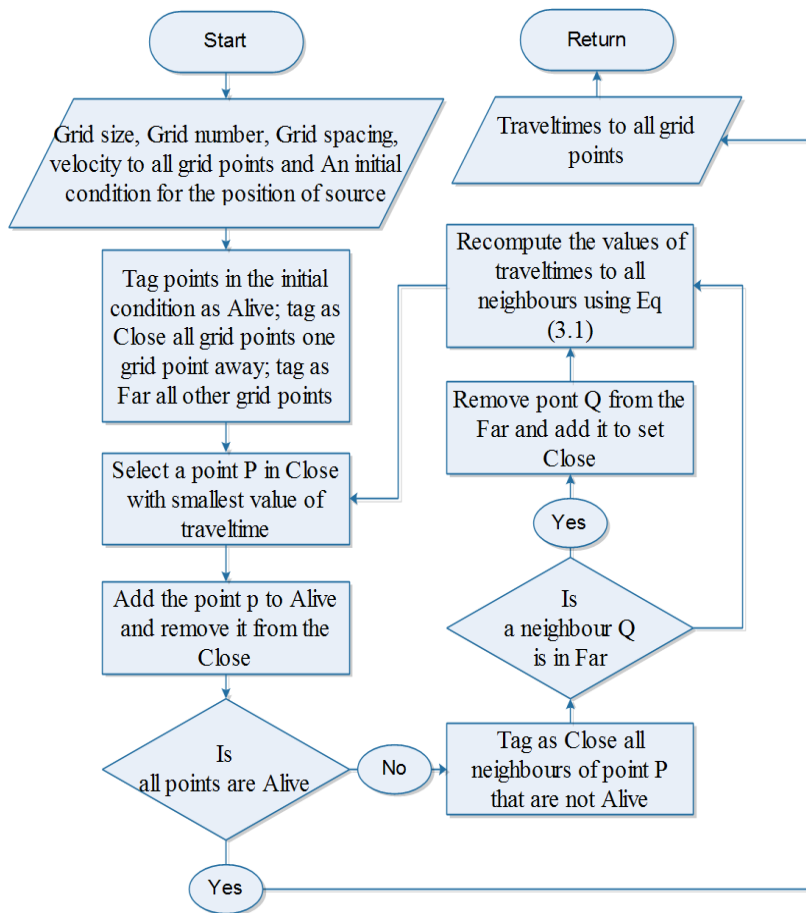


Figure 3.2: An algorithm to compute traveltimes to a set of grid points.

3.4 INCORPORATION OF HEAP SORTING IN NARROW BAND

The key to an efficient version of the above technique lies in the fast way of locating the grid point in the narrow band with the smallest value for T . For this three types of different priority mini-heap have been constructed.

A heap is a complete binary tree that can support the two operation (select or delete) efficiently in $O(\log n)$ time, where n is a set of elements in the binary tree. Selecting the minimum element from the heap takes $O(1)$ time and deleting the minimum element from the heap takes $O(\log n)$ time. A binary tree has a root at the topmost level. Each node has zero, one or two children. A binary tree can be complete or incomplete both are shown in Figure 3.3. A complete binary has exactly two children in every internal node.

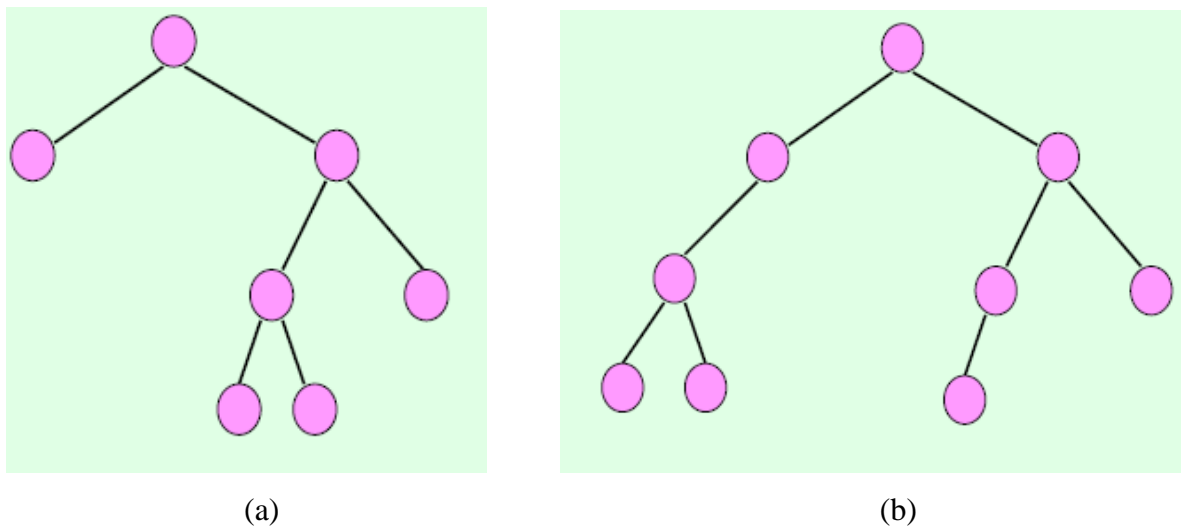


Figure 3.3: Schematic diagram showing two types of binary tree; a complete binary tree (a) and an incomplete binary tree (b).

The value stored at a node is smaller than or equal to the values stored at its children. A heap possessing this property is referred to as a min-heap. The property of a mini heap is that if any node value is changed, or a data is added at the bottommost node or if the root is removed then the tree restores its mini heap property again. The mini heap is implemented in the algorithm respecting the priority and value of data. A data value which is less than parent always moves towards the root but never if the data value is greater. A data value which has gone through maximum number of updating process is always assigned to higher number of priority. Depending upon the value of data and its priority in the algorithm how data flow takes place are given below:

- 1) When a far point value is newly computed then this value is added to the bottom and this data moves towards the root only when the value of this data is smaller than the

data value stored at its parent. That means if both the value are equal even then the newly computed value is not permitted to move towards parents. This is because of priority that the data value which is added is new but data value of parent might have gone through the process of updating or re-computing.

- 2) When a close point is updated that means at certain node of the binary tree the value is changing. To restore the mini-heap property respecting the priority this data value moves towards the root when its value is less than or equal to the value stored at its parents. Here even if two values are equal the updated value is permitted to move towards root because it might have gone through maximum number of updating process than the parent. If the updated data value is greater than its parent's data value then the updated value will move towards bottommost level comparing with its own children's data values, so that mini heap property restores back.
- 3) When the minimum value is deleted from the root to make it live point then the bottommost data value takes its position. This data moves towards bottom if the value of this data is equal to or greater than the data value of its own children. Even if the data value equals to any of (both) the data values of children this data moves toward the branches because it has less number of priority which in turn because it has come from the bottommost level where the newly computed data value is added.

The result of applying the above concepts in algorithm makes the algorithm much faster than the linear operation. If there are N total points in the grid and NB is the maximum number of points in the narrow band, then the scheme solves the marching equation in $O(N \log NB)$ steps. When the maximum number of points in the narrow band is unknown, the upper bound is $O(N \log N)$ steps.

3.5 NUMERICAL CASE STUDIES

The Fast marching method has been used in a variety of numerical models to compute the traveltime responses. The traveltime contours for these models are plotted correspondingly to study their patterns. For the sake of discussion, only two dimensional sections have been shown but whenever need of three dimensional view comes into picture, that has been respected.

3.5.1 EXPERIMENT 1

The aim of this numerical experiment was to justify a general statement that in a homogeneous medium wavefronts travel equal distance at equal interval of time. To obtain the behaviour of wavefronts in a homogenous medium a three dimensional homogenous model, as shown in Figure 3.4 was considered and a source was placed inside the model. The model was practically simulated by gridding parameterization. The parameters for source coordinates and model are shown in Table 3.1.

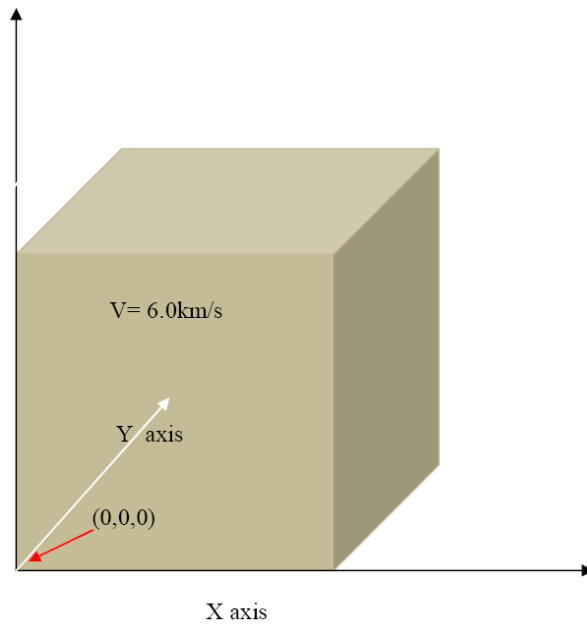


Figure 3.4: Schematic diagram showing three dimensional homogenous model.

Table 3.1: Parameters for the model considered in Figure 3.4

PARAMETERS	VALUE
Model dimension	(300×300×300) km
No. of grid	(151×151×151)
Grid spacing	(2×2×2) km
Source position	(50×50×50) km
Medium velocity	6.0 km/s

With these parameters the FMM was imposed and depth slice or two dimensional contours across the source at a depth of 50 km were obtained and are shown in Figure 3.5. The time slices or the three dimensional wavefronts at 20 s, 30 s, and 45 s were also obtained and are shown in Figure 3.6, 3.7 and 3.8 respectively.

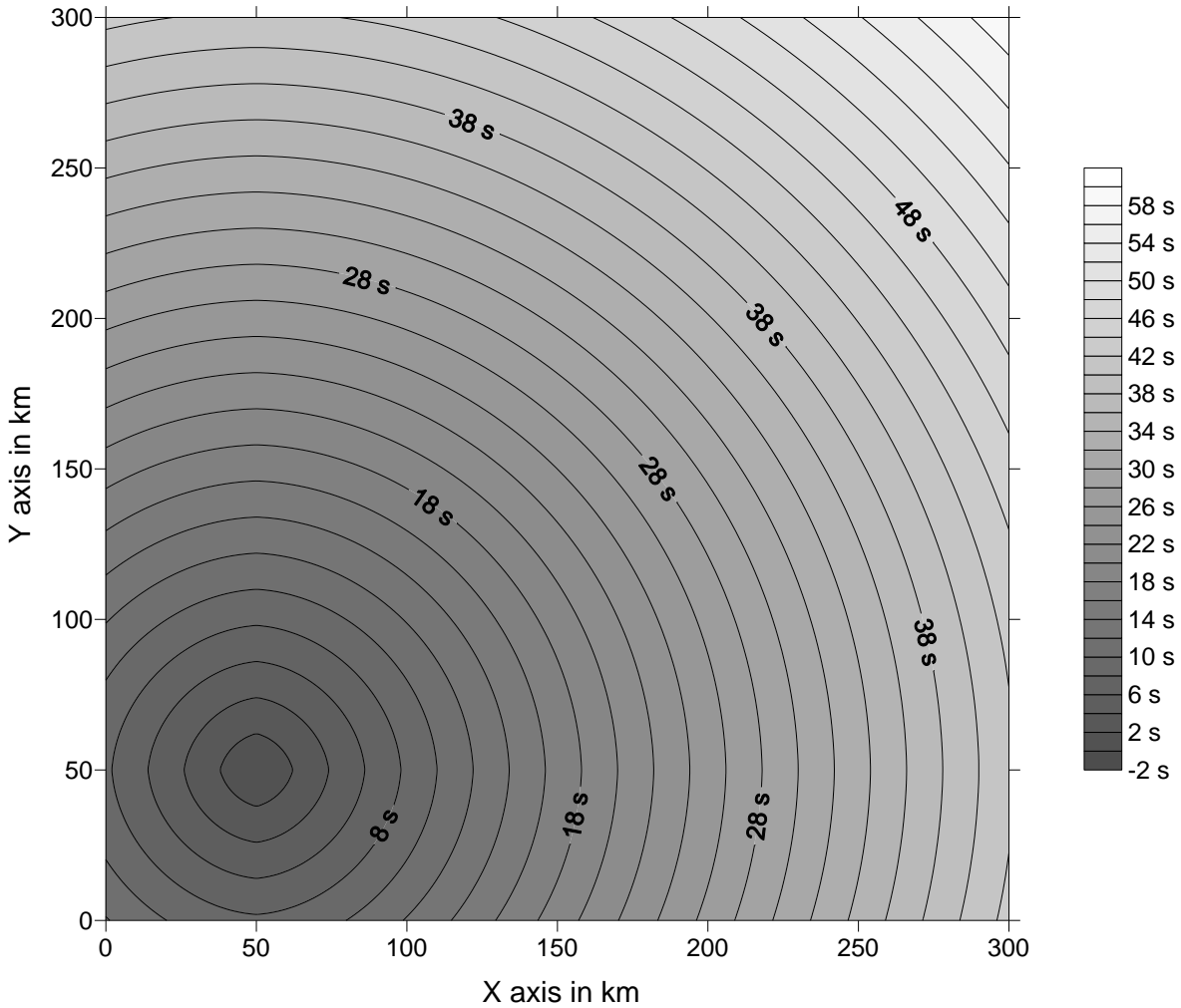


Figure 3.5: A depth slice of the wavefronts through source, showing that at equal interval of time wavefronts propagate equal distance in a homogenous medium (the results obtained for model in Figure 3.4). The time interval between two successive wavefronts is two seconds, which is also shown on the colour scale for the contour.

From the Figure 3.5, it is clear that contour lines are equally spaced and since the contour interval is constant so it justifies that at equal interval of time wavefronts propagate equal distance in a homogenous medium. The velocity, time and distance relation can be verified mathematically if for a given S second contour line, the contour line crosses the X , Y axis at an offset given by:

$$offset(XorY) = \left[\sqrt{\{(6S)^2 - (50)^2\}} + 50 \right] km \quad (3.3)$$

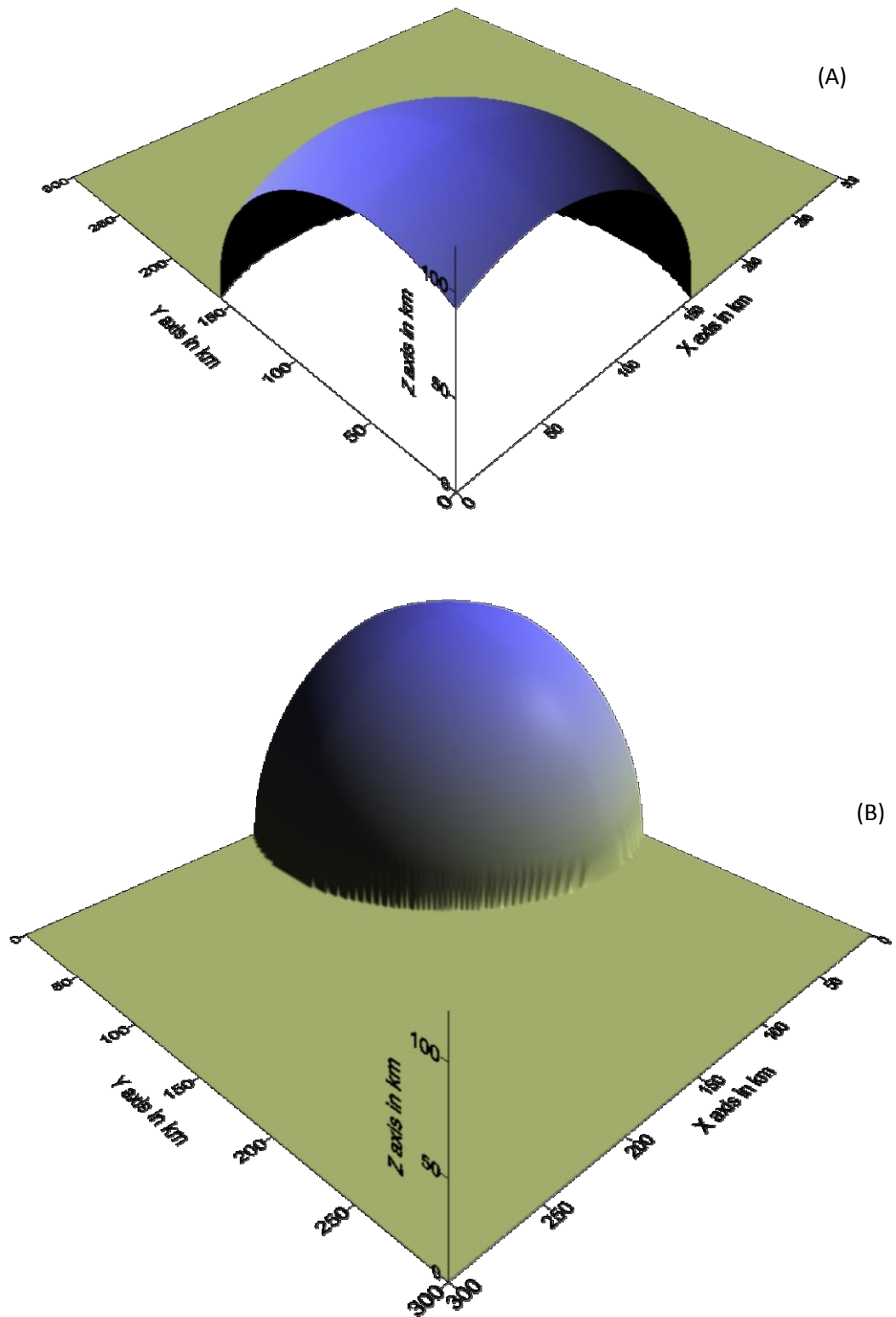
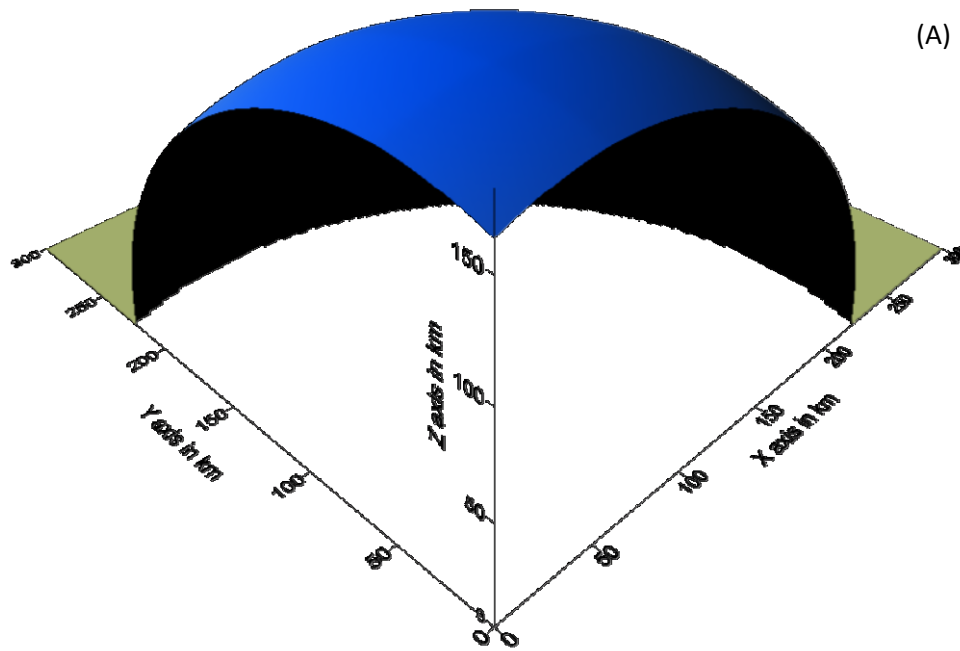
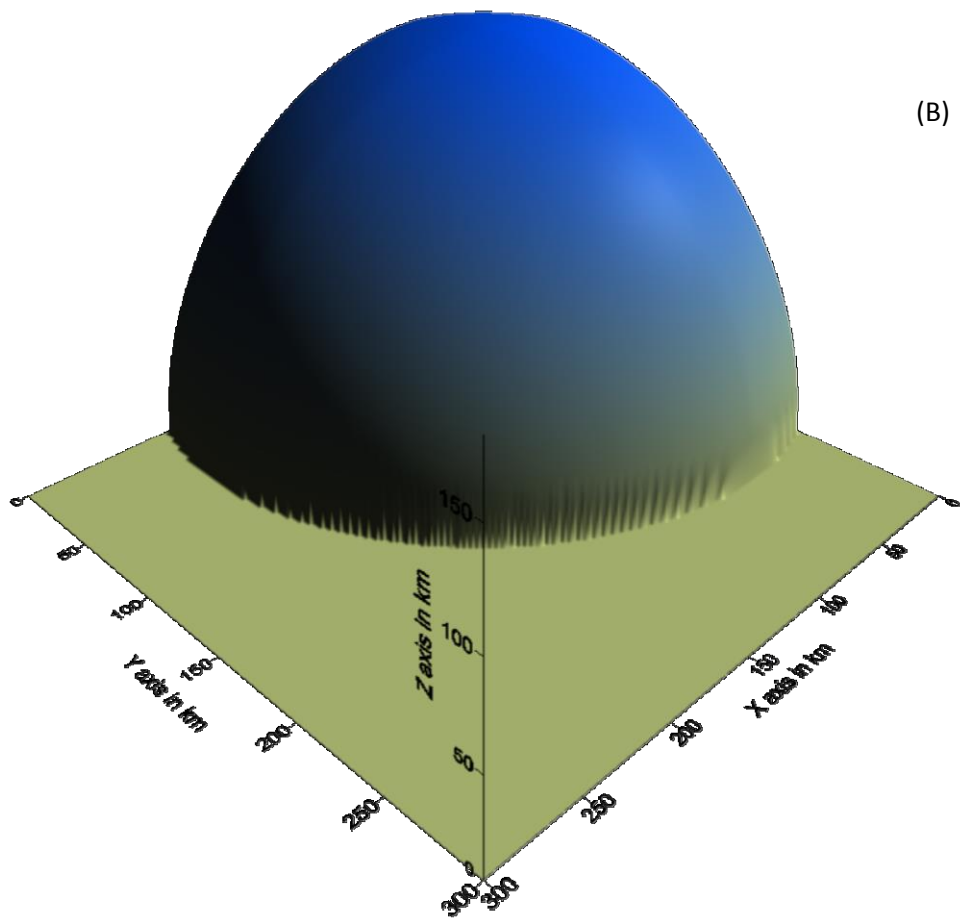


Figure 3.6: Position of the wavefront above the source or $Z=50$ km at 20 s within the model in Figure 2.1 (After plotting the results obtained for model in Figure 3.4) (A) A view from above $(0,0,0)$ coordinates (B) a view from above $(300,300,0)$ coordinates.



(A)



(B)

Figure 3.7: Position of the wavefront above the source or $Z=50$ km at 30 s within the model in Figure 3.4 (After plotting the results obtained for model in Figure 3.4) (A) A view from above $(0,0,0)$ coordinates (B) a view from above $(300,300,0)$ coordinates.

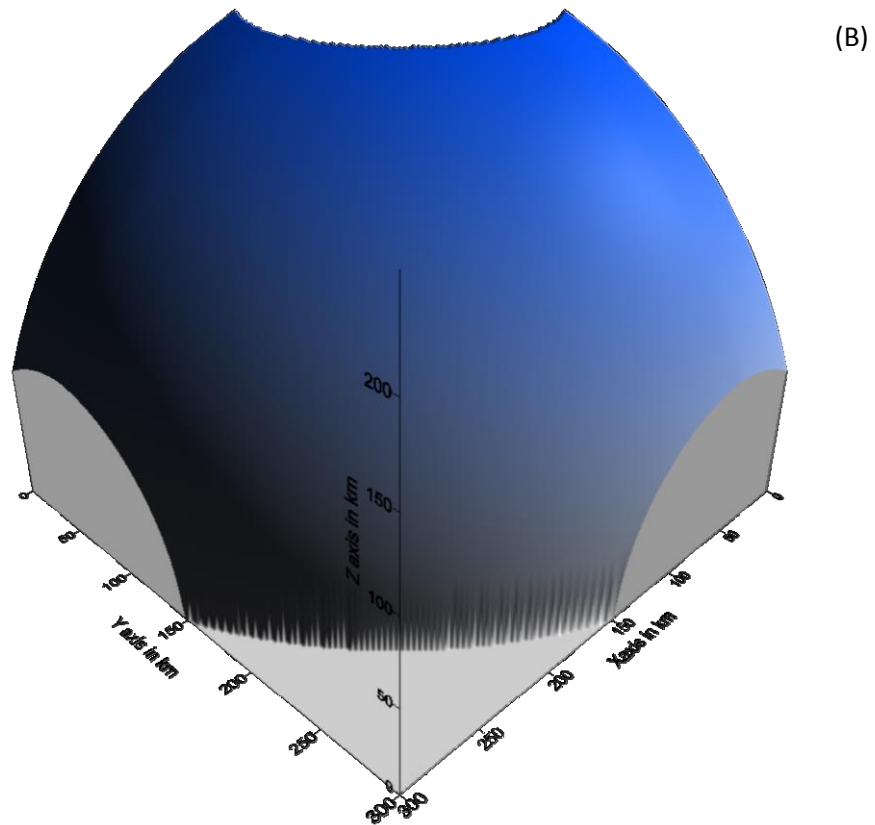
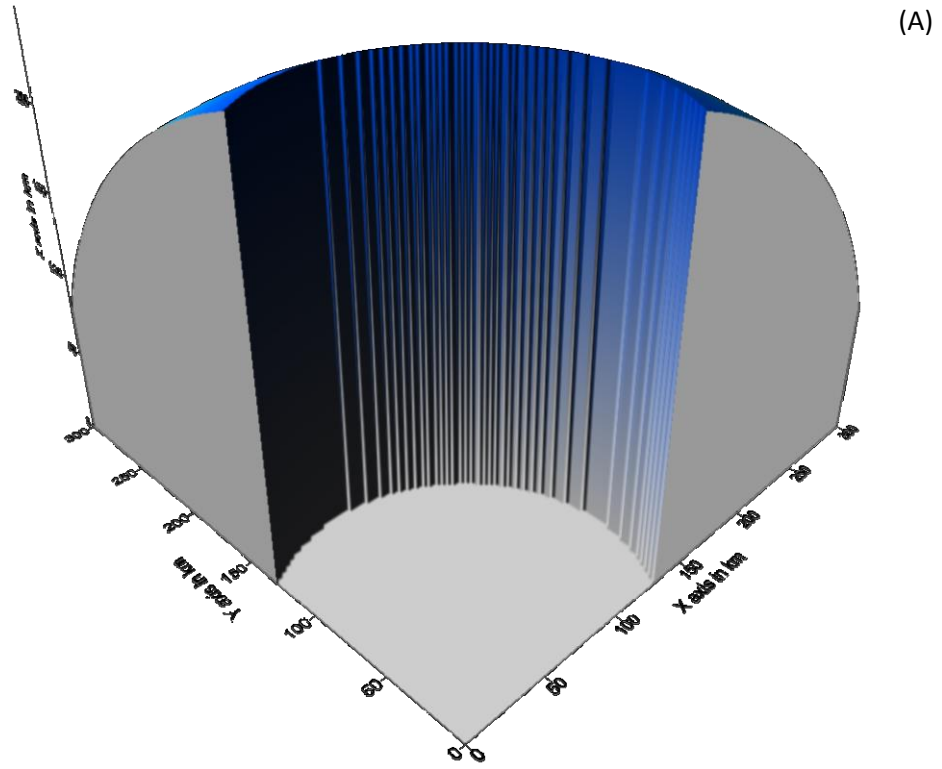


Figure 3.8: Position of the wavefront above the source or $Z=50$ km at 45 s within the model in Figure 3.4 (After plotting the results obtained for model in Figure 3.4) (A) A view from above (0,0,0) coordinates (B) a view from above (300,300,0) coordinates.

It can be easily shown that for any contour line the velocity, distance and time relation is satisfied. It is also observed that the contour lines are circular except the contour lines very close to the source. The reason for this has been discussed in the theoretical part of this paper. Since the contours are circular in nature so it can be stated that velocity, time distance relation is satisfied in a horizontal plane (X-Y plane).

The complete wavefront at 20 s are shown in Figure 3.6. From the relation (3.3), the X and Y offset should be 159 km which is clear from the Figure 3.6. The Z offset can be obtained from the relation given below.

$$\text{offset}(Z) = \left[\sqrt{\{6S^2 - 50^2 - 50^2\}} \right] \text{km} \quad (3.4)$$

For 20 s wavefront this is 97 km which is clear from the figure. Hence from these analyses it is found that wavefront satisfies the distance, time and velocity relationship in all three axes. From the back view of all figures it is clear that the wavefronts are spherical. Hence it can be justified that for all the wavefronts the distance, time and velocity relation are satisfied in any direction.

3.5.2 EXPERIMENT 2

In this numerical experiment it has been justified that solutions obey the Snell's law. For this a model as shown in Figure 3.9 was considered and a source was placed inside the model. The model was practically simulated by gridding parameterization. The parameters for source and model are shown in table 3.2.

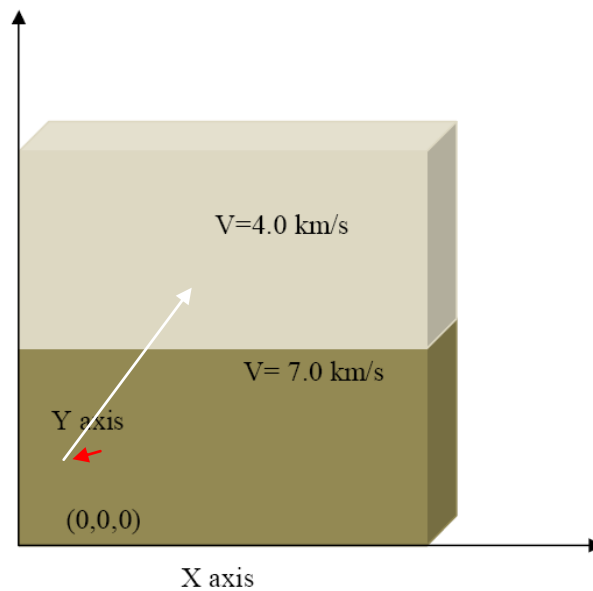


Figure 3.9: A three dimensional model having two media of different velocities (After sketching). The velocity of upper medium is 4.0 km/s and that of lower is 7.0 km/s.

Table 3.2: Parameters for the model considered in Figure 3.9

PARAMETERS	VALUE
Model dimension	(500×20×800) km
No. of grid	(251×11×401)
Grid spacing	(2×2×2) km
Source position	(20×10×800) km
Medium velocities	4 km/s (upper medium) and 7 km/s (lower medium)

With these parameters the FMM was imposed and the results were obtained. The vertical section of the wavefronts through the source, from Z=100 km to Z=500 km, are shown in Figure 3.10.

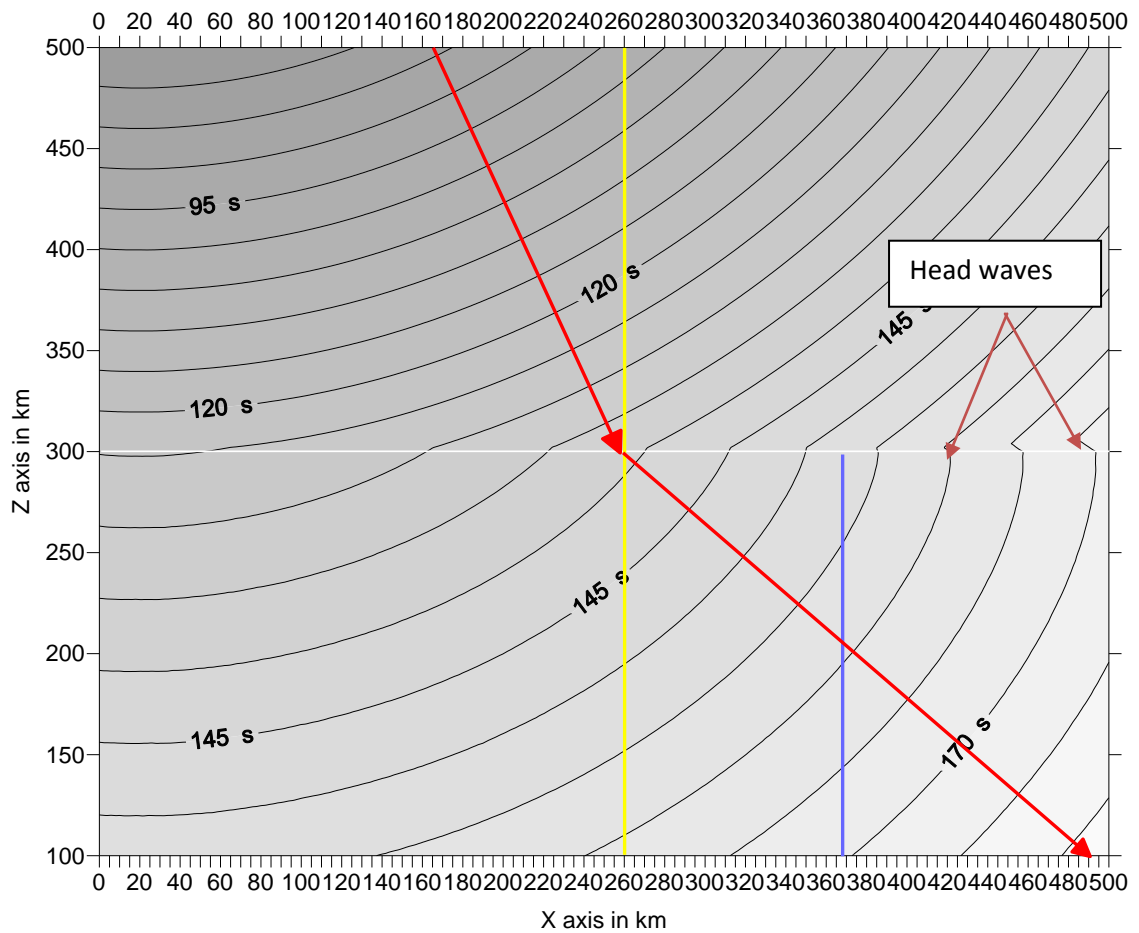


Figure 3.10: A portion of vertical slice of the wavefronts through the source, illustrating the Snell's law (After plotting the results obtained for model in Figure 3.6). A ray path (red line in the above figure) has been drawn for offset verification by Snell's law. The offsets at the boundary and at Z=100 km along the X axis travelled by the sketched ray obey the Snell's law of refraction. The blue line shows the critical offset along the X axis beyond which head waves starts generating. The yellow line shows a normal at the boundary at which refraction of red line (red ray) takes place. The time interval between two successive wavefronts is 5 seconds.

To prove the Snell's law it is sufficient to prove that if a ray incident at the boundary separated by two medium at a distance $X=A$ along X axis then the distance $X=B$ along the X axis at the bottom of the model covered by refracted ray should be (as predicted by Snell's law):

$$B = A + C \tan \tan \left[\sin^{-1} \sin^{-1} \left\{ \frac{V_2}{V_1} \times \sin \sin \left(\tan^{-1} \tan^{-1} \left(\frac{A - X_1}{S - C} \right) \right) \right\} \right] \quad (3.5)$$

Where, C is the distance of boundary along Z axis from the bottom of the model, S is the distance of point source along Z axis from bottom of the model and V_1, V_2 are the velocities of upper and lower medium. If the bottom of the model is not given then the distance B_1 travelled by the refracted ray along the X axis, Z_1 above the model, is given by:

$$B_1 = A + (C - Z_1) \tan (C - Z_1) \tan \left[\sin^{-1} \sin^{-1} \left\{ \frac{V_2}{V_1} \times \sin \sin \left(\tan^{-1} \tan^{-1} \left(\frac{A - X_1}{S - C} \right) \right) \right\} \right] \quad (3.6)$$

Where, X_1 is the offset of point source along X axis.

One ray has been considered that strike at the boundary at a distance of 260 km along X axis the refracted ray when traced was found to strike at a distance of 291 km along the X axis, 100 km above the bottom of the model. This value is predicted by the above formula. So the Snell's law is justified. The critical offset along the X axis is shown by blue line which is approximately 368 km. It is further clear from the figure that above the critical offset there are no complementary wave fronts in the second medium for any wavefronts in the first medium; this proves that there is no refracted wave in the in the second medium for any incident wave in the first medium beyond the critical offset. This again proves the validity of Snell's law. It can further be observed that head wave starts generating beyond the critical offset whose propagation will be discussed in forgoing discussion.

3.5.3 EXPERIMENT 3

The aim of this numerical experiment was to show that beyond the crossover distance the first arrivals are critically refracted head waves and hence to justify that the solutions give the first arrival waves. For this a similar model as that of in Figure 3.6 was taken but with different model parameter as shown in Table 3.3.

Table 3.3: Modified parameters for the model considered in Figure 3.9

PARAMETERS	VALUE
Model dimension	(500×20×350) km
No. of grid	(251×11×176)
Grid spacing	(2×2×2) km
Source position	(20×10×350) km
Medium velocities	4 km/s in upper medium and 7 km/s in lower medium

With these parameters the FMM was imposed and the results were obtained. A portion of vertical section of the wavefronts through the source is shown in Figure 3.11.

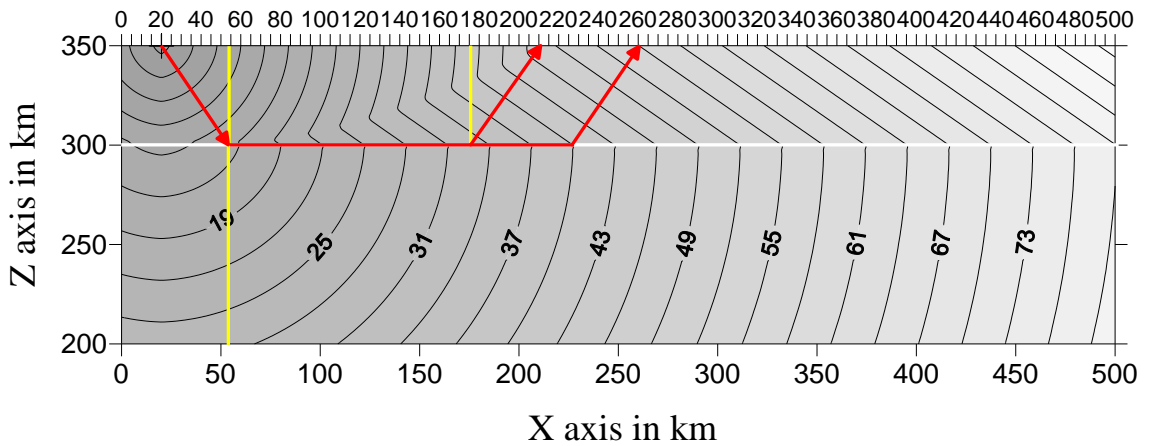


Figure 3.11: A portion of vertical slice of the wavefronts through the source; illustrating that beyond the crossover distance it is the critically refracted head waves that are the first arrivals (After plotting the results obtained for model parameter in Table 3.3). The red lines in the figure are the ray paths for critically refracted head waves. The white line indicates the boundary separating two media and the yellow lines are normals at the boundary at different position shown in the figure. The longest yellow line marks the critical offset along X axis. The time interval between two successive wavefronts is three seconds.

From the model parameters, the critical offset is 54.82 km which is marked by yellow line. It can be observed that beyond the critical offset head waves starts generating. The crossover distance from the model parameters is 211.5 km. From the figure it is clear that it is the first offset where the head waves come first. It can also be observed that beyond this distance all are head waves which are coming to the surface. This is possible only when the algorithm gives first arrival solution. This statement is further supported by the fact that all the head waves are parallel and their angle with vertical axis is critical angle which in turn means that, among all the head waves, the critically refracted head waves are coming to the surface. As we know that critically refracted head waves are the first wave among any other head waves so it again justifies that the solution gives first arrivals.

3.5.4 EXPERIMENT 4

In this numerical experiment it has been shown that if a uniform high velocity slab is placed in the path of waves propagating in a uniform low velocity medium then the wavefronts after crossing the slab remains parallel to the wavefronts what would have existed if the slab were absent. For this a model as shown in Figure 3.12 was considered and a source was placed inside the model. The model was practically simulated by gridding parameterization. The parameters for source and model are shown in Table 3.4.

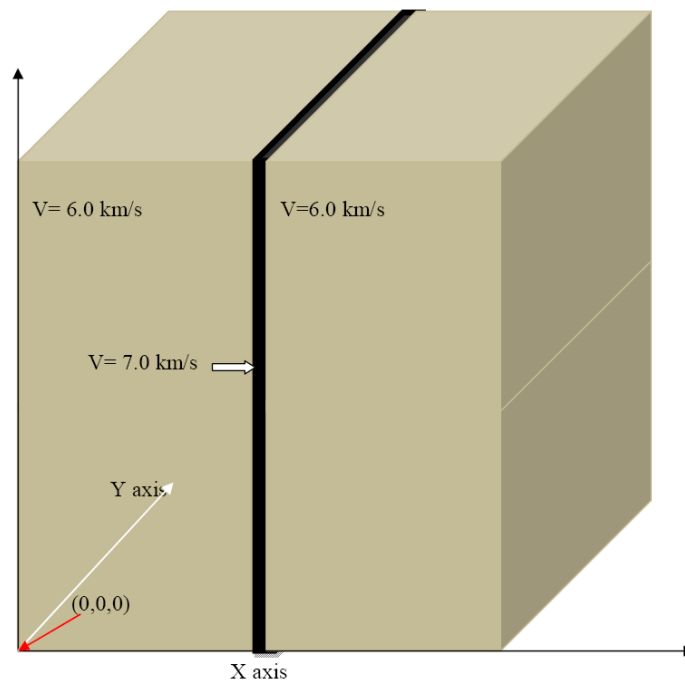


Figure 3.12: A three dimensional model showing a high velocity vertical slab parallel to Y-Z plane of the model; cutting a three dimensional homogeneous medium (After drawing).

Table 3.4: Parameters for the model considered in Figure 3.9

PARAMETERS	VALUE
Model dimension	(250×200×250) km
No. of grid	(126×101×126)
Grid spacing	(2×2×2) km
Source position	(20×11×20) km
Medium velocities	6 km/s for medium and 7 km/s for slab

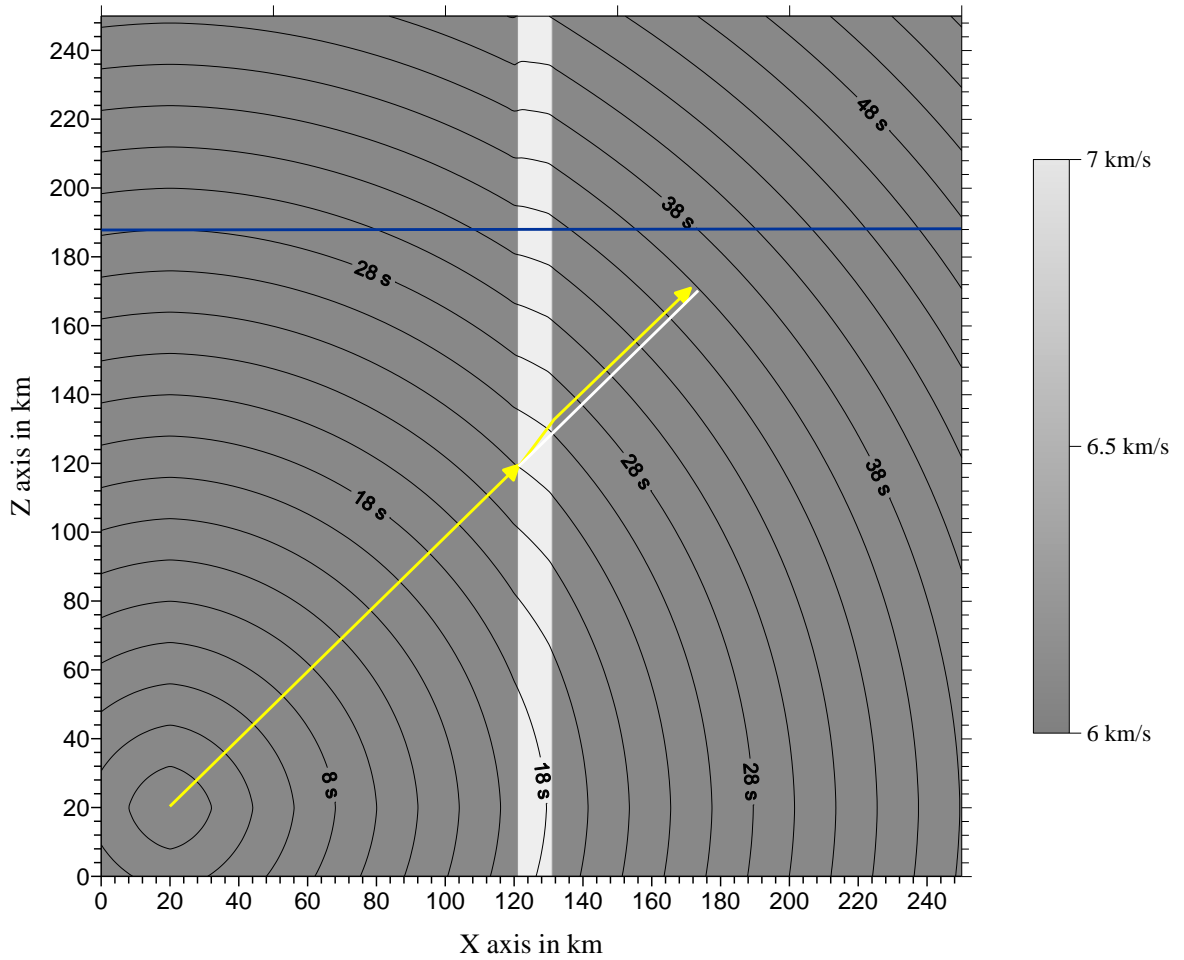


Figure 3.13: A vertical section of the wavefronts through the source showing that the disturbance of wavefronts propagating in a uniform low velocity medium by a high velocity uniform slab happens in such a way that the wavefronts after crossing the slab remains parallel to the wavefronts what would have existed if the slab were not present (After plotting the results obtained for model in Figure 3.9). The blue line marks, at the surface of the slab, the critical offset along Z axis. The ray path (yellow line) after crossing the boundary makes an offset from its original path indicated by white line. The velocities are shown on the colour scale on the right side of the figure. The time interval between two successive wavefronts is two seconds.

The FMM was imposed and the results were obtained and a vertical section of the wavefronts through the source is shown in Figure 3.13. From the figure it is clear that slab disturbs the wave and all the wavefronts after crossing the surface remains equally spaced and parallel to the wavefronts what would have observed if there were no slab. The shift in the ray path as shown in the Figure 3.13 by separation of blue line and white line is given by the formula:

$$Shift = Z \frac{\sin(\theta_r - \theta_i)}{\cos \theta_i}$$

Where, Z is the thickness of the slab, θ_r is the angle of refraction and θ_i is the angle of incidence at the surface of the slab.

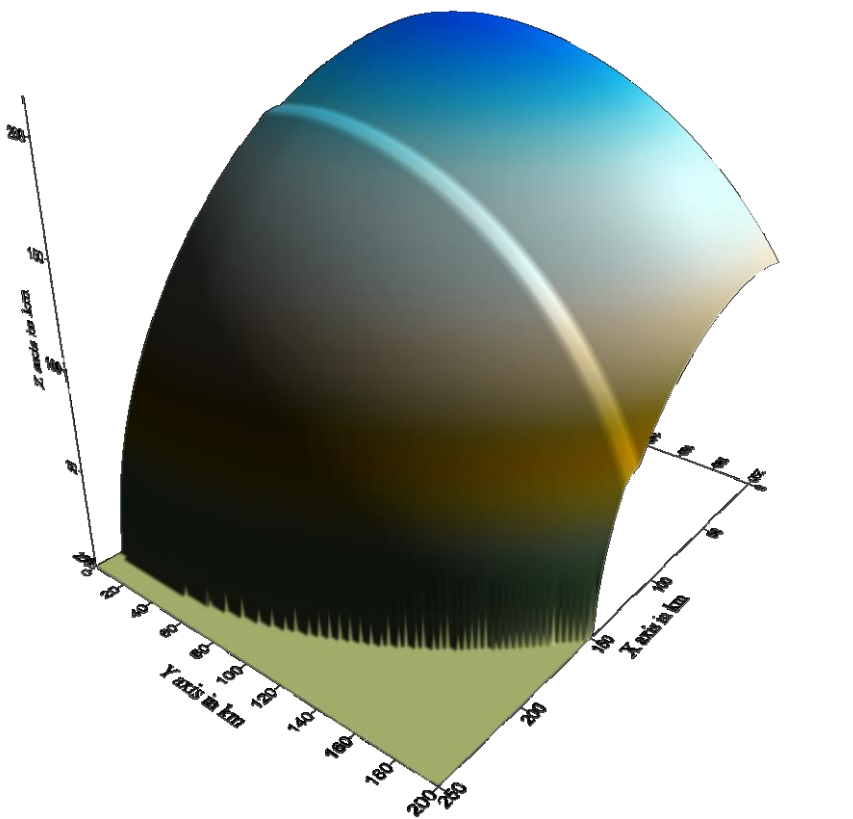
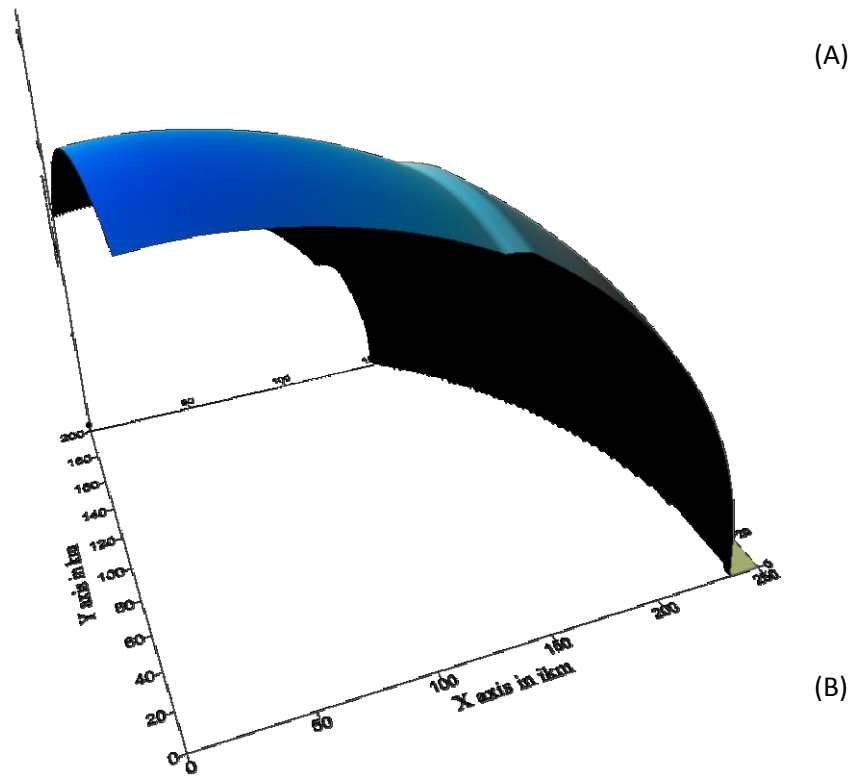


Figure 3.14: A three dimensional view of the wavefront within the model at 36 s and above the source or $Z=20$ km (After plotting the results obtained for model in Figure 3.12). (A) A view from above $(0,0,0)$ coordinates; (B) a view from above $(250,200,20)$ coordinates.

3.5.5 EXPERIMENT 5

The aim of this experiment is to show that in a heterogeneous medium the spacing between two wavefronts shrink as velocity decreases and separation increases as velocity increases. For this experiment a three dimensional model as shown in Figure 3.15 was considered and a source was placed inside the model. The model was practically simulated by gridding parameterization. The parameters for source and model are shown in Table 3.5.

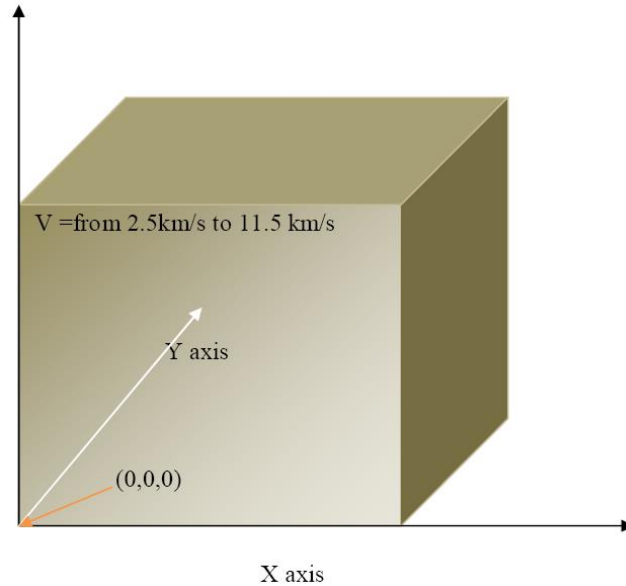


Figure 3.15: A three dimensional heterogeneous model whose velocity function is given in the Table 3.5.

Table 3.5: Parameters for the model considered in Figure 3.15

PARAMETERS	VALUE
Model dimension	(300×20×300) km
No. of grid	(151×11×151)
Grid spacing	(2×2×2) km
Source position	(50×10×50) km
Medium velocity function	$V=7.0+0.015X-0.015Z$ km/s

The velocity continuously increases from the top left corner to bottom right corner of the model and there is no change of velocity along the Y axis. The FMM was imposed and the results were obtained and the vertical section of the wavefronts through the source is shown in Figure 3.16. From this Figure 3.16 it is clear that the separation between the two wavefronts increases from top left corner to the bottom right corner which is due to increase of velocity.

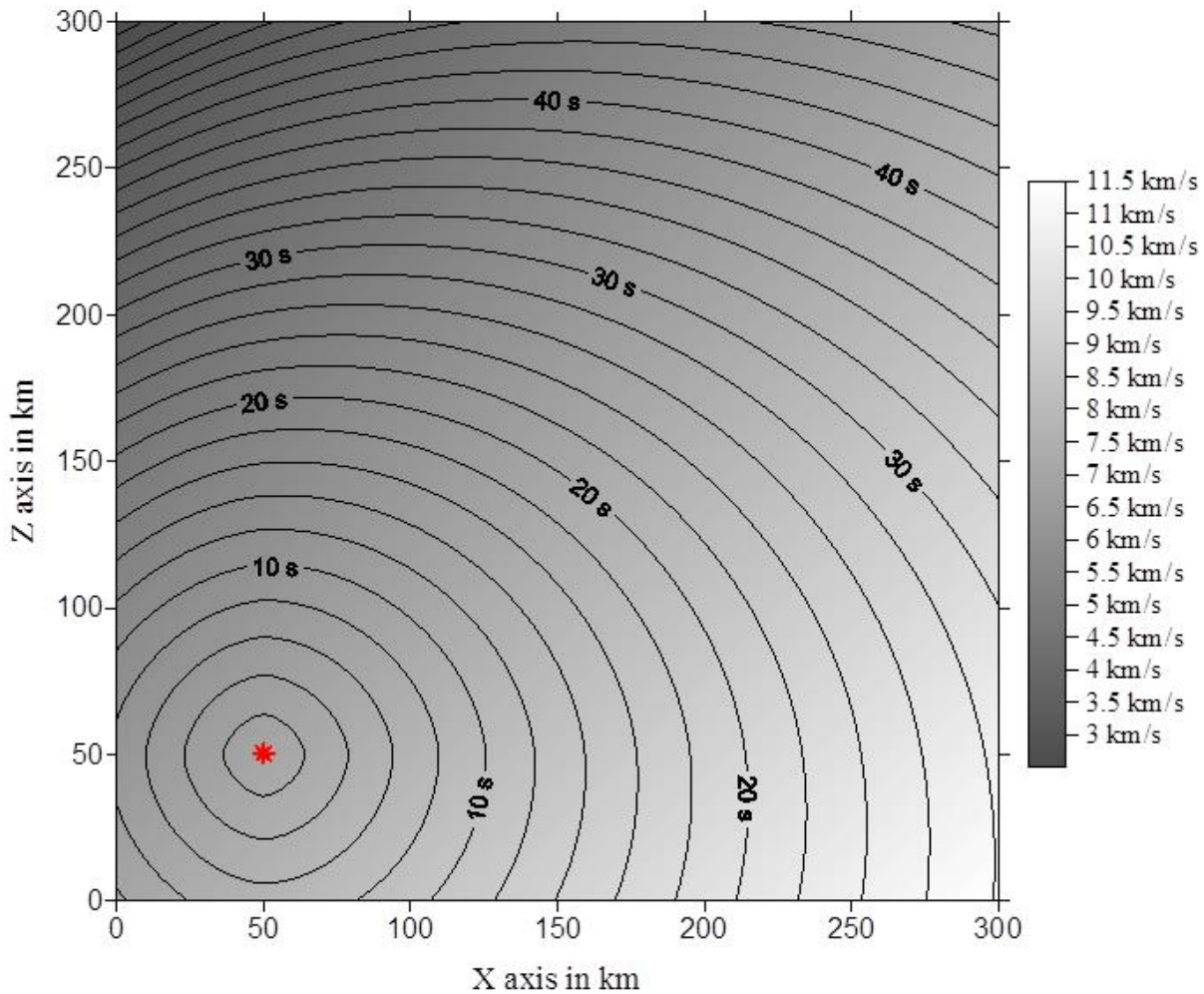


Figure 3.16: A vertical slice of the wavefronts through the source; showing how the spacing between two consecutive wavefronts depends upon time and position of the wavefronts (After plotting the results obtained for the model in Figure 3.12). The time interval between two successive wavefronts is two seconds. The velocities of the medium are shown on the colour scale on the right side of the figure and the red star indicates the source position.

3.5.6 EXPERIMENT 6

In this numerical experiment it has been shown that the solutions are logical in highly heterogeneous media. For this the same model as in Figure 3.15 was considered and a heterogeneous high velocity square body was kept within the model. The velocity of this body is 0.3 times more than the velocities of surrounding medium. This case simulates a heterogeneous buried body in a heterogeneous medium.

The block size is (38×38×38) km and it was placed exactly in the middle of the model. The FMM was imposed and the results were obtained. The vertical section of the wavefronts through the source is shown in Figure 3.18.

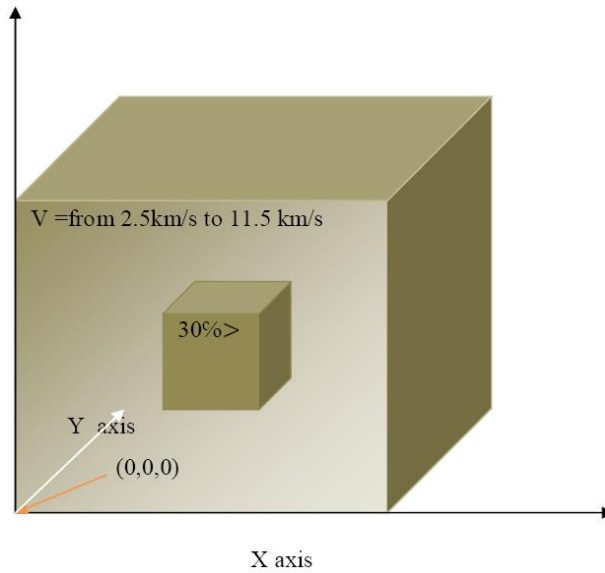


Figure 3.17: A three dimensional model showing a heterogeneous buried body within a heterogeneous medium.

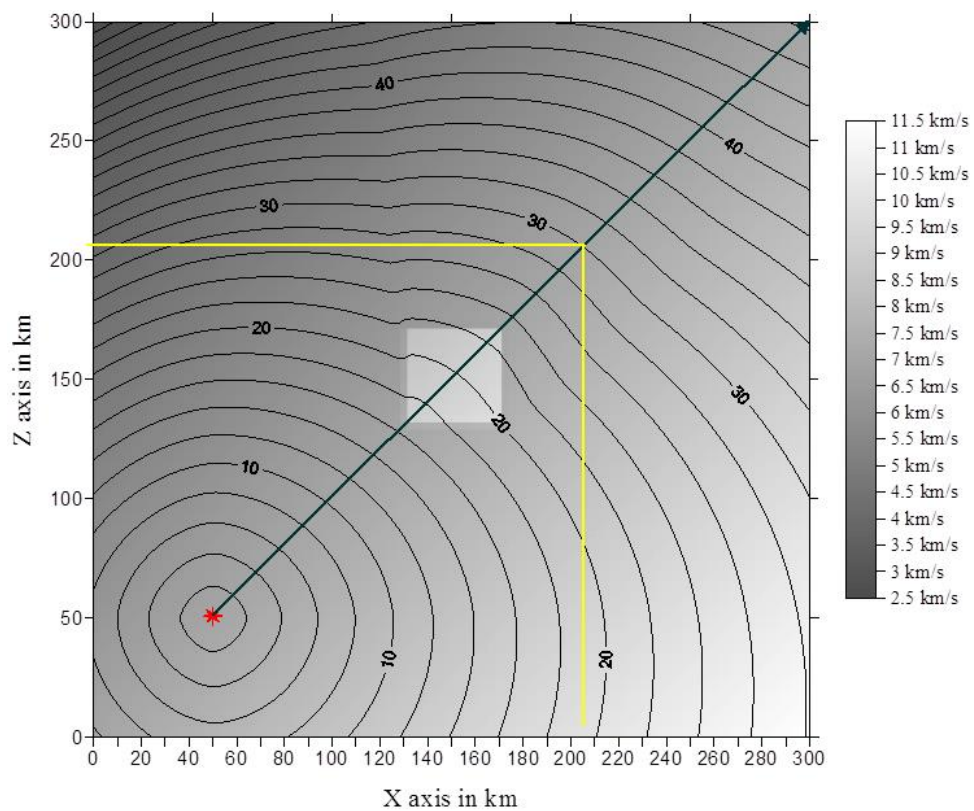


Figure 3.18: A vertical slice of the wavefronts through the source; showing the behaviour of the wavefronts within the heterogeneous model (After plotting the results obtained for model the in Figure 3.14). The deep green line shows the path along which there is no change of velocity (except within the buried body where it becomes 0.3 times more than the surrounding medium) and hence along this direction at any point the relation of distance, time and velocity can be easily verified. The yellow lines are drawn for verification of the latter statement. The time interval between two successive wavefronts is two seconds. The velocities of the medium are shown on the colour scale on the right side of the figure and the red star indicates the source position.

From the Figure 3.18 the effect of buried body is clear. Since along the bottom left corner to top right corner the velocity remains constant except within the body where the velocity increases by 0.3 times, the velocity, time and distance relation can easily be shown to be satisfied along this direction. For this a wavefront beyond the buried body at 30 s was considered and offset along X direction and along Z direction are marked by yellow line. This offset is 205 km. It can be shown that this offset satisfy the wave propagation theory. In other direction similar way the velocity time and distance relation can be shown to be satisfied but with numerous calculations as the velocity does not remain constant along these arbitrary directions.

3.5.7 EXPERIMENT 7

A subducted plate model as shown in Figure 3.19 was considered. The model and source parameters are given in Table 3.6.

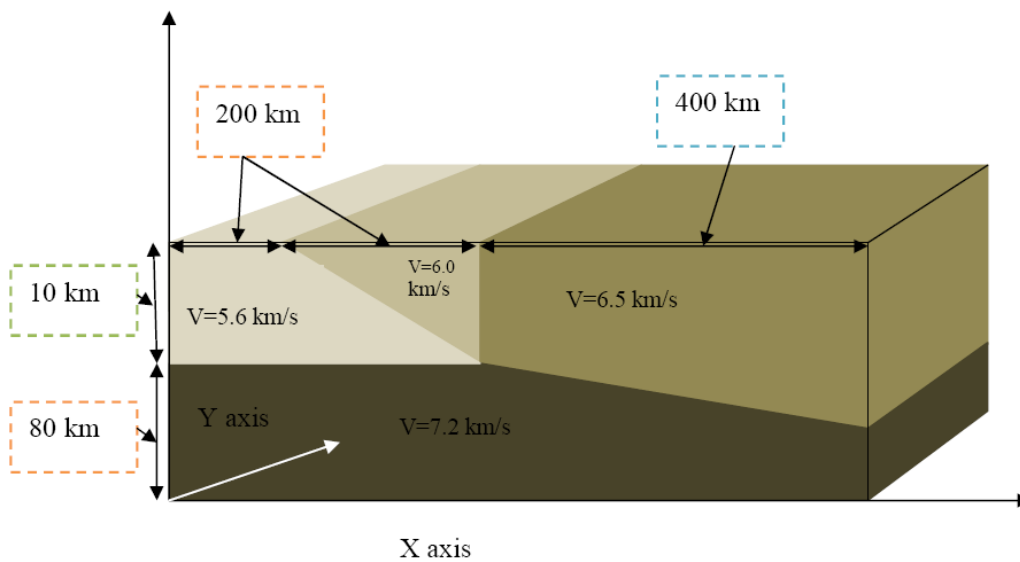


Figure 3.19: A simplistic three dimensional subduction model (After drawing).

Table 3.6: parameters for the model considered in Figure 3.16

PARAMETERS	VALUE
Model dimension	(800×50×90) km
No. of grid	(401×26×90)
Grid spacing	(2×2×2) km
Source position	(320×25×82) km
Medium velocities	As shown in the model

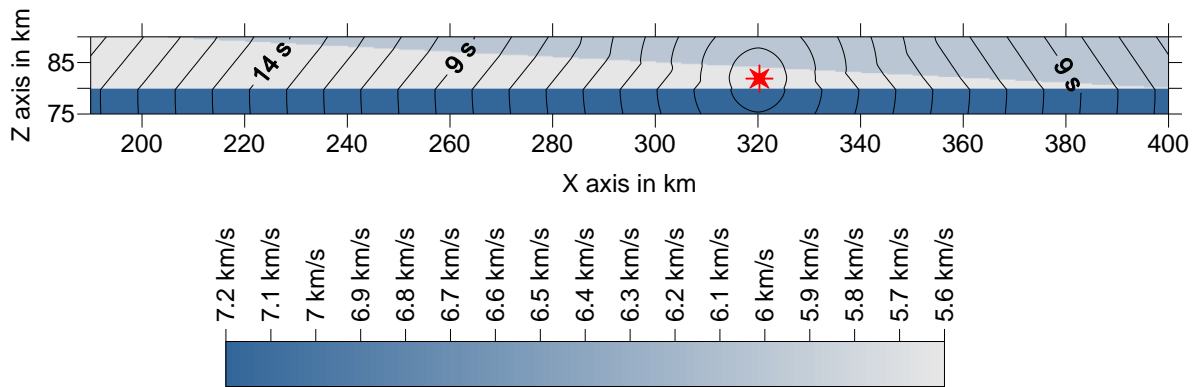


Figure 3.20: A portion of vertical section of the wavefronts through the source; showing that only head waves are first arrivals on the exposed surface of subducted plate for the model under consideration (After plotting the results obtained for the model in Figure 3.19). The time interval between two successive wavefronts is one second. The velocities of different plates are shown on colour scale below the figure and the red star indicates the source position.

The FMM was imposed and solution was obtained. A strip of vertical section of the wavefronts through the source is shown in Figure 3.20. From this figure it is clear that only head waves will be the first arrivals on the exposed surface of subducted plate for the model and source position considered.

3.5.8 EXPERIMENT 8

In Figure 3.21 a simplistic model of a plumbing system of a volcano was shown together with waves generated for two locations of sources. In both the figure the position of the source is marked by red star. It is clear from the figure that the wavefronts get slower through the plums due to their low velocities and this effect keeps on propagating towards the surface.

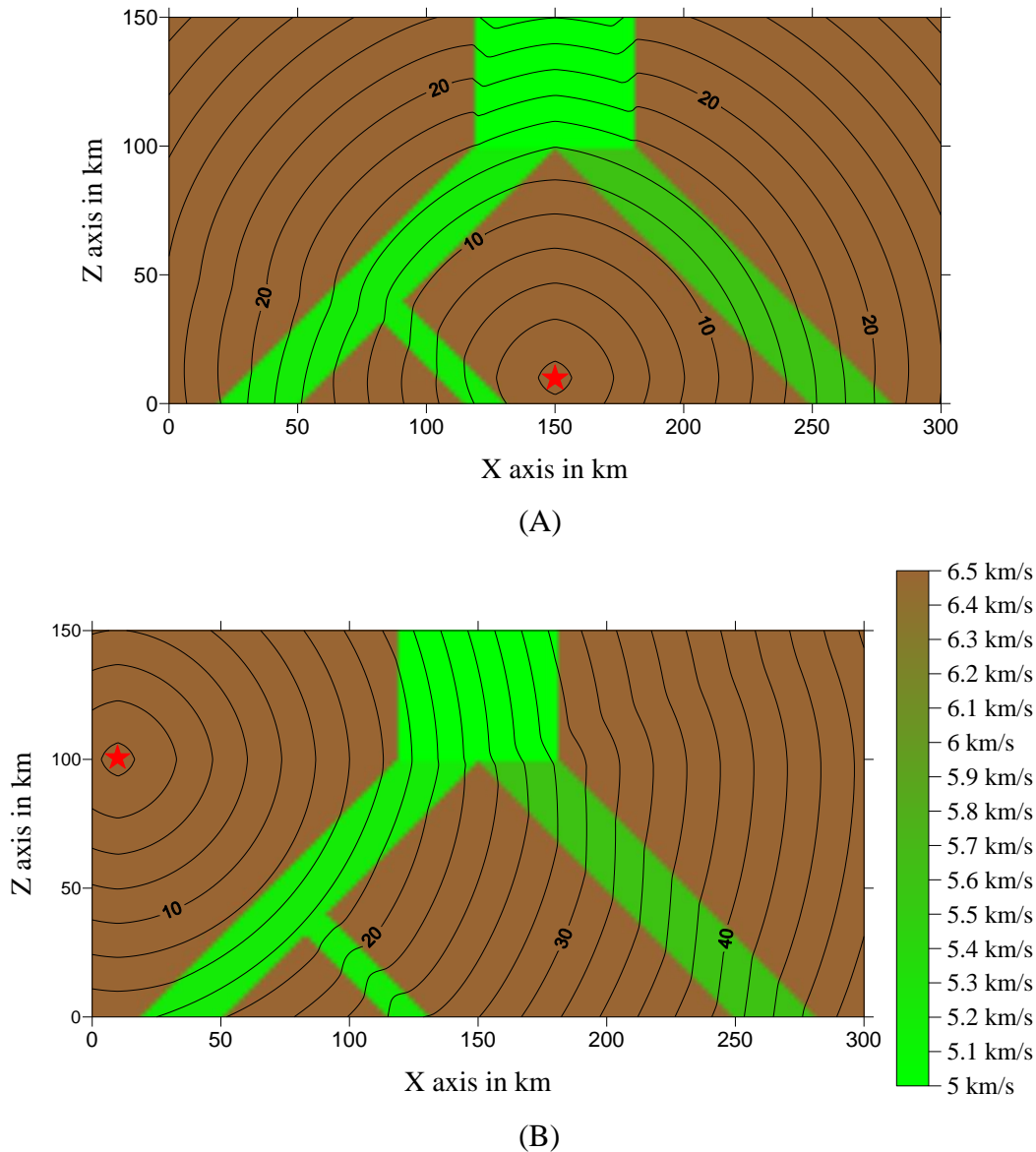


Figure 3.21: A vertical section of the wavefronts through the source; showing the behaviour of waves through the plumbing system (After plotting the results for the model considered in section 3.21). The medium velocities and the velocities of the plumes are shown on the colour scale on right side of the figure. (A) A vertical section for the source position at (150,10,10) km; (B) a vertical section for the source position at (10,10,100) km. The time interval between two successive wavefronts is two seconds and the source position are indicated by red star.

3.4.9 EXPERIMENT 9

In this case the traveltimes contours for anticline and syncline folds are discussed. The parameters of model considered are given in Table 3.7. The traveltimes contours for the numerical model defined in Table 3.7 for source positions at (50,50,1) km and (100,50,1) km are obtained using Fast Marching Method for the same model with and without applying dip in the Y-direction which is the direction of strike. The contours are shown in Figure 3.23 (a, b, c and d).

Table 3.7: Parameters of a model to study anticline and syncline

Parameters	Values
Model Dimension	(150,100,25) km
Number of grid points	(151,101,26)
Grid Spacing	(1,1,1) km
Source Position	(50,50,1) km and (100,50,1) km
Medium Velocity	As shown in Figure 3.22

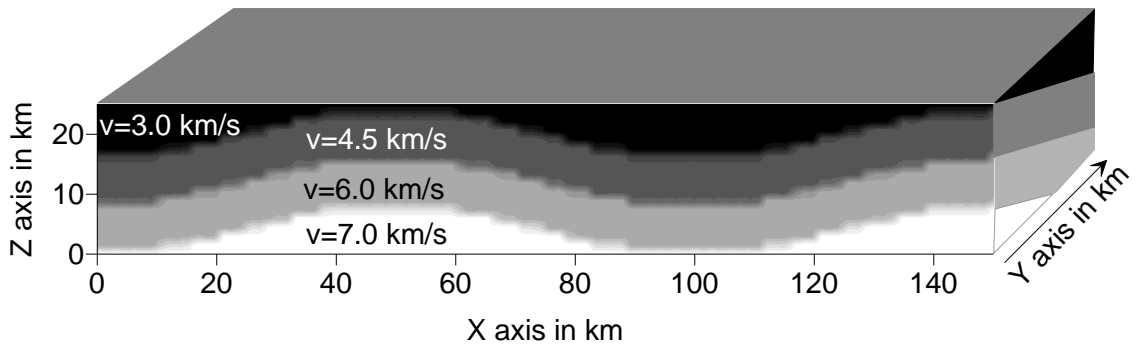


Figure 3.22: Anticline and syncline model; in one case the Y-direction is considered without dip and in another case the Y-direction is considered with a dip of 6.7° . Direction of strike is along Y-axis in the model.

Figure 3.23(a) and Figure 3.23(b) are obtained without applying dip in the Y-direction in the model. Figure 3.23(a) is obtained when the source is at (50,50,1) km; either when source lies below the anticline structure. Figure 3.23(b) is obtained when the source is at (100,50,1) km; either when source lies below the syncline structure. From the observation of these two it is clear that contours are elliptical in shape with major axis along strike direction in case of anticline structure and along dip direction in case of syncline structure. Further it can be observed that the spacing between adjacent contours increases in the dip direction in case of anticline structure and decreases in the same direction in case of syncline structure. Thus it is observed that the shape of travelttime contours is different for anticline and syncline fold.

Figure 3.23(c) and Figure 3.23(d) are obtained when a dip of amount 6.7° is applied in the Y-direction of the model. Figure 3.23(c) is for anticline structure and Figure 3.23(d) is for syncline structure. It is observed from both the figures that due to application of dip in the direction of positive Y-axis the spacing between adjacent contours decreases in the same direction for anticline and syncline structures. Thus it is observed that due to change of understructure the travelttime contours change symmetrically for anticline and syncline folds.

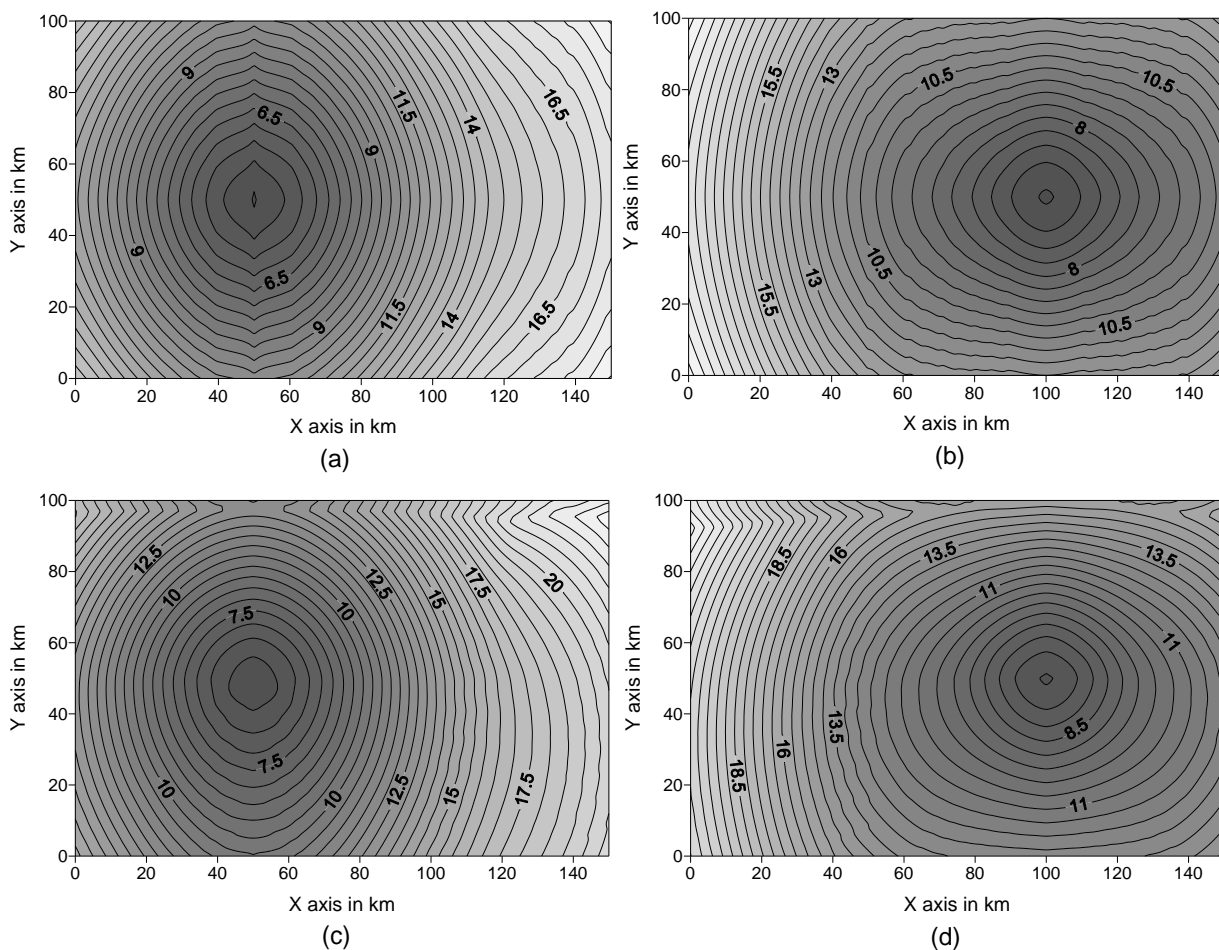


Figure 3.23: The computed traveltime contours; (a) when source is at (50,50,1) km and (b) when source is at (100,50,1) km obtained using the model in Figure. 3.22 without applying dip in the Y-direction. The computed traveltime contours; (c) when source is at (50,50,1) km and (d) when source is at (100,50,1) km obtained using the model in Figure. 3.22 after applying dip of 6.7° in the Y-direction

3.5.10 EXPERIMENT 10

In this section, we present a numerical study of two types of faults, a normal fault and a Graben-Horst type of faults. The model parameters for model dimensions, number of grid points and grid spacing for both types of faults are same as given in Table 3.7. The vertical section of velocity structure for both normal fault and Graben and Horst types of faults are shown in Figure 3.24(a) and in Figure 3.24(c) respectively. Traveltime responses for both types of fault are obtained using Fast Marching Method keeping the source at (100, 3.240, 1) km in case of normal fault and at (73.24, 3.240, 1) km in case of Graben-Horst type of fault, as shown in Figure 3.24(b) and Figure 3.24(d) respectively. Contours of traveltimes in Figure 3.24(b) for both normal fault and in Figure 3.24(d) for Graben-Horst type of fault clearly simulate the position of faults considered in the models; hence these kinds of approaches can be utilized to identify the position of real fault of actual earth.

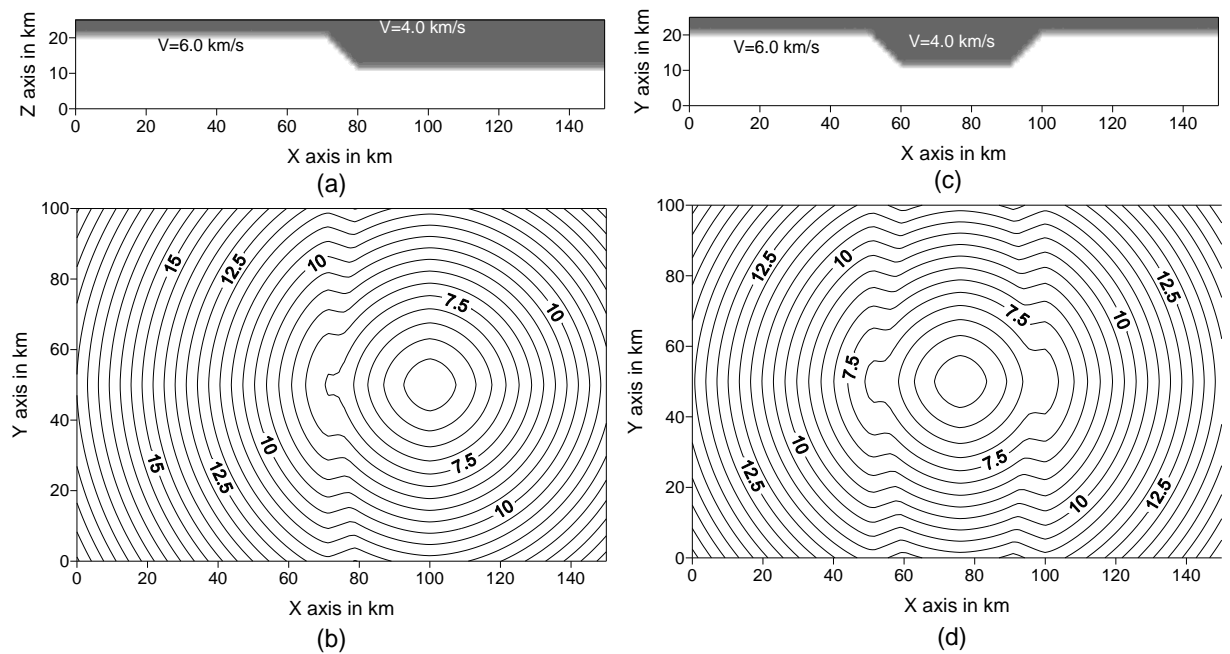


Figure 3.24: Vertical section of the normal fault model in the X-Z plane, with X-axis as dip direction, (a); Contours of traveltime for the normal fault considered in case study, (b); Vertical section of Horst and Graben type of fault model in the X-Z plane, (c); Contours of traveltime for Gaben and Horst type fault considered in case study, (d).

3.6 CONCLUSIONS

The first marching method is an efficient tool to obtain accurate traveltime response of heterogeneous media. The efficiency lies in the fact that it gives guarantee to the first arrival; it is stable because it approximates the discontinuity with weak solution; and it is fast because it utilizes the narrow band technique with heap sorting.

The identification of nature of geological structure of a region is essential in tomography problems in seismology. This study gives the comprehensive idea about traveltime contours associated with different numerical and geological models. The traveltime of different geological models can be compared with the traveltime responses derived from traveltime record from a seismic network in a region of earth to understand the approximate nature of geological structure of that region. The head waves which are extremely useful for locating of thin layer are handled by this method which is one of the biggest advantages of this method.





MULTISTENCILS PSEUDOANISOTROPIC FAST MARCHING METHOD

4.1 INTRODUCTION

One of the most important characteristics of Fast Marching Method (FMM) as described in Chapter 3 is that, during the propagation of fronts, it always makes a distinction between grid points with known solution and the grid points with unknown solution by the propagating front itself which actually constitutes a dynamic narrow band in computational domain that simulates the wave propagation. Monotonic evolution of fronts are essential in many applications where order of information is important such as robotic path planning (Hassouna, 2005), image inpainting (Telea, 2004) and computing the fast arrival phases in seismology (Rawlinson, 2006).

It has been observed that major errors in the solutions of FMM in homogeneous media using Cartesian coordinate system orient along the diagonal directions of Cartesian domain (Sethian, 1997). These errors can be removed to a greater degree by solving the FMM in spherical domain but changing the domain of computation from Cartesian to Spherical helps to improve the method only in homogeneous media. In inhomogeneous media the diagonal errors are distributed randomly in all directions and hence changing the computational domain will not decrease the computational error (Sethian, 1997). In spite of its several advantages as discussed in Chapter 3, the associated error in FMM limits its optimal applicability.

Many authors (§1.2.2.3) in the recent past have documented a number of approaches to reduce the numerical error associated with FMM and to improve the method for it to be either computationally efficient (Kim, 2001; Yatziv et al., 2006) or more accurate (Sethian, 1999; Danielsson and Lin, 2003). All these methods except what proposed by Danielsson and Lin (2003) ignore the information provided by diagonal grid points and hence suffer from large numerical error along diagonal direction.

One of the most recent methods in which diagonal information of grid points is considered is Multistencils Fast Marching (MSFM) Method as introduced by Hassouna and Farag (2007). The MSFM Method invokes the concept of several stencils on Cartesian domains to dilute the diagonal effect in the solution of FMM. Unfortunately, the method works well in isotropic or nearly isotropic grid only. In a strongly anisotropic Cartesian grid, as the grid spacing is strongly different in different dimensions, the computational error of MSFM Method is higher (§5.3) compared with FMM and hence the use of the method does not help to improve the basic FMM.

This chapter presents a novel methodology which has been called as Multistencils Pseudo-anisotropic Fast Marching Method (MPFMM) where the concept of pseudo-anisotropic gradient in computational field, and angular weighted approximation in pseudo-anisotropic gradient to interpolate directional derivatives in desired directions, have been introduced. The use of these concepts in the method opens the possibility to construct desired hypothetical stencils in the computational domain to solve the upwind equation without depending on natural stencil provided by a given grid system. Since the method gives us freedom to construct any shape of stencil; therefore, all possible symmetric stencils in a Cartesian grid have been considered to dilute the anisotropic effect of natural stencil in computation. The entire methodology improves FMM and MSFM Method to a much higher degree.

4.2 MULTISTENCILS FAST MARCHING (MSFM) METHOD

The MSFM Method basically uses the information of axial as well as diagonal grid point to solve the gradient term in the eikonal equation. It computes the solution at each grid point by solving the eikonal equation on several stencils that cover its entire neighbouring points and then picks the solutions that satisfy the upwind condition. The solution for those stencils which are not aligned with the natural coordinate system, the eikonal equation is simplified using directional derivatives and then solved using higher order finite difference schemes. The two stencils in 2D and six stencils in 3D are used in this method respectively.

4.3 CONCEPT OF PSEUDOANISOTROPIC GRADIENT

Consider a field, $T(x, y, z)$ with its gradient as $\nabla T(x, y, z)$. Directional derivative, $U_r(x, y, z)$ of $T(x, y, z)$ along a unit vector, \mathbf{r} is then given as:

$$U_r(x, y, z) = \mathbf{r} \cdot \nabla T(x, y, z) \quad (4.1)$$

The relationship between T and U_r in Equation (4.1) is valid if ∇T is defined in the medium using some analytical function which in turn means that if T is defined to be analytical and differentiable at least upto first degree. Consider the situation where both T and ∇T are to be evaluated in numerical domain where numerical error cannot be neglected. In numerical domain, ∇T at different grid point must be represented in terms of directional derivatives which further computed numerically using different value of T at different grid points. The vector ∇T will still satisfy the relation given in Equation (4.1) if the directional derivative U_r along unit vector \mathbf{r} is used in representation of ∇T . Consider now a directional derivative $U_{r'}$ along unit vector, \mathbf{r}' which do not contribute in representation of ∇T then the directional derivative along this unit vector cannot be represented by simply replacing \mathbf{r} by \mathbf{r}' in Equation (4.1), either:

$$U_{r'}(x, y, z) \neq \mathbf{r}' \cdot \nabla T(x, y, z) \quad (4.2)$$

This can be written as:

$$U_{r'}(x, y, z) = \mathbf{r}' \cdot \nabla T(x, y, z) + w \quad (4.3)$$

The term w in Equation (4.3) appears because $U_{r'}$ is represented by ∇T which itself is represented by different directional derivatives which have no role in the evaluation of ∇T . In other words, one directional derivate is represented in terms of other directional derivatives in numerical field and as we know that all directional derivatives in numerical domain have some associated numerical error therefore Equation (4.1) cannot be used to define a general directional derivative in any direction. Since ∇T depends upon direction from which it is computed so the term pseudo-anisotropy is introduced because actual gradient is not anisotropic instead it comes because of numerical error. The term w in Equation (4.3) also depends upon direction and hence it is also termed as pseudo-anisotropic adjustment term.

4.4 ANGULAR WEIGHTED INTERPOLATION

An interpolation technique is required to be used in FMM which does not dilute the concept of singularity in traveltime field as well as which would be easy to use under the condition that the parameters responsible for solution of the eikonal equation are real time variables. Consider a physical quantity, P on 2D space whose value depends on the angle of measurements. Further, suppose that the value of P is known along at least two directions, \mathbf{r}_1 and \mathbf{r}_2 as P_1 and P_2 respectively. Then, the value of P along an arbitrary direction, \mathbf{s} as shown in Figure 4.1(a) is given by using weighted interpolation as:

$$P_s = \frac{P_1(\mathbf{r}_2 \cdot \mathbf{s}) + P_2(\mathbf{r}_1 \cdot \mathbf{s})}{(\mathbf{r}_1 \cdot \mathbf{s}) + (\mathbf{r}_2 \cdot \mathbf{s})} \quad (4.4)$$

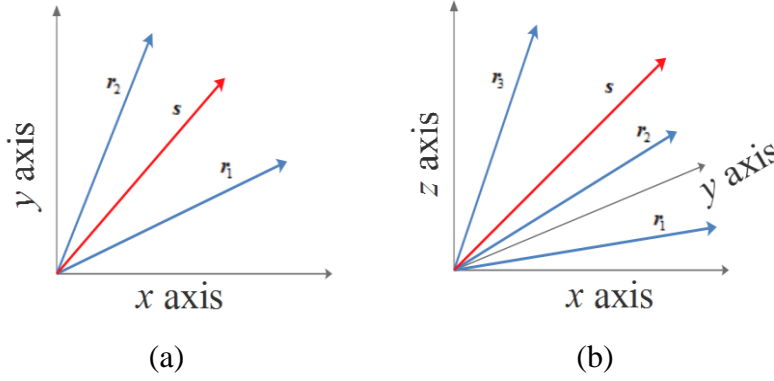


Figure 4.1: Schematic diagram showing angular interpolation in 2D (a) and 3D (b).

Similarly in 3D if P is known in three directions then along a direction \mathbf{s} (Figure 4.1(b)) its value, P_s is given as:

$$P_s = \frac{P_1(\mathbf{r}_2 \cdot \mathbf{s})(\mathbf{r}_3 \cdot \mathbf{s}) + P_2(\mathbf{r}_3 \cdot \mathbf{s})(\mathbf{r}_1 \cdot \mathbf{s}) + P_3(\mathbf{r}_1 \cdot \mathbf{s})(\mathbf{r}_2 \cdot \mathbf{s})}{(\mathbf{r}_1 \cdot \mathbf{s})(\mathbf{r}_2 \cdot \mathbf{s}) + (\mathbf{r}_2 \cdot \mathbf{s})(\mathbf{r}_3 \cdot \mathbf{s}) + (\mathbf{r}_3 \cdot \mathbf{s})(\mathbf{r}_1 \cdot \mathbf{s})} \quad (4.5)$$

The Equation (4.5) can be generalize to obtain the value of P as P_s along a unit vector \mathbf{s} , given the values of P along m number of unit vector, $\mathbf{r}_i, i \in [1, m]$, as:

$$P_s = \frac{\sum_{i=1}^m \left(\frac{P_i}{\mathbf{r}_i \cdot \mathbf{s}} \right)}{\sum_{i=1}^m \frac{1}{\mathbf{r}_i \cdot \mathbf{s}}} \quad (4.6)$$

Two of the most important properties of weighted interpolation techniques are: first, it does not dilute the singularity in the traveltime field and second it is easy to use in a situation where the known parameters in the interpolation are real time variable. Since FMM handle the singularity of traveltime field so the first statement is important with regard to FMM. The parameter which is responsible to solve upwind equation (1.19) is real time variable. The second statement can be made realistic if a parameter G is introduced to indicate the availability of information along a suitable direction. Suppose G_1, G_2, \dots, G_m indicate the availability of information along $\mathbf{r}_1, \mathbf{r}_2, \dots, \mathbf{r}_m$ directions then Equation (4.6) can be modified to write as:

$$P_s = \frac{\sum_{i=1}^m \left(\frac{G_i P_i}{\mathbf{r}_i \cdot \mathbf{s}} \right)}{\sum_{i=1}^m \frac{G_i}{\mathbf{r}_i \cdot \mathbf{s}}} \quad (4.7)$$

Equation (4.7) represents the angular interpolation of physical quantity P along a direction \mathbf{s} for a given set of values of P as P_i ; $i \in [1, m]$ along different directions \mathbf{r}_i ; $i \in [1, m]$ respectively. The parameter G_i can take either 1 or 0 value, depending on availability or unavailability of information (quantity P_i) along direction \mathbf{r}_i .

4.5 MULTISTENCILS PSEUDOANISOTROPIC FAST MARCHING METHOD

All the related methods of FMM (§1.2.2.3) except MSFM method (§4.2) ignore the information provided by diagonal points and hence suffer from large numerical error. MSFM method considers the information of diagonal points in solution of the eikonal equation and solves the same using the directional derivatives from eight neighboring grid points in 2D and 26 neighboring grid points in 3D. However, MSFM method neither differentiates the solutions computed using different sets of directional derivatives in different stencils nor it considers the role of different grid sizes in the Cartesian domain. This leads to suffer from large numerical error particularly in anisotropic grid structure in an inhomogeneous media. In the proposed method, MPFMM the first problem is addressed by the introduction of pseudo anisotropic gradient (§4.3) whereas the second problem is removed by proper respecting the grid spacing in the formulation of MPFMM.

4.5.1 2D MULTISTENCILS PSEUDOANISOTROPIC FAST MARCHING METHOD

In 2D MPFMM weighted angular interpolation is carried out in 2D followed by the solution of basic upwind equation given in Chapter 1 (Equation 1.19).

4.5.1.1 INTERPOLATION OF DIRECTIONAL DERIVATIVES IN 2D STENCILS

Consider a grid of 9 adjacent grid points, p_u , $u \in [0, 8]$ in 2D Cartesian domain in which a stencil, S_v intersects the diagonal grid points p_5, p_6, p_7 and p_8 as shown in Figure 4.2. Consider a traveltime field $T(x, y)$ which is a function of (x, y) . Let $\mathbf{r}_v = (r_{v1}, r_{v2})^T$, $v \in [1, 8]$ be unit vectors along $p_0 p_v$ and U_v be the directional derivatives of traveltime along \mathbf{r}_v which are given as:

$$U_v = \mathbf{r}_v \cdot \nabla T(x, y), \quad v \in [1, 8] \quad (4.8)$$

Where, $\nabla T(x, y)$ is the gradient of traveltime field $T(x, y)$ as a function of (x, y) . Let U_5 and U_7 are known directional derivatives in the stencil then from Equation (4.8) these can be written as:

$$\left. \begin{aligned} U_5 &= \mathbf{r}_5 \cdot \nabla T(x, y) = r_{51}T_x + r_{52}T_y \\ U_7 &= \mathbf{r}_7 \cdot \nabla T(x, y) = r_{71}T_x + r_{72}T_y \end{aligned} \right\} \quad (4.9)$$

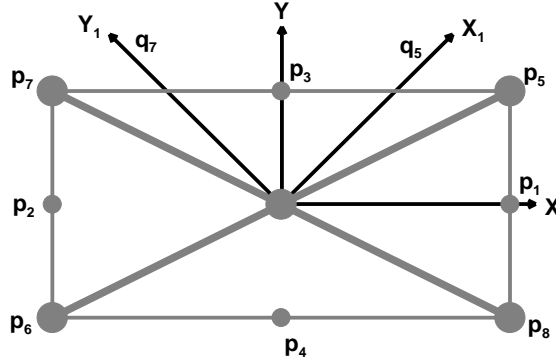


Figure 4.2: The stencil S_v centered at point (x, y) that intersects the 2D lattice at diagonal grid points p_5, p_6, p_7 and p_8 . The natural stencil intersects the 2D lattice at grid points p_1, p_2, p_3 and p_4, q_5 and q_7 are two hypothetical grid points.

The equation set (4.9) can be written in terms of matrix form as:

$$\begin{pmatrix} U_5 \\ U_7 \end{pmatrix} = \begin{pmatrix} r_{51} & r_{52} \\ r_{71} & r_{72} \end{pmatrix} \begin{pmatrix} T_x \\ T_y \end{pmatrix} \quad (4.10)$$

Thus,

$$U = R \nabla T(x, y) \quad (4.11)$$

$$\nabla T(x, y) = R^{-1} U \quad (4.12)$$

Where, matrix representation of vectors is used as:

$$U = \begin{pmatrix} U_5 \\ U_7 \end{pmatrix}, \quad R = \begin{pmatrix} r_{51} & r_{52} \\ r_{71} & r_{72} \end{pmatrix} \quad \text{and} \quad \nabla T(x, y) = \begin{pmatrix} T_x \\ T_y \end{pmatrix}.$$

In absence of numerical errors in traveltime, the above traveltime gradient defines directional derivatives U_1, U_2 and U_3 as:

$$\left. \begin{aligned} U_1 &= \mathbf{r}_1 \cdot \nabla T(x, y) \\ U_3 &= \mathbf{r}_3 \cdot \nabla T(x, y) \end{aligned} \right\} \quad (4.13)$$

On the other hand, in presence of numerical errors U_1 and U_3 do not satisfy the above relationship; either,

$$\left. \begin{aligned} U_1 &\neq \mathbf{r}_1 \cdot \nabla T(x, y) \\ U_3 &\neq \mathbf{r}_3 \cdot \nabla T(x, y) \end{aligned} \right\} \quad (4.14)$$

Consider a variable parameter w corresponding to directional derivatives along p_1, p_3, p_5 and p_7 such as:

$$\left. \begin{aligned} w_1 &= U_1 - \mathbf{r}_1 \cdot \nabla T(x, y) \\ w_3 &= U_3 - \mathbf{r}_3 \cdot \nabla T(x, y) \\ w_5 &= U_5 - \mathbf{r}_5 \cdot \nabla T(x, y) = 0 \\ w_7 &= U_7 - \mathbf{r}_7 \cdot \nabla T(x, y) = 0 \end{aligned} \right\} \quad (4.15)$$

Thus

$$\left. \begin{aligned} U_1 &= \mathbf{r}_1 \cdot \nabla T(x, y) + w_1 \\ U_3 &= \mathbf{r}_3 \cdot \nabla T(x, y) + w_3 \end{aligned} \right\} \quad (4.16)$$

To remove the effect of rectangular shape of stencil in computation of traveltime consider two hypothetical grid points q_5 and q_7 as shown in Figure 4.2 such that the directions along p_0q_5 and p_0q_7 are mutually perpendicular and given by unit vectors $\mathbf{s}_5 = (s_{51}, s_{52})^T$ and $\mathbf{s}_7 = (s_{71}, s_{72})^T$ respectively. To remove the effect of rectangular shape of the stencil, solution of traveltime is required to be obtained from these two directions. The directional derivatives U_{s_5} and U_{s_7} along unit vectors \mathbf{s}_5 and \mathbf{s}_7 , using the analogy of Equation 4.16, can be written as:

$$\left. \begin{aligned} U_{s_5} &= \mathbf{s}_5 \cdot \nabla T(x, y) + \bar{w}_5 \\ U_{s_7} &= \mathbf{s}_7 \cdot \nabla T(x, y) + \bar{w}_7 \end{aligned} \right\} \quad (4.17)$$

Where, \bar{w}_5 and \bar{w}_7 are the parameter w along unit vectors \mathbf{s}_5 and \mathbf{s}_7 . The parameter \bar{w}_5 and \bar{w}_7 are obtained using angular weighted interpolation as:

$$\left. \begin{aligned} \bar{w}_5 &= \frac{w_3 \theta_5 + w_5 \theta_3}{\theta_3 + \theta_5} = \frac{w_3 (\mathbf{r}_{s_5} \cdot \mathbf{r}_5) + w_5 (\mathbf{r}_{s_5} \cdot \mathbf{r}_3)}{(\mathbf{r}_{s_5} \cdot \mathbf{r}_3) + (\mathbf{r}_{s_5} \cdot \mathbf{r}_5)} \\ \bar{w}_7 &= \frac{w_3 \theta_7 + w_7 \theta_3}{\theta_3 + \theta_7} = \frac{w_3 (\mathbf{r}_{s_7} \cdot \mathbf{r}_7) + w_7 (\mathbf{r}_{s_7} \cdot \mathbf{r}_3)}{(\mathbf{r}_{s_7} \cdot \mathbf{r}_3) + (\mathbf{r}_{s_7} \cdot \mathbf{r}_7)} \end{aligned} \right\} \quad (4.18)$$

Using Equations (4.16) and (4.18), U_{s_5} and U_{s_7} in Equation (4.17) become:

$$\left. \begin{aligned} U_{s_5} &= \nabla T \cdot (\mathbf{s}_5 - \mathbf{r}_3 \mathbf{K}_5) + \mathbf{K}_5 U_3 \\ U_{s_7} &= \nabla T \cdot (\mathbf{s}_7 - \mathbf{r}_3 \mathbf{K}_7) + \mathbf{K}_7 U_3 \end{aligned} \right\} \quad (4.19)$$

Where,

$$\left. \begin{aligned} K_5 &= \frac{(\mathbf{r}_{s5} \cdot \mathbf{r}_5)}{(\mathbf{r}_{s5} \cdot \mathbf{r}_3) + (\mathbf{r}_{s5} \cdot \mathbf{r}_5)} \\ K_7 &= \frac{(\mathbf{r}_{s7} \cdot \mathbf{r}_7)}{(\mathbf{r}_{s7} \cdot \mathbf{r}_3) + (\mathbf{r}_{s7} \cdot \mathbf{r}_7)} \end{aligned} \right\} \quad (4.20)$$

Using Equation (4.12), gradient of T multiplied by vectors $(\mathbf{s}_5 - \mathbf{r}_3 K_5)^T$ can be written in terms of linear combination directional derivatives as:

$$\begin{aligned} (\mathbf{s}_5 - \mathbf{r}_3 K_5)^T \cdot \nabla T &= (\mathbf{s}_5 - \mathbf{r}_3 K_5)^T \cdot R^{-1} U \\ &= L_5 U = L_{51} U_5 + L_{52} U_7 \end{aligned} \quad (4.21)$$

Where,

$$L_5 = (L_{51} \quad L_{52}) = (\mathbf{s}_5 - \mathbf{r}_3 K_5)^T R^{-1} \quad (4.22)$$

Similar to above the quantity $(\mathbf{s}_7 - \mathbf{r}_3 K_7)^T \cdot \nabla T$ can be written as:

$$(\mathbf{s}_7 - \mathbf{r}_3 K_7)^T \cdot \nabla T = L_7 U = L_{71} U_5 + L_{72} U_7 \quad (4.23)$$

Where,

$$L_7 = (L_{71} \quad L_{72}) = (\mathbf{s}_7 - \mathbf{r}_3 K_7)^T R^{-1} \quad (4.24)$$

Therefore using Equations (4.21) and (4.23) in the set of Expressions (4.19), it becomes

$$\left. \begin{aligned} U_{s5} &= L_{51} U_5 + L_{52} U_7 + K_5 U_3 \\ U_{s7} &= L_{71} U_5 + L_{72} U_7 + K_7 U_3 \end{aligned} \right\} \quad (4.25)$$

Similarly, interpolated directional derivatives along the unit vectors $\mathbf{s}_6 = -\mathbf{s}_5$ and $\mathbf{s}_8 = -\mathbf{s}_7$

can be written as:

$$\left. \begin{aligned} U_{s6} &= L_{61} U_6 + L_{62} U_8 + K_6 U_4 \\ U_{s8} &= L_{81} U_6 + L_{82} U_8 + K_8 U_4 \end{aligned} \right\} \quad (4.26)$$

Where,

$$\left. \begin{aligned} L_6 &= (L_{61} \quad L_{62}) = (\mathbf{s}_6 - \mathbf{r}_4 K_6)^T R^{-1} \\ L_8 &= (L_{81} \quad L_{82}) = (\mathbf{s}_8 - \mathbf{r}_4 K_8)^T R^{-1} \\ K_6 &= \frac{(\mathbf{r}_{s6} \cdot \mathbf{r}_6)}{(\mathbf{r}_{s6} \cdot \mathbf{r}_4) + (\mathbf{r}_{s6} \cdot \mathbf{r}_6)} \\ K_8 &= \frac{(\mathbf{r}_{s8} \cdot \mathbf{r}_8)}{(\mathbf{r}_{s8} \cdot \mathbf{r}_4) + (\mathbf{r}_{s8} \cdot \mathbf{r}_8)} \end{aligned} \right\} \quad (4.27)$$

Therefore in general, interpolated directional derivatives along the defined directions can be written as:

$$U_{sg} = \sum_{m=3}^8 A_{gm} U_m ; \quad g = 5, 6, 7, 8 \quad (4.28)$$

Where, $A_{gm}, g \in [5, 8]; m = [3, 8]$ for different values of g and m are given as:

$$\begin{array}{cccc}
 A_{53} = K_5 & A_{63} = 0 & A_{73} = K_7 & A_{83} = 0 \\
 A_{54} = 0 & A_{64} = K_6 & A_{74} = 0 & A_{84} = K_8 \\
 A_{55} = L_{51} & A_{65} = 0 & A_{75} = L_{71} & A_{85} = 0 \\
 A_{56} = 0 & A_{66} = L_{61} & A_{76} = 0 & A_{86} = L_{81} \\
 A_{57} = L_{52} & A_{67} = 0 & A_{77} = L_{72} & A_{87} = 0 \\
 A_{58} = 0 & A_{68} = L_{62} & A_{78} = 0 & A_{88} = L_{82}
 \end{array}$$

4.5.1.2 THE UPWIND EQUATION

Using Equation (1.19), the following upwind scheme in 2D is given as:

$$\max(U_{s5}, U_{s6}, 0)^2 + \max(U_{s7}, U_{s8}, 0)^2 = s_{ij}^2 \quad (4.29)$$

Where, s_{ij} is slowness value at the grid point (i, j) where T_{ij} is to be evaluated. Let

$U_{su} \in (U_{s5}, U_{s6})$ and $U_{sv} \in (U_{s7}, U_{s8})$ such that $U_{su} > 0$ and $U_{sv} > 0$ then the upwind

Equation (4.29) reduces to

$$U_{su}^2 + U_{sv}^2 = s_{ij}^2 \quad (4.30)$$

Writing $U_m = a_m T_{ij} + b_m$ and squaring both sides of Equation (4.28), following equation can be written:

$$|U_{sg}|^2 = u_g T_{ij}^2 + 2v_g T_{ij} + w_g \quad (4.31)$$

Where,

$$\left. \begin{array}{l}
 u_g = \sum_{m,n=3}^8 A_{gm} A_{gn} a_m a_n \\
 v_g = \frac{1}{2} \sum_{m,n=3}^8 A_{gm} A_{gn} (a_m b_n + a_n b_m) \\
 w_g = \sum_{m,n=3}^8 A_{gm} A_{gn} b_m b_n
 \end{array} \right\} \quad (4.32)$$

Using Equations (4.31) the quadratic Equation (4.30) can be simplified to:

$$u T_{ij}^2 + 2v T_{ij} + w = 0 \quad (4.33)$$

Where, following parameters have been used:

$$\begin{aligned}
u &= (u_\mu + u_\eta) \\
v &= (v_\mu + v_\eta) \\
w &= w_\mu + w_\eta - s_{ij}^2
\end{aligned} \tag{4.34}$$

If the conditions $U_{su} > 0$ and $U_{sv} > 0$ are not satisfied and assume that we have $U_{su} > 0$ and $U_{sv} < 0$. Under this situation the solution to the upwind Equation (4.29) is given as:

$$T_{ij} = \min \left(\frac{s_{ij} - \sum_{m=3}^8 A_{um} a_m}{\sum_{m=3}^8 A_{um} b_m} \right), \quad u = 5, 6 \tag{4.35}$$

To compute an unbiased solution in a anisotropic grid structure we have selected unit vectors s_5 and s_7 in perfect diagonal directional of a square, either:

$$\left. \begin{aligned}
s_5 &= \frac{\mathbf{i} + \mathbf{j}}{\sqrt{2}} \\
s_7 &= \frac{-\mathbf{i} + \mathbf{j}}{\sqrt{2}}
\end{aligned} \right\} \tag{4.36}$$

Two stencils, one natural which is aligned along coordinate axes and other diagonal as shown in Figure 4.2, are used in the computation of T_{ij} from either Equation (4.33) or (4.35), therefore two solution comes from these. The final solution is obtained giving the proper weight of the grid spacing, to these solutions. The exact computations of the weights are very difficult, therefore application of proportional weight factor is considered. The maximum error from natural stencil is proportional to h and the same from diagonal stencil is $\sqrt{2}h$, therefore if T_a and T_b are two solutions computed from natural and diagonal stencil then final solution T_{ij} is given as:

$$T_{ij} = \frac{\sqrt{2}T_a + T_b}{1 + \sqrt{2}} \tag{4.37}$$

4.5.1.3 UPWIND CONDITION

Solving the quadratic Equation (4.33) results in two solutions. The minimum is rejected because it does not maximize the Equation (4.29). Since the solution has to satisfy the causality relationship and as the value of T is not known in advance, the computed solution must be checked to see if it is higher than the travelttime values of two adjacent neighboring grid points that participate in the solution. If the check is true then the solution is accepted otherwise solution is given by Equation (4.35). When the solution is obtained using Equation (4.37), solution still has to satisfy the causality relationship and hence it must be

checked if it is higher than the traveltime values of neighboring grid points that participate in the solution T_a and T_b .

4.5.2 3D MULTISTENCILS PSEUDOANISOTROPIC FAST MARCHING METHOD

In 3d MPFMM weighted angular interpolation is carried out in 3D followed by the solution of basic upwind equation given in Chapter 4 (Equation 1.19).

4.5.2.1 INTERPOLATION OF DIRECTIONAL DERIVATIVES IN 3D STENCILS

The concept of weighted interpolation of directional derivatives from 2D to 3D can be extended. To simplify the discussion a 3D lattice is shown in Figure 4.3 in which center grid point p_0 is shown to be covered by all its 26 neighboring grid points $P_i, i \in [1, 26]$. Consider a 3D stencil which intersects the 3D lattice at the grid points $p_{11}, p_{12}, p_{19}, p_{20}, p_{21}$ and p_{22} in which $p_0 p_{19}, p_0 p_{21}$ and $p_0 p_{11}$ are assumed to be principal rotated x, y and z axes. Let $\mathbf{r}_1 = (r_{11}, r_{12}, r_{13})^T$, $\mathbf{r}_2 = (r_{21}, r_{22}, r_{23})^T$ and $\mathbf{r}_3 = (r_{31}, r_{32}, r_{33})^T$ be three unit vectors along $p_0 p_{19}, p_0 p_{21}$ and $p_0 p_{11}$ respectively and U_{r_1} , U_{r_2} and U_{r_3} be directional derivatives of traveltime field along vector \mathbf{r}_1 , \mathbf{r}_2 and \mathbf{r}_3 .

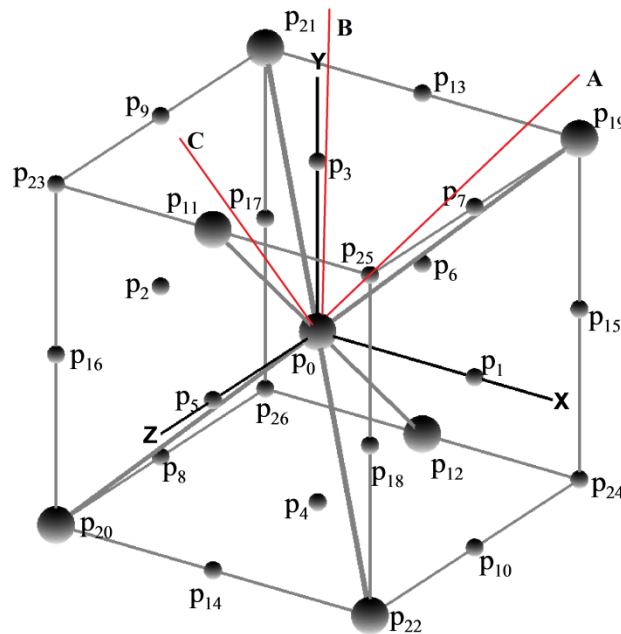


Figure 4.3: Stencil S_w centered at point (x, y, z) that intersects the 3D lattice at the grid points $p_{11}, p_{12}, p_{19}, p_{20}, p_{21}$ and p_{22} . OA, OB and OC are three straight line depicting direction along which interpolation scheme is applied.

Consider further three defined directions: from centered grid point to A, B and C in Figure 4.3 along which interpolation of the derivatives are to be carried out. To perform this let $\mathbf{s}_1 = (s_{11}, s_{12}, s_{13})^T$, $\mathbf{s}_2 = (s_{21}, s_{22}, s_{23})^T$ and $\mathbf{s}_3 = (s_{31}, s_{32}, s_{33})^T$ be three unit vectors along the directions from centered grid point towards A, B and C and U_{s_1} , U_{s_2} and U_{s_3} be three directional derivatives along vectors $\mathbf{s}_1, \mathbf{s}_2$ and \mathbf{s}_3 . It can be seen that when an interpolation is to be carried out in the diagonal direction such as centered grid point to A and B, a maximum of four non-stencil grid points participate in the interpolation such as p_3, p_7, p_{13}, p_{19} points for the direction from centered grid point towards A and p_3, p_9, p_{13}, p_{21} points for the direction from centered grid point towards B. If the line from centered grid to C lies in the plane formed by $p_0 p_3$ and $p_0 p_{11}$ then a maximum of two grid points such as p_3 and p_{11} helps in the interpolation. Therefore it is concluded that a maximum of four grid point will help to construct U_{s_1} , U_{s_2} and U_{s_3} .

Let $\mathbf{a}_{nm} = (a_{nm1}, a_{nm2}, a_{nm3})$; ($n=1,2,3$; $m=1,2,3,4$) be the unit vectors along the point of intersection corresponding to \mathbf{s}_n . Let U_{r_1} , U_{r_2} and U_{r_3} be directional derivatives along \mathbf{r}_1 , \mathbf{r}_2 and \mathbf{r}_3 ; U_{nm1}, U_{nm2} and U_{nm3} the directional derivatives along a_{nm1}, a_{nm2} and a_{nm3} respectively. The directional derivatives along \mathbf{r}_1 , \mathbf{r}_2 and \mathbf{r}_3 can be written in matrix form as:

$$\begin{bmatrix} U_{r_1} \\ U_{r_2} \\ U_{r_3} \end{bmatrix} = \begin{bmatrix} r_{11} & r_{12} & r_{13} \\ r_{21} & r_{22} & r_{23} \\ r_{31} & r_{32} & r_{33} \end{bmatrix} \begin{bmatrix} \dot{T}_x \\ \dot{T}_y \\ \dot{T}_z \end{bmatrix} \quad (4.38)$$

Or,
$$U = R \nabla T(x, y) \quad (4.39)$$

Where,

$$\begin{bmatrix} \dot{T}_x \\ \dot{T}_y \\ \dot{T}_z \end{bmatrix} = \left(\frac{\partial T}{\partial x} \quad \frac{\partial T}{\partial y} \quad \frac{\partial T}{\partial z} \right)^T, \quad U = (U_{r_1}, U_{r_2}, U_{r_3})^T, \quad R = \begin{bmatrix} r_{11} & r_{12} & r_{13} \\ r_{21} & r_{22} & r_{23} \\ r_{31} & r_{32} & r_{33} \end{bmatrix}, \quad \nabla T = (\dot{T}_x, \dot{T}_y, \dot{T}_z)^T.$$

Similar to Equation set (4.16) it is possible to write the directional derivatives along unit vector \mathbf{a}_{nm} as:

$$U_{nm} = \mathbf{r}_{nm} \cdot \nabla T(x, y) + w_{nm}, \quad n=1,2,3; \quad m=1,2,3,4 \quad (4.40)$$

The directional derivatives along unit vectors $\mathbf{s}_1, \mathbf{s}_2$ and \mathbf{s}_3 can be interpolated as:

$$U_{s_n} = \mathbf{r}_n \cdot \nabla T(x, y) + \bar{w}_n, \quad n=1,2,3 \quad (4.41)$$

Where, the interpolated Pseudo-anisotropic adjustment term \bar{w}_n is given as:

$$\bar{w}_n = \sum_{m=1}^4 \frac{G_{nm} w_{nm}}{(s_n \cdot a_{nm})} \quad (4.42)$$

The value of parameter G_{nm} is either 1 or 0 depending upon the availability and unavailability of grid point information along unit vector a_{nm} . Using Equations (4.40) and (4.42), Equation (4.41) can be written as:

$$U_{sn} = \mathbf{r}_n \cdot \nabla T(x, y) + \sum_{m=1}^4 \frac{G_{nm} (U_{nm} - \mathbf{r}_{nm} \cdot \nabla T)}{(s_n \cdot a_{nm})} \quad (4.43)$$

Equation (4.43) can further be written as:

$$U_{sn} = (\mathbf{r}_n - K_{nm} \mathbf{r}_{nm}) \cdot \nabla T(x, y) + \sum_{m=1}^4 K_{nm} U_{nm} \quad (4.44)$$

Where,

$$K_{nm} = \frac{G_{nm}}{(s_n \cdot a_{nm})} \quad (4.45)$$

Consider the multiplication of two vectors in matrix representation as:

$$(\mathbf{r}_n - K_{nm} \mathbf{r}_{nm})^T \cdot \nabla T(x, y) = L_{nm1} U_{r1} + L_{nm2} U_{r2} + L_{nm3} U_{r3} \quad (4.46)$$

In which:

$$\mathbf{L}_{nm} = (L_{nm1} \quad L_{nm2} \quad L_{nm3}) = (\mathbf{r}_n - K_{nm} \mathbf{r}_{nm})^T \mathbf{R}^{-1} \quad (4.47)$$

U_{sn} in Equation (4.44) becomes:

$$U_{sn} = \sum_{i=1}^3 L_{nmi} U_{ri} + \sum_{m=1}^4 K_{nm} U_{nm} \quad (4.48)$$

Equation (4.48) represents the interpolated directional derivatives along the unit vectors s_1 , s_2 and s_3 in terms of linear combination of unit vectors along r_1 , r_2 , r_3 and a_{nm} .

4.5.2.2 THE UPWIND EQUATION

The upwind Equation in Chapter 1 (Equation 1.19) in 3D can be written as:

$$\max(V_{s1}, V_{-s1}, 0)^2 + \max(V_{s2}, V_{-s2}, 0)^2 + \max(V_{s3}, V_{-s3}, 0)^2 = s_{ijk}^2 \quad (4.49)$$

Where s_{ijk} is slowness value at the grid point (i, j, k) where T_{ijk} is to be evaluated. V_{s1}, V_{s2}, V_{s3} , V_{-s1}, V_{-s2} and V_{-s3} are the directional derivatives of travelttime along unit vectors $s_1, s_2, s_3, -s_1, -s_2$ and $-s_3$ respectively. Let $V_{su} \in (V_{s1}, V_{-s1})$, $V_{sv} \in (V_{s2}, V_{-s2})$ and $V_{sw} \in (V_{s3}, V_{-s3})$ such that $V_{su} > 0, V_{sv} > 0$ and $V_{sw} > 0$ then the upwind Equation (4.49) reduces to

$$V_{su}^2 + V_{sv}^2 + V_{sw}^2 = s_{ijk}^2 \quad (4.50)$$

The directional derivatives U_{ri} and U_{tm} in Equation (4.48) can together be written by a common symbol $V_l; l \in [1, 26]$; that describe the directional derivatives along all 26 directions $p_0 p_l; l \in [1, 26]$. Using this new variable Equation (4.48) can be written as:

$$U_{sn} = \sum_{l=1}^{26} B_{nl} V_l; n = 1, 2, 3 \quad (4.51)$$

Where, different values of coefficients B_{nl} are obtained by comparing Equation (4.51) with Equation (4.48). Writing directional derivatives generally as $V_l = a_l T_{ijk} + b_l$ and squaring both sides of Equation (4.51) it is possible to write:

$$|U_{sn}|^2 = u_n T_{ijk}^2 + 2v_n T_{ijk} + w_n \quad (4.52)$$

Where,

$$\left. \begin{aligned} u_n &= \sum_{j,i=1}^{26} B_{nj} B_{ni} a_j a_i \\ v_n &= \frac{1}{2} \sum_{j,i=1}^{26} B_{nj} B_{ni} (a_j b_i + a_i b_j) \\ w_n &= \sum_{j,i=1}^{26} B_{nj} B_{ni} b_j b_i \end{aligned} \right\} \quad (4.53)$$

Using Equation (4.52), the quadratic Equation (4.50) can be simplified to:

$$u T_{ijk}^2 + 2v T_{ijk} + w = 0 \quad (4.54)$$

Where, following parameters have been used:

$$\begin{aligned} u &= (u_1 + u_2 + u_3) \\ v &= (v_1 + v_2 + v_3) \\ w &= w_1 + w_2 + w_3 - s_{ijk}^2 \end{aligned} \quad (4.55)$$

In other conditions the solution of the upwind equation is given by Equation (4.55) where the expression of u, v and w is replaced by:

$$\begin{aligned} u &= (c_1 u_1 + c_2 u_2 + c_3 u_3) \\ v &= (c_1 v_1 + c_2 v_2 + c_3 v_3) \\ w &= c_1 w_1 + c_2 w_2 + c_3 w_3 - s_{ijk}^2 \end{aligned} \quad (4.56)$$

Where, c_1, c_2 and c_3 are coefficients depending upon the values of availability of information from grid point p_{19}, p_{21} and p_{11} .

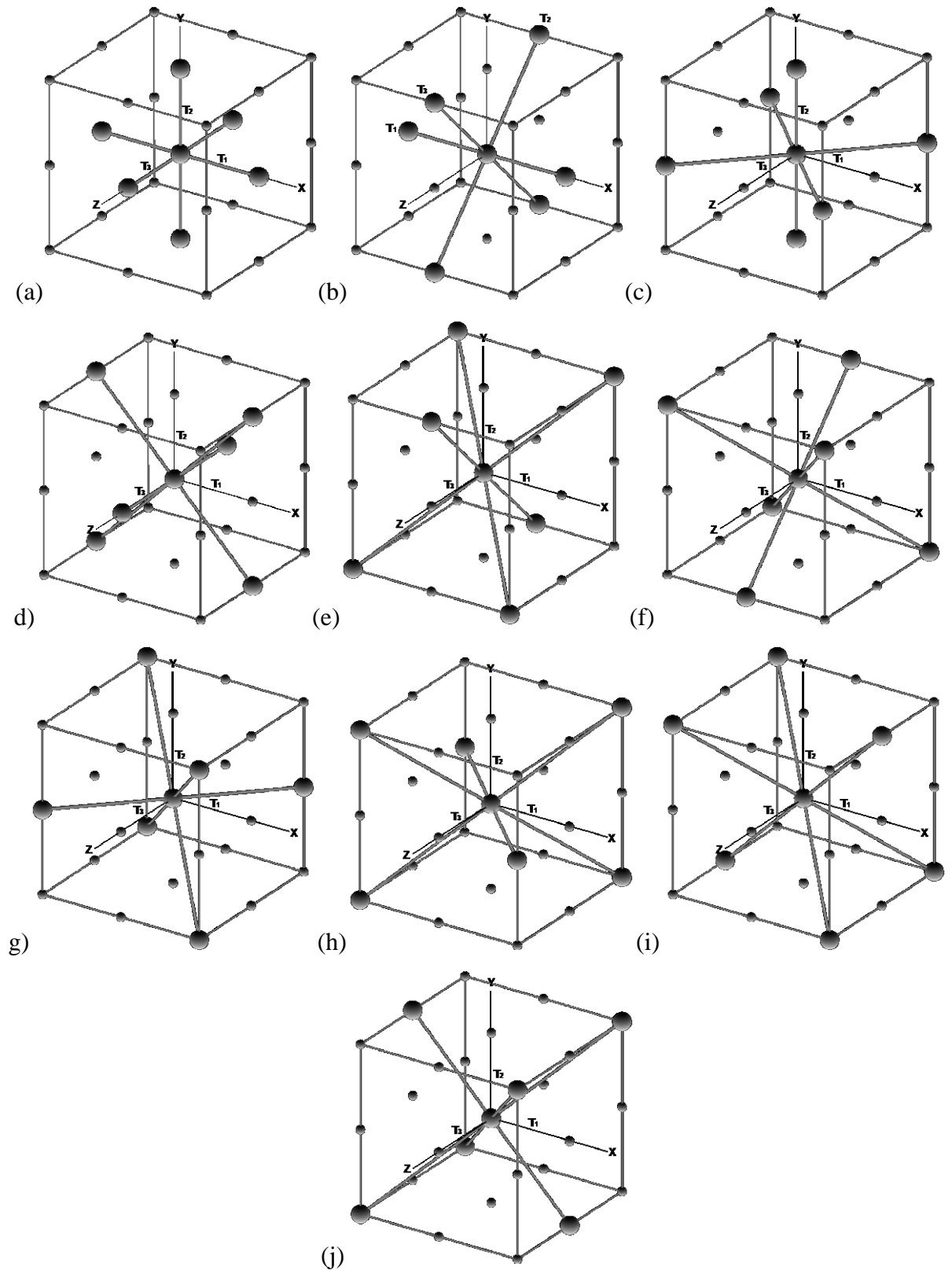


Figure 4.4: The proposed stencils for the 3D Cartesian domain. T_1 , T_2 and T_3 are minimum traveltime along each arm of the stencil. (a) S_1 . (b) S_2 . (c) S_3 . (d) S_4 . (e) S_5 . (f) S_6 . (g) S_7 . (h) S_8 . (i) S_9 . (j) S_{10} .

The solution of the upwind equation in other quadrant of the stencil can be obtained by simply replacing the unit vector that participates in the Expression (4.44) by appropriate

unit vectors in the quadrants. The final solution of the quadratic Equation (4.54) is taken by applying upwind condition.

A total of ten stencils S_w ; $w \in [1,10]$ are used to compute the traveltime T_{ijk} . All ten stencils are shown in Figure 4.4. Ten symmetric sets of unit vectors given in Table 4.1 have been proposed, where each set of vector corresponds to a particular stencil. There may be a maximum of ten possible solutions of traveltime from these 10 stencils. The selection of final solution is subjected to the upwind condition described in §4.5.2.30. Let T_w , $w=1,2,\dots,10$ represents the solution from ten stencils S_w , then to respect more weight to the solution obtained from stencil having lower grid spacing compared to the solution obtained from stencil having higher grid spacing, an weighted solution can be given by:

$$T_{ijk} = \frac{\sum_{w=1}^{10} \left(\frac{T_w}{C_w} \right)}{\sum_{w=1}^{10} \frac{1}{C_w}}$$

Where, $C_1 = 1$, $C_2 = C_3 = C_4 = \sqrt{2}$, $C_j = \sqrt{3}$; $j = 5, 6, \dots, 10$

However, this type of solution is also subjected to the upwind condition described below.

Table 4.1: Proposed Unit Vectors

Stencil	First unit vector	Second unit vector	Third unit vector
S_1	i	j	k
S_2	i	$(j+k)/\sqrt{2}$	$(-j+k)/\sqrt{2}$
S_3	j	$(-i+k)/\sqrt{2}$	$(i+k)/\sqrt{2}$
S_4	k	$(i+j)/\sqrt{2}$	$(-i+j)/\sqrt{2}$
S_5	$(-j+k)/\sqrt{2}$	$(\sqrt{2}i+j+k)/2$	$(-\sqrt{2}i+j+k)/2$
S_6	$(j+k)/\sqrt{2}$	$(-\sqrt{2}i-j+k)/2$	$(\sqrt{2}i-j+k)/2$
S_7	$(i+k)/\sqrt{2}$	$(-i+\sqrt{2}j+k)/2$	$(-i-\sqrt{2}j+k)/2$
S_8	$(-i+k)/\sqrt{2}$	$(i-\sqrt{2}j+k)/2$	$(i+\sqrt{2}j+k)/2$
S_9	$(i+j)/\sqrt{2}$	$(-i+j+\sqrt{2}k)/2$	$(i-j+\sqrt{2}k)/2$
S_{10}	$(-i+j)/\sqrt{2}$	$(-i-j+\sqrt{2}k)/2$	$(i+j+\sqrt{2}k)/2$

4.5.2.3 UPWIND CONDITION

Solving the quadratic Equation (4.54) results in two solution solutions. The minimum solution is rejected because it does not maximize the upwind equation (4.49). It is required to make sure that the traveltime solution from each stencil is higher than the traveltimes T_1, T_2 and T_3 of the adjacent three grid points that participate in the solution. If this check is true then the solution is accepted. Otherwise, grid point with odd traveltime value contributing in the solution to make it lesser is rejected by making its coefficient zero and the solution is obtained using the same equation. There will be ten solutions from ten stencils, therefore there will be a maximum of 10 solutions for traveltime solution. Either least solution is accepted or to give the proper respect of grid spacing the weighted average solution is determined as described in §4.5.2.2.

4.6 COMPUTATIONAL COMPLEXITIES

FMM computes traveltime always in the neighborhood of narrow band which means the computational region always includes both known grid points and unknown grid points, which in terms means that the gradient term in any quadrant of any stencils may not be defined completely by the solution procedure. Consider the gradient of T defined by directional derivatives along $\mathbf{r}_1, \mathbf{r}_2$ and \mathbf{r}_3 which are not mutually perpendicular to each other. Consider the situation when \mathbf{r}_1 a directional derivative is unknown. An ideal gradient must then lies in the plane formed by \mathbf{r}_2 and \mathbf{r}_3 . By making directional derivative along \mathbf{r}_1 to be zero, the Equation (4.39) does not give the true gradient relationship, rather it will give gradient that will lie in the direction having some offset depending upon intercept angle between $\mathbf{r}_1, \mathbf{r}_2$ and \mathbf{r}_3 . To obtain the true gradient in plane given by \mathbf{r}_2 and \mathbf{r}_3 , it is essential to consider zero directional derivatives perpendicular to \mathbf{r}_2 and \mathbf{r}_3 and the gradient is required to be represent in terms of \mathbf{r}_2 and \mathbf{r}_3 only.

4.7 NUMERICAL EXPERIMENTS

In order to study the accuracy and effect of use of multiple stencils in the solution of the proposed method in both 2D and 3D Cartesian domains, several numerical experiments have been conducted. The results of the experiments are compared with the results of FMM and MSFM method (MSFMM).

4.7.1 ACCURACY

The exact analytical solution of the eikonal equation for a particular slowness model is assumed to be gold standard. Since the exact analytical solution is hard to find at least for a complex slowness models, I began a continuous and differentiable traveltime functions $T_a(x, y)$ and then computed the traveltime $T(x, y)$ by each method using the slowness derived from the eikonal equation:

$$s_a = |\nabla T_a| \quad (4.57)$$

The computed traveltime $T(x, y)$ is then compared with analytical function T_a using different error norms. This kind of tests have been described by Danielsson and Lin (2003), and Hassouna and Farag (2007). The selected different form of functions $T_a(x, y)$, $a \in [1, 6]$ have been listed in Table 4.2.

Table 4.2: Traveltime Functions for both 2D and 3D Cartesian Domains

T_a	Closed Form Traveltime Functions
T_1	$d = \sqrt{(x-x_0)^2 + (y-y_0)^2}$
T_2	$\frac{(x-x_0)^2}{20} + \frac{(y-y_0)^2}{40}$
T_3	$2d + \frac{25}{4\pi} \left\{ \cos\left(\frac{4\pi d}{25}\right) - 1 \right\}$
T_4	$d \left[1 + \frac{2}{3} \sin^2 \left\{ 2 \tan^{-1} \left(\frac{y-y_0}{x-x_0} \right) \right\} \right]$
T_5	$\sqrt{(x-x_0)^2 + (y-y_0)^2 + (z-z_0)^2}$
T_6	$\frac{(x-x_0)^2}{20} + \frac{(y-y_0)^2}{40} + \frac{(z-z_0)^2}{60}$

The contours of these traveltime functions are shown in Figure 4.5. Three types of error norms which were considered are given as (Hassouna and Farag, 2007):

$$\left. \begin{aligned} L_1 &= \frac{1}{n} \sum_{i=1}^n |T - T_a| \\ L_2 &= \frac{1}{n} \sum_{i=1}^n |T - T_a|^2 \\ L_\infty &= \max |T - T_a| \end{aligned} \right\} \quad (4.58)$$

Using the above ideology of test the following experiments compare the accuracy of the proposed MPFMM with FMM and MSFM method.

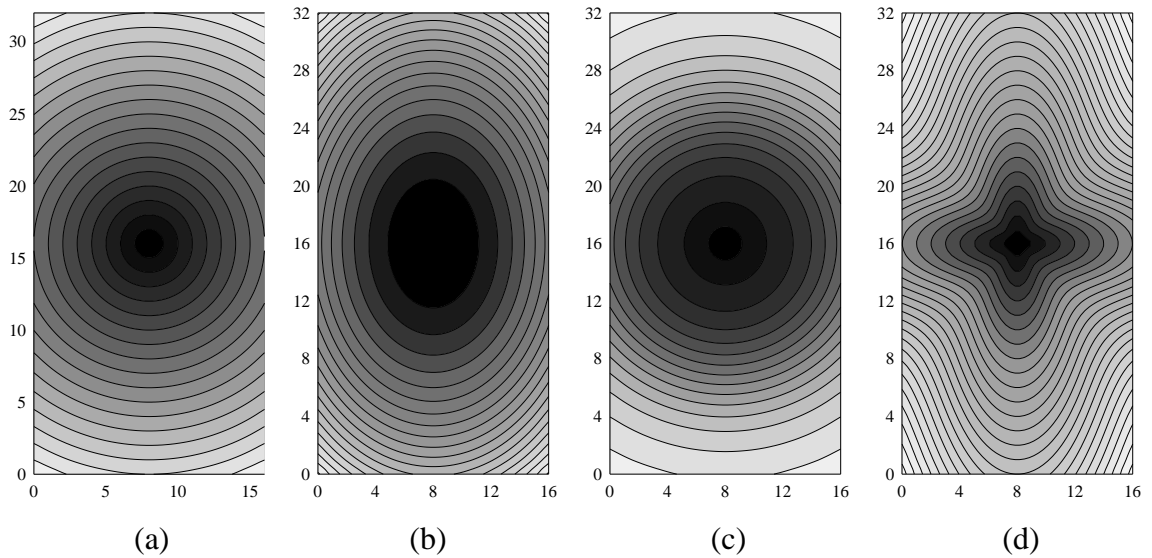


Figure 4.5: Contours of T_1 , (a); T_2 , (b); T_3 , (c) and T_4 , (d).

4.7.1.1 EXPERIMENT 1

This experiment compares the accuracy of the proposed method MPFMM against FMM and MSFMM in 2D space under traveltime function, T_1 . The test grid is isotropic and size of the test grid is 81×81 points, with $\Delta x = \Delta y = 0.5$. The traveltime function corresponds to a moving front from the point (x_0, y_0) with unit slowness. The computed traveltime in this case correspond to Euclidean distance field, which is of interest in many scientific applications. The test was performed two times from two source points: one at the center of the grid to test the high-curvature solution and other at the corner of the grid to test the smooth solution. To measure the numerical error L_1, L_2 and L_∞ norms described by Equation (4.58) were employed. The numerical errors of this experiment are listed in Table 4.3. Figure 4.6(a) and 4.6(b) shows the contours of error curves when solving for T_1 using FMM and MPFMM, respectively. It is seen that the errors are small along the axial directions and increase rapidly in the region around 45 degree when using FMM as shown in Figure 4.6(a). However, when using proposed method, the errors are small along the axial as well as diagonal directions as shown in Figure 4.6(b).

It is clear from the Table 4.3 that the improvement of the solution quality provided by proposed method against FMM is much better; however improvement against MSFM method is very minor. The reason is obvious as the grid type used is isotropic; therefore,

effect of interpolation is almost negligible but due to higher numbers of stencil in the proposed method it gives better results compared to MSFMM.

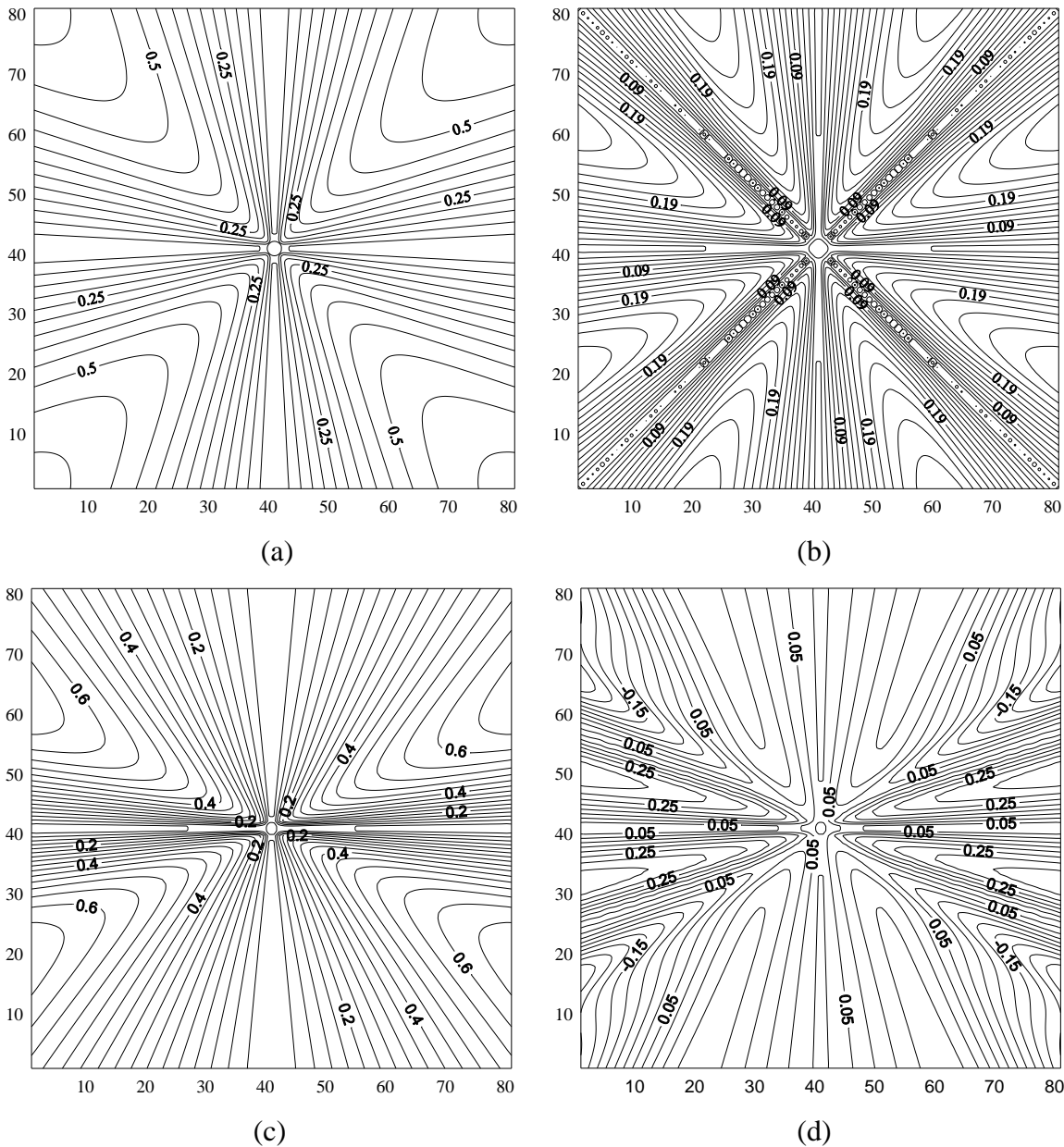


Figure 4.6: Contours of error norm L_1 computed from FMM (a,c) and MPFMM (b,d) using grids of size 81×81 and isotropic spacing 0.5×0.5 (a,b) and anisotropic spacing 0.4×0.8 (c,d). The source position in all the cases is at the center of the grid structure.

To test the effect of interpolation used in the proposed method, the same experiment was performed two times by changing the source positions similar to above in a grid of the same size but with anisotropic spacing of 0.4×0.8 . The results are shown in Table 4.4. It is clear from the table that proposed method gives much better results compared to that provided by FMM and MSFMM. It is seen that because of lack of proper care grid spacing and biased evaluation of gradient, MSFMM fails to improve the results provided by basic

FMM in a homogeneous medium with highly anisotropic grid structure. The contours of error curves obtained from the FMM and the proposed method are shown in Figure 4.6(c) and 4.6(d), respectively. It is clear from the figures that the proposed method gives better results compared to that provided by FMM. It is to be noted that higher errors (Figure 4.6(c)) in the solutions provided by FMM unlike previous tests under this experiment are not aligned along diagonal directions rather the alignment of the errors makes an offset against diagonal due to different grid spacing in the grid type used.

Table 4.3: Error Norms of the Computed T_1 from Different Source Points in an Isotropic Grid of Size 81×81 and Grid Spacing 0.5×0.5

Time T	T_1					
Source point	41×41			1×1		
Method/Error	L_1	L_2	L_∞	L_1	L_2	L_∞
FMM	0.351	0.154	0.621	0.415	0.219	0.735
MSFMM	0.151	0.029	0.286	0.186	0.045	0.362
MPFMM	0.149	0.029	0.286	0.169	0.040	0.359

Table 4.4: Error Norms of the Computed T_1 from Different Source Points in an anisotropic Grid of Size 81×81 and Grid Spacing 0.4×0.8

Time T	T_1					
Source point	41×41			1×1		
Method/Error	L_1	L_2	L_∞	L_1	L_2	L_∞
FMM	0.354	0.162	0.667	0.417	0.230	0.799
MSFMM	1.055	2.336	4.624	2.408	13.322	11.699
MPFMM	0.127	0.023	0.360	0.174	0.043	0.477

4.7.1.2 EXPERIMENT 2

This experiment compares the accuracy of the proposed MPFMM against FMM and MSFMM in 2D space under travelttime field, T_2 . The field is inhomogeneous and its contours show angular asymmetric (Figure 4.5(b)). The slowness of this travelttime field is also inhomogeneous and angular asymmetric, which is given as (Equation 4.57):

$$s(x, y) = \sqrt{\frac{(x - x_0)^2}{10^2} + \frac{(y - y_0)^2}{20^2}}$$

Two tests, one by considering the source at the center and second by considering the source at the corner of the grid, were performed using all three methods; either, FMM, MSFMM and the proposed one, in an isotropic grid of size 81×81 and grid spacing 0.5×0.5 . The results of these tests are given in Table 4.5. It is clear from the table that the accuracy provided by

proposed method is much better than that provided by FMM. The improvement of accuracy against MSFMM is minor because of isotropic grid spacing and symmetry of contours of T_2 as shown in Figure 4.5(b). When the same tests were performed using same grid size but with anisotropic spacing 0.4×0.8 , the improvement in the solution quality provided by proposed method is found to be much better compared to both FMM and MSFMM as shown in Table 4.6. The higher improvement of results against MSFMM in this case is mainly because of the effect of interpolation scheme used in the proposed method.

Table 4.5: Error Norms of the Computed T_2 from Different Source Points in an Isotropic Grid of Size 81×81 and Grid Spacing 0.5×0.5

Time T	T_2					
Source point	41×41			1×1		
Method/Error	L_1	L_2	L_∞	L_1	L_2	L_∞
FMM	0.108	0.015	0.240	0.223	0.064	0.486
MSFMM	0.042	0.003	0.125	0.110	0.016	0.282
MPFMM	0.031	0.002	0.103	0.091	0.011	0.222

Table 4.6: Error Norms of the Computed T_2 from Different Source Points in an anisotropic Grid of Size 81×81 and Grid Spacing 0.4×0.8

Time T	T_2					
Source point	41×41			1×1		
Method/Error	L_1	L_2	L_∞	L_1	L_2	L_∞
FMM	0.232	0.063	0.458	0.444	0.234	0.888
MSFMM	0.136	0.061	1.268	0.368	0.536	4.062
MPFMM	0.081	0.013	0.469	0.363	0.331	2.298

4.7.1.3 EXPERIMENT 3

This experiment compares the accuracy of the proposed method MPFMM against FMM and MSFMM in 2D space under traveltime function, T_3 . The slowness of this traveltime field is radially inhomogeneous which is given as (Equation 4.57):

$$s(x, y) = 2 - \sin \left\{ \frac{4\pi}{25} \left(\sqrt{(x - x_0)^2 + (y - y_0)^2} \right) \right\} \quad (4.59)$$

Similar to previous experiments, two tests were performed: one by considering the source at the center and other by considering it in the corner, in an isotropic grid of size 71×71 and grid spacing 0.5×0.5 using the proposed method, MSFMM and FMM and the results of these tests are summarized in Table 4.7. It is clear from the table that MPFMM gives better results compared to FMM and MSFMM. The improvement of MPFMM against MSFMM is

minor because of use of isotropic grid structure where the interpolation scheme used in MPFMM affects very little. However, when the same tests were repeated in a grid of same size but with different anisotropic spacing 0.4×0.8 the improvements in accuracy provided by the proposed method is found to be much higher than the MSFM method. The results of these two tests are given in Table 4.8. It is clear that MSFMM fails again in these tests as it do not improves the results of basic FMM but the overall better results can be seen by the proposed method.

Table 4.7: Error Norms of the Computed T_3 from Different Source Points in an Isotropic Grid of Size 71×71 and Grid Spacing 0.5×0.5

Time T	T_3					
Source point	36×36			1×1		
Method/Error	L_1	L_2	L_∞	L_1	L_2	L_∞
FMM	0.445	0.258	0.865	0.554	0.393	0.957
MSFMM	0.162	0.036	0.358	0.264	0.124	1.072
MPFMM	0.155	0.021	0.342	0.211	0.061	0.613

Table 4.8: Error Norms of the Computed T_3 from Different Source Points in an anisotropic Grid of Size 71×71 and Grid Spacing 0.4×0.8

Time T	T_3					
Source point	36×36			1×1		
Method/Error	L_1	L_2	L_∞	L_1	L_2	L_∞
FMM	0.497	0.329	1.099	0.592	0.463	1.496
MSFMM	0.930	1.269	2.648	1.738	4.244	4.034
MPFMM	0.386	0.252	1.467	0.899	1.210	2.292

4.7.1.4 EXPERIMENT 4

Under this experiments, the proposed method is tested against FMM and MSFMM using a slightly more complex travelttime field, T_4 . The slowness of this field is given as (Equation 4.57):

$$s(x, y) = \sqrt{\left[\frac{\sigma_1(x-x_0)}{d} - \frac{\sigma_2\sigma_3}{(x-x_0)} \right]^2 + \left[\frac{\sigma_1(y-y_0)}{d} + \frac{\sigma_2}{(x-x_0)} \right]^2} \quad (4.60)$$

Where,

$$\left. \begin{aligned}
\sigma_2 &= \frac{4d \sin(4 \tan^{-1} \sigma_3)}{3(1 + \sigma_3^2)} \\
\sigma_3 &= \frac{(y - y_0)}{(x - x_0)} \\
d &= \sqrt{(x - x_0)^2 + (y - y_0)^2}
\end{aligned} \right\} \quad (4.61)$$

Two tests were performed similar to previous experiments where the source is considered at the center and then at the corner in a different grid of size 51×51 and spacing 0.4×0.4 . The results of these tests are given in Table 4.9. It is clear from the table that improvement of accuracy by MSFMM is very little over the results provided by FMM as opposed to our proposed method which shows a much better improvements in accuracy over that of FMM. These two tests were again repeated using the same grid size but with different grid spacing 0.4×0.6 and the results are presented in Table 4.10. It is noted again that the all the error norms given by the proposed method show significant improvement over both the FMM and MSFMM.

Table 4.9: Error Norms of the Computed T_4 from Different Source Points in an Isotropic Grid of Size 51×51 and Grid Spacing 0.4×0.4

Time T	T_4					
	26×26			1×1		
Source point						
Method/Error	L_1	L_2	L_∞	L_1	L_2	L_∞
FMM	4.816	28.398	10.000	7.058	86.348	20.000
MSFMM	4.753	27.663	9.777	7.065	86.424	18.003
MPFMM	3.179	18.570	6.667	4.707	57.599	16.000

Table 4.10: Error Norms of the Computed T_1 from Different Source Points in an anisotropic Grid of Size 51×51 and Grid Spacing 0.4×0.6

Time T	T_4					
	26×26			1×1		
Source point						
Method/Error	L_1	L_2	L_∞	L_1	L_2	L_∞
FMM	7.604	67.611	10.684	5.443	63.766	20.000
MSFMM	7.340	62.710	10.399	5.417	63.839	18.656
MPFMM	4.953	42.887	6.933	3.608	42.551	16.010

4.7.1.5 EXPERIMENT 5

This experiment compares the accuracy of the proposed MPFMM against FMM and MSFMM in 3D space under traveltime function, T_5 which has unit slowness. The size of the test grid is $41 \times 41 \times 41$ with isotropic grid spacing $0.5 \times 0.5 \times 0.5$. Two tests were performed by considering a source at the center and at the corner of the grid to test the curvature and the smooth solutions respectively. The error norms L_1 , L_2 and L_∞ were computed in these tests and are summarized in Table 4.11. It is clear from the table that the proposed method in both the source positions provides better results compared to MSFMM which in turn improves FMM to some degree. A cross section of the contours of computed T_5 by FMM and MPFMM is given in Figure 4.7. It is to be noted that the curvature provided by MPFMM is better than that given by FMM.

To make a comprehensive test of the methods, the two tests of this experiment is repeated again in a grid of same size but with anisotropic spacing $0.4 \times 0.8 \times 0.6$. The results of these tests are given in Table 4.12. It can be noted from the table that similar to the experiments in the case of 2D in §4.7.1.1, the MSFMM fail to improve the accuracy provided by the basic FMM; however the proposed method because of use of symmetric vectors in the scheme of interpolation of directional derivatives and because of proper care of grid spacing into the solution, provide much better results against basic FMM.

Table 4.11: Error Norms of the Computed T_5 from Different Source Points in an Isotropic Grid of Size $41 \times 41 \times 41$ and Grid Spacing $0.5 \times 0.5 \times 0.5$

Time T	T_5					
Source point	$21 \times 21 \times 21$			$1 \times 1 \times 1$		
Method/Error	L_1	L_2	L_∞	L_1	L_2	L_∞
FMM	0.469	0.250	0.824	0.469	0.250	0.824
MSFMM	0.233	0.062	0.421	0.233	0.063	0.421
MPFMM	0.166	0.034	0.333	0.166	3.441	0.333

Table 4.12: Error Norms of the Computed T_5 from Different Source Points in an Isotropic Grid of Size $41 \times 41 \times 41$ and Grid Spacing $0.4 \times 0.8 \times 0.6$

Time T	T_5					
Source point	$21 \times 21 \times 21$			$1 \times 1 \times 1$		
Method/Error	L_1	L_2	L_∞	L_1	L_2	L_∞
FMM	0.609	0.413	1.002	0.719	0.583	1.181
MSFMM	0.880	1.502	4.494	1.874	6.959	9.299
MPFMM	0.253	0.071	0.457	0.263	0.083	0.547

4.7.1.6 EXPERIMENT 6

This experiment were conducted to tests the proposed method against FMM and MSFMM in a inhomogeneous 3D medium of travelttime field T_6 . The slowness of this field is given by (Equation 4.57):

$$s(x, y, z) = \sqrt{\frac{(x-x_0)^2}{10^2} + \frac{(y-y_0)^2}{20^2} + \frac{(z-z_0)^2}{30^2}} \quad (4.62)$$

The size of the test grid was $51 \times 51 \times 31$ and grid spacing was $0.5 \times 0.5 \times 0.5$. Two tests similar to previous experiments were performed here also from two source position: one at the center of the grid and other at the corner of the grid. All the three error norms were computed under these tests using the FMM, MSFMM and the proposed method MPFMM. The results are summarized in Table 4.13. It is clear from the table that the results provided by the proposed method are much better against the FMM and MSFMM. It is to be noted that the improvement in accuracy by the proposed method is much higher in this case. The higher improvement of results is due to proper care of grid spacing in the MPFMM. These two tests were again repeated in the grid of same size but with different spacing $0.4 \times 0.5 \times 0.6$. The results of this experiment are provided in Table 4.14. It is obvious from the table that the accuracy provided by the proposed method is again much better than the same provided by FMM and MSFMM.

Table 4.13: Error Norms of the Computed T_6 from Different Source Points in an Isotropic Grid of Size $51 \times 51 \times 31$ and Grid Spacing $0.5 \times 0.5 \times 0.5$

Time T	T_6					
	$26 \times 26 \times 16$			$7 \times 7 \times 7$		
Source point						
Method/Error	L_1	L_2	L_∞	L_1	L_2	L_∞
FMM	0.115	0.016	0.258	0.237	0.068	0.522
MSFMM	0.047	0.003	0.157	0.133	0.023	0.351
MPFMM	0.021	0.001	0.079	0.060	0.007	0.320

Table 4.14: Error Norms of the Computed T_6 from Different Source Points in an anisotropic Grid of Size $51 \times 51 \times 31$ and Grid Spacing $0.4 \times 0.5 \times 0.6$

Time T	T_6					
	$26 \times 26 \times 16$			$7 \times 7 \times 7$		
Source point						
Method/Error	L_1	L_2	L_∞	L_1	L_2	L_∞
FMM	0.098	0.011	0.214	0.199	0.047	0.434
MSFMM	0.050	0.003	0.144	0.127	0.021	0.340
MPFMM	0.020	0.001	0.075	0.060	0.006	0.256

4.7.2 EFFECTS OF MULTISTENCILS IN ACCURACY

To study the effects of multistencils considered in the proposed method MPFMM, the 3D method were tested under travelttime field T_1 using different combination of stencils in a same grid structure. A grid of size $51 \times 51 \times 31$ with spacing $0.4 \times 0.8 \times 0.6$ was considered and at first test was performed using natural stencil (S_1) and the results were noticed, after which second test were performed using combine first and second stencils, third test by combine first, second and third stencil and continuing in this way the test using 10 stencils were performed. The results of all these tests under this experiment are given in Table 4.15. It is clear from the table that with gradual increase in the number of stencils in the proposed method the results becomes better and better.

Table 4.15: Error Norms of the Computed T_1 for different set of stencils incorporated in MSFM and MPFMM

Method Stencil (S_m)/Error	3D MPFMM		
	L_1	L_2	L_∞
$m = 1$	0.609	0.413	1.002
$m = 1, 2$	0.452	0.229	0.770
$m = 1, 2, 3$	0.412	0.191	0.726
$m = 1, 2, 3, 4$	0.337	0.127	0.545
$m = 1, 2, \dots, 5$	0.304	0.103	0.545
$m = 1, 2, \dots, 6$	0.275	0.084	0.476
$m = 1, 2, \dots, 7$	0.269	0.080	0.475
$m = 1, 2, \dots, 8$	0.264	0.077	0.466
$m = 1, 2, \dots, 9$	0.258	0.074	0.466
$m = 1, 2, \dots, 10$	0.253	0.071	0.457

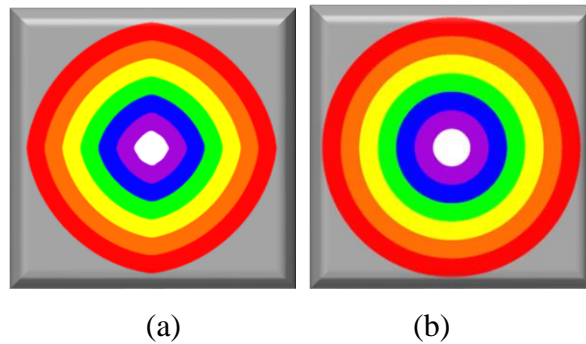


Figure 4.7: Cross sections in the travelttime field of a 3D unit speed wave that propagate from the center of a coarse grid of size $81 \times 81 \times 25$ and spacing $0.4 \times 0.8 \times 0.5$ using (a) FMM and (b) the proposed MPFMM. It is seen that the proposed MPFMM provides better high-curvature solution that the FMM.

4.8 CONCLUSIONS

This Chapter introduces a method called as Multistencil Pseudoanisotropic Fast Marching Method (MPFMM) which is a highly accurate version of isotropic FMM for solving the eikonal equation in both 2D and 3D Cartesian domains. The MPFMM solves the eikonal equation at each grid points that covers the entire nearest neighbours of the point and then picks the solution that satisfies the upwind condition. To invoke the information of the nearest neighbours into the solution, the method interpolates the available the directional derivatives along the defined symmetric directions and then solves the upwind equation respecting the grid spacing. Since the method utilizes symmetrically defined stencils to solve the eikonal equation, the obtained solutions always hold directional symmetry regardless of the degree of grid anisotropy. To maintain the stencil-symmetry versus computation symmetry, the method uses a maximum of 10 stencils to cover 26-neighbours of a single grid point in 3D space whereas in 2D space it uses 2 stencils to cover 8-neighbours of a single grid point.

The accuracy of the proposed method has been tested against FMM and MSFM method by several numerical experiments in 2D and 3D using isotropic and anisotropic grid structures. In all cases, it has been found that the proposed MPFMM gives much better results than FMM and MSFM method.





SEISMIC TOMOGRAPHY OF NATURAL LAYERED EARTH: MULTIPARAMETER INVERSION

5.1 INTRODUCTION

Since the birth of modern seismic tomography by Keiiti Aki in 1976 (Thurber, 2003), the problems of determining the velocity structures of model earths for a given set of hypocenters have long been tackled by my authors (Meier et al., 2004; Hazler et al., 2001). With the advancement of solid earth geophysics, the requirements of precise model of earth structures become very common. The solution to any tomographic approaches become more precise when the velocity and hypocenters both are considered to be variables in the same tomographic problem and up-gradation is simultaneously carried out in the associated inversion process. This is because in majority of problem hypocenters of earthquakes are computed using horizontal layered model of earth in which velocity of each layer is suitably defined and therefore, with the change of velocity it becomes reasonable to change the hypocenters to get an overall precise model of the earth (Tian and Chen, 2006; Mao and Suhadolc, 1992).

The definition of horizontal layer model of earth has solved many of the tomographic problems at smaller scale where the fluctuation of layers can be neglected. At large scale study both the curvature of earth as well as fluctuation of layers play a significant role in wave propagation. Although the curvature of earth can be handled in tomography by solving it in spherical domain rather than Cartesian but the solution of tomographic inversion in spherical domain is more complicated compared to the same in Cartesian. Further, the problem of natural variation of layers in three dimensions remains in the same order as in Cartesian.

At its core it becomes essential to define natural layered earth model where boundary (interfaces) of each layers have variation in three dimensions, and then to consider the parameters associated with 3D variation of layers in the formulation of tomography.

This chapter introduces a method of tomographic inversion to simultaneously invert P and S phases to obtain body-wave velocities, hypocenters with origin times and interface or

layer parameters in a naturally defined layered earth model. As it is associated with inversion of more than three types of parameters, so it may be called as Multiparameter Inversion. Damped Least Square (DLS) method has been considered as a tool of inversion to compute model parameters. The gradient path search algorithm introduced in Chapter 2, to solve the forward problem is discussed in §5.8. The joint working of spiral path search method and gradient path search method is also discussed at the end of this Chapter.

5.2 MODEL CONSIDERATION

Consider a layered earth model in which layers may have 3D characteristics under the following constraints:

- 1) Different layers may have different velocities for p-waves and s-waves but within a layers velocity remains constant both for P-wave and S-wave.
- 2) The surfaces bounding the layers are continuous and differentiable at least up to second degree.
- 3) The two adjacent surfaces bounding the layers may come very close but never touch each other.

A typical schematic simplified form of model is shown in Figure 5.1, where $1, 2, \dots, q, \dots, N_L$ on the model are layer numbers and the same outside the model are number of surfaces of discontinuity, with N_L being the total number of layers or the surfaces and $q = 1, 2, \dots, N_L$.

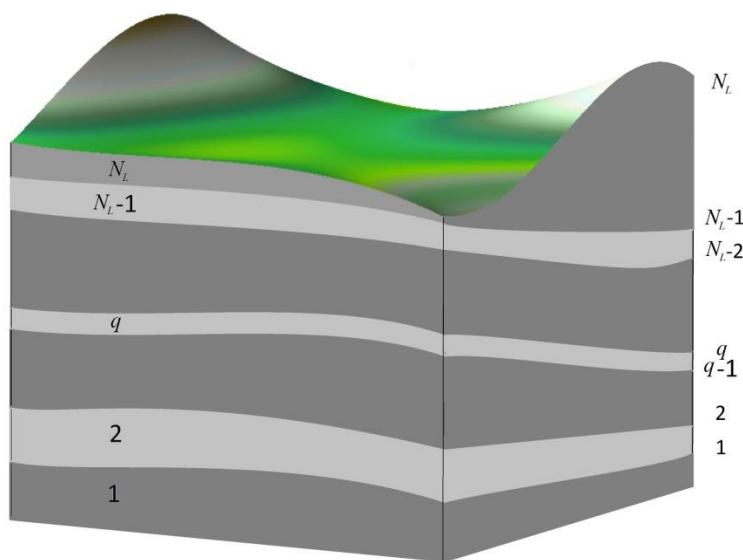


Figure 5.1: A schematic 3D layered structural model where q indicate layer number as well as upper discontinuity-surface bounding the same layer. N_L is the total number of layers considered in the model.

The importance of the above definition of model, as shown in Figure 5.1 in its simplified form, is worthwhile as it is more close to the real earth. When the layers are straight and horizontal, the assumption 1 gives a stratified earth model in which P-wave and S-wave velocities are constants. Such stratified model earth cannot be used to precisely define a large subsurface structure of the earth due to the spherical nature of real earth and curved layers of the subsurface structure. Such problem can be removed by considering the model in spherical domain rather than Cartesian domain, but defining minor variation of layer geometry in spherical domain is often difficult compared to that in Cartesian domain. Although proposed definition of model does not put any restriction to use shape of layers having three or more order of variation under different situation, however only bicubic interfaces have been considered in the present work to define the interfaces and layers. A definition of more precise model which is close to the actual earth is possible when the lateral variation of velocity is considered but that is beyond the scope of present study and has been considered using a different method in Chapter 6.

The assumption 2 is essential for smooth variation of discontinuity between adjacent layers. The assumption 3 is very interesting as it says in other words that layers can be as thin as one can imagine but two layers cannot cross each other. In a mathematical sense a layer can be vanished by considering it ultrathin. Such definition is very useful to define a geological scenario as shown in Figure 5.2. In Figure 5.2, three layers are shown in which the left portion of middle thin bed in Figure 5.2(a) is removed to achieve realistic two bed structure in the left portion as shown in Figure 5.2(b).

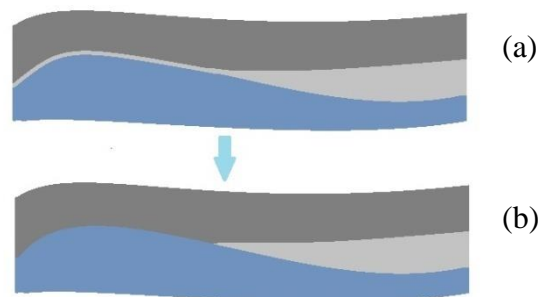


Figure 5.2: A special configuration of three adjacent layers in the model in Figure 5.1 in which the left side of middle layer of upper figure is very thin and can be approximated to a realistic situation shown in lower figure, where middle layer have sharp end.

5.3 REPRESENTATION OF MODEL VECTOR AND DATA VECTOR

The discontinuity-surfaces (interfaces) in Figure 5.1 can be defined by a B-cubic spline interpolation function or simply a bicubic polynomial interpolation function as given by Prenter (1975). These functions can be represented in general as:

$$z_q = \zeta_q(\mathbb{C}_q, x, y) \quad (5.1)$$

With, $g_{q,\mathbb{N}} \in \mathbb{C}_q$ and $\mathbb{N} = 0, 1, 2, \dots$

In Equation (5.1), z_q represent z coordinate of the q^{th} surface corresponding to coordinates x , y and \mathbb{C}_q is a set of coefficients, $g_{q,\mathbb{N}}$ coefficients which define the characteristic of q^{th} surface function, ζ_q is function which must be differentiable upto second degree as required by assumption 2. One such function is given as (Lekien and Marsden, 2005):

$$z_q = \sum_{i,j=0}^3 g_{q,\mathbb{N}(i,j)} x^i y^j \quad (5.2)$$

The function given in Equation 5.2 is defined on 16 nodes as shown in Figure 5.3(a), therefore the maximum value of \mathbb{N} is 16. The 16 $g_{q,\mathbb{N}}$ unknown coefficients can be computed in 16 known value of z on 16 nodes. A typical surface described by Equation (5.2) is shown in Figure 5.3(b). A detailed description on polynomial interpolation can be found in Lekienand Marsden (2005) and Prenter (1975).

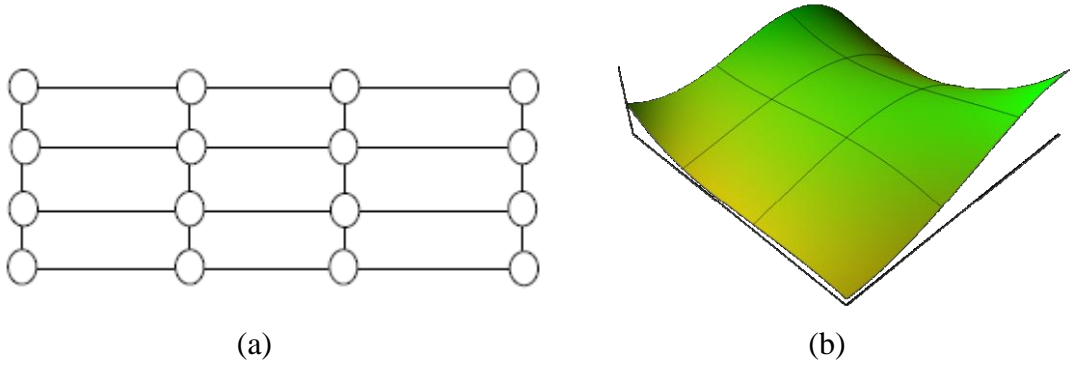


Figure 5.3: Schematic diagrams showing 16 nodes of a bicubic Surface (a) and a typical bicubic surface (b) given by 16 nodes.

The surface coefficients are termed as layer parameters as these define the interfaces that provide shape to the layers. These parameters serve as the one type of model parameters of the present inverse problem and can altogether be represented by model vector, \mathbf{m}_1 as:

$$\mathbf{m}_1 = \left(g_{11}, g_{12}, g_{13}, \dots, g_{1N_{LP}}, g_{21}, g_{22}, g_{23}, \dots, g_{2N_{LP}}, \dots, g_{3N_{LP}}, \dots, g_{N_L 1}, g_{N_L 2}, g_{N_L 3}, \dots, g_{N_L N_{LP}} \right)^T \quad (5.3)$$

Where, N_{LP} is total number of layer parameters, either the maximum value of \mathbb{N} and T indicates transpose. The vector in Equation (5.3) can be written in more compact form as:

$$\mathbf{m}_1 = \left(\kappa_1, \kappa_2, \kappa_3, \dots, \kappa_N, \dots, \kappa_{N_p} \right)^T \quad (5.4)$$

Where, $\kappa_N = \kappa_{(N_1-1)N_{LP}+N_2} = g_{N_1 N_2}$ with $N_1 = 1, 2, 3, \dots, N_L$ and $N_2 = 1, 2, 3, \dots, N_{LP}$

The model considered in Figure 5.1 can be well described seismically by body-wave velocities of different layers. Therefore P-wave and S-wave velocities are another type of model parameters which are included in the present inverse problem. If s_q^p and s_q^s represent P-wave and S-wave slowness of q^{th} layer, then these model parameters for all the layers in model in Figure 5.1 can be written as model vector \mathbf{m}_2 as:

$$\mathbf{m}_2 = \left(s_1^p, s_2^p, s_3^p, \dots, s_{N_L}^p, s_1^s, s_2^s, s_3^s, \dots, s_{N_L}^s \right)^T \quad (5.5)$$

As the hypocenters with origin times of earthquakes are also included into the inversion problem, so the hypocenters, origin time also serve as the typical model parameters. If τ_0 represent origin time and $\lambda_1, \lambda_2, \lambda_3$ represent three ordinates of the Cartesian domain, then introducing second subscripts to these parameters, for event number, these altogether can be written with model vector \mathbf{m}_3 as:

$$\mathbf{m}_3 = \left(\tau_{01}, \lambda_{11}, \lambda_{21}, \lambda_{31}, \tau_{02}, \lambda_{12}, \lambda_{22}, \lambda_{32}, \tau_{03}, \lambda_{13}, \lambda_{23}, \lambda_{33}, \dots, \tau_{0N_E}, \lambda_{1N_E}, \lambda_{2N_E}, \lambda_{3N_E} \right)^T \quad (5.6)$$

Where, N_E is total number of events or earthquakes. Therefore, with reference to Figure 5.1, the effective model parameters for all the N_L layers can be written by a single model vector, \mathbf{m} as:

$$\mathbf{m} = \left(\mathbf{m}_3^T, \mathbf{m}_2^T, \mathbf{m}_1^T \right)^T \quad (5.7)$$

Or,

$$\mathbf{m} = \left(\tau_{01}, \lambda_{11}, \lambda_{21}, \lambda_{31}, \tau_{02}, \lambda_{12}, \lambda_{22}, \lambda_{32}, \tau_{03}, \lambda_{13}, \lambda_{23}, \lambda_{33}, \dots, \tau_{0N_E}, \lambda_{1N_E}, \lambda_{2N_E}, \lambda_{3N_E}, s_1^p, s_2^p, s_3^p, \dots, s_{N_L}^p, s_1^s, s_2^s, s_3^s, \dots, s_{N_L}^s, K_1, K_2, K_3, \dots, K_{N_p} \right)^T \quad (5.8)$$

The data of the present inverse problem are source-receiver traveltimes of first arrival phases of body-waves of seismograms recorded at different receivers (stations) on the surface. For each earthquake (event) there will be a set of traveltimes of P-waves observed at a set of station positions. Therefore, for a number of earthquakes there will be a number of sets of traveltimes for P-waves observed at different stations. All such sets of observed traveltimes constitute the P-phase data vector which can be written as:

$$\mathbf{\Gamma}^p = \left(\mathbf{\Gamma}_1^{pT}, \mathbf{\Gamma}_2^{pT}, \mathbf{\Gamma}_3^{pT}, \dots, \mathbf{\Gamma}_m^{pT}, \dots, \mathbf{\Gamma}_{N_E}^{pT} \right)^T \quad (5.9)$$

Where,

$$\mathbf{\Gamma}_m^p = \left(\tau_{m1}^p, \tau_{m2}^p, \tau_{m3}^p, \dots, \tau_{mn}^p, \dots, \tau_{N_E N_S(m)}^p \right)^T \quad (5.10)$$

$$m = 1, 2, 3, \dots, N_E \quad ; \quad n = 1, 2, 3, \dots, N_S(m)$$

In the above equations superscript, p denotes P-phase and N_E is total number of earthquakes considered. As number of stations recorded different earthquakes may not be the same, therefore a functional integer $N_{SP}(m)$ is introduced to represent the number of stations that recorded first arrival P-phases from m^{th} earthquake. As S-phases are also considered in the problem therefore replacing superscript, p by s in Equations (5.9), (5.10) an S-phase data vector constituting the first arrivals of S-phases recorded at different stations can be represented similar to above as:

$$\Gamma^s = \left(\Gamma_1^{sT}, \Gamma_2^{sT}, \Gamma_3^{sT}, \dots, \Gamma_m^{sT}, \dots, \Gamma_{N_E}^{sT} \right)^T \quad (5.11)$$

Where,

$$\Gamma_m^s = \left(\tau_{m1}^s, \tau_{m2}^s, \tau_{m3}^s, \dots, \tau_{mn}^s, \dots, \tau_{N_E N_S(m)}^s \right)^T \quad (5.12)$$

$$m = 1, 2, 3, \dots, N_E \quad ; \quad n = 1, 2, 3, \dots, N_{SS}(m)$$

And similar to above $N_{SS}(m)$ is introduced to represent the number of stations that recorded first arrival S-phases from m^{th} earthquake. Combining Γ^p and Γ^s the total data vector can be written as:

$$\Gamma = \left(\Gamma^{pT}, \Gamma^{sT} \right)^T \quad (5.13)$$

5.4 FORMULATION OF THE INVERSE PROBLEM

The time of travel or the traveltime of seismic waves from a source to a station in a medium is primarily depends upon the path in the medium through which seismic energy travel from the source to the station. Although there many parameters which affect source-receiver ray paths of seismic waves, however for the present problem the medium velocities for P-waves and S-waves, the coefficients of interfaces, hypocenters with origin times and the stations are sufficient controlling parameters to approximate the exact ray paths in the considered model. Out of five parameters the last one is supposed to be known and the former are unknowns and are of special interest for seismotectonic investigation of structural features of the earth. Let us suppose that the receiver (station) coordinates are perfectly known and slowness, coefficients for interfaces and hypocenter with origin times are four typical parameters that control the source receiver ray paths.

Let us suppose that source-receiver traveltime of P-wave is related to all these four unknown types of model parameters by an arbitrary nonlinear function, f^p ; then with reference to Figure 5.1 for a trial source-receiver ray path it is possible to write:

$$\tau^p = f^p \left(\tau_0, \lambda_1, \lambda_2, \lambda_3, s_1^p, s_2^p, s_3^p, \dots, s_{N_L}^p, \kappa_1, \kappa_2, \kappa_3, \dots, \kappa_{N_p} \right) \quad (5.14)$$

In the Equation (5.14), τ_0 is origin time, $\lambda_1, \lambda_2, \lambda_3$ the three ordinates of a trial source with $\{\tau_0, \lambda_1, \lambda_2, \lambda_3\} \in \mathbf{m}_3$ and rest of the parameters in the parenthesis are defined through Equations (5.4) and (5.5). The total differential of traveltime governed by the Equation (5.14) can be written as:

$$d\tau^p = d\tau_0 + \sum_{i=1}^3 \frac{\partial f^p}{\partial \lambda_i} d\lambda_i + \sum_{j=1}^{N_L} \frac{\partial f^p}{\partial s_j^p} ds_j^p + \sum_{k=1}^{N_p} \frac{\partial f^p}{\partial \kappa_k} d\kappa_k \quad (5.15)$$

The Equation (5.15) describes that for infinitesimal change in model parameter the change in traveltime for the trial ray-path. To use the Equation (5.15) in practical tomography it is approximated as:

$$\Delta \tau^p \approx \Delta \tau_0 + \sum_{i=1}^3 \frac{\partial f^p}{\partial \lambda_i} \Delta \lambda_i + \sum_{j=1}^{N_L} \frac{\partial f^p}{\partial s_j^p} \Delta s_j^p + \sum_{k=1}^{N_p} \frac{\partial f^p}{\partial \kappa_k} \Delta \kappa_k \quad (5.16)$$

Where, Δ is standard difference operator. The Equation (5.16) describes that for a finite change in model parameters the approximate finite change in traveltime. In computational tomography the difference operator, Δ on the left hand side is identified as the difference between observed and computed values of a traveltimes, and on the right hand side it indicates the discrepancy of computed model parameters with respect to apriori model parameters, therefore excluding the superscript we represent in general as:

$$\begin{aligned} \Delta \tau &= \tau_{\text{observed}} - \tau_{\text{computed}} \\ \Delta \xi &= \xi_{\text{apriori}} - \xi_{\text{computed}} \end{aligned} \quad (5.17)$$

Where, ξ is a general component of model vector, \mathbf{m} . As the equation is valid for a trial ray-path therefore associating the subscripts m and n with $f^p, \tau^p, \tau_0, \lambda_1, \lambda_2$, and λ_3 to assign the same equation for a ray path connecting m^{th} earthquake and n^{th} station we write:

$$\Delta \tau_{mn}^p \approx \Delta \tau_{0m} + \sum_{i=1}^3 \frac{\partial f_{mn}^p}{\partial \lambda_{im}} \Delta \lambda_i^p + \sum_{j=1}^{N_L} \frac{\partial f_{mn}^p}{\partial s_j^p} \Delta s_j^p + \sum_{k=1}^{N_p} \frac{\partial f_{mn}^p}{\partial \kappa_k} \Delta \kappa_k \quad (5.18)$$

With, $m = 1, 2, 3, \dots, N_E$; $n = 1, 2, 3, \dots, N_{sp}(m)$

In Equation (5.18), f_{mn}^p is the function which maps model parameters affecting propagation of P-wave from m^{th} earthquake to n^{th} station, into corresponding traveltime, τ_{mn}^p . The set of hypocenter parameters $(\tau_{0m}, \lambda_{1m}, \lambda_{2m}, \lambda_{3m})$ belongs to m^{th} earthquake and is defined in Equation (5.6). Replacing the superscripts p in Equation (5.18) by superscripts s a similar expression can be written with reference to S-wave as:

$$\Delta\tau_{mn}^s \approx \Delta\tau_0^m + \sum_{i=1}^3 \frac{\partial f_{mn}^s}{\partial \lambda_i^m} \Delta\lambda_i^p + \sum_{j=1}^{N_L} \frac{\partial f_{mn}^s}{\partial S_j^s} \Delta S_j^s + \sum_{k=1}^{N_P} \frac{\partial f_{mn}^s}{\partial \kappa_k} \Delta\kappa_k \quad (5.19)$$

Where, $m=1,2,3,\dots,N_E$; $n=1,2,3,\dots,N_{SS}(m)$. f_{mn}^s is a function similar to f_{mn}^p that maps model parameters, affecting propagation S-waves from m^{th} earthquake to n^{th} station, into S-wave traveltime, τ_{mn}^s . The finite differential Equations (5.18) and (5.19) for all the stations either for all value of n can be organized into a matrix form as:

$$\begin{bmatrix} \Delta\Gamma_m^p \\ \Delta\Gamma_m^s \end{bmatrix} \approx \begin{bmatrix} P_m^p & Q_m^p & 0 & S_m^p \\ P_m^s & 0 & Q_m^s & S_m^s \end{bmatrix} \begin{bmatrix} \Delta P_m \\ \Delta m_2 \\ \Delta m_1 \end{bmatrix} \quad (5.20)$$

Inserting a common letter w for superscripts p and s in Equation (5.20), we define:

$$P_m^w = \begin{bmatrix} 1 & \frac{\partial f_{m1}^w}{\partial \lambda_{1m}} & \frac{\partial f_{m1}^w}{\partial \lambda_{2m}} & \frac{\partial f_{m1}^w}{\partial \lambda_{3m}} \\ 1 & \frac{\partial f_{m2}^w}{\partial \lambda_{1m}} & \frac{\partial f_{m2}^w}{\partial \lambda_{2m}} & \frac{\partial f_{m2}^w}{\partial \lambda_{3m}} \\ 1 & \frac{\partial f_{m3}^w}{\partial \lambda_{1m}} & \frac{\partial f_{m3}^w}{\partial \lambda_{2m}} & \frac{\partial f_{m3}^w}{\partial \lambda_{3m}} \\ \vdots & \vdots & \vdots & \vdots \\ 1 & \frac{\partial f_{mn}^w}{\partial \lambda_{1m}} & \frac{\partial f_{mn}^w}{\partial \lambda_{2m}} & \frac{\partial f_{mn}^w}{\partial \lambda_{3m}} \\ \vdots & \vdots & \vdots & \vdots \\ 1 & \frac{\partial f_{mN_S(m)}^w}{\partial \lambda_{1m}} & \frac{\partial f_{mN_S(m)}^w}{\partial \lambda_{2m}} & \frac{\partial f_{mN_S(m)}^w}{\partial \lambda_{3m}} \end{bmatrix} \quad (5.21)$$

$$Q_m^w = \begin{bmatrix} \frac{\partial f_{mi}^w}{\partial s_j^w} \end{bmatrix}_{N_S(m) \times N_E} = \begin{bmatrix} \frac{\partial f_{m1}^w}{\partial s_1^w} & \frac{\partial f_{m1}^w}{\partial s_2^w} & \frac{\partial f_{m1}^w}{\partial s_3^w} & \dots & \frac{\partial f_{m1}^w}{\partial s_{N_i}^w} \\ \frac{\partial f_{m2}^w}{\partial s_1^w} & \frac{\partial f_{m2}^w}{\partial s_2^w} & \frac{\partial f_{m2}^w}{\partial s_3^w} & \dots & \frac{\partial f_{m2}^w}{\partial s_{N_i}^w} \\ \frac{\partial f_{m3}^w}{\partial s_1^w} & \frac{\partial f_{m3}^w}{\partial s_2^w} & \frac{\partial f_{m3}^w}{\partial s_3^w} & \dots & \frac{\partial f_{m3}^w}{\partial s_{N_i}^w} \\ \vdots & \vdots & \vdots & \ddots & \vdots \\ \frac{\partial f_{mn}^w}{\partial s_1^w} & \frac{\partial f_{mn}^w}{\partial s_2^w} & \frac{\partial f_{mn}^w}{\partial s_3^w} & \dots & \frac{\partial f_{mn}^w}{\partial s_{N_i}^w} \\ \vdots & \vdots & \vdots & \ddots & \vdots \\ \frac{\partial f_{mN_{Sw}(m)}^w}{\partial s_1^w} & \frac{\partial f_{mN_{Sw}(m)}^w}{\partial s_2^w} & \frac{\partial f_{mN_{Sw}(m)}^w}{\partial s_3^w} & \dots & \frac{\partial f_{mN_{Sw}(m)}^w}{\partial s_{N_i}^w} \end{bmatrix} \quad (5.22)$$

$$S_m^w = \begin{bmatrix} \frac{\partial f_{mi}^w}{\partial \kappa_j} \end{bmatrix}_{N_S(m) \times N_P} = \begin{bmatrix} \frac{\partial f_{m1}^w}{\partial \kappa_1} & \frac{\partial f_{m1}^w}{\partial \kappa_2} & \frac{\partial f_{m1}^w}{\partial \kappa_3} & \dots & \frac{\partial f_{m1}^w}{\partial \kappa_{N_P}} \\ \frac{\partial f_{m2}^w}{\partial \kappa_1} & \frac{\partial f_{m2}^w}{\partial \kappa_2} & \frac{\partial f_{m2}^w}{\partial \kappa_3} & \dots & \frac{\partial f_{m2}^w}{\partial \kappa_{N_P}} \\ \frac{\partial f_{m3}^w}{\partial \kappa_1} & \frac{\partial f_{m3}^w}{\partial \kappa_2} & \frac{\partial f_{m3}^w}{\partial \kappa_3} & \dots & \frac{\partial f_{m3}^w}{\partial \kappa_{N_P}} \\ \vdots & \vdots & \vdots & \ddots & \vdots \\ \frac{\partial f_{mn}^w}{\partial \kappa_1} & \frac{\partial f_{mn}^w}{\partial \kappa_2} & \frac{\partial f_{mn}^w}{\partial \kappa_3} & \dots & \frac{\partial f_{mn}^w}{\partial \kappa_{N_P}} \\ \vdots & \vdots & \vdots & \ddots & \vdots \\ \frac{\partial f_{mN_S(m)}^w}{\partial \kappa_1} & \frac{\partial f_{mN_S(m)}^w}{\partial \kappa_2} & \frac{\partial f_{mN_S(m)}^w}{\partial \kappa_3} & \dots & \frac{\partial f_{mN_S(m)}^w}{\partial \kappa_{N_P}} \end{bmatrix} \quad (5.23)$$

$$\left. \begin{aligned} \Delta P &= (\Delta \tau_{0m}, \Delta \lambda_{1m}, \Delta \lambda_{2m}, \Delta \lambda_{3m})^T \\ \Delta \mathbf{m}_1 &= (\Delta \kappa_1, \Delta \kappa_2, \Delta \kappa_3, \dots, \Delta \kappa_N, \dots, \Delta \kappa_{N_P})^T \\ \Delta \mathbf{m}_2 &= (\Delta s_1^P, \Delta s_2^P, \Delta s_3^P, \dots, \Delta s_{N_i}^P, \Delta s_1^S, \Delta s_2^S, \Delta s_3^S, \dots, \Delta s_{N_i}^S)^T \\ \Delta \Gamma_m^P &= (\Delta \tau_{m1}^P, \Delta \tau_{m2}^P, \Delta \tau_{m3}^P, \dots, \Delta \tau_{mn}^P, \dots, \Delta \tau_{N_E N_S(m)}^P)^T \\ \Delta \Gamma_m^S &= (\Delta \tau_{m1}^S, \Delta \tau_{m2}^S, \Delta \tau_{m3}^S, \dots, \Delta \tau_{mn}^S, \dots, \Delta \tau_{N_E N_S(m)}^S)^T \end{aligned} \right\} \quad (5.24)$$

Extending Equation (5.20) to include all the recorded earthquakes, it becomes:

$$\Delta \Gamma \approx \mathbf{M} \Delta \mathbf{m} \quad (5.25)$$

In which,

$$\begin{aligned}\Delta\Gamma &= \left(\Delta\Gamma_1^{pT}, \Delta\Gamma_2^{pT}, \Delta\Gamma_3^{pT}, \dots, \Delta\Gamma_{N_E-1}^{pT}, \Delta\Gamma_{N_E}^{pT}, \Delta\Gamma_1^{sT}, \Delta\Gamma_2^{sT}, \Delta\Gamma_3^{sT}, \dots, \Delta\Gamma_{N_E-1}^{sT}, \Delta\Gamma_{N_E}^{sT} \right)^T \\ \Delta\mathbf{m} &= \left(\Delta\mathbf{m}_3^T, \Delta\mathbf{m}_2^T, \Delta\mathbf{m}_1^T \right)^T \\ \Delta\mathbf{m}_3 &= \left(\Delta\tau_{01}, \Delta\lambda_{11}, \Delta\lambda_{21}, \Delta\lambda_{31}, \Delta\tau_{02}, \Delta\lambda_{12}, \Delta\lambda_{22}, \Delta\lambda_{32}, \Delta\tau_{03}, \Delta\lambda_{13}, \Delta\lambda_{23}, \Delta\lambda_{33}, \dots, \Delta\tau_{0N_E}, \Delta\lambda_{1N_E}, \Delta\lambda_{2N_E}, \Delta\lambda_{3N_E} \right)^T\end{aligned}\quad (5.26)$$

And

$$\mathbf{M} = \begin{bmatrix} P_1^p & 0 & 0 & \dots & 0 & 0 & Q_1^p & 0 & S_1^p \\ 0 & P_2^p & 0 & \dots & 0 & 0 & Q_2^p & 0 & S_2^p \\ 0 & 0 & P_3^p & \dots & 0 & 0 & Q_3^p & 0 & S_3^p \\ \vdots & \vdots & \vdots & \ddots & \vdots & \vdots & \vdots & \vdots & \vdots \\ 0 & 0 & 0 & 0 & P_{N_E-1}^p & 0 & Q_{N_E-1}^p & 0 & S_{N_E-1}^p \\ 0 & 0 & 0 & 0 & 0 & P_{N_E}^p & Q_{N_E}^p & 0 & S_{N_E}^p \\ P_1^s & 0 & 0 & 0 & 0 & 0 & 0 & Q_1^s & S_1^s \\ 0 & P_2^s & 0 & 0 & 0 & 0 & 0 & Q_2^s & S_2^s \\ 0 & 0 & P_3^s & 0 & 0 & 0 & 0 & Q_3^s & S_3^s \\ \vdots & \vdots & \vdots & \ddots & \vdots & \vdots & \vdots & \vdots & \vdots \\ 0 & 0 & 0 & 0 & P_{N_E-1}^s & 0 & 0 & Q_{N_E-1}^s & S_{N_E-1}^s \\ 0 & 0 & 0 & 0 & 0 & P_{N_E}^s & 0 & Q_{N_E}^s & S_{N_E}^s \end{bmatrix}\quad (5.27)$$

Equation (5.25) is linearized expression that connects model vector to the data vector. This difference operator on the left hand side is identified as the difference between observed traveltimes vector and computed traveltimes vector. The difference operator on the right hand side is the difference between apriori model vector and computed model vector. These with the help of Equation (5.17) can be written as:

$$\begin{aligned}\Delta\Gamma &= \Gamma|_{observed} - \Gamma|_{computed} \\ \Delta\mathbf{m} &= \mathbf{m}|_{apriori} - \mathbf{m}|_{computed}\end{aligned}\quad (5.28)$$

The matrix \mathbf{M} in Equation (5.25) is consisted of derivative of functions governing source-receiver ray path and traveltimes with respect to model parameters that controls the ray-paths. In inverse theory such derivatives are called Fréchet derivatives. To obtain a solution of model using Equation (5.25), it is required that these derivatives must be expressed in

terms of known model parameters and data, therefore we presents detailed derivation of these derivatives in §5.5.

5.5 DERIVATION OF FRÉCHET DERIVATIVES

The interfaces or discontinuity surfaces considered in the model in Figure 5.1 vary in three dimensions, therefore a phenomenon of self intersection of ray paths and theses surfaces may occur as shown in Figure 5.4.

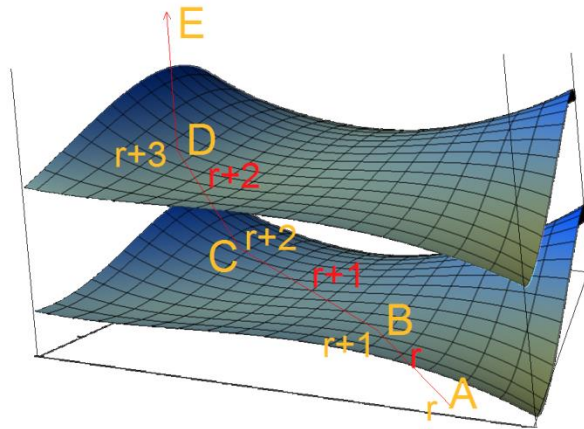


Figure 5.4: Phenomena of internal reflection by discontinuity surface by a segment of arbitrary ray path. The numbering of elementary points, starting from r^{th} point is shown. The layer number between r and $r+1$ is r . The false layer or pseudo layer, $r+1$ lies between elementary point $r+1$ and $r+2$ in the figure.

In Figure 5.4, ABCD is an arbitrary ray path segment consisted of incident ray path sub segment, AB, refracted ray path sub segment, BC, the reflected ray path sub segment CD and refracted ray path sub segment, DE. The reflection phenomena similar to ray path segment ABCD may occur for an arbitrary ray path within the model given in Figure 5.1, due to 3D nature of discontinuity surfaces. Therefore the phenomenon of reflection has to be considered in combination with refraction in the formulation of Fréchet derivatives. As the point (C in Figure 5.4) of reflection and the point (B and D in Figure 5.4) of refraction are unknown for an arbitrary ray path therefore it is very difficult to establish an exclusive mathematical formulation of the derivatives using the layers and discontinuity surfaces of the model.

A ray path contains the points of refraction and the points of reflection and for an arbitrary ray path in model in Figure 5.1, these are the elementary points because these points are sufficient to reconstruct the entire ray path as the ray path segment between two such adjacent points are straight. The elementary points of ray paths are essentially the

intersection points between the ray paths intersected by discontinuity surfaces of the model. The coordinates of these points are computed in the forward problem hence these are known. The numbering of these elementary points is illustrated in Figure 5.4. These elementary points can be used to obtain the Fréchet derivatives if we relate these points with the number of discontinuity surfaces using a function, Π as:

$$q = \Pi(r) \quad (5.29)$$

$$\text{With, } r = 1, 2, 3, \dots, N_C ; \quad q = 1, 2, 3, \dots, N_L$$

The value of q in Equation (5.29) denotes layer number or interface number as suggested in model description in §5.2, whereas r denotes the intersection points (elementary points) between ray-paths and discontinuity-surfaces with N_C being the total number of elementary points in a ray path. The value of r also denotes the number of pseudo-layer bounding pseudo surfaces (as layer $r+1$ in Figure 5.4) in the same way as q does for actual layer, except $r=1$ where it indicates position of hypocenter. This definition of function, Π says that two pseudo-layers may indicate a single actual layers but the inverse is not true. It is also clear that if the phenomenon of reflection is not considered into the problem then each pseudo-layer denotes a single unique actual layer in the model. The value of q in the above function for each value of r is obtained during the solution of forward problem; in other words it is computed during the computation of ray-path and traveltimes in forward problem.

It is useful to define here a general set of model parameters that is common to both P-wave and S-wave; therefore we define a set \mathfrak{S} as:

$$\mathfrak{S} = \left\{ \tau_0, \lambda_1, \lambda_2, \lambda_3, s_1, s_2, s_3, \dots, s_{N_L}, \kappa_1, \kappa_2, \kappa_3, \dots, \kappa_{N_p} \right\} \quad (5.30)$$

Where, τ_0 is, as before, the origin time of an earthquake and $\lambda_1, \lambda_2, \lambda_3$ are three ordinates of hypocenter of the earthquake. The parameters $s_1, s_2, s_3, \dots, s_{N_L}$ are the slownesses of either P-wave or S-wave in layers $1, 2, 3, \dots, N_L$ with N_L being the total number of layers as before. The 4th type of parameters in the parenthesis of Equation (5.30) is defined in §5.3.

The ray paths for P-wave or S-wave in any layer are straight lines as the velocities for both P and S-waves at different points within any layer are same due to assumption 1. In other words the function appeared in §5.4 can be written as:

$$f = \sum_{r=1}^{N_C} l_r s_r \quad (5.31)$$

With the definition of length segment, l_r of ray path between two adjacent intersections with the surfaces as:

$$l_r = \sqrt{(x_{r1} - x_{r-1,1})^2 + (x_{r2} - x_{r-1,2})^2 + (x_{r3} - x_{r-1,3})^2} \quad (5.32)$$

The value of N_C in Equation (5.31) as earlier indicates the total number of elementary points of a ray path and in Equation (5.32), x_{r1} , x_{r2} and x_{r3} denote three ordinates of r^{th} elementary point. The following derivatives can be written using Equation (5.31) and (5.32);

$$\left. \begin{aligned} \frac{\partial f}{\partial \lambda_i} &= \sum_{r=1}^{N_C} s_r \frac{\partial l_r}{\partial \lambda_i} \\ \frac{\partial f}{\partial s_j} &= \sum_{r=1}^{N_C} s_r \frac{\partial l_r}{\partial s_j} + l_j \\ \frac{\partial f}{\partial \kappa_k} &= \sum_{r=1}^{N_C} s_r \frac{\partial l_r}{\partial \kappa_k} \end{aligned} \right\} \quad (5.33)$$

With, $i \in \{1, 2, 3\}$, $j \in \{1, 2, 3, \dots, N_L\}$, $k \in \{1, 2, 3, \dots, N_p\}$

It is clear from the above equation that the derivatives of function f with respect to model parameters can be computed if the derivative of l_r with respect model parameters is given. Consider a parameter ξ such that:

$$\xi \in \mathfrak{S} \quad (5.34)$$

Differentiating Equation (5.32) with respect to ξ we have

$$\frac{\partial l_r}{\partial \xi} = \frac{1}{l_r} \left[\Delta x_r \left(\frac{\partial x_{r1}}{\partial \xi} - \frac{\partial x_{r-1,1}}{\partial \xi} \right) + \Delta y_r \left(\frac{\partial x_{r2}}{\partial \xi} - \frac{\partial x_{r-1,2}}{\partial \xi} \right) + \Delta z_r \left(\frac{\partial x_{r3}}{\partial \xi} - \frac{\partial x_{r-1,3}}{\partial \xi} \right) \right] \quad (5.35)$$

The problem of computation of derivative of function, f in Equation (5.33) is reduced to the problem of computing derivatives of different position vector with respect to the model parameter ξ .

Let s_r and s_{r+1} be the body wave slownesses of r^{th} and $(r+1)^{\text{th}}$ layers then, for a given unit incident vector ray-path, \mathbf{l}_r from r^{th} layer on a r^{th} surface separating adjacent $(r+1)^{\text{th}}$ layer, the unit refraction and unit reflection vector ray-paths, respectively \mathbf{l}_{r+1}^{fr} and \mathbf{l}_{r+1}^{fl} can be written as (Equations 3.14 and 3.19):

$$\mathbf{l}_{r+1}^{fr} = \frac{s_r}{s_{r+1}} (\mathbf{l}_r + Q_r \mathbf{n}_{r+1}) \quad (5.36)$$

$$\mathbf{l}_{r+1}^{fl} = \mathbf{l}_r - 2(\mathbf{l}_r \cdot \mathbf{n}_{r+1}) \mathbf{n}_{r+1} \quad (5.37)$$

Where, \mathbf{n}_{r+1} is the unit normal vector on $(r+1)^{\text{th}}$ surface at the point of ray incident and the scalar quantity Q_r is given by:

$$Q_r = \left\{ \left(\frac{s_{r+1}}{s_r} \right)^2 - 1 + (\mathbf{l}_r \cdot \mathbf{n}_{r+1})^2 \right\}^{\frac{1}{2}} - \mathbf{l}_r \cdot \mathbf{n}_{r+1} \quad (5.38)$$

Removing the superscript in Equations (5.36) and (5.37) and considering the phenomena of reflection and refraction as two mutually exclusive events, the generalized unit vector ray-path segment in any two adjacent layers can be written recursively as:

$$\mathbf{l}_{r+1} = F_r \frac{s_r}{s_{r+1}} (\mathbf{l}_r + Q_r \mathbf{n}_{r+1}) + (1 - F_r) \{ \mathbf{l}_r - 2(\mathbf{l}_r \cdot \mathbf{n}_{r+1}) \mathbf{n}_{r+1} \} \quad (5.39)$$

With,

$$\left. \begin{array}{l} F_r = 1; \quad \text{for refraction} \\ F_r = 0; \quad \text{for reflection} \end{array} \right\} \quad (5.40)$$

In Equation (5.39) \mathbf{l}_r represent the same incident unit vector ray-path but \mathbf{l}_{r+1} represents unit vector ray-path segment after the event of reflection or refraction. Differentiating the vector Equation (5.39) from both sides with respect to the parameter ξ and applying some algebraic operation, we come to:

$$\frac{\partial \mathbf{l}_{r+1}}{\partial \xi} = I_r \frac{\partial \mathbf{l}_r}{\partial \xi} + \mu_r \mathbf{n}_{r+1} \left(\mathbf{n}_{r+1} \cdot \frac{\partial \mathbf{l}_r}{\partial \xi} \right) + \mathbf{J}_r \quad (5.41)$$

Where,

$$I_r = F_r \frac{s_r}{s_{r+1}} + 1 - F_r \quad (5.42)$$

$$\mu_r = -F_r \frac{s_r}{s_{r+1}} \left(\frac{Q_r}{Q_r + \mathbf{l}_r \cdot \mathbf{n}_{r+1}} \right) - 2(1 - F_r) \quad (5.43)$$

$$\mathbf{J}_r = \mu_r \mathbf{n}_{r+1} \left(\mathbf{l}_r \cdot \frac{\partial \mathbf{n}_{r+1}}{\partial \xi} \right) + \nu_r \frac{\partial \mathbf{n}_{r+1}}{\partial \xi} + \Lambda_r \left\{ \frac{1}{s_{r+1}} \frac{\partial s_{r+1}}{\partial \xi} - \frac{1}{s_r} \frac{\partial s_r}{\partial \xi} \right\} \quad (5.44)$$

With,

$$\nu_r = F_r Q_r \frac{s_r}{s_{r+1}} - 2(1 - F_r) (\mathbf{l}_r \cdot \mathbf{n}_{r+1}) \quad (5.45)$$

$$\Lambda_r = F_r \left(\frac{s_{r+1} \mathbf{n}_{r+1}}{s_r (Q_r + \mathbf{l}_r \cdot \mathbf{n}_{r+1})} - \mathbf{l}_{r+1} \right) \quad (5.46)$$

Writing $\mathbf{l}_r = (a_{r1}, a_{r2}, a_{r3})$, $\mathbf{n}_r = (n_{r1}, n_{r2}, n_{r3})$ and $\mathbf{J}_r = (J_{r1}, J_{r2}, J_{r3})$, the unit vector \mathbf{l}_{r+1} from Equation (5.41) can be split in its three components as:

$$\frac{\partial a_{r+1,j}}{\partial \xi} = \sum_{k=1}^3 B_{r,3+k,j} \frac{\partial a_{rj}}{\partial \xi} + J_r^j \quad ; \quad j = 1, 2, 3 \quad (5.47)$$

$$\left. \begin{aligned} B_{r41} &= I_r + \mu_r n_{r+1,1}^2 ; & B_{r51} &= \mu_r n_{r+1,1} n_{r+1,2} ; & B_{r61} &= \mu_r n_{r+1,1} n_{r+1,3} \\ B_{r42} &= B_{r21} ; & B_{r52} &= I_r + \mu_r n_{r+1,2}^2 ; & B_{r62} &= \mu_r n_{r+1,2} n_{r+1,3} \\ B_{r43} &= B_{r31} ; & B_{r53} &= B_{r32} ; & B_{r63} &= I_r + \mu_r n_{r+1,3}^2 \end{aligned} \right\} \quad (5.48)$$

To split the unit vector \mathbf{J}_r in its components, it is essential to express the unit vector \mathbf{n} in terms of surface variables. The unit normal vector, \mathbf{n} at point (x_{r1}, x_{r2}) on the surface represented by the Equation (5.1) is given by:

$$\mathbf{n} = (n_{r1}, n_{r2}, n_{r3}) = \left(-\frac{\psi_{r1}}{\sqrt{1+\psi_{r1}^2+\psi_{r2}^2}}, -\frac{\psi_{r2}}{\sqrt{1+\psi_{r1}^2+\psi_{r2}^2}}, \frac{1}{\sqrt{1+\psi_{r1}^2+\psi_{r2}^2}} \right) \quad (5.49)$$

Where, n_{r1}, n_{r2} and n_{r3} are components of \mathbf{n} along x, y and z directions in Cartesian domain and

$$\left. \begin{aligned} \psi_{r1} &= \frac{\partial \zeta_r}{\partial x} \\ \psi_{r2} &= \frac{\partial \zeta_r}{\partial y} \end{aligned} \right\} \quad (5.50)$$

The derivatives of the components of \mathbf{n} with respect to arbitrary parameter ξ can be written in terms of derivatives of x_{r1} and x_{r2} with respect to the same arbitrary parameter, ξ as:

$$\left. \begin{aligned} \frac{\partial n_{r1}}{\partial \xi} &= \Psi_{r1} \frac{\partial x_{r1}}{\partial \xi} + \Theta_{r1} \frac{\partial x_{r2}}{\partial \xi} + \Phi_{r1} \\ \frac{\partial n_{r2}}{\partial \xi} &= \Psi_{r2} \frac{\partial x_{r1}}{\partial \xi} + \Theta_{r2} \frac{\partial x_{r2}}{\partial \xi} + \Phi_{r2} \\ \frac{\partial n_{r3}}{\partial \xi} &= \Psi_{r3} \frac{\partial x_{r1}}{\partial \xi} + \Theta_{r3} \frac{\partial x_{r2}}{\partial \xi} + \Phi_{r3} \end{aligned} \right\} \quad (5.51)$$

In Equation (5.51) the parameters $\Psi_{r1}, \Psi_{r2}, \Psi_{r3}, \Theta_{r1}, \Theta_{r2}, \Theta_{r3}, \Phi_{r1}, \Phi_{r2}$ and Φ_{r3} are defined as below:

$$\left. \begin{aligned}
\Psi_{r1} &= w_r \left\{ \psi_{r1} \psi_{r2} \alpha_r - (1 + \psi_{r2}^2) \beta_r \right\}, & \Psi_{r2} &= w_r \left\{ \psi_{r1} \psi_{r2} \alpha_r - (1 + \psi_{r1}^2) \beta_r \right\} \\
\Psi_{r3} &= -w_r (\psi_{r2} \alpha_r + \psi_{r1} \beta_r), & \Theta_{r1} &= w_r \left\{ \psi_{r1} \psi_{r2} \gamma_r - (1 + \psi_{r2}^2) \alpha_r \right\} \\
\Theta_{r2} &= w_r \left\{ \psi_{r1} \psi_{r2} \gamma_r - (1 + \psi_{r1}^2) \alpha_r \right\}, & \Theta_{r3} &= -w_r (\psi_{r2} \gamma_r + \psi_{r1} \alpha_r) \\
\Phi_{r1} &= w_r \left\{ \psi_{r1} \psi_{r2} \varphi_r - (1 + \psi_{r2}^2) \theta_r \right\}, & \Phi_{r2} &= w_r \left\{ \psi_{r1} \psi_{r2} \varphi_r - (1 + \psi_{r1}^2) \theta_r \right\} \\
\Phi_{r3} &= -w_r (\psi_{r2} \varphi_r + \psi_{r1} \theta_r), & w_r &= 1 / (1 + \psi_{r1}^2 + \psi_{r2}^2)^{3/2} \\
\alpha_r &= \frac{\partial^2 \zeta_r}{\partial y \partial x}, & \beta_r &= \frac{\partial^2 \zeta_r}{\partial x^2}, & \gamma_r &= \frac{\partial^2 \zeta_r}{\partial y^2} \\
\theta_r &= \sum_{i=1}^{N_p} \frac{\partial^2 \zeta_r}{\partial \kappa_i \partial x} \frac{\partial \kappa_i}{\partial \xi}, & \varphi_r &= \sum_{i=1}^{N_p} \frac{\partial^2 \zeta_r}{\partial \kappa_i \partial y} \frac{\partial \kappa_i}{\partial \xi}
\end{aligned} \right\} \quad (5.52)$$

With the help of set of Equations (5.51) the components J_{rj} of vector \mathbf{J}_r can be expressed as:

$$J_{rj} = \sum_{k=1}^3 \left(B_{r,k,j} \frac{\partial x_{r+1,k}}{\partial \xi} \right) + B_{r7j} \quad (5.53)$$

$$\left. \begin{aligned}
B_{r1j} &= \mu_r n_{r+1,j} \sum_{k=1}^3 a_{rk} \Psi_{r+1,k} + \nu_r \Psi_{r+1,j} \\
B_{r2j} &= \mu_r n_{r+1,j} \sum_{k=1}^3 a_{rk} \Theta_{r+1,k} + \nu_r \Theta_{r+1,j} \\
B_{r3j} &= 0 \\
B_{r7j} &= \mu_r n_{rj} \sum_{k=1}^3 a_{rk} \Phi_{r+1,k} + \nu_r \Phi_{r+1,j} + u_{rj} \mathfrak{g}_r(\xi)
\end{aligned} \right\}; \quad j = 1, 2, 3 \quad (5.54)$$

The functions u_{rj} and $\mathfrak{g}_r(\xi)$ are defined as

$$u_{rj} = F_r \left(\frac{n_{r+1,j}}{s_r^2 (Q_r + \mathbf{l}_r \cdot \mathbf{n}_{r+1})} - \frac{a_{r+1,j}}{s_r s_{r+1}} \right) \quad (5.55)$$

$$\left. \begin{aligned}
\mathfrak{g}_r(\xi) &= s_r; & \xi &= s_{r+1} \\
&= -s_{r+1}; & \xi &= s_r
\end{aligned} \right\} \quad (5.56)$$

Equation (5.47) using the results of sets of Equations (5.53), (5.54) can be written as:

$$\frac{\partial a_{r+1,j}}{\partial \xi} = \sum_{k=1}^3 B_{r,k,j} \frac{\partial x_{r+1,k}}{\partial \xi} + \sum_{k=1}^3 B_{r,3+k,j} \frac{\partial a_{rk}}{\partial \xi} + B_{r7j} \quad (5.57)$$

With, $j = 1, 2, 3$.

The differential expressions for components of unit vector in set of Equation (5.57) show recursive characteristic and these are possible to solve only when we have another set of recursive relations. However, a second set of equations result from the interaction of ray-paths and surfaces of discontinuities. As the ray-path segments in any layer are straight lines so they are governed by the following equations:

$$\frac{x_{r+1,1} - x_{r1}}{a_{r1}} = \frac{x_{r+1,2} - x_{r2}}{a_{r2}} = \frac{x_{r+1,3} - x_{r3}}{a_{r3}} \quad (5.58)$$

And because of Equation (5.1)

$$x_{r+1,3} = \zeta_{r+1}(g_{r+1,N}, x_{r+1,1}, x_{r+1,2}) \quad (5.59)$$

Using the expressions (5.58) and (5.59) following relations result:

$$\frac{a_{r3}}{a_{r1}} x_{r+1,1} - \frac{a_{r3}}{a_{r1}} x_{r1} + x_{r3} = \zeta_{r+1} \left(g_{r+1,N}, x_{r+1,1}, \frac{a_{r2}}{a_{r1}} x_{r+1,1} - \frac{a_{r2}}{a_{r1}} x_{r1} + x_{r2} \right) \quad (5.60)$$

$$\frac{a_{r3}}{a_{r2}} x_{r+1,2} - \frac{a_{r3}}{a_{r2}} x_{r2} + x_{r3} = \zeta_{r+1} \left(g_{r+1,N}, \frac{a_{r1}}{a_{r2}} x_{r+1,2} - \frac{a_{r1}}{a_{r2}} x_{r2} + x_{r3}, x_{r2} \right) \quad (5.61)$$

Differentiating the equations (5.60), (5.61) and (5.59) with respect to parameter ξ and applying some algebraic operation following set of recursive relation can be written:

$$\frac{\partial x_{r+1,j}}{\partial \xi} = \sum_{k=1}^3 C_{r,k,j} \frac{\partial x_{rk}}{\partial \xi} + \sum_{k=1}^3 C_{r,3+k,j} \frac{\partial a_{rk}}{\partial \xi} + C_{r,7,j} \quad (5.62)$$

With, $j = 1, 2, 3$ and coefficients are given in Table 5.1.

Table 5.1: Coefficients in Equation set (5.62)

$C_{r11} = (\psi_{r2} \Delta y_r - \Delta z_r) / t_r$	$C_{r12} = -\psi_{r1} \Delta y_r / t_r$	$C_{r13} = -\psi_{r1} \Delta z_r / t_r$
$C_{r21} = -\psi_{r2} \Delta x_r / t_r$	$C_{r22} = (\psi_{r1} \Delta x_r - \Delta z_r) / t_r$	$C_{r23} = -\psi_{r2} \Delta z_r / t_r$
$C_{r31} = \Delta x_r / t_r$	$C_{r32} = \Delta y_r / t_r$	$C_{r33} = (\psi_{r1} \Delta x_r + \psi_{r2} \Delta y_r) / t_r$
$C_{r41} = R_r C_{r11}$	$C_{r42} = R_r C_{r12}$	$C_{r43} = R_r C_{r13}$
$C_{r51} = R_r C_{r21}$	$C_{r52} = R_r C_{r22}$	$C_{r53} = R_r C_{r23}$
$C_{r61} = R_r C_{r31}$	$C_{r62} = R_r C_{r32}$	$C_{r63} = R_r C_{r33}$
$C_{r71} = -\psi_{r3} \Delta x_r / t_r$	$C_{r72} = -\psi_{r3} \Delta y_r / t_r$	$C_{r73} = -\psi_{r3} \Delta z_r / t_r$

In the above table

$$\left. \begin{aligned}
R_r &= \sqrt{\Delta x_r^2 + \Delta y_r^2 + \Delta z_r^2} \\
t_r &= \psi_{r1} \Delta x_r + \psi_{r2} \Delta y_r - \Delta z_r \\
\Delta x_r &= x_{r+1} - x_r \\
\Delta y_r &= y_{r+1} - y_r \\
\Delta z_r &= z_{r+1} - z_r \\
\psi_{r3} &= \sum_{k=1}^{N_p} \frac{\partial \zeta}{\partial \kappa_k} \frac{\partial \kappa_k}{\partial \xi}
\end{aligned} \right\} \quad (5.63)$$

With the help of equation (5.62), the set of relations (5.57) can further be simplified as

$$\frac{\partial a_{r+1,j}}{\partial \xi} = \sum_{k=1}^3 C_{r,k,3+j} \frac{\partial x_{rk}}{\partial \xi} + \sum_{k=1}^3 C_{r,3+k,3+j} \frac{\partial a_{rk}}{\partial \xi} + C_{r7,3+j} \quad (5.64)$$

Where,

$$\begin{aligned}
C_{r,k,3+j} &= \sum_{l=1}^3 (C_{r,k,l} B_{r,l,j}) \\
C_{r,3+k,3+j} &= B_{r,3+k,j} + \sum_{l=1}^3 (C_{r,3+k,l} B_{r,l,j}) \\
k &= 1, 2, 3, 4
\end{aligned} \quad (5.65)$$

The Equation set (5.62) defines the derivative of ordinates of elementary points of a ray path and Equation set (5.64) defines the derivative of unit vector parallel to ray path at those elementary points, in terms of known coefficients which are defined using ray path, function ζ and parameter ξ . To solve the Equation (5.62) and (5.64) exclusively for such derivatives, it is essential to reduce the Equation (5.62) in r . To do this objective we define an equation similar to Equation (5.62) but with different notation of coefficients as:

$$\frac{\partial x_{r+1,j}}{\partial \xi} = \sum_{k=1}^3 U_{r,k,j} \frac{\partial x_{rk}}{\partial \xi} + \sum_{k=1}^3 U_{r,3+k,j} \frac{\partial a_{rk}}{\partial \xi} + U_{r,7,j} \quad (5.66)$$

Where,

$$U_{rij} = C_{rij}; i = 1, 2, \dots, 6; j = 1, 2, 3 \quad (5.67)$$

Equation (5.66) can be reduced using Equation (5.62) and (5.64) as:

$$\frac{\partial x_{r+1,j}}{\partial \xi} = \sum_{k=1}^3 U_{r-1,k,j} \frac{\partial x_{r-1,k}}{\partial \xi} + \sum_{k=1}^3 U_{r-1,3+k,j} \frac{\partial a_{r-1,k}}{\partial \xi} + U_{r-1,7,j} \quad (5.68)$$

Where, it can be proved with minor algebraic operation that

$$\begin{aligned}
U_{r-1,p,j} &= \sum_{k=1}^6 U_{r,k,j} C_{r-1,p,k} \\
U_{r-1,7,j} &= U_{r,7,j} + \sum_{k=1}^6 (U_{r,k,j} C_{r-1,7,k})
\end{aligned} \quad (5.69)$$

Equation (5.68) and recurrence relation set (5.69) form the basis of reduction of Equation (5.62) and Equation (5.64) in terms of r . Equation (5.68) using Equation (5.69) can be reduced from the point of station to the point of hypocenter where we have

$$\frac{\partial x_{N_c+1,j}}{\partial \xi} = 0 = U_{1,4,j} \frac{\partial a_{11}}{\partial \xi} + U_{1,5,j} \frac{\partial a_{12}}{\partial \xi} + U_{1,6,j} \frac{\partial a_{13}}{\partial \xi} + W_j \quad (5.70)$$

$$W_j = U_{1,1,j} \frac{\partial x_{11}}{\partial \xi} + U_{1,2,j} \frac{\partial x_{12}}{\partial \xi} + U_{1,3,j} \frac{\partial x_{13}}{\partial \xi} + U_{1,7,j} \quad (5.71)$$

$j = 1, 2, 3$

The left hand side of Equation (5.70) holds to be true as the station coordinates in the present problem are well known and fixed. The value of parameter W_j in Equation (5.71) is exactly known at the point of hypocenters because:

$$\left. \begin{aligned} \frac{\partial x_{1j}}{\partial \lambda_j} &= 1 \quad \text{when } \xi = \lambda_j \\ &= 0 \quad \text{when } \xi \neq \lambda_j \end{aligned} \right\} \quad (5.72)$$

Equation set (5.70) can be solved for $\frac{\partial a_{1j}}{\partial \xi}$ as there are three unknown and three known

parameters. In other words it is always possible to know $\frac{\partial x_{1j}}{\partial \lambda_j}$ and $\frac{\partial a_{1j}}{\partial \xi}$ for all three value of

j . Once for a ray path $\frac{\partial x_{1j}}{\partial \lambda_j}$ and $\frac{\partial a_{1j}}{\partial \xi}$ for three values of j are known, all the derivatives in

recursive Equations (5.62) and (5.64) can be solved. The ordinate derivatives are then used to obtain length derivatives in Equation (5.35) which help ultimately to solve all the derivatives in Equation (5.33) for a ray path.

5.6 ALGORITHM TO COMPUTE FRÉCHET DERIVATIVES

We present an algorithm in this section to solve Fréchet derivatives for a single ray path between source and station using surface function given in Equation (5.2). The algorithm consists of three basic units namely, *TOF*, *COF* and *DEVL* which respectively compute coefficients in Equation set (5.64), (5.62) and solve Equation (5.33) for the required derivatives. Algorithm of the unit *TOF* is shown in Figure 5.5.

The variable integer, *ind* in the algorithm is used to decide the type of model parameter with which the derivatives are required. Its 1, 2, 3 value correspond to hypocenter ordinates $\lambda_1, \lambda_2, \lambda_3$, 4 value correspond to model parameter slowness, s and 5 value correspond to layer parameters, g . Variable integer *in* is an array of dimension three where

$in(1), in(2)$ correspond to i, j respectively and $in(3)$ indicate q in Equation (5.2). Variable $intpt$ is an array of dimension 2 and it stores the coordinates of all the elementary points of a ray path. Variable npt is total number of elementary points, N_c in the ray path. Variable cf is an array of dimension three which defines g in Equation (5.2) with r being the first dimension, i and j respectively second and third dimension. Variable ink is a one dimension array that store value of function Π . Variable rf is an array of one dimension that carries the value of F_r and variable s is an array of one dimension that store slowness of all the layers in the model. The output of this algorithm is all the coefficients, B_{rjk} in Equation (5.57).

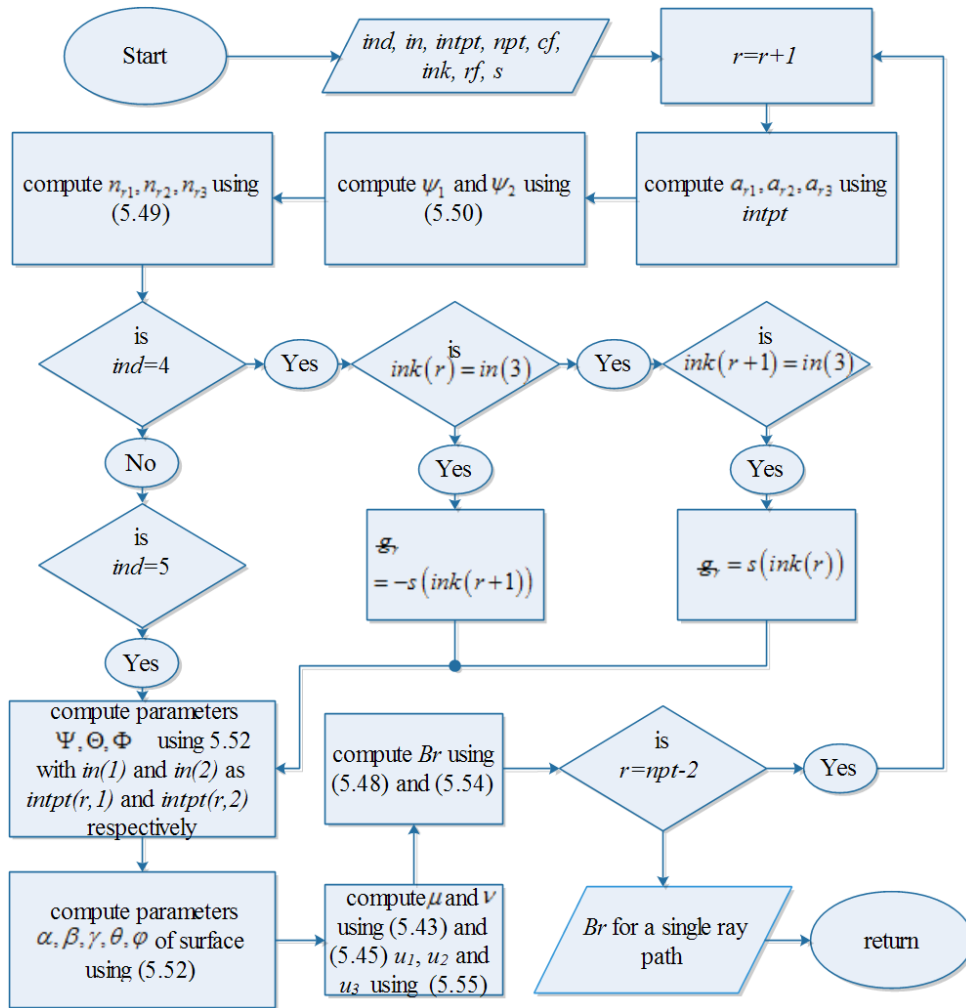


Figure 5.5: A unit of algorithm to compute coefficients B in Equation (5.57) for a source station ray path.

The unit COF which computes all the coefficients, C_{rkj} in Equation (5.62) is shown below in Figure 5.6. Once the coefficients, B_{rkj} and C_{rkj} are computed using sub processes TOF and COF, the rest of the operations to obtain derivatives in Equation (5.33) can be combined into a single sub process DEVL, which compute length derivative either $\frac{\partial l_r}{\partial \xi}$ in Equation (5.33). This DEVL is shown in Figure 5.7.

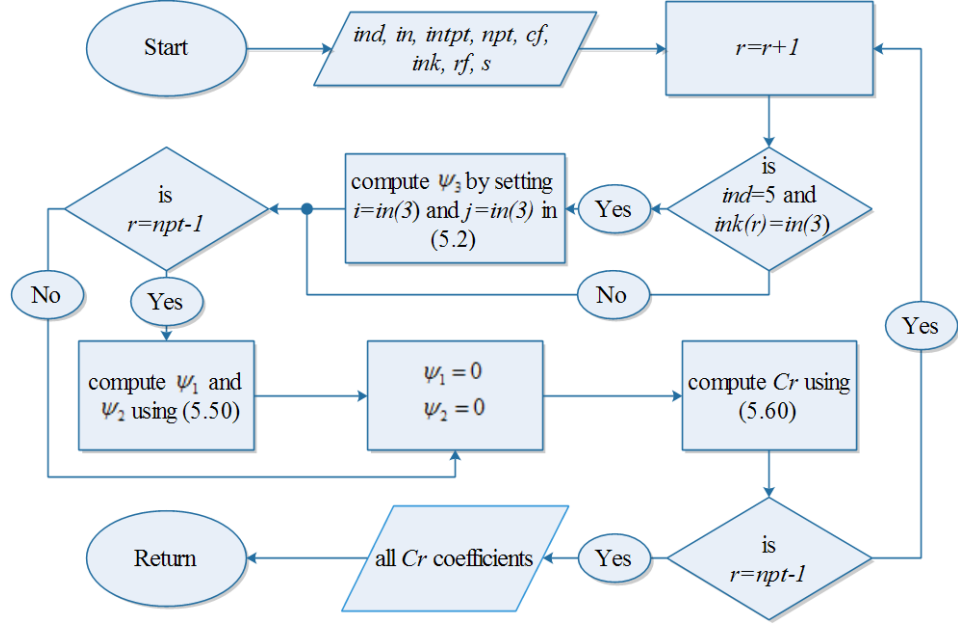


Figure 5.6: A unit of algorithm to compute coefficients C in Equation (5.64) for a source station ray path.

The unit DEVL performs operations: conversion of B_{rkj} to C_{rkj} using Equation (5.65), conversion of C_{rkj} to U_{rkj} using Equation (5.69), reduction of U_{rkj} to $U_{1,k,j}$ using equation (5.68), computation of $\frac{\partial a_{11}}{\partial \xi}, \frac{\partial a_{12}}{\partial \xi}, \frac{\partial a_{13}}{\partial \xi}$ using $\frac{\partial x_{11}}{\partial \xi}, \frac{\partial x_{12}}{\partial \xi}, \frac{\partial x_{13}}{\partial \xi}$ and Equation (5.70), solution for $\frac{\partial x_{rj}}{\partial \xi}$ and $\frac{\partial a_{rj}}{\partial \xi}$ using Equations (5.62) and (5.64) and finally the length derivatives, $\frac{\partial l_r}{\partial \xi}$ appeared in Equation (5.33) using relation in Equation (5.32). The variable real array, d and ld used in DEVL are respectively of two dimensions and one dimension and help to sum up the whole sub process. The real variable array len is of one dimension and store all l_r in Equation (5.32).

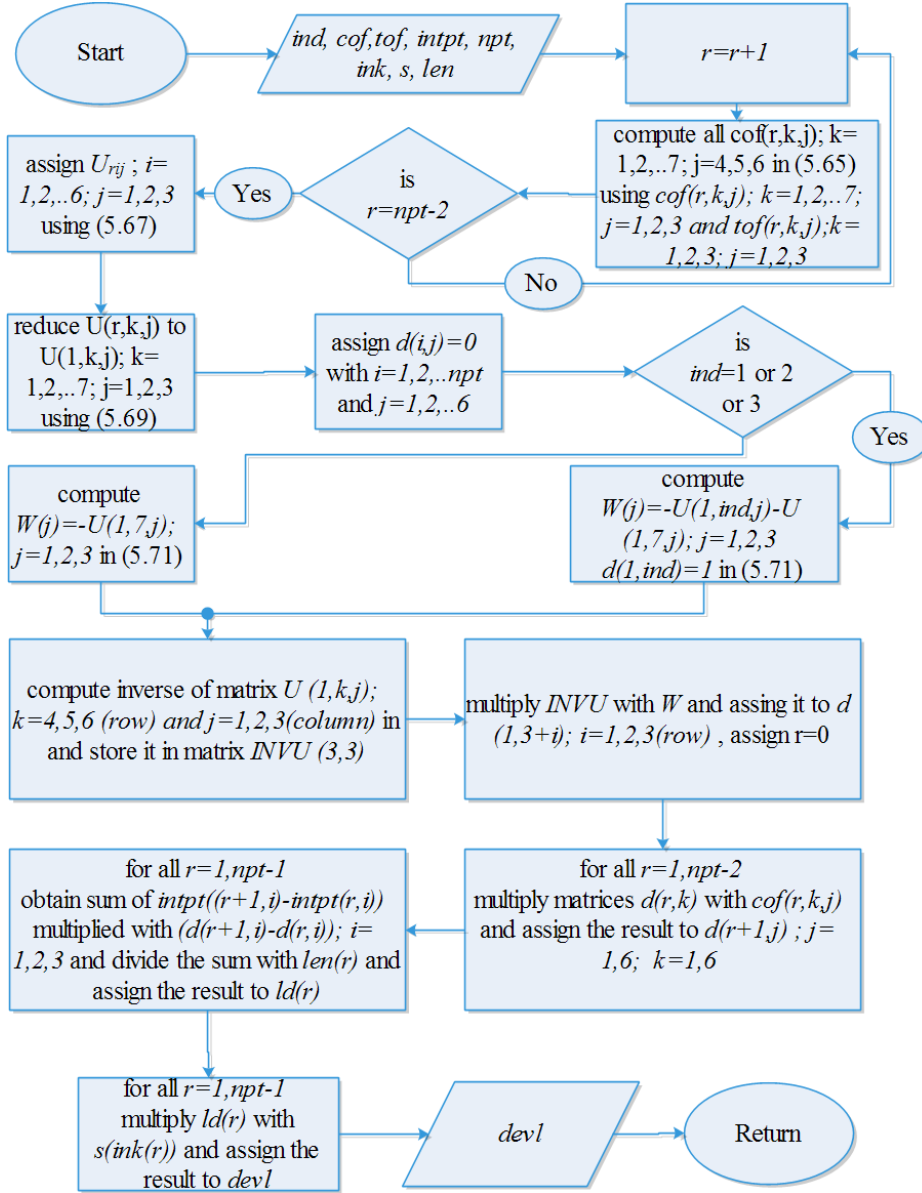


Figure 5.7: A unit of algorithm, DEVL to compute length derivatives in Equation (5.33).

The unit TOF, COF and DEVL are combined using three switches SW1, SW2 and SW3 to construct an algorithm, IL-P to compute desired types of Fréchet derivatives. When switch SW1 is 1 the algorithm IL-P gives derivatives, ldx of traveltime with respect to hypocenters. When switch SW2 is 1 the algorithm gives derivatives, lds of traveltime with respect to body wave slowness, s and when switch SW3 is 1 the same algorithm gives derivatives, ldh of traveltime with respect to layer parameters, g which can be converted to the derivative with respect to modified layer parameter, κ using relation given in §5.3. The real variable arrays ldx , lds and ldh are of one dimension. The new integer variable nsp carries the layer number in which the source lies.

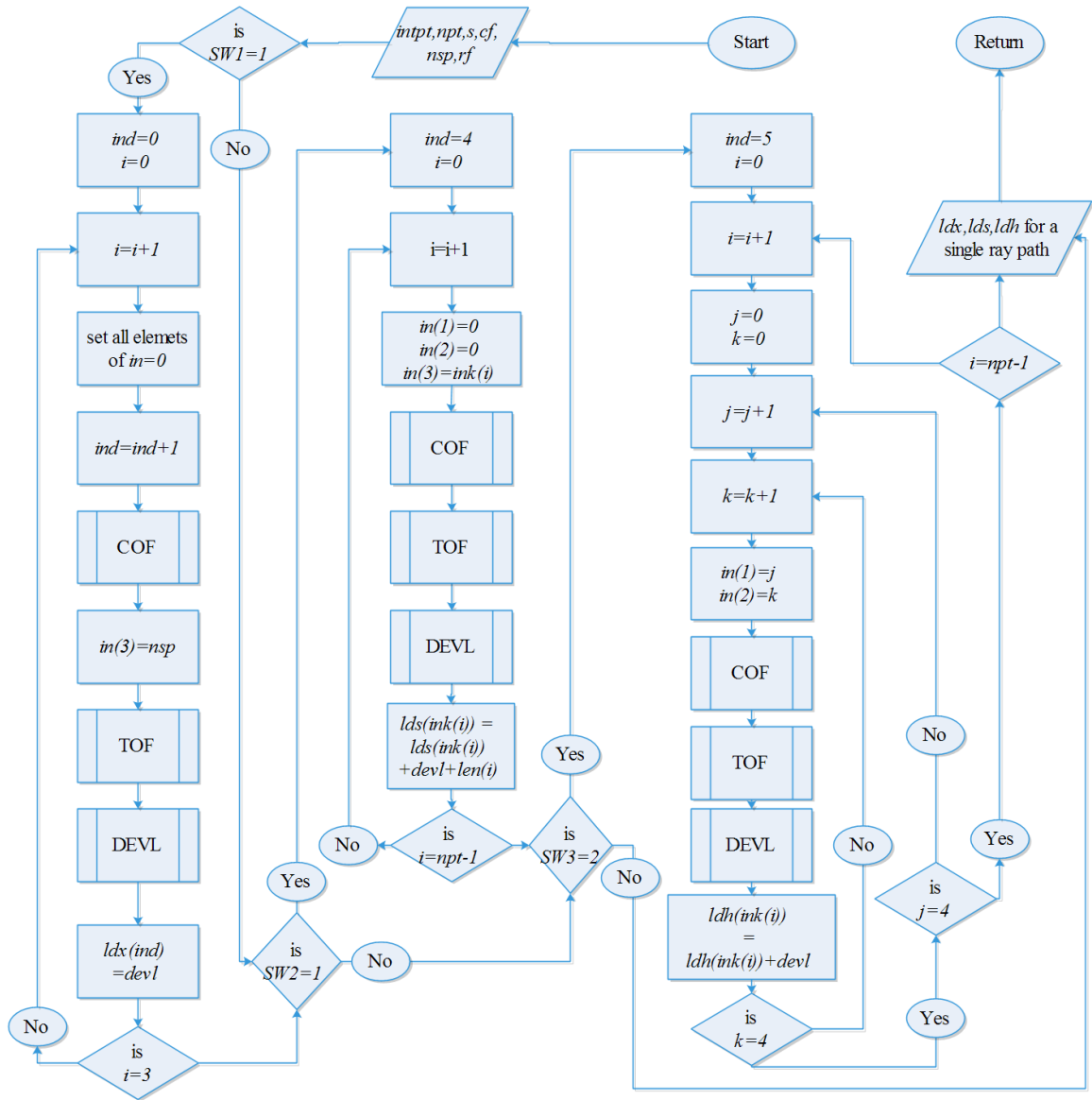


Figure 5.8: Integrated algorithm to compute Fréchet derivatives for a source-station ray path.

5.7 ALGORITHM TO INVERSION

An algorithm to tomographic inversion using Damped Least Square method given in Chapter 1 is presented in Figure 5.9. There are five basic sub processes which are integrated as in Figure 5.9 to solve the tomographic inversion. These sub processes for simplicity of discussion are named as follows:

- 1) **Traveltime Computation:** It computes total traveltime of a ray-path connecting a source and a station. The forward problem discussed in Chapter 2 gives the idea to obtain the elementary points of ray-paths. Once the elementary points of a ray path are determined, the elementary traveltimes for the same ray-path is determined by multiplying the length segments between two adjacent elementary points with the

slowness of the layer between those two points. The outputs of this sub-process are elementary points and total traveltimes of all source-station ray paths as well as the refraction coefficient, F and function Π in Equation (5.39) and Equation (5.29) respectively. The refraction coefficient, F and function, Π are computed during the solution of forward problem.

- 2) Fréchet Derivatives: It computes the whole matrix, \mathbf{M} in Equation (5.25) for all ray-paths for a given number of source and station, using algorithm given in §5.8. It also computes $\mathbf{M}^T\mathbf{M}$ from \mathbf{M} .
- 3) Maximum Eigen value: it computes the maximum Eigen value using a standard method.
- 4) DLS Inversion: It inverses $[\mathbf{M}^T\mathbf{M} + \lambda_l\mathbf{I}]$ using a standard matrix inversion method such as inversion using Gauss Seidel Iteration Method with complete pivoting (Xavier, 2006).
- 5) Model Update: A new model is created using $\mathbf{m}_{new} \approx \mathbf{m}_{old} + [\mathbf{M}^T\mathbf{M} + \lambda_l\mathbf{I}]^{-1} \mathbf{M}^T \Delta\Gamma$.

Variable S, P, C, T and IT are of integer types, where IT represents number of iteration in the inversion process and rest variables are self defined in the algorithm. The Eigen value, λ_l in $[\mathbf{M}^T\mathbf{M} + \lambda_l\mathbf{I}]$ is determined iteratively by choosing the least root mean square error in traveltimes between observed and computed after temporarily updating the model, \mathbf{M} . In the beginning the eigen value is chosen to be the maximum Eigen value of $\mathbf{M}^T\mathbf{M}$ and in each iteration the eigen value is reduces by half to perform next iteration. During the process of iteration the switch S remain in zero state. The maximum number of iteration allowed is N. Since, every single iteration to update the model, the process for eigen value computation requires N number of iteration, therefore for a total of ITM number of iteration, the total iteration is $N \times ITM$ which is sometimes become very large and hence the computation process becomes slower. To remove this problem we have used three integer variables P, C and T as controlling parameters in the algorithm. Here, once an eigen value is iteratively determined, it continues to update the model 2 times and then it reduces by half. This process continues unless the value of parameters P becomes 10 or root mean square (rms) traveltime error, E exceed the rms traveltime error, E_p computed one step earlier.

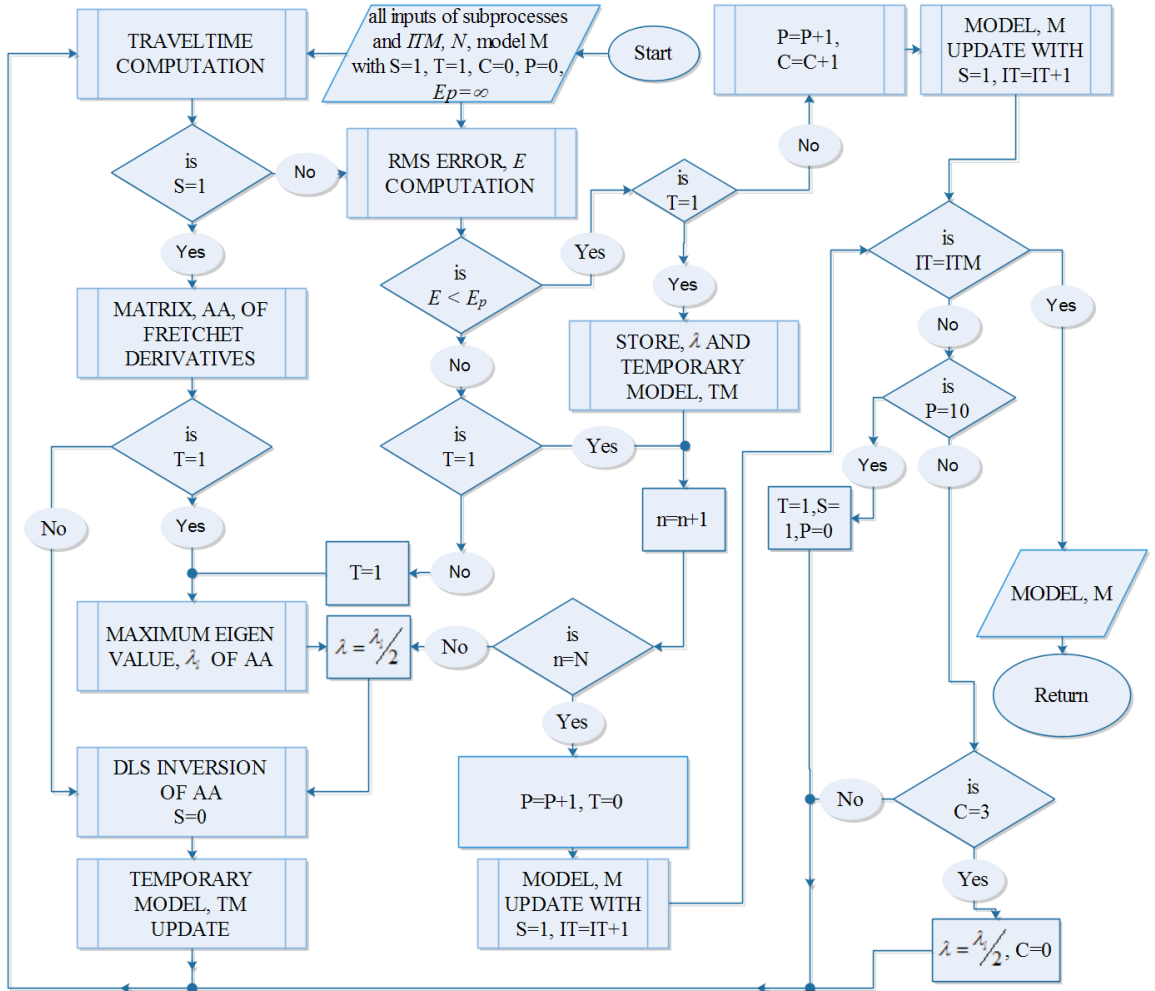


Figure 5.9: The work flow tomographic inversion using DLS inversion.

5.8 GRADIENT PATH SEARCH METHOD (GPSM)

Equations (5.62), (5.64) and (5.68) are used to obtain the derivative of ray path with respect to source position in terms of change in ordinates of elementary points of ray path and change in unit vector parallel to ray path segments connecting two adjacent elementary points when a small change in source position is made. The same equations can be used to obtain derivative of position coordinates of any station on the surface of model, with respect to take off vector. Here the final intersection point between ray path and model surface is variable and the hypocenter is fixed so it is a one point boundary problem and is solved in the following way.

Consider $\xi \in (x_{N_c,1}, x_{N_c,2}, x_{N_c,3})$ where N_c indicate elementary point corresponding to station. As the hypocenter is fixed therefore from Equation (5.71)

$$\frac{\partial x_{11}}{\partial \xi} = \frac{\partial x_{12}}{\partial \xi} = \frac{\partial x_{13}}{\partial \xi} = 0 \text{ and } W_j = U_{1,7,j}; \quad j = 1, 2, 3$$

Using these results the Equation (5.70) becomes

$$\frac{\partial x_{N_c+1,j}}{\partial \xi} = U_{1,4,j} \frac{\partial a_{11}}{\partial \xi} + U_{1,5,j} \frac{\partial a_{12}}{\partial \xi} + U_{1,6,j} \frac{\partial a_{13}}{\partial \xi} + U_{1,7,j}; \quad j = 1, 2, 3 \quad (5.73)$$

Which can be written in matrix form as:

$$\begin{bmatrix} \delta(1,k) - U_{1,7,1} \\ \delta(2,k) - U_{1,7,2} \\ \delta(3,k) - U_{1,7,3} \end{bmatrix} = \begin{bmatrix} U_{1,4,1} & U_{1,5,1} & U_{1,6,1} \\ U_{1,4,2} & U_{1,4,2} & U_{1,4,2} \\ U_{1,4,3} & U_{1,4,3} & U_{1,4,3} \end{bmatrix} \begin{bmatrix} \frac{\partial a_{11}}{\partial x_{N_c+1,k}} \\ \frac{\partial a_{12}}{\partial x_{N_c+1,k}} \\ \frac{\partial a_{13}}{\partial x_{N_c+1,k}} \end{bmatrix} \quad (5.74)$$

Which further can be written as:

$$\begin{bmatrix} \frac{\partial a_{11}}{\partial x_{N_c+1,k}} \\ \frac{\partial a_{12}}{\partial x_{N_c+1,k}} \\ \frac{\partial a_{13}}{\partial x_{N_c+1,k}} \end{bmatrix} = \begin{bmatrix} U_{1,4,1} & U_{1,5,1} & U_{1,6,1} \\ U_{1,4,2} & U_{1,4,2} & U_{1,4,2} \\ U_{1,4,3} & U_{1,4,3} & U_{1,4,3} \end{bmatrix}^{-1} \begin{bmatrix} \delta(1,k) - U_{1,7,1} \\ \delta(2,k) - U_{1,7,2} \\ \delta(3,k) - U_{1,7,3} \end{bmatrix} \quad (5.75)$$

Consider the following:

$$\begin{bmatrix} U_{1,4,1} & U_{1,5,1} & U_{1,6,1} \\ U_{1,4,2} & U_{1,4,2} & U_{1,4,2} \\ U_{1,4,3} & U_{1,4,3} & U_{1,4,3} \end{bmatrix}^{-1} = \begin{bmatrix} V_{1,4,1} & V_{1,5,1} & V_{1,6,1} \\ V_{1,4,2} & V_{1,5,2} & V_{1,6,2} \\ V_{1,4,3} & V_{1,5,3} & V_{1,6,3} \end{bmatrix} \quad (5.76)$$

Using Equation (5.75) and (5.76) the derivatives of takeoff vector can exclusively be written as:

$$\frac{\partial a_{1j}}{\partial x_{N_c+1,k}} = (V_{1,4,j} \delta(1,k) + V_{1,5,j} \delta(2,k) + V_{1,6,j} \delta(3,k)) - (V_{1,4,j} U_{1,7,1} + V_{1,5,j} U_{1,7,2} + V_{1,6,j} U_{1,7,3}) \quad (5.77)$$

Where, $j = 1, 2, 3$, $k = 1, 2, 3$ and δ is delta Dirac function defined as:

$$\left. \begin{aligned} \delta(j,k) &= 1; & j &= k \\ &= 0; & j &\neq k \end{aligned} \right\} \quad (5.78)$$

As we can see in Equation (5.77) that the change in any ordinate of elementary points of a ray path is associated with the change in all three components of takeoff vectors, the inverse is also true; either the change in any one take off vector at hypocenter is associated with the change in all three component of basis vectors of ray path. This statement is not only true at hypocenter rather it is true for all the points in the basis of ray path and corresponding take off vectors (Equation 5.62 and 5.64). Therefore the total derivative of takeoff vector at hypocenters can be written as:

$$\begin{aligned}
da_{1j} &= \sum_{k=1}^3 \frac{\partial a_{1j}}{\partial x_{N_c+1,k}} dx_{N_c+1,k} \\
&= \sum_{k=1}^3 dx_{N_c+1,k} \left[V_{1,3+k,j} + \sum_{i=1}^3 V_{1,3+i,j} U_{1,7,i} \right]; \quad j=1,2,3
\end{aligned}
\tag{5.79}$$

Equation (5.79) describe the total change in unit take off vector corresponding to a change in final ray point and hence this forms the basic equation to obtain the true takeoff vector at hypocenter position in other word an initial takeoff vector that position the ray such as the final point nearly or completely math with the station position. An algorithm to the whole process is given below in Figure 5.10.

Variable array W in the algorithm is of three dimensions which store the discrepancies between ordinates of N_c th elementary point and station and is defined as:

$$W(j) = x_{station,j} - x_{N_c,j}; \quad j=1,2,3 \tag{5.80}$$

Variable array ota and nta correspond to old and new take off vector at hypocenter, either these are $a_{1j}; \quad j=1,2,3$ and rest of the variables used in the algorithm is defined in §5.6.

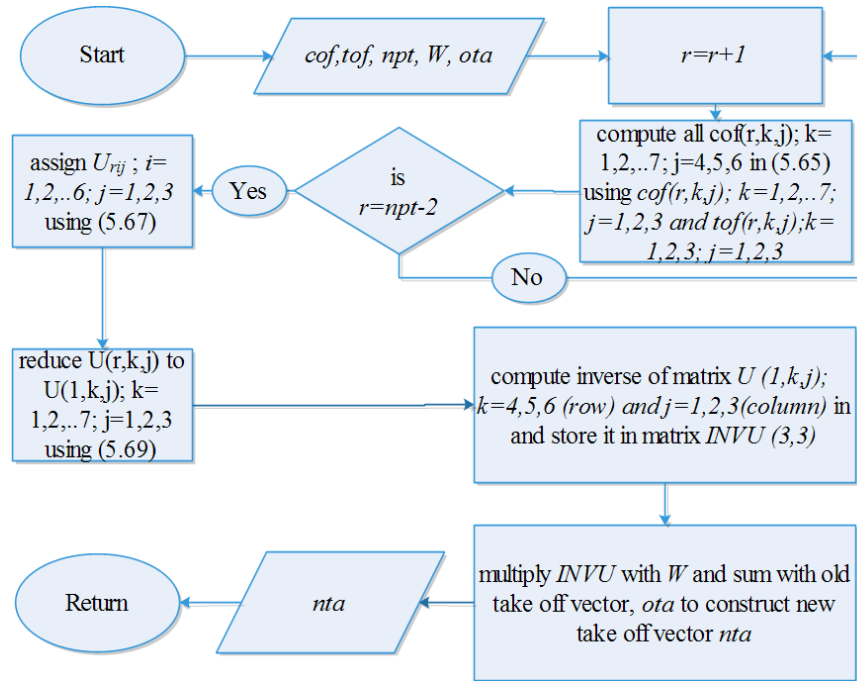


Figure 5.10: An algorithm (IL-Q) to update the takeoff vector at the position of a hypocenter using GPSM.

5.9 JOINT WORKING OF GPSM AND SPSM

An incomplete algorithm without input variables, using integrated algorithms IL-A (described in Chapter 3 in Figure 3.6) and IL-Q is shown below in Figure 5.11. It computes

point series and *block series* defined in Chapter 3, only if an initial W (in Equation 5.80) is supplied. Variable integer IN2 is maximum number of iteration required by this algorithm to get a true take off vector for a ray path under admissible error, gme ; which is considerable value defined as:

$$gme = \sqrt{W(1)^2 + W(2)^2 + W(3)^2} \quad (5.81)$$

The value of gme , in every iteration, is compared with minimum error of a ray path, supplied by integrated algorithm IL-A.

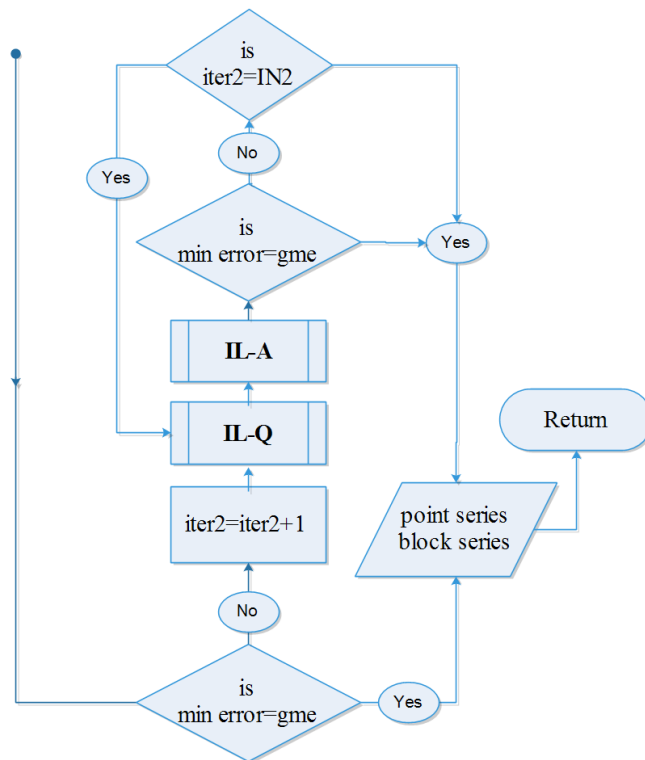


Figure 5.11: A part of an algorithm to solve forward problem using Gradient Path Search Method.

As one of the outputs of IL-C is W , therefore, a new complete algorithm joining GPSM and SPSM can be given if the round node of incomplete algorithm in Figure 5.11 is connected to point, \mathcal{F} in IL-C. As IL-C is primarily a scanning process so it is essential to assign a small value to IN1 in IL-C so as to make it faster. The small value of IN1 may not give the true ray path with admissible error, gme however combine working of incomplete algorithm (Figure 5.11) give nearly the true ray path in just 7 to 8 iteration. In other words the resultant algorithm gives faster result. The scanning process in SPSM search true take off vectors at hypocenter in a particular constant step and hence the possible degree of accuracy in a given number of iteration is less compared to GPSM as it is based on inverse theory and do not search takeoff angle in a constant step. Although the combined operation of GPSM and SPSM is expected to give faster and accurate results, however the optimal values for IN1

and IN2 are subjected to the complexity of a particular problem and hence to a faster results in forward computation these constants (IN1 and IN2) must be determined by numerical tests.

5.10 CONCLUSIONS

A Multiparameter Inversion method is presented in this chapter. This method simultaneously inverts P-phase and S-phase to compute body wave velocities, layer parameter and hypocenter with origin time. These model parameters can be determined individually or separately with the help of three switches, SW1, SW2 and SW3 which are discussed in §5.6. As compared to straight layer model of earth, the model used to derive the formulation is more close to the real earth and hence can be used to resolve the discontinuity present in the subsurface structure. Because of the 3D nature of the discontinuity surfaces the refraction is considered along with reflection to compute the proper first arrival ray path rather than false one. An algorithm of tomography using damped least square method is given in §5.7. The speed of the total processes is increased by the introduction of integer variable C, P and T. The Gradient Path Search Method (GPSM) and the combined working GPSM and Spiral Path Search Method in forward computation are also discussed later in this Chapter. As the GPSM is based on inverse theory, therefore unlike Spiral Path Search Method (SPSM), the GPSM do not search take off vector in a constant steps, which increase the chance of getting more accurate source station ray path. The SPSM is primarily a scanning method and hence the time take to achieve an admissible error in ray path computation is more compared to GPSM. As the GPSM need some initial value of discrepancy between station ordinates and elementary point of ray path close the station, therefore we consider the working of SPSM followed by GPSM.





SEISMICITY AND SUBSURFACE STRUCTURES OF THE KUMAON HIMALAYA

6.1 INTRODUCTION

The body wave velocity of a homogeneous and isotropic medium is related to elasticity and density of that medium. As the different layers of earth have different elasticity and density, therefore, accurate knowledge of body wave velocities of the earth has remained one of the most important keys from the beginning of seismology to investigate the internal structure of the earth (§1.1) both for research and exploration purpose. Besides, the study of Earth's internal structural, the knowledge of subsurface velocity is important to locate earthquake, to study seismicity, to generate synthetic seismogram, to obtain attenuation and hazard map (Shapiro et al., 2000) which help to determine several crucial parameters in building and damp construction.

There exists many methods for the determination of seismic velocity; however, its accurate determination is still challenging and most common problems both in earthquake and exploration seismology. The problem is less difficult for a known region, having simpler subsurface structures, where some studies related to subsurface velocity have already is available. However, the same problem becomes more difficult for a virgin region having complex terrain like the Himalayan belt. This problem is further complicated due to scarcity of data in complex terrain. This is the case with the Kumaon Himalaya in and surrounding region of Pithoragarh district, Uttarakhand. Due to scarcity of data in this region the in-depth knowledge of velocity is poor.

One way of increasing the amount of information from the data is by considering more than one type of waves such as first arrival P- and S-phases. These phases contain

precious information of subsurface structure through which these propagate from the position of sources to the observation points. Therefore it is highly essential before looking for any detailed velocity structure that the positions of sources or the hypocenters must be located or relocated to their true positions.

The raw data that is extracted from a seismograph in travelttime inversion are first arrival P- and S- phases in standard time units. To convert these standard time units to travelttime of phases it is essential to obtain the origin times in simultaneous with hypocenters. Preliminary locations of hypocenters and origin times of earthquakes (together called as hypocenter parameters) in a region are generally obtained using a 1D velocity model of that region. Once the preliminary locations of hypocenters and origin times are obtained, the simultaneous inversion is desired to improve velocity model as well as locations of hypocenters and origin times. This is required because velocity parameter of a model alone cannot be forced any how to satisfy the data due to various structural constraints of the model and due to its intimate relationship with the hypocenters (sources) as given in Equation (1.3). The simultaneous inversion for velocity and hypocenter parameters is done in 1D, 2D or 3D study depending on the requirements. If a 1D velocity model and a set of hypocenter parameters are used as initial model parameters in 2D simultaneous inversion that results in 2D velocity and hypocenters parameters with insignificant change hypocenters distribution then it is sufficient to lock these before proceeding for 3D velocity study to avoid unnecessary computation.

In the present study, both P- and S phases are considered for the study of hypocenters and velocity models. Hypocenters are located first by using 1D reference velocity model given by Mukhopadhyay (2008) and the developed algorithm presented in Chapter 5. The obtained hypocenters and 1D velocity model are then simultaneously recalculated using the same algorithm. The travelttime (data) residuals are analyzed before and after the inversion process. The resultant 1D velocity model and hypocenters are then used as initial parameters for development of 2D velocity model and for further improvement of hypocenters location. Once the 2D velocity model is obtained the location of hypocenters are locked and 3D velocity model are obtained using a tomography method that is presented in this Chapter.

The relocated hypocenters are explained in terms of seismicity of the Kumaon Lesser Himalaya and compared with other zone of Himalayan belt. The velocity models are analyzed using resolution parameters and the same are discussed and compared with other study.

6.2 STRONG MOTION NETWORK AND DATA

The presents study area come under Kumaon region of Lesser Himalaya including the districts of Pithoragarh, Bageswar and some portion of Champawat district. The region including Pithoragarh and Bageswar is bounded by the MCT in the north and North Almora Thrust (NAT) in the south. The only station which our study area covers in the districts of Champawat is Lohaghata. Under different projects of Ministry of Earth Sciences (MoES), a total of 15 mobile strong motion seismographs of Kinematics, USA have been installed in these areas in 18 locations in recent past. Table 6.1 summarizes the detailed position of the instrument with station height above Mean Sea Level (MSL). The station names are coded with four letters to figure the same in appropriate map. A map view of the station position is shown in the tectonic map covering study area in Figure 6.1; where solid triangles show the position of stations. Seismographs in this network from 2006 to 2012 have recorded several earthquakes in all three components. A total of 373 first arrival P phases and a total of 497 first arrival S phases from 116 earthquakes are picked up for arrival times with the help of QLWIN quick look software supplied by Kinematics Inc., which serves as data for the present study.

Table 6.1: Strong Motion Network

Sl. no.	Station name	Station code	Longitude in degree	Latitude in degree	Station height in meter
1	Askot	ASKT	80.33	29.76	1258
2	Baluakot	BLKT	80.42	29.79	644
3	Berinag	BENG	80.05	29.77	1684
4	Bageshwar	BGSR	79.77	29.83	873
5	Dharchula	DRCL	80.53	29.84	935
6	Didihat	DDHT	80.25	29.80	1628
7	Joljibi	JLJB	80.38	29.75	612
8	KamediDevi	KMDD	79.96	29.84	1820
9	Knalichina	KNLC	80.27	29.67	1656
10	Lohaghat	LGHT	80.08	29.39	1630
11	Mangti	MNGT	80.71	30.00	1609
12	Muwani	MWNI	80.13	29.74	822
13	Munsyari	MNSR	80.25	30.06	2100
14	Pithoragarh	PTGR	80.21	29.58	1574
15	Sobla	SBLA	80.58	30.05	1628
16	Tejam	TJAM	80.12	29.95	968
17	Thal	THAL	80.14	29.82	783
18	Kapkot	KPKT	79.89	29.94	1133

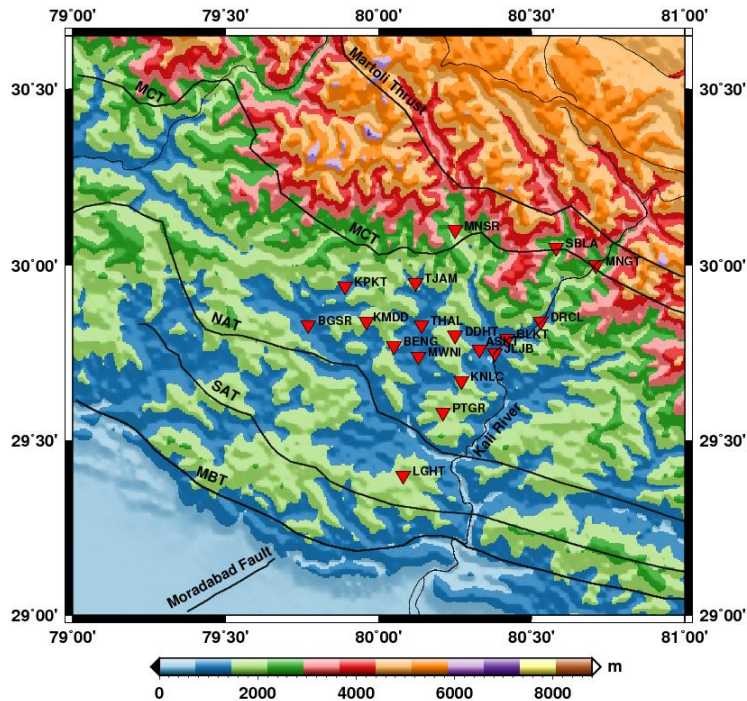


Figure 6.1: Overview map with the topography and major tectonic settings of the Himalayan terrain covering the Kumaon Lesser Himalaya. The strong motion stations of local network are marked by red solid triangles.

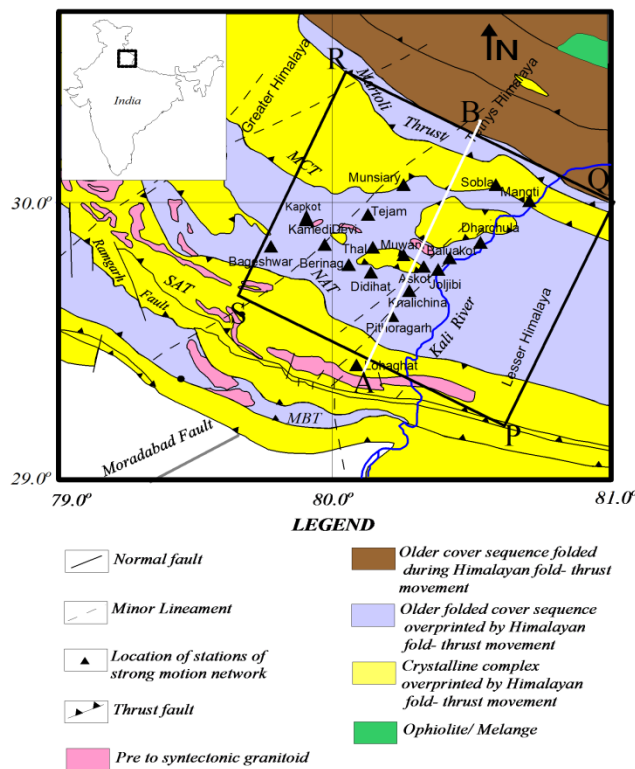


Figure 6.2: The geology and tectonic setting of the region after Dasgupta et al. (2000). The study region is marked by rectangle SPQR. Direction from A to B, marked by white line dividing the rectangle SPQR into two equal halves and making an angle of 26° with respect to north, is the direction along which vertical section of velocity structure is investigated. Locations of seismographs are denoted by solid black triangles.

For simplicity of discussion, the geological map showing the study region with major tectonic features and station locations is shown in Figure 6.2. The study region which has been considered for determination of 3D velocity structures is marked by rectangle SPQR. The direction of white line is 26° NE and it is the direction along which the two dimensions velocity structures have been investigated.

6.3 SEISMICITY AND 1D VELOCITY MODELS OF KUMAON HIMALAYA

Seismicity of a region are generally explained in terms of distribution of earthquakes occurred in that region in past. Velocity information is essential to obtain accurate earthquake location. The velocity and hypocenters are intimately related quantity (Equation 1.3), therefore it is better to consider simultaneous computation of these parameters instead of computing any one of these at a time. This has been practically carried out for the data of Kumaon Himalaya and is described below.

6.3.1 Practical consideration and Method

The lithosphere of the study region up to a depth of 75 km (72 km below msl and 3 km above msl) is divided into 25 horizontal straight layers each having equal thickness. Seismic velocity is defined with the help of an appropriate 1D velocity model. 1D velocity model strictly for the region under consideration is not available. However a regional velocity model can be considered in this case after testing the same for its error in the inversion scheme. Some of the important 1D velocity models are those given by Mukhopadhyay and Sharma (2010a), Yu et al. (1995) and Monsalve et al. (2006). These models are tabulated in Table 6.2, where V_p and V_s represent seismic velocity for P and S wave respectively.

The algorithm for multiparameter inversion presented in Chapter 5 is considered to generate velocity model as well as to compute the locations of hypocenters. A sum of 870 first arrival observation times of P and S phases have been considered as data. With the help of multiparameter inversion algorithm, three tests were performed using three given velocity models and the final results were checked in terms of root mean square errors (rms) computed between observed arrival times and computed arrival times corresponding to all the three models. It has been found that the 1D velocity model reported by Mukhopadhyay and Sharma (2010a) gives least rms error and hence this was selected as initial 1D velocity model for the study. With this 1D velocity model and observed arrival times of body wave phases, hypocenters of all the considered earthquakes were determined. The located hypocenters and 1D velocity model were then considered simultaneously in the

multiparameter inversion scheme to accurately compute these parameters. The computed 1D velocity model and refined hypocenters were later used in developing 2D and 3D velocity structures.

Table 6.2: 1D Velocity Models in the Himalayan Terrain

Garhwal-Kumaon (Mukhopadhyay and Sharma, 2010a)			Uttarkashi (Yu et al., 1995)			North-East Nepal (Monsalve et al., 2006)		
Depth (km)	V _p (km/s)	V _s (km/s)	Depth (km)	V _p (km/s)	V _s (km/s)	Depth (km)	V _p (km/s)	V _s (km/s)
00-10	5.47	3.05	0-0.4	3.50	2.00	0-2.7	5.40	3.25
10-15	5.92	3.29	0.4-1.4	5.00	2.86	2.7-23.2	5.64	3.25
15-20	5.98	3.51	1.4-16.4	5.20	2.97	23.2-55	6.30	3.65
20-30	6.22	3.51	16.4-46.4	6.00	3.43	55-∞	8.11	4.54
30-50	6.64	3.84	46.4-∞	8.33	4.83			
50-∞	8.21	4.75						

6.3.2 Results

The results of this inversion have been presented in Figure 6.3, 6.4, 6.5 and Table 6.3. Figure 6.3(a) shows the epicenters of the located earthquakes. Major tectonics of the study area is shown by solid black lines and the located epicenters are marked by blue circles. Figure 6.3(b) shows a zoomed version of the same figure (Figure 6.3(a)) between latitude 29.5-30.5° and longitude 80-81°. This shows that number of earthquakes along MT is greater than the same along MCT. Figure 6.3(c) shows the latitude versus depth section of the event locations whereas Figure 6.3(d) shows the longitude versus depth section of the event locations. In both these figures, the probable location of Indian moho is marked by discontinuous red lines. In Figure 6.3(c), the probable depth range of MHT is also marked by discontinuous red lines.

Figure 6.3(e) shows the initial root mean square (rms) error for traveltime residuals, which were obtained in the beginning when the data were set to the initial velocity models. Figure 6.3(f) shows the same rms traveltime residuals after final iteration of inversion of the algorithm. The located events have also been given in a topographic map in Figure 6.4 in which yellow filled circles are located epicenters of events, red solid triangles are stations.

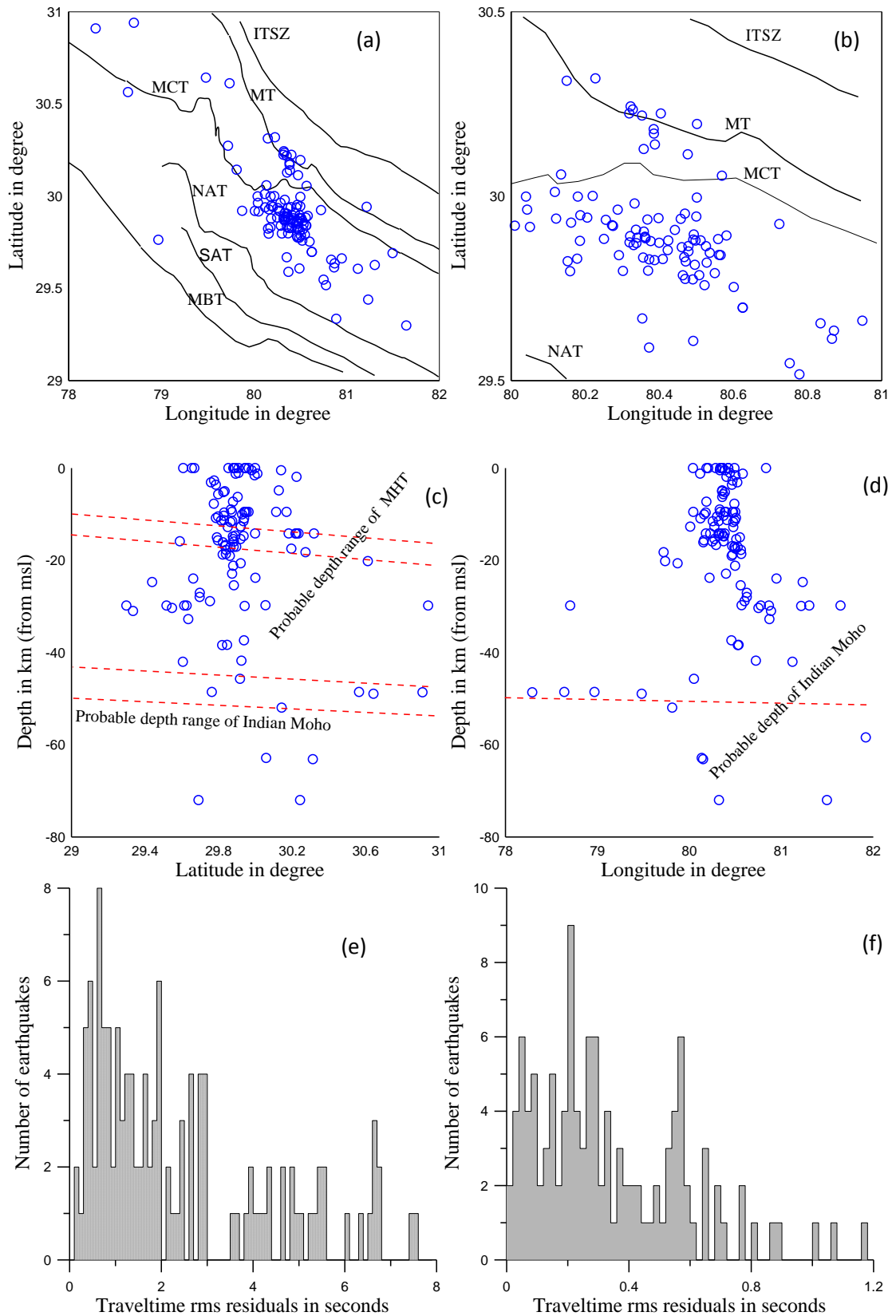


Figure 6.3: The above figures depict epicentral distribution of relocated earthquakes, (a); an enlarge view of figure (a), (b); depth wise distribution along constant longitudes, (c); depth wise distribution along constant latitudes, (d); initial rms traveltime residuals, (e); final rms traveltime residuals, (f).

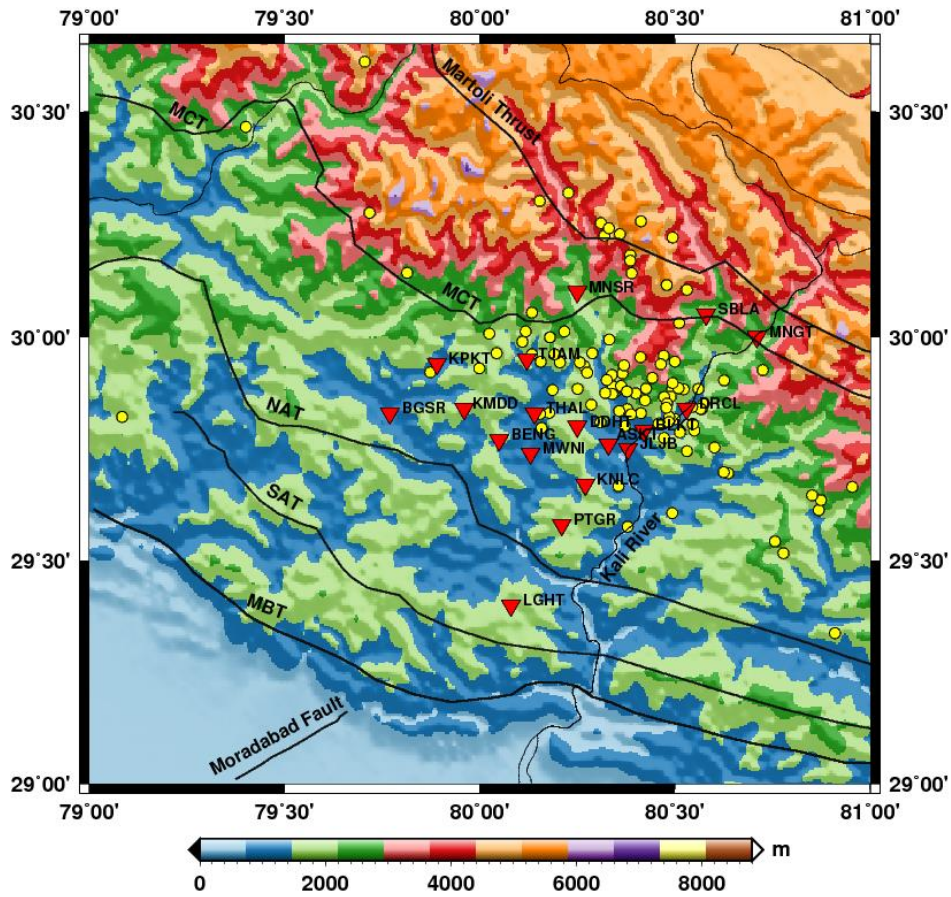


Figure 6.4: Map showing the positions of relocated events.

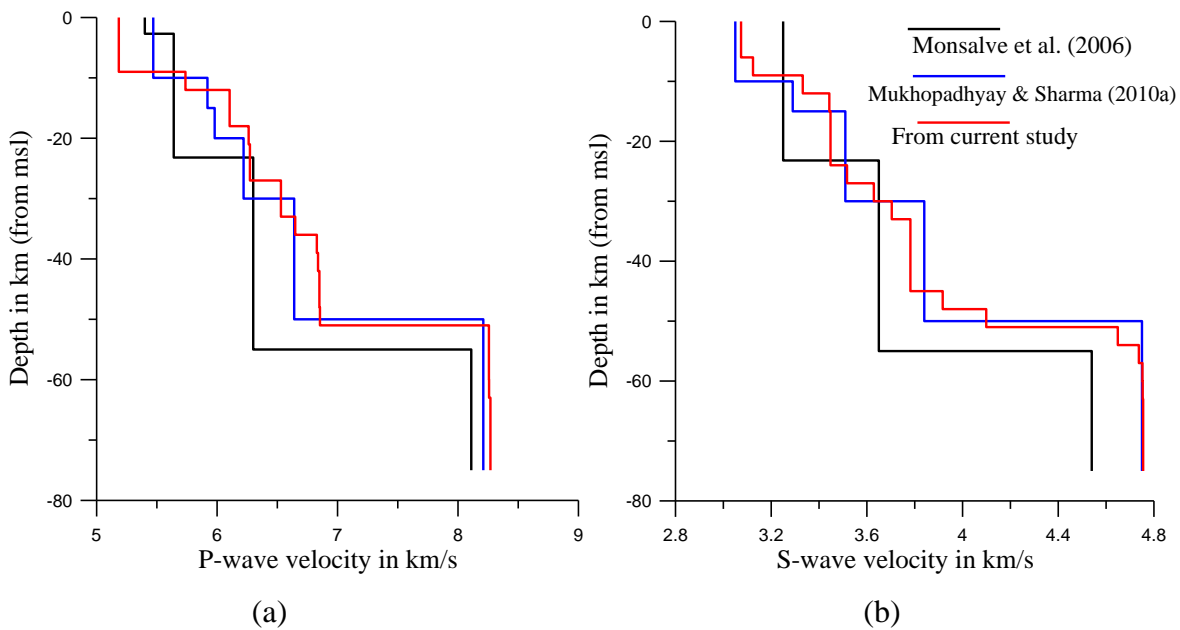


Figure 6.5: The above figures show the 1D velocity models of the Himalayan terrain. With the obtained velocity models shown by red line plot, two other velocity models for P-waves and S-waves given by Mukhopadhyay and Sharma (2010a) and Monsalve et al. (2006) are also shown to study the depth variation of Moho.

The obtained 1D velocity models (red plot) that were obtained in the inversion are shown in Figure 6.5 and also in Table 6.3. Table 6.3 summarizes depth-wise variation of body wave velocity with resolutions and absolute values of standard errors. The developed velocity models have been compared with the initial models (blue plot) given by Mukhopadhyay and Sharma (2010a). One more velocity model (black plot) by Monsalve et al. (2006) for eastern Nepal has been given for comparison purpose.

Table 6.3: Obtained 1D velocity models

Model type	P-Wave velocity model			S-Wave velocity model		
Depth range in km	Velocity in km/s	Resolution	Absolute value of standard error in km/s	Velocity in km/s	Resolution	Absolute value of standard error in km/s
0-3	5.184	0.9912	0.010	3.074	0.9898	0.019
3-6	5.184	0.9838	0.041	3.074	0.9848	0.046
6-9	5.184	0.9824	0.047	3.124	0.9829	0.056
9-12	5.737	0.9821	0.048	3.332	0.9831	0.055
12-15	6.104	0.9855	0.035	3.443	0.9864	0.038
15-18	6.104	0.9938	0.001	3.448	0.9909	0.012
18-21	6.262	0.9820	0.048	3.448	0.9845	0.048
21-24	6.273	0.9886	0.022	3.448	0.9823	0.059
24-27	6.273	0.9814	0.050	3.517	0.9816	0.063
27-30	6.530	0.9810	0.052	3.629	0.9839	0.051
30-33	6.530	0.9991	0.001	3.704	0.9991	0.011
33-36	6.649	0.9812	0.052	3.782	0.9838	0.052
36-39	6.828	0.9831	0.044	3.782	0.9869	0.035
39-42	6.838	0.9810	0.052	3.782	0.9802	0.070
42-45	6.849	0.9813	0.051	3.782	0.9802	0.070
45-48	6.849	0.9818	0.050	3.917	0.9800	0.071
48-51	6.854	0.9818	0.049	4.099	0.9800	0.070
51-54	8.257	0.9808	0.053	4.649	0.9969	0.021
54-57	8.257	0.9873	0.027	4.737	0.9804	0.069
57-60	8.257	0.9815	0.050	4.752	0.9957	0.019
60-63	8.258	0.9800	0.056	4.753	0.9700	0.070
63-66	8.269	0.9720	0.056	4.755	0.9627	0.070
66-75	8.269	0.9613	0.056	4.755	0.9500	0.071

6.4 2D AND 3D VELOCITY MODELS OF KUMAON LESSER HIMALAYA

The proposed method, MPFMM has been considered in the forward part of tomography and DLS inversion method has been used in the inversion part. The formulation of the 2D and 3D tomography methods is given in this section.

6.4.1 Methodology

Consider a three dimensional model with velocity v as type of model parameter that is defined at the nodes of a three dimensional Cartesian grid. Consider $v_{i,j,k}; (i, j, k) \in R$ be the velocity value defined at $(i, j, k)^{\text{th}}$ node. To define the velocity inside the model, consider piece-wise tricubic interpolation function (Lekien and Marsden, 2005):

$$v(x, y, z) = \sum_{l,m,n=0}^3 c_{l,m,n} (v_{i,j,k}) x^l y^m z^n \quad (6.1)$$

Where, $v(x, y, z)$ is interpolated velocity at any point inside a unit cell of the grid. The parameter c_{lmn} is coefficients which are functions of defined velocity nodes.

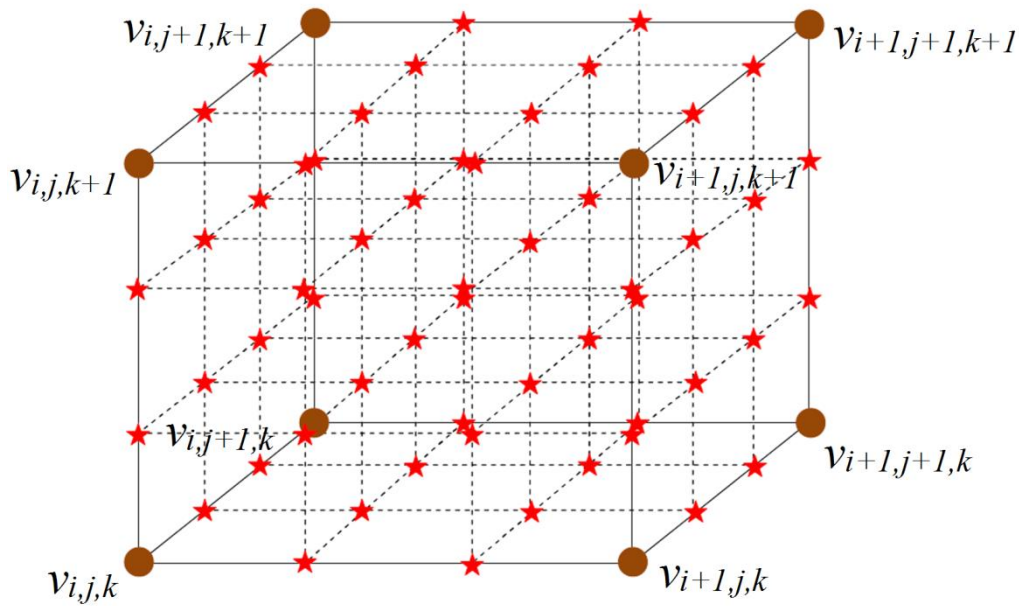


Figure 6.6: A cell of grid showing inversion and interpolated non-inversion nodes. The inversion nodes are shown with brown spheres and non-inversion nodes are shown by red stars. The primary velocities are figured.

Equation (6.1) contain 64 unknown coefficients, therefore it requires 64 known parameters at the eight nodes constituting a unit cell to solve. Lekien and Marsden (2005) suggest that at each node of a unit cell following eight parameters (velocity and its derivatives):

$$\left\{ v, \frac{\partial v}{\partial x}, \frac{\partial v}{\partial y}, \frac{\partial v}{\partial z}, \frac{\partial^2 v}{\partial x \partial y}, \frac{\partial^2 v}{\partial y \partial z}, \frac{\partial^2 v}{\partial z \partial x}, \frac{\partial^3 v}{\partial x \partial y \partial z} \right\} \quad (6.2)$$

are sufficient to describe Equation (6.1). The coefficients obtained that provides smooth velocity variation within grid system. The nodes where velocity is defined are called as

inversion nodes or primary nodes to differentiate the same from other types of nodes called as non-inversion nodes or secondary nodes that are often required in forward computation only and do not take part in inversion process. The velocities associated with the inversion grid are called as primary velocity and the velocity associated with the non-inversion nodes are called as secondary velocities.

To solve the forward problem very accurately the grid is refined as shown in Figure 6.6 to create secondary nodes. The velocity values at all the secondary nodes are obtained using Equation (6.1). For a given source inside the model, traveltimes to all the nodes can be obtained using FMM or MPFMM. The elementary Frechet derivative (derivative of traveltime to a node with respect to its velocity) at each node is obtained directly from the eikonal equation during the computation of forward problem using FMM (Rawlinson, 2008) or MPFMM. These elementary Frechet derivatives can be associated to source-receiver ray paths to obtain complete Frechet derivatives for all the source-receiver ray paths. However this is a complex procedure. An alternative way of computing Frechet derivative for an arbitrary ray path connecting source S and receiver (station) R is to differentiate the ray equation directly as:

$$\tau_{SR} = \int_S^R \frac{dl}{v} \quad (6.3)$$

Where, τ_{SR} is source receiver traveltime, dl is the elementary path. Partial derivative of τ_{RS} with respect to velocity of inversion node (i, j, k) can be written as:

$$\left(\frac{\partial \tau}{\partial v_{ijk}} \right)_{RS} = - \int_S^R \frac{dl}{v^2} \left(\frac{\partial v}{\partial v_{ijk}} \right) \quad (6.4)$$

Where, $\frac{\partial v}{\partial v_{ijk}}$ can be determined from Equation (6.1) directly. Equation (6.4) gives the Frechet derivatives for ray path connecting source S and receiver R with respect to inversion node (i, j, k) . The total frechet derivative for the ray path RS can be obtained using the following formula:

$$d\tau_{SR} = \sum_{i,j,k=1}^{N,M,L} \frac{\partial \tau_{SR}}{\partial v_{ijk}} dv_{ijk} \quad (6.5)$$

Where, N , M and L are the number of inversion nodes along x, y and z direction respectively. Equation (6.5) for a given number \mathbb{N} of source-receiver ray paths can be written in matrix form as:

$$\mathbf{\Gamma} = \mathbf{GV} \quad (6.6)$$

Where,

$$\mathbf{V} = [dv_{111} \quad dv_{112} \quad \cdots \quad dv_{121} \quad dv_{122} \quad \cdots \quad dv_{211} \quad dv_{212} \quad \cdots \quad dv_{221} \quad dv_{222} \quad \cdots \quad dv_{NML}]^T \quad (6.7)$$

$$\mathbf{G} = \begin{bmatrix} \frac{\partial \tau_1}{\partial v_{111}} & \frac{\partial \tau_1}{\partial v_{112}} & \cdots & \frac{\partial \tau_1}{\partial v_{121}} & \frac{\partial \tau_1}{\partial v_{122}} & \cdots & \frac{\partial \tau_1}{\partial v_{211}} & \frac{\partial \tau_1}{\partial v_{212}} & \cdots & \frac{\partial \tau_1}{\partial v_{221}} & \frac{\partial \tau_1}{\partial v_{222}} & \cdots & \frac{\partial \tau_1}{\partial v_{NML}} \\ \frac{\partial \tau_2}{\partial v_{111}} & \frac{\partial \tau_2}{\partial v_{112}} & \cdots & \frac{\partial \tau_2}{\partial v_{121}} & \frac{\partial \tau_2}{\partial v_{122}} & \cdots & \frac{\partial \tau_2}{\partial v_{211}} & \frac{\partial \tau_2}{\partial v_{212}} & \cdots & \frac{\partial \tau_2}{\partial v_{221}} & \frac{\partial \tau_2}{\partial v_{222}} & \cdots & \frac{\partial \tau_2}{\partial v_{NML}} \\ \vdots & \vdots & \ddots & \vdots & \vdots & \ddots & \vdots & \vdots & \ddots & \vdots & \vdots & \ddots & \vdots \\ \frac{\partial \tau_N}{\partial v_{111}} & \frac{\partial \tau_N}{\partial v_{112}} & \cdots & \frac{\partial \tau_N}{\partial v_{121}} & \frac{\partial \tau_N}{\partial v_{122}} & \cdots & \frac{\partial \tau_N}{\partial v_{211}} & \frac{\partial \tau_N}{\partial v_{212}} & \cdots & \frac{\partial \tau_N}{\partial v_{221}} & \frac{\partial \tau_N}{\partial v_{222}} & \cdots & \frac{\partial \tau_N}{\partial v_{NML}} \end{bmatrix} \quad (6.8)$$

and

$$\mathbf{\Gamma} = [d\tau_1 \quad d\tau_2 \quad \cdots \quad d\tau_N]^T \quad (6.9)$$

Equation (6.6) is analogous to Equation (5.25) in Chapter 5 and can be solved using the same analogy with the help of DLS inversion algorithm (5.7) given in Chapter 5 to obtain velocity at different inversion nodes.

6.4.2 2D Results

The study region along A to B in Figure 6.2 is described using a grid of velocity nodes. The size of grid is 21×27 (horizontal, depth) and spacing 7×3 km. A total of 373 phases of first arrival P waves have been used for determination of P wave velocity structure while a total of 497 first arrival S phases have been used for determination of S wave velocity structure. The methodology given in section 6.4.1 has been used as a tool of inversion to obtain 2D velocity structures.

The obtained 2D solution for velocity structure in a vertical section along the white line AB shown in Figure 6.2 is plotted in Figure 6.7. Figure 6.7(a) and (b) describe 2D velocity variation along line AB (Figure 6.2) for P-wave and S-wave velocity structures respectively. Distributions of absolute values of standard errors are also shown for 2D P-wave and S-wave velocity structures in Figure 6.7 (c) and (d) respectively. The solution described here clearly shows three of the common layers of continents: the upper crust, lower crust and mantle and together with the presence of some of the striking features that can be correlated with the geology feature of the concerned area. The low velocity zones are marked by letter K, L, M and N which are described later in discussions.

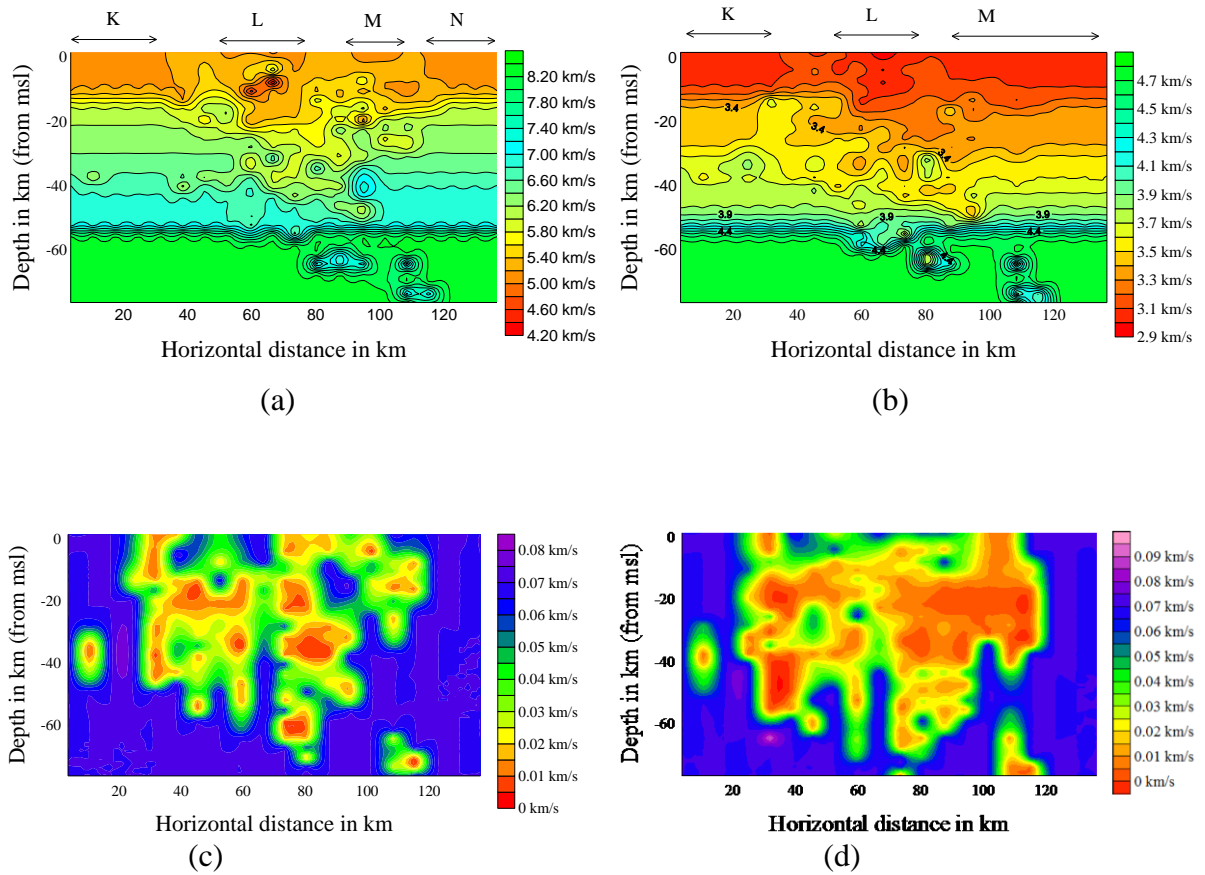


Figure 6.7: Vertical section of P-wave velocity structure (a) and S-wave velocity structure (b) of the Kumaon Himalaya along line AB in map (Figure 6.2). The distribution of absolute values of standard errors for P-wave and S-wave velocity structures are shown in (c) and (d) respectively.

6.4.3 3D Results

The lithosphere of the study region denoted by rectangle box in Figure 6.2 was defined in terms of velocity in grid system. The number of grid nodes in X, Y and Z direction has been considered as 7, 11 and 12 and grid spacing in the corresponding direction is 20 km, 10 km and 3 km respectively. A total of 405 first arrival S phases from a total of 98 earthquakes have been used to determine velocity structure. Using the method described in §6.4.1, tomography were performed and the results are shown in Figure 6.8 and Figure 6.9. Figure 6.8(a) describes 3D velocity variation and Figure 6.8(b) describes distribution of elements of resolution matrix. Figure 6.9 indicate the absolute values of standard errors for 3D velocity variation.

6.5 DISCUSSIONS

Seismicity of the region is described in terms of locations of hypocenters and their trends in the Himalayan region. 1D, 2D and 3D velocity models obtained are discussed here.

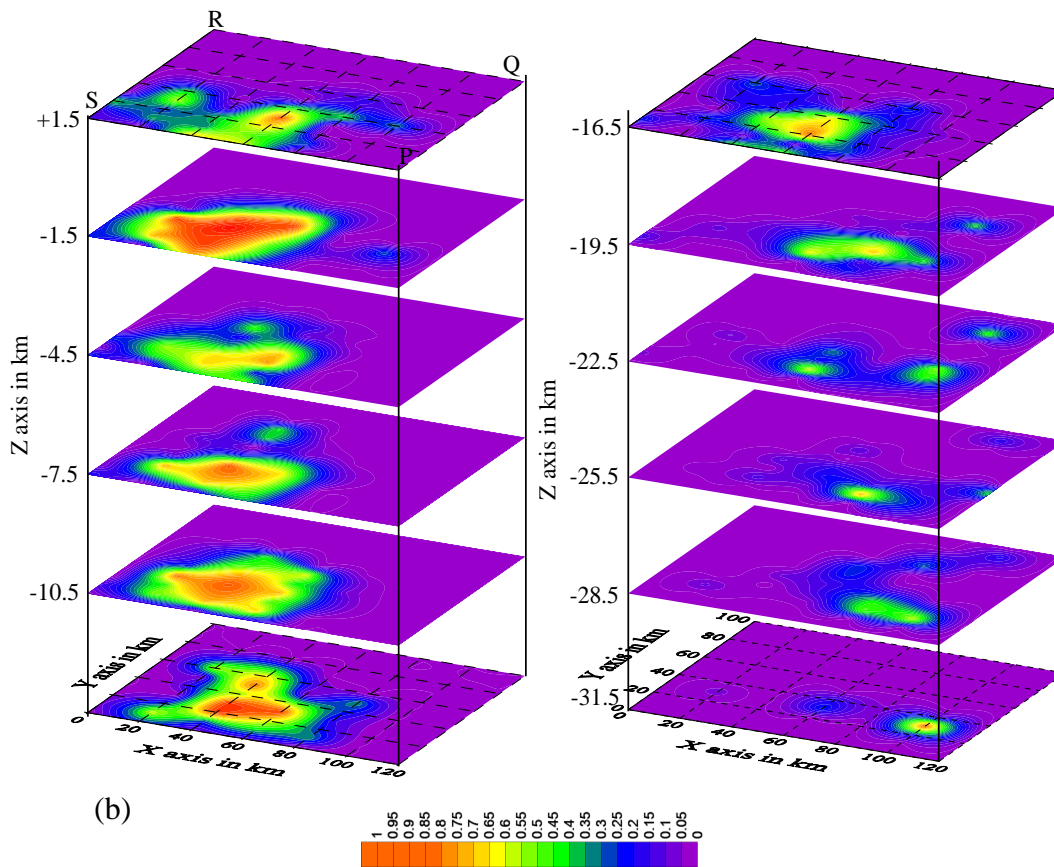
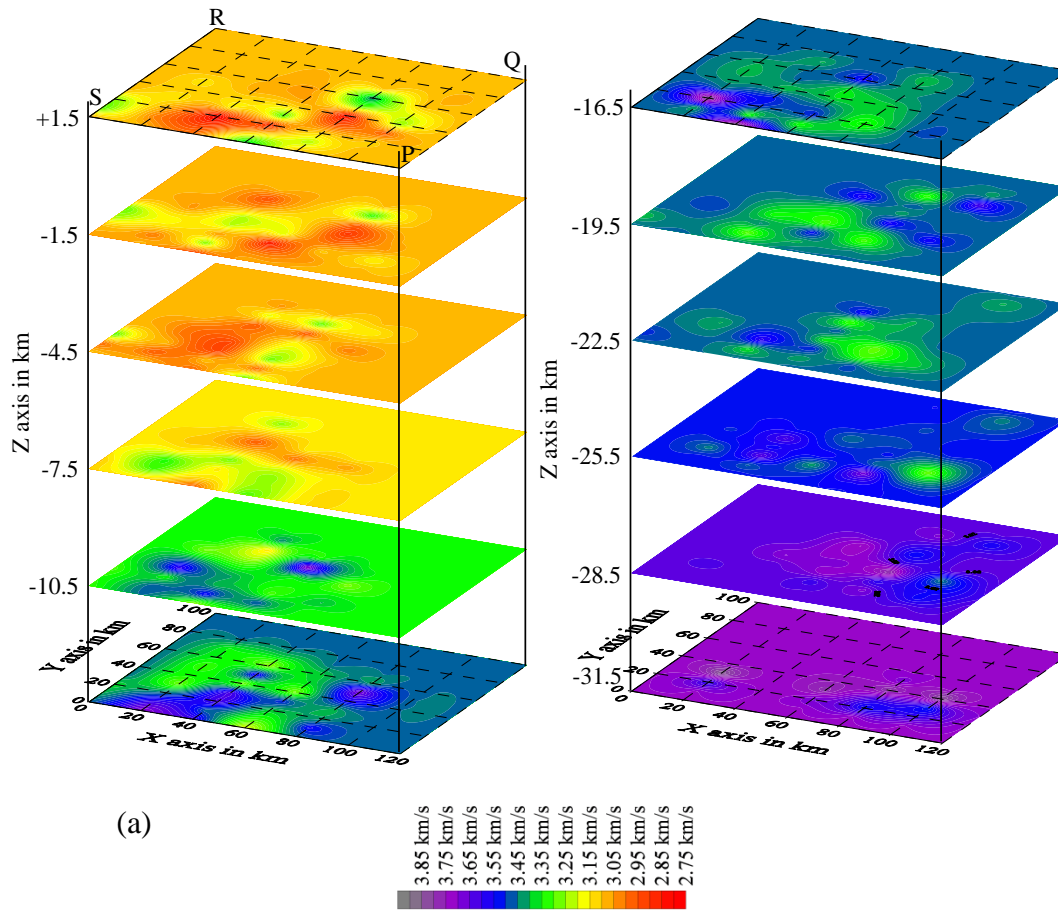


Figure 6.8: Depth slices of velocity structure (a) and resolution matrix (b) at different depths from about 1.5 km above msl to 31.5 km below msl. The velocity structure is obtained beneath the Kumaon Himalaya in the region marked by SPQR in Figure 6.2.

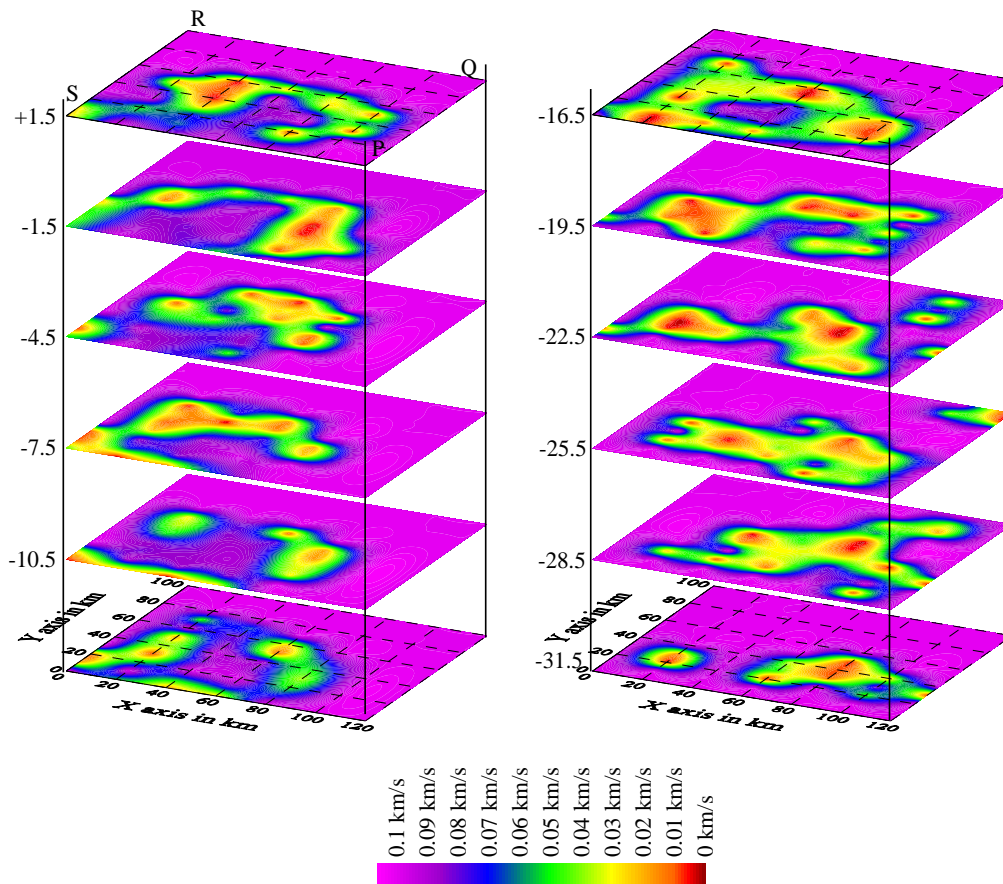


Figure 6.9: Depth slices of absolute values of standard errors at different depths from about 1.5 km above msl to 31.5 km below msl. Standard errors correspond to 3D velocity variation in Figure 6.8 (a).

6.5.1 Seismicity

Distribution of hypocenters given in surface view show (Figure 6.3(a), 6.3(b) and 6.4) a trend that are valid for this region as most of the earthquake of the Himalayan belt are oriented along this fashion (Monsalve et al., 2006). Most of the epicenters form a group that lies between MCT and NAT in the areas of Baluakot, Dharchula and Joljibi. Another group of epicenters lie along the Munsiary Thrust in the north western side of Sobla. The number of earthquakes along MCT is less than that along MT. This may be due to the fact that currently MT is more active compared to MCT.

Vertical projection of hypocenters shows that most of the earthquakes in the Kumaon Lesser Himalaya occur at shallow depths (~20 km). This is supported several studies including Mukhopadhyay and Sharma (2010a) in the Garhwal and Kumaon Himalaya. The hypocenters are scattered in the lower crust and some of the earthquakes occur in the upper mantle. This may be due to the fact that the upper part of mantle is lesser ductile and fracturing is common (Monsalve et al., 2006). The vertical distribution of the earthquakes also show the probable rang of Indian moho (Figures 6.3(c) and 6.3(d)). The Main Himalayan Thrust (MHT) may be marked as shown in Figure 6.3(c). The traveltme residuals

are plotted in cumulative way and shown in Figure 6.3(e) and Figure 6.3(f). It is clear from the figures that traveltime residuals after the inversion show a significant improvement. The initial maximum traveltime residuals were 7.5 s whereas after inversion the same become less than 1.2 s.

6.5.2 Velocity models

The 1D velocity models for P-wave (Figure 6.5(a)) and for S-wave (Figure 6.5(b)) show Indian Moho near about 50 km depth from mean sea level. The obtained model are shown by red curve which has been compared with 1D velocity models given by Mukhopadhyay and Sharma (2010a) (blue curve) and Monsalve et al. (2006) (black curve). The position of study in the Himalayan belt in Mukhopadhyay and Sharma (2010a) was mainly in Garhwal whereas the Monsalve et al. (2006) documented their study on eastern Nepal and Tibet region of Himalayan belt which is approximately 700 km away eastward from the zone of present study region. Gradual increase in the depth of Moho can be seen easily from these models as the study of Mukhopadhyay and Sharma (2010a) show slightly lower than 50 km, the present study show near about 50 km and the study of Monsalve et al. (2006) show much higher than 50 km. This may be due to the fact that the strike of the MHT is not 90 degree with respect to North. The P-wave velocity increases from ~5.2 km/s at surface to ~5.7 km/s at ~9 km depth while the S-wave velocity show increases from ~3.1 km/s to ~3.3 km/s. The body wave velocity gradually increases from 10 km depth to the depth of Indian Moho at ~50 km depth. At Moho velocity suddenly rises from ~6.85 km/s to ~8.26 km/s for P-wave and from ~4.1 km/s to ~4.65 km/s for S-wave.

The plane depicting moho depth can be determined approximately using coordinates of three points lying in that plane. Two such points, one in the eastern Nepal and other in the southern Tibet have been determined using velocity model of Monsalve et al. (2006). The present study gives one point of moho depth. Using all these three point following equation represents plane of moho depth approximately.

$$5065.4x + 9793.4y + 136099.12z + 6804956 = 0$$

The strike and dip of this plane are respectively N27E and 4.6° north-eastward.

Computed resolution of 1D P-wave velocity variation lies between 0.99 and 0.96 and the same for S-wave velocity variation lies between 0.99 and 0.95. Dominant resolution values come near 0.98, which states that the body wave velocities are well resolved in the tomography problem. The higher resolution declares that the obtained results are more close to the actual earth. The absolute values of standard errors corresponding to P-wave velocity lie between 0.001 and 0.056 and the same for S-wave velocity lie between 0.011 and 0.071.

2D Velocity models for body waves show the extensive disturbances of crust due to underthrusting of Indian plate beneath the Eurasian plate. From the Figure 6.7(a) and 6.7(b), it is also clear that the crust is highly deformed towards the collision zone of Himalaya. The Conrad discontinuity that separates the upper crust from lower crust seems to lie around 12 km depth below msl. The depth to the Moho in this region seems to lie at a depth of 50-52 km below msl which complements similar founding using receiver function analysis in western Lesser Himalaya by Hazarika et al. (2013). Unlike the study documented by Kim et al. (2012) beneath the region of High Himalaya close to Nepal Tibet border, no low velocity layer close to the Moho is found. The P wave velocity of upper crust in most of the portion in the section, vary from 4.2 km/s to 5.6 km/s and the same in lower crust vary from 5.6 km/s to slightly more than 7.8 km/s. The S wave velocity of upper crust in most of the portion in the section, vary from 2.9 km/s to 3.3 km/s and the same in lower crust vary from 3.3 km/s to slightly more than 4.4 km/s.

A total of four anomalous velocity zones marked by K, L, M and N can be seen in the Figure 6.7(a) along AB close to the msl. The anomalous low velocity zone, K, L, M and N may be due to the presence of older rocks with granitoids. The high velocity anomalous zones between L and M and between M and N may be due to the presence of crystalline complexes as outcrops in Lesser Himalaya near Thal and Dharchula respectively, as shown in Figure 6.2. The shear wave velocity structure also show almost analogous upper surface anomalous zones, however the low velocity zone N is not resolved in this case.

Down to the mantle at a horizontal distance around 68-78km, injection of magma like water droplets can be traced upto depth around 17 km from MSL. This kind of injection is not uncommon in a region like Himalaya where one plates underthrusts the other plate. A more precise and highly resolved tomography is needed to actually observe the contribution such injection in disturbing the lithosphere.

3D velocity sections in Figure 6.8(a) show S-wave velocity variation down to 31.5 km depth below mean sea level. The velocity varies from 2.75 km/s to 3.85 km/s throughout the volume of study. Considering the location of point S in Figure 6.2 as origin and SP and SR as direction along X axis and Y axis the obtained velocity structure is explained as below.

The best resolve part of the upper crust is 80×80 km from center point S in Figure 6.8(b). Figure 6.8(a) clearly depicts alternating high and low velocity zones upto a depth slice of -10.5 km from msl. This may be due to alternate layers of deoban and mandhali, chakrata and rautgara berinag, ramagarh formation in the Kumaon Himalaya. High velocity zone at 80 km along SP from S, and 60 km along SR from S in the uppermost depth slice is due crystalline complex near Dharchula. High velocity zone at 60 km along SP from S, and

40 km along SR from S in the uppermost depth slice is due crystalline complex near Didihat. The high velocity zone near 60 km along SP from S and 10 km along SR from S may be due to presence of crystalline complex in the Almora crystalline zone.

Depth slices at +1.5 km, -1.5 km and -4.5 km show shear wave velocity variation from 2.75 km/s to 3.0 km/s, with few high velocity zones along north east direction. Depth slices at -7.5 km shows a trace of low velocity zone in between two high velocity zones along North-West and South-East direction, beneath the triangle SPR. The NW-SE trend of low velocity zone at depth +1.5 km seems to be rotated clockwise at depth -7.5 km. At depths -10.5 km, the low velocity zone around 40×60km expanded at depth -13.5 km. Down to the depths below -13.5km resolution is poor (Figure 6.8(b)). At depths -16.5, -19.5 and -22.5 km zones of low velocity ~3.4 km/s are common against the background velocity 3.55 km/s (Figure 6.8(a)). The low velocity zones show a shift towards eastern side, with increasing depth from -16.5 km to -22.5 km. Down to the depth at -31.5 km and -28.5 km the resolution further becomes poor, however low velocity zones can still be observed near about a direction beneath PQ line. The change of velocity is steep from depth -7.5 km to depth -13.5 km, which may be due to change of velocity from upper crust to lower crust around -10 km depth. Standard errors (Figure 6.9) corresponding to unresolved or poorly resolved part of 3D velocity variation are higher compared with well resolved part of the same.

6.6 CONCLUSIONS

The trend of seismicity of the study region is similar to the other parts of the Himalayan terrain. The upper mantle having brittle nature fractures an idea that is supported by many investigator including Monsalve et al. (2006). The depth of Indian Moho falls in between the Moho reported by Mukhopadhyay and Sharma (2010a) and Monsalve et al. (2006). This can be concluded that the Moho depth almost linearly increases from west to east along the belt. The 2D velocity models show extensive disturbances of the crust of the Himalaya in this zone. Two outcrops of crystalline complexes can be seen in the high velocity contrasting zones. 3Dvelocity structure shows clearly the high velocity zones associated with the crystalline complexes near Dharchula, Didihat and Almora nappe. The upper crust shows alternating high and low velocity zones downward from mean sea level to a depth of -10.5 km which may be due to alternating layers of different formation in this region.





3D ATTENUATION STRUCTURES OF THE KUMAON HIMALAYA

7.1 Introduction

Seismic attenuation is the loss of energy contained in propagating seismic waves. The energy loss happens both due to spherical divergence of seismic waves and anelastic nature of material medium. Spherical divergence is an inherent phenomenon related to any types of waves radiated from a point source. On the other hand the effect of anelasticity is caused due to fluid movement and grain boundary friction during the propagation of waves. As the seismic waves propagate the elastic energy associated with the waves gradually decreases due to attenuation and eventually ends up as heat energy because of anelastic attenuation.

The study of anelastic attenuation is very important in earthquake seismology as it is dependent on the medium properties which shape the amplitude of seismic waves released during earthquakes; therefore estimation of anelastic attenuation is related to hazard estimation (Jean et al., 2006) of an area and accurate design of early warning system (Hsu et al., 2013). This is also essential for better simulation (Sørensen et al., 2007) of strong motion. As the anelasticity is associated with the frictional loss of energy, therefore the study of anelastic attenuation is a key to measure heterogeneity as well to estimate the effect of thermo-chemical properties of media.

Three dimensional seismic attenuation studies are rare in the Himalayan belt. Most of the studies that have been carried out deal only with the estimation of frequency dependent coda $Q_c(f)$ (Mandal et al., 2001; Gupta et al., 1995; Paul et al., 2003). One of the reasons for few studies related to three dimensional attenuation properties of subsurface in this part of Himalaya is lack of sufficient digital data. Among those few studies, Joshi (2010) has reported three dimensional variation of quality factor for the Kumaon Himalaya.

In the present study a method of attenuation tomography is developed using grid type of model parameterization. The strong motion data were taken from strong motion network deployed in Kumaon Lesser Himalaya. The site amplifications at the surface of earth at different station have been determined using the method discussed in Joshi et al. (2010).

These site amplification terms have been used for correcting the raw data to avoid the effects from near site soil amplifications. Using self developed software the tomography results have been obtained and discussed.

7.2 TOMOGRAPHY METHOD

Consider a model earth with grid type of parameterization in which the frequency dependent quality factor at different nodes are assigned to be $Q_{ijk}(f)$. In which, $i=1,2,\dots,N$; $j=1,2,3,\dots,M$; $k=1,2,3,\dots,L$ denote the nodes in the x, y and z directions respectively. Imagine a source S and an observation point (receiver) R for which source-receiver ray path and traveltime is known. The spectral acceleration value at the surface of model at the receiver point is related to the quality factor distribution of the model. One such relationship is given by Hashida and Shimazaki (1984) which has been used successively by Joshi et al. (2010) in their tomography method using rectangular block type of parameterization to obtain 3D quality factor distribution of the Kumaon Himalaya. In the current study this relationship is modified in the exponential part to use the same in tomography using grid type of parameterization. The modified relationship is:

$$A = A_0 e^{-\pi f \int_S^R \frac{dt}{Q}} \quad (7.1)$$

Where, f denote frequency, $Q(f, \mathbf{x})$ is frequency dependent quality factor distribution within the model. dt is the elementary traveltime along the ray path between the source S and receiver R and:

$$A_0 = \frac{S(f)g}{R} \quad (7.2)$$

In Equation (7.2), $S(f)$ is the source spectral acceleration value at frequency f ; R is the hypocentral distance between source and receiver and g denote amplifying effect at the surface of the earth. Total derivative of the Equation (7.1) can be written as:

$$\frac{dA}{A} = \frac{dA_0}{A_0} + \pi f \sum_{i=1}^N \left(\int_S^R \frac{dt}{Q^2} \frac{\partial Q}{\partial Q_i} \right) dQ_i \quad (7.3)$$

Which can further be written as:

$$d(\log A) = d(\log A_0) + \pi f \sum_{i=1}^N \left(\int_S^R \frac{dt}{Q^2} \frac{\partial Q}{\partial Q_i} \right) dQ_i \quad (7.4)$$

To use the Equation (7.4) in real earth, we approximate the total derivative by finite differential as:

$$\Delta \log A \approx \Delta \log A_0 + \pi f \sum_{i=1}^N \left(\int_S^R \frac{dt}{Q^2} \frac{\partial Q}{\partial Q_i} \right) \Delta Q_i \quad (7.5)$$

Introducing the suffices i and j for i^{th} source and j^{th} receiver we write Equation (7.5) as:

$$\Delta \log A_{ij} \approx \Delta \log A_{0i} + \pi f \sum_{k=1}^N \left(\int_{S_i}^{R_j} \frac{dt}{Q^2} \frac{\partial Q}{\partial Q_k} \right) \Delta Q_k \quad (7.6)$$

Let $\pi f \int_{S_i}^{R_j} \frac{dt}{Q^2} \frac{\partial Q}{\partial Q_k} = g_{ijk}$, $B = \log A$ and $B_0 = \log A_0$ then Equation (7.6) can be written in

compact form as:

$$\Delta B_{ij} \approx \Delta B_{0i} + \sum_{k=1}^N g_{ijk} \Delta Q_k \quad (7.7)$$

Where,

$$\begin{bmatrix} \Delta B_{i1} \\ \Delta B_{i2} \\ \Delta B_{i3} \\ \vdots \\ \Delta B_{iM} \end{bmatrix} = \begin{bmatrix} 1 & g_{i11} & g_{i12} & g_{i13} & \cdots & g_{i1N} \\ 1 & g_{i21} & g_{i22} & g_{i23} & \cdots & g_{i2N} \\ 1 & g_{i31} & g_{i32} & g_{i33} & \cdots & g_{i3N} \\ 1 & \vdots & \vdots & \vdots & \ddots & \vdots \\ 1 & g_{iM1} & g_{iM2} & g_{iM3} & \cdots & g_{iMN} \end{bmatrix} \begin{bmatrix} \Delta B_{0i} \\ \Delta Q_1 \\ \Delta Q_2 \\ \Delta Q_3 \\ \vdots \\ \Delta Q_{ng} \end{bmatrix} \quad (7.8)$$

Which can be written as:

$$D_i = \begin{bmatrix} I & G_i \end{bmatrix} \begin{bmatrix} \Delta B_{0i} \\ M_i \end{bmatrix} \quad (7.9)$$

This Equation can be expanded for all sources as:

$$\begin{bmatrix} D_1 \\ D_2 \\ D_3 \\ \vdots \\ D_N \end{bmatrix} = \begin{bmatrix} I & 0 & 0 & \cdots & 0 & G_1 \\ 0 & I & 0 & \cdots & 0 & G_2 \\ 0 & 0 & I & \cdots & 0 & G_3 \\ \vdots & \vdots & \vdots & \vdots & \ddots & \vdots \\ 0 & 0 & 0 & \cdots & I & G_N \end{bmatrix} \begin{bmatrix} \Delta B_{01} \\ \Delta B_{02} \\ \Delta B_{03} \\ \vdots \\ \Delta B_{0N} \\ M_i \end{bmatrix} \quad (7.10)$$

Which can be written as:

$$D = WM \quad (7.11)$$

With

$$W = \begin{bmatrix} I & 0 & 0 & \cdots & 0 & G_1 \\ 0 & I & 0 & \cdots & 0 & G_2 \\ 0 & 0 & I & \cdots & 0 & G_3 \\ \vdots & \vdots & \vdots & \vdots & \ddots & \vdots \\ 0 & 0 & 0 & \cdots & I & G_N \end{bmatrix} \quad (7.12)$$

$$\mathbf{M} = [\Delta B_{01} \quad \Delta B_{02} \quad \Delta B_{03} \quad \Delta B_{0N} \quad \cdots \quad M_i]^T \quad (7.13)$$

$$\mathbf{D} = [D_1 \quad D_2 \quad D_3 \quad \cdots \quad D_N]^T \quad (7.14)$$

Equation (7.11) is of standard form that relates model parameter vector \mathbf{M} with data vector \mathbf{D} with a kernel matrix \mathbf{W} . Matrix Equation (7.11) can be solved for model vector using standard method of inversion such as DLS method.

7.3 SITE AMPLIFICATION

Acceleration spectra recorded on the surface of earth are often found to be strongly affected by amplification of the seismic wave near to the surface. The effect is called site effect or site amplification (Sørensen et al., 2006; Huang et al., 2007; Joshi et al., 2010; Chopra et al., 2013a). There are many methods for the determination of site amplification. One of the conventional methods is given by Borchardt (1970). In this method, site effect at a station is obtained by dividing the acceleration spectra recorded at that site with the observed acceleration spectra recorded in some nearby site. For quantitative estimation of site effect one of the methods is proposed by Andrews (1986). This method was modified in Joshi et al. (2010) to account for anelastic attenuation, unknown source and site amplification. For quantitative estimation of site amplification the same method has been applied here.

7.4 STUDY REGION, STRONG MOTION NETWORK AND DATA

The area of study is same where velocity tomography is performed. Data of acceleration spectra were taken from the same strong motion network from where data for velocity analysis were considered. A total of 344 S phase spectra recorded by 17 stations from a total of 82 events are considered for the attenuation study. Station Lohaghat is excluded for 3D attenuation study however it is considered in site amplification study. All the spectra which were considered were processed for base line correction, filtering and scaling. The processed spectra were converted from time domain to frequency domain. Using a variable band of frequency that starts from first arrival S-wave to the end of its part, the acceleration spectra were extracted from the entire spectra. The final spectra denote the record of acceleration versus frequency within a limited band of interest. At those frequencies which are of research and engineering interest such as from 1 Hz to 10 Hz the amplitudes of acceleration of all the processed shear wave band spectra were selected and saved for attenuation and site amplification study.

7.5 COMPUTATION OF SITE AMPLIFICATION AND RESULTS

Using the method presented in Joshi (2010), site amplification factors at all the 18 stations given in Table (6.1) were obtained at 10 different frequencies in the band 1-10 Hz. The results have been plotted in Figure 7.1.

7.6 COMPUTATION OF ATTENUATION TOMOGRAPHY AND RESULTS

The study region denoted by rectangle box in Figure 6.2 was defined in terms of quality factor in Cartesian grid. The number of grid nodes in X, Y and Z direction has been considered as 7, 11 and 12 and grid spacing in the corresponding direction is 20 km, 10 km and 3 km respectively. The method described in §7.2 has been used for determination of quality factor in these nodes. The initial quality factor at each node is given as summarized in Table 7.1.

Table 7.1: Initial model of shear wave quality factor considered

Depth in km	Model of Q (Shear)
0-6	200
6-12	500
12-20	750
20-30	1000
30-42	2000

Using the method in §7.2, the initial model (Table 7.1) 3D tomography has been performed for determination of quality factor at different nodes. The results of the tomography are presented in Figure 7.2 and Figure 7.3. Figure 7.3 shows vertical sections along the white line in Figure 6.2 of study region.

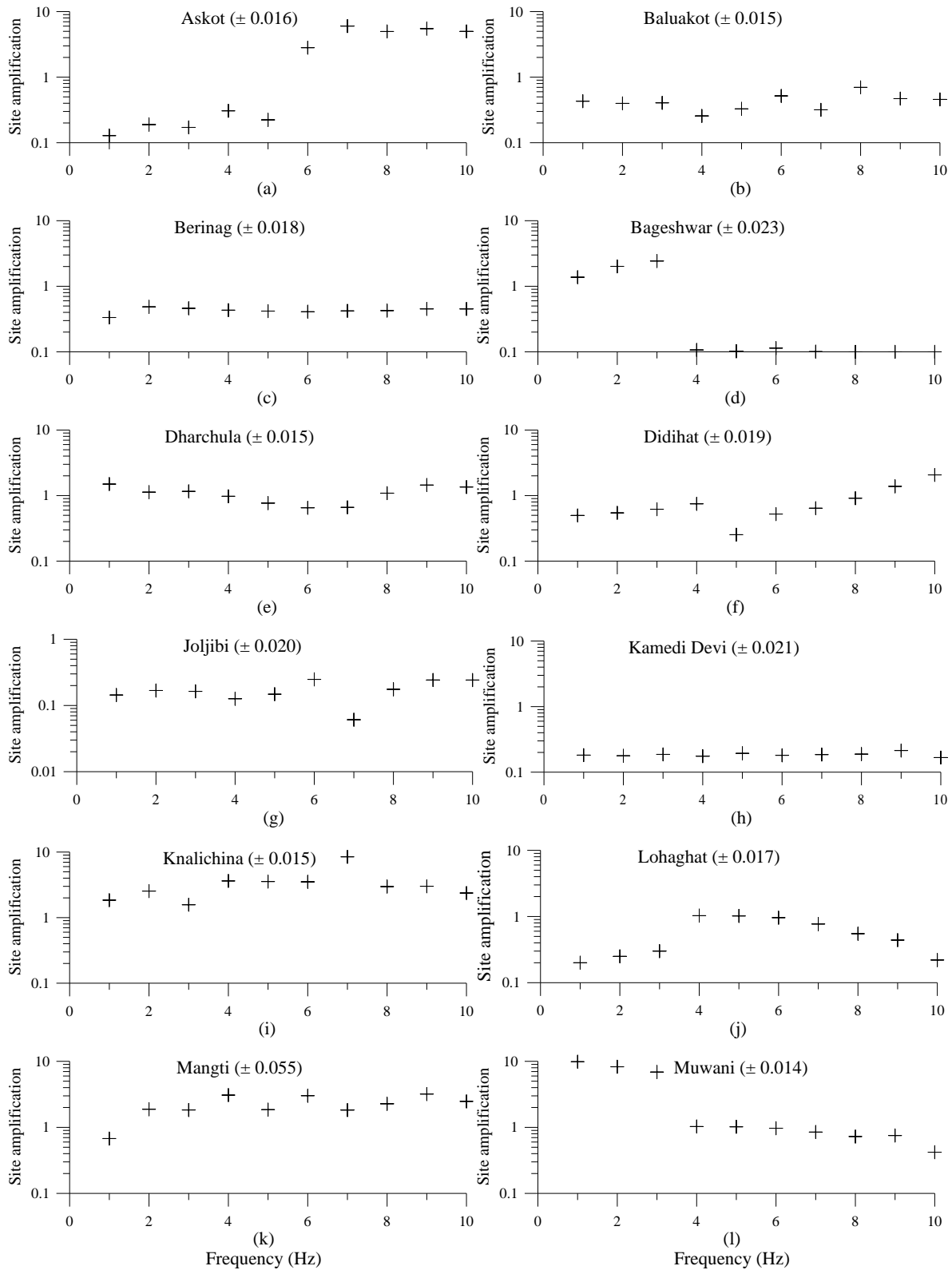
7.7 DISCUSSIONS

The results of site amplification presented in Figure 7.1 and results of attenuation tomography presented in Figure 7.2 and 7.3 are discussed with respect to geology of the present study region.

7.7.1 Site amplification

Askot and Didihat (Figure 7.1(a) and (f)) are the two areas which show gradual increase in site amplifications with the increases of frequencies and Bageshwar and Muwani (Figure 7.1(d) and (l)) are two areas which show gradual decrease of site amplifications with

the increase of frequency. Knalichina, Lohaghat and Munsiary (Figure 7.1(i), (j) and (m)) show convex upward curves showing higher site amplification in middle of the frequency band. On the other hand Dharchula (Figure 7.1(e)) alone shows concave upward curve showing lower site amplification in the middle of the frequency band.



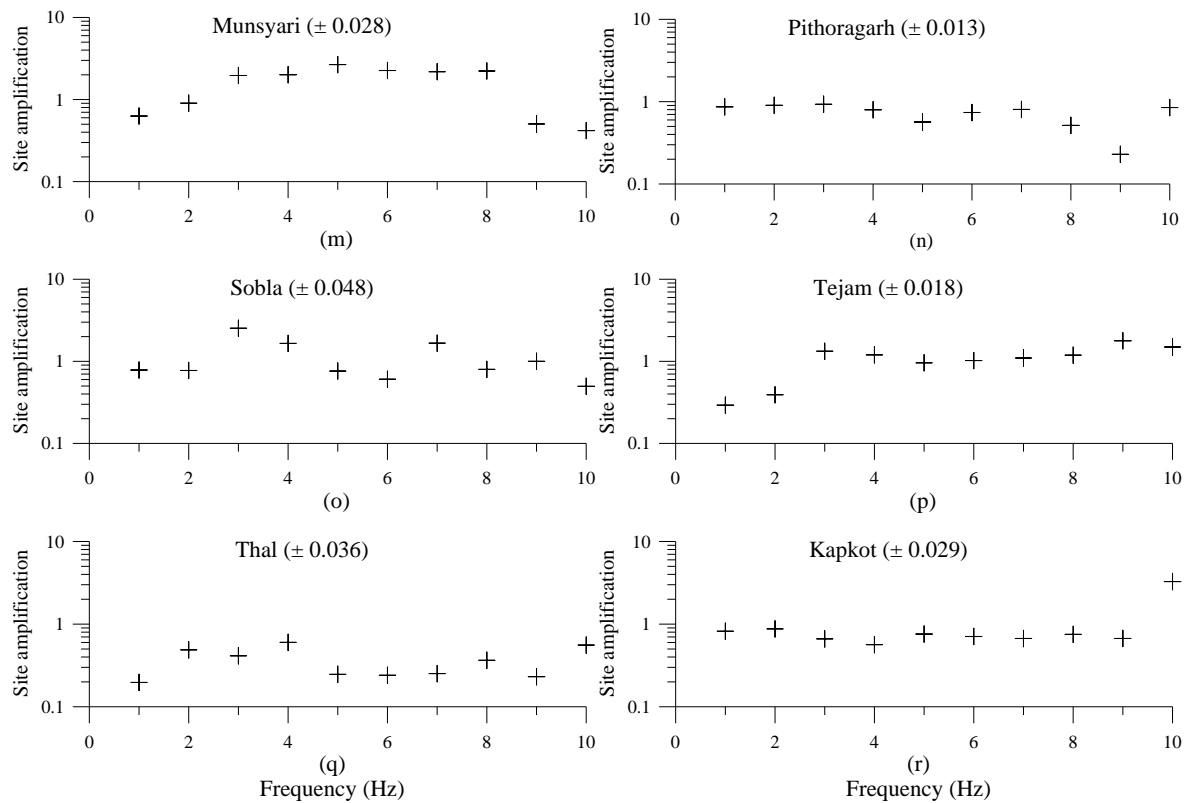


Figure 7.1: The obtained value of site amplification factors at each station (a-r) using strong motion data. The factors are shown in scatter plot by cross. The mean standard errors in computed factors for different stations are shown on right sides of station names in parentheses.

The amplification curves for Pithoragarh and Thal (Figure 7.1(n) and (q)) show almost similar type of variation. First site factors increase then decrease in between 1Hz and 5Hz then again increase and decrease in between 5Hz and 8 Hz. The first band (1-5 Hz) shows higher site amplification values than the second band (5-8 Hz) does in both areas. At 10 Hz random high value is noted for both the areas.

The site amplification for Sobla (Figure 7.1(o)) shows a characteristic similar to Pithoragarh except that unlike Pithoragh, sobla does not show any random high value at 10 Hz. The site amplification for Mangti and Tejam (Figure 7.1(k) and Figure 7.1(p)) increase first and then overall nature become nearly invariables with frequency while Joljibi (Figure 7.1(g)) shows overall increase except a low value notch at 7 Hz. Site amplification of Kapkot (Figure 7.1(r)) remains nearly constant except at 10 Hz frequency where it shows random high value. Berinag and Kamedi Devi (Figure 7.1(c) and (h)) are the two areas which show almost frequency independent site amplification characteristics.

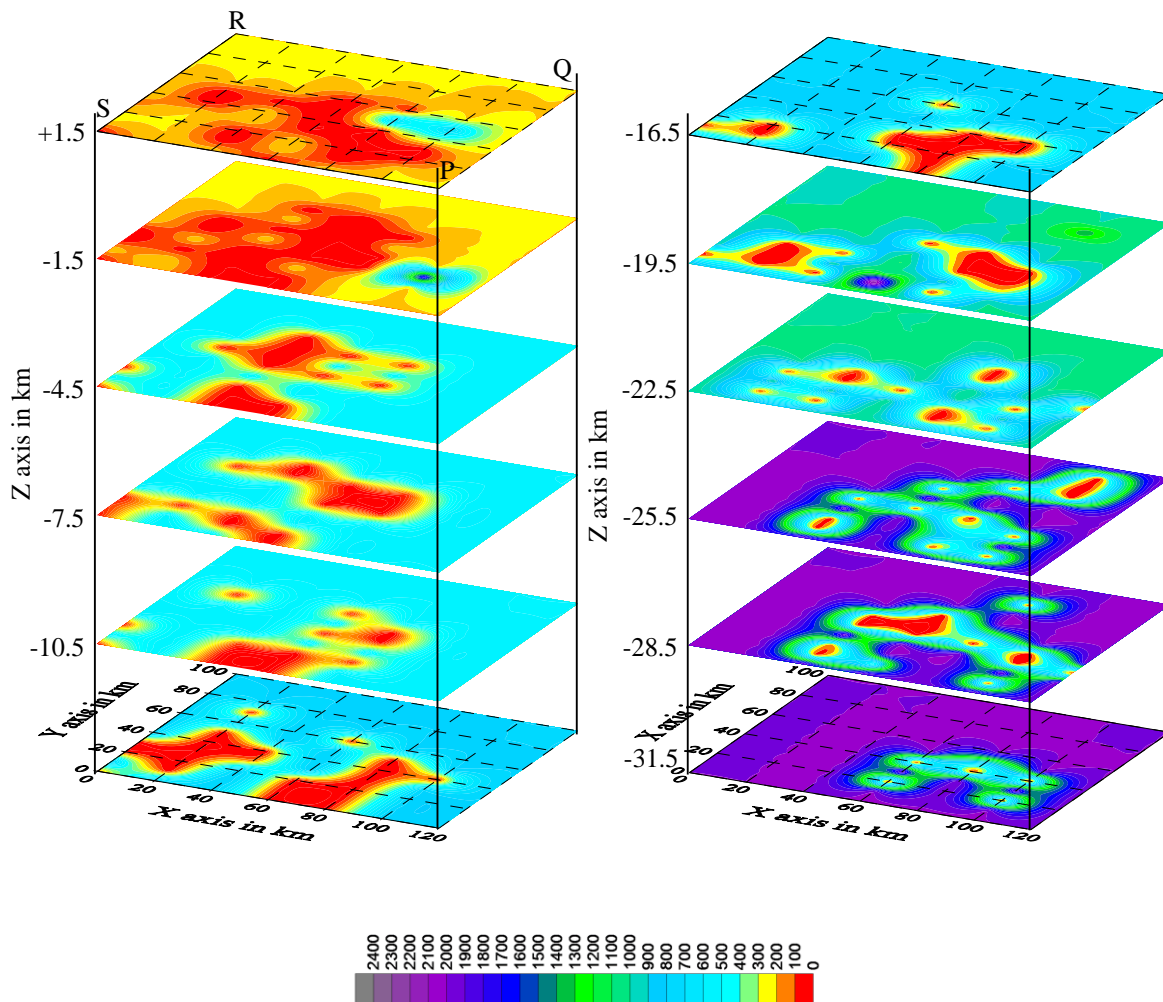


Figure 7.2: Depth slices of quality factor contours at an interval of 3 km in the study region (Figure 6.2) marked by rectangle SPQR.

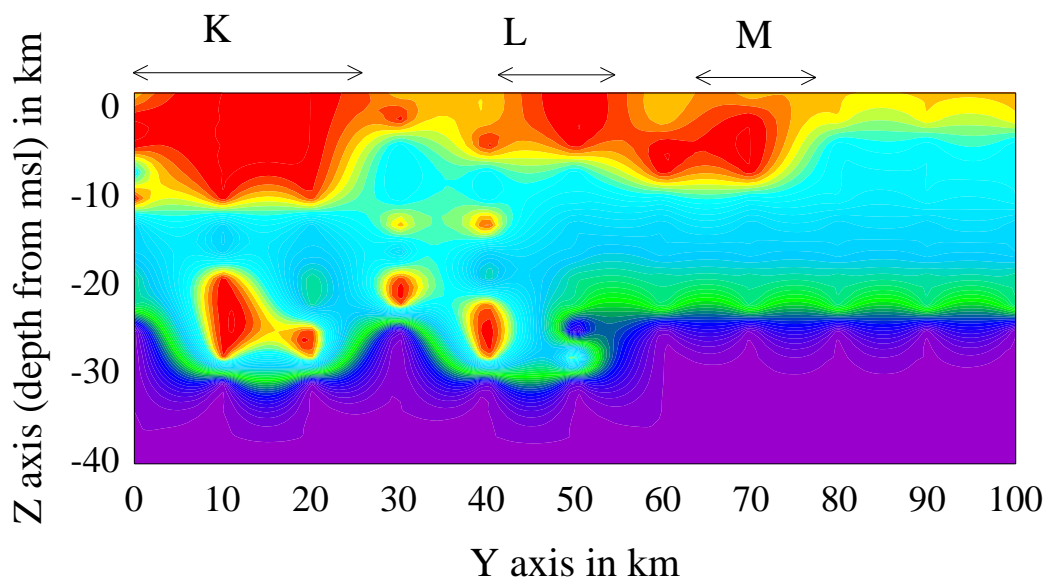


Figure 7.3: A vertical section of quality factor variation along the white line in Figure 6.2. The colour scale is same as that of Figure 7.2.

7.7.2 Attenuation tomography

The quality factor in the study region shows a variation from ~ 0 to ~ 2300 , which indicates high level of heterogeneity of the subsurface under study. The surface value of quality factor as shown in Figure 7.2(a) clearly depicts a trend that can be correlated with the older folded cover sequence as shown in Figure 6.2.

Two crystalline complexes in between Didihat and Dharchula can be correlated with the high values of quality factor ($\sim 650-700$) shown in Figure 7.2 in between $\sim 80-100$ km (X axis) and $\sim 40-60$ km (Y axis). However the location of this low attenuating zone at surface is towards eastward with respect to the zones representing high velocity (Figure 6.8) at surface.

At a depth of 1.5 km from mean sea level the quality factors vary from near about 0 to 1100 as shown in Figure 7.2(b). In most part of this depth slice the value of attenuation are restricted to 200 except at the region between $\sim 90-110$ km (X axis) and $\sim 20-30$ km (Y axis) which may be due to extension of the quality factor distribution values shown by crystalline complexes. The southward shifting of this high zone of quality factor are confirmed from the vertical cross section quality factor presented Figure 7.3. The heterogeneity of the crust of Kumaon Himalaya increases from depth 6 km to a depth of 24 km. The contrast of quality factor is increases below depth 22 km which indicate that the lower crust is highly disturbed. This high contrasting quality factor can be correlated with the high activity of along the detachment plane.

Two low Q zones can be observed from depth -4.5 km to 19.5 km. The orientation of these high attenuation zones at depth -4.5 km is north-east. This trend is gradually rotated with increasing depth in clockwise direction, and the same orientation becomes northwest and south east at depth -19.5 km. This is analogous to the velocity structure of the same region, where two low velocity zones are found to be rotated clockwise with increasing depth from +1.5 km to -7.5 km.

To study depth wise variation of quality factor a 2D section along white line in Figure 6.2 is shown in Figure 7.3. The zones marked by K, L and M show low values of Q, similar to the low values of velocity in Figure 6.7(a). The interval areas, either; between K and L and between L and M show high values of Q. These two high Q zones show the crystalline complexes near Didihat and Dharchula. This fact is also supported by high values of velocity structures in the same region. The middle crust (depth $\sim 12-24$ km) shows Q variation from ~ 400 to ~ 1100 in most of the parts. Low Q zones are found in 10, 30 and 40 km distance along Y axis.

7.8 CONCLUSIONS

The attenuation structure of the subsurface of the Kumaon Himalaya show fair contrasts at near surface but the same becomes very high along the detachment plane. The crystalline complexes near Didihat and Dharchula in the Kumaon Himalaya are resolved well in this study. The overturning nature of the formation presented in Figure 1.10 is supported by this study. Clockwise rotation of trends of low Q values is observed. This may be due to rotation and overturning of the layers beneath the Kumaon region. The high value of attenuation in this area may be due to the fact that the region under study falls in the subducting zone. Askot and Didihat are the two areas which show gradual increase in site amplifications with the increases of frequencies. This behavior is just opposite to that of Bageshwar and Muwaniareas which show gradual decrease of site amplifications with the increase of frequency.





CONCLUSIONS

The major conclusions of the works presented in this thesis are as follows:

- In the present work ray tracing algorithm has been developed using spiral path search method in a parameterization where interfaces have been included in constant velocity voxels. Self-reflections within adjacent interfaces have been considered in the developed method. A FORTRAN code has been developed for this algorithm which was tested using several numerical experiments which satisfy the normal wave propagation theory. A gradient path search method to this algorithm has been added to improve the same.
- An algorithm of Fast Marching Method has been derived by incorporating the concept of binary tree in the narrow band. This speed up the algorithm. The algorithm has been tested using several numerical models and found to satisfy general wave propagation principle. Two of the most important properties of FMM that are to compute head waves and first arrivals have been validated.
- One improved version of MSFM method has been proposed. The method solves the eikonal equation by taking information of all 8 grid points in 2D and 26 grid points in 3D. The proposed method is based on angular interpolation of directional derivatives and hence anisotropic grid structure has little effect on it. Several numerical experiments have been carried out and in all experiments the proposed method has been found to be better.
- The Multiparameter inversion technique has been formulated in this work which is based on developed ray tracing algorithm. This inversion technique was design to simultaneously invert P- and S-phases to obtain at a time or separately, the

hypocenters with origin time, P-wave velocity, S-wave velocity and interface parameters. A FORTRAN code has been developed based on the same method. This method has been used extensively for practical studies.

- Based on the improved FMM, a full 3D traveltime tomographic algorithm has been developed to implement the same in the present work. The algorithm was coded in FORTRAN.
- An algorithm for 3D attenuation tomography in numerical domain has been developed to implement the same in the present work. The FORTRAN code based on the same algorithm was developed.
- A total of 870 phases from a total of 116 earthquakes recorded in strong motion network in the Kumaon Himalaya, have been used in the developed multiparameter inversion method to simultaneously compute hypocenters of the earthquakes and one dimensional velocity model in Kumaon region. The located earthquakes and velocity model show several characteristics.
- Epicenters of located earthquakes in the Kumaon Himalaya form a shape that is oriented along the Himalayan arc. This is supported by almost all studies including Monsalve et al. (2006), performed in the Himalayan terrain. Most of the epicenters form a group that lies between MCT and NAT in the areas of Baluakot, Dharchula and Joljibi. Another group of epicenters lie along the Munsiri Thrust in the north western side of Sobla. The number of epicenters along MCT is found to be fewer. Therefore, it is concluded that the MT is more active than MCT at present time.
- Vertical projection of hypocenters shows that most of the earthquakes in the Kumaon Lesser Himalaya occur at shallow depths (~20 km). This is supported several studies including Mukhopadhyay and Sharma (2010) in the Garhwal and Kumaon Himalaya. The hypocenters are scattered in the lower crust and some of the earthquakes occur in the upper mantle. The occurrence of earthquakes at sub-Moho depths support the idea that the continental upper mantle deforms by brittle processes (Monsalve et al., 2006).

- One dimensional velocity model depicts Indian Moho, which lie beneath the Kumaon region, at a depth of nearly 50 km from mean sea level. The depth of the Moho beneath the study region when tied with other studies forms a plane of MHT with strike and dip respectively, N27E and 4.6° northeastern.
- Two sudden jumps of body wave velocity are observed at near about 10 km and 50 km depths from mean sea level. At depth near about 10 km P-wave velocity change from ~5.7 km/s to ~6.1 km/s and S-wave velocity change from ~3.1 km/s to ~3.3 km/s. At depth near about 50 km P-wave velocity change from ~6.9 km/s to ~8.3 km/s and S-wave velocity change from ~4.1 km/s to ~3.7 km/s. The velocity contrast at ~10 km may indicate the boundary between upper crust and lower crust and the same at ~50 km may indicate the Indian Moho beneath Kumaon Lesser Himalaya.
- A method of tomography using the proposed MPFMM has been developed which has been used to obtain 2D and 3D tomography images of velocity structure beneath the Kumaon Himalaya. In 2D tomography both P and S phases have been considered from a total of 98 earthquakes. A total of 373 phases of first arrival P waves have been used for determination of P wave velocity structure while a total of 497 first arrival S phases have been used for determination of S wave velocity structure. In 3D tomography only shear wave velocity structure has been obtained using 405 first arrival S phases from 98 earthquakes.
- 2D vertical body wave velocity images have been obtained from Lohaghat to northwestern side of Sobla, along a plane that strikes N26E. The 2D velocity variation describes the complexity of this region. 2D Velocity models for body waves show the extensive disturbances of crust due to underthrusting of Indian plate beneath the Eurasian plate. The Conrad discontinuity that separates the upper crust from lower crust seems to lie around 12 km depth below msl. The depth to the Moho in this region seems to lie at a depth of 50-52 km below msl which complements similar founding using receiver function analysis in western Lesser Himalaya by Hazarika et al. (2013). The P wave velocity of upper crust in most of the portion in the section, vary from 4.2 km/s to 5.6 km/s and the same in lower crust vary from 5.6 km/s to slightly more than 7.8 km/s. The S wave velocity of upper crust in most of the portion in the section, vary from 2.9 km/s to 3.3 km/s and the same in lower crust vary from 3.3 km/s to slightly more than 4.4 km/s. The outcrops of crystalline complexes in

Lesser Himalaya near Thal and Dharchula respectively are well resolved in 2D velocity section specially in P wave velocity section.

- A 3D shear wave velocity structure up-to a depth of 33 km beneath the Kumaon region has been obtained using the data and developed methodology of tomography using MPFMM. Within the resolved part, the obtained velocity structure clearly resolved the outcrops of crystalline complexes present in the study region. Alternating zones of low and high velocities are observed with increasing depth in the upper crust. This may be due to the overturning nature of the crustal layers beneath the Kumaon Himalaya.
- Site amplification for all the station locations have been obtained and found some important characteristics. Askot and Didihat are the two areas which show gradual increase in site amplifications with the increases of frequencies, and Bageshwar and Muwani are two areas which show gradual decrease of site amplifications with the increase of frequency. Berinag and Kamedi Devi are the two areas which show almost frequency independent site amplification characteristics.
- 3D Attenuation tomography has been performed up-to a depth of 33 km using the developed tomography method in the Kumaon Himalaya to study attenuating characteristic of the region. The quality factor Q shows variation from near about 0 to 2300 beneath this region. The crystalline complexes are resolved with high values of quality factor (~650-700) compared to neighbouring region which shows Q variation from ~0 to ~200.
- Both velocity and Q structure show probable rotation of low velocity and Q clockwise in the upper crust, therefore it may be concluded that the crustal layers were overturned and rotated simultaneously in the process of orogeny.

The Kumaon region of Uttarakhand falls in the Lesser Himalayan belt. The region is highly mountainous and difficult to reach many places. The subsurface structures beneath this region are highly complex and have overturned and rotated layers. To resolve these layers properly, 3D tomography is required to be obtained with large quantity of data. However, using proposed multiparameter inversion scheme the same objective can be

fulfilled to some extent. But in this case quantity of data required is almost same as that of 3D tomography and quantity of data is always a problem in the Kumaon Himalaya.

Inversion schemes used in the study is damped least square inversion which is good because it does not differentiates underdetermined and overdetermined problems and give reasonable results in linearizable problems. However, a global inversion technique such as Genetic algorithm is an alternative choice specially in a highly nonlinear problem.



LIST OF PUBLICATIONS FROM THE RESEARCH WORK



Kumbhakar, C. and Joshi, A., (2013). Subsurface imaging of Kumaon region of lesser Himalaya using fast marching method, In: Proceedings of International Conference on Information and Mathematical Sciences, Oct. 24-26, pp. 469-472.

Kumbhakar, C., Joshi, A. and Kumari, P., (2014). Fast marching method to study traveltime responses of three dimensional numerical models of subsurface, In: Pant, M., Deep, K., Nagar, A. and Bansal, J. C. (Eds.), Proceedings of Third International Conference on Soft Computing for Problem Solving, Advances in Intelligent Systems and Computing, 259, 411-421, Doi: 10.1007/978-81-322-1768-8_37.

Kumbhakar, C. and Joshi, A., Multistencils Pseudoanisotropic Fast Marching Method: A highly accurate solution to the eikonal equation by analyzing traveltime gradient and space-symmetry in Cartesian domain, IEEE Trans. on Pattern Analysis and Machine Intelligence (TPAMI), (to be submitted).

Kumbhakar, C. and Joshi, A., An algorithm for fast computation of ray tracing in a media having 3D natural layers, J. Comput. Phys., (to be submitted).

Kumbhakar, C. and Joshi, A., An algorithm for simultaneous inversion of P- and S-phases to obtain body wave velocities, hypocenter- and interface-parameters using 3D natural layer parameterization, Geophys. J. Int., (to be submitted).

Kumbhakar, C. and Joshi, A., Simultaneous inversion for one dimensional velocity structure and hypocenters in the Kumaon Himalaya: Seismicity in the crust and upper mantle, Geophys. J. Int., (to be submitted).

Kumbhakar, C. and Joshi, A., Two dimensional velocity structure of the Kumaon Himalaya using Improved Fast Marching Method: A reappraisal, Bull. Seism. Soc. Am., (to be submitted).

BIBLIOGRAPHY

Acton, C. E., Priestley, K., Gaur, V. K. and Rai, S. S., (2010). Group velocity tomography of the Indo-Eurasian collision zone, *J. Geophys. Res.*, 115, doi: 10.1029/2009JB007021.

Aki, K. and Chouet, B., (1975). Origin of coda waves: source, attenuation and scattering effects. *J. Geophys. Res.*, 80, 3322–3342.

Aki, K. and Lee, W. H. K., (1976). Determination of three-dimensional velocity anomalies under a seismic array using first P arrival times from local earthquakes:1. A homogeneous initial model, *J. Geophys. Res.*, 81, 4381-99.

Aki, K. and Richards, P. G., (1980). *Quantitative seismology: theory and methods*, W. H. Freeman, San Francisco.

Aki, K., (1980a). Scattering and attenuation of shear waves in the lithosphere, *J. Geophys. Res.*, 85, 6496–6504.

Aki, K., (1980b). Attenuation of shear-waves in the lithosphere for frequencies from 0.05 to 25 Hz, *Phys. Earth Planet. Inter.*, 21, 50–60.

Aki, K., Christoffersson, A. and Husebye, E. S., (1977). Determination of the three-dimensional seismic structure of the lithosphere, *J. Geophys. Res.*, 82, 277–296.

Akinci, A., Del Pezzo, E. and Ibañez, J. M., (1995). Separation of scattering and intrinsic attenuation in southern Spain and western Anatolia (Turkey), *Geophys. J. Int.*, 121, 337-353.

Alkhalifah, T. and Fomel, S., (2001). Implementing the fast marching eikonal solver: Spherical versus Cartesian coordinates, *Geophys. Prospect*, 49, 165–178.

Allen, T. I., Cummins, P. R., Dhu, T. and Schneider, J. F., (2007). Attenuation of ground motion spectral amplitudes in Southeastern Australia. *Bull. Seism. Soc. Am.*, 97, 1279-1292.

Ammon, C. J., Randall, G. E. and Zandt, G., (1990). On the nonuniqueness of receiver function inversions, *J. Geophys. Res.* 95, 15303-15318.

Andrews, D. J., (1986). Objective determination of source parameters and similarity of earthquakes of different size, In: Dsa, S., Boatwright, J. and Scholz, C. H. (Eds.), *Earthquake source mechanics*, AGU, Washington, DC, pp. 259-268.

Ankeny, L. A., Braile, L. W. and Olsen, K. H., (1986). Upper crustal structure beneath the Jemez Mountains volcanic field, New Mexico, determined by three-dimensional simultaneous inversion of seismic refraction and earthquake data, *J. Geophys. Res.*, 91, 6188–6198.

Backus, G. E. and Gilbert, J. F., (1967). Numerical Applications of a formalism for geophysical inverse problems, *Geophys. J. Roy. Astr. Soc.*, 13, 247–276.

Baranowski, J., Armbruster, J., Seeber, L. and Molnar, P., (1984). Focal depths and fault plane solutions of earthquakes and active tectonics of the Himalaya. *J. Geophys. Res.*, 89, 6918-6928.

Benz, H. M. and Smith, R. B., (1984). Simultaneous inversion for lateral velocity variations and hypocenters in the Yellowstone region using earthquake and refraction data, *J. Geophys. Res.*, 89, 1208–1220.

Benz, H. M., Zandt, G. and Oppenheimer, D. H., (1992). Lithospheric structure of northern California from teleseismic images of the upper mantle, *J. Geophys. Res.*, 97, 4791–4807.

Beresnev, I. A. and Atkinson, G. M., (1997). Modeling Finite-fault Radiation from the o n Spectrum, *Bull. Seism. Soc. Am.* 87, 67–84.

Bianco, F., Castellano, M., Del Pezzo, E. and Ibañez, J. M., (1999). Attenuation of short-period seismic waves at Mt. Vesuvius, Italy, *Geophys. J. Int.*, 138, 67-76.

Bianco, F., Del Pezzo, E., Castellano, M., Ibañez, J. and Di Luccio, F., (2002). Separation of intrinsic and scattering seismic attenuation in the Southern Apennine zone, Italy, *Geophys. J. Int.*, 150, 10–22.

Birtill, J. W. and Whiteway, F. E., (1965). The application of phased arrays to analysis of seismic body waves, *Philos. Trans. R. Soc. London, Ser. A*, 258, 421–493, doi:10.1098/rsta.1965.0048.

Bishop, T. P., Bube, K. P., Cutler, R. T., Langan, R. T., Love, P. L., Resnick, J. R., Shuey, R. T., Spindler, D. A. and Wyld, H. W., (1985). Tomographic determination of velocity and depth in laterally varying media, *Geophysics*, 50, 903–923.

Blundell, C. A., (1993). Resolution analysis of seismic P-wave velocity estimates using reflection tomographic inversion, Ph.D. thesis, Monash University.

- Boore, D. M. and Atkinson, G. M., (1987). Stochastic prediction of ground motion and spectral response parameters at hard-rock sites in Eastern North America, *Bull. Seism. Soc. Am.* 77, 440–467.
- Boore, D. M., (1983). Stochastic simulation of high-frequency ground motions based on seismological models of the radiated spectra, *Bull. Seism. Soc. Am.* 73, 1865–1894.
- Borcherdt, R. D., (1970). Effects of local geology on ground motion near San Francisco bay, *Bull. Seism. Soc. Am.*, 60, 29-61.
- Brookfield, M. E., (1993). The Himalayan passive margin from Precambrian to Cretaceous times, *Sedimentary Geology*, 84, 1-35.
- Bungum, H., Husebye, E. S., and Ringdal F., (1971). The NORSAR array and preliminary results of data analysis, *Geophys. J. Int.*, 25: 115–126.
- Burchfiel, B. C., Cowan, D. S. and Davis, G. A., (1992). Tectonic overview of the Cordilleran orogen in the western United States. In: Burchfiel, B. C., Lipman, P. W., Zoback, M. L. (Eds.), *The Cordilleran Orogen: Conterminous US*. Geological Society of America, Boulder, CO, pp. 407–479.
- Buske, S., (1996). Finite-difference solution of the transport equation: First results, *Pure Appl. Geophys.*, 148, 565-581.
- Caldwell, W. B., Klemperer, S. L., Rai, S. S. and Lawrence J. F., (2008). Crustal velocity structure from surface wave dispersion tomography in the Indian Himalaya, *Himalayan J. Sci.*, 5, 33.
- Caldwell, W. B., Klemperer, S. L., Rai, S. S. and Lawrence, J. F., (2009). Partial melt in the upper-middle crust of the northwest Himalaya revealed by Rayleigh wave dispersion, *Tectonophysics*, doi:10.1016/j.tecto.2009.01.013.
- Cassell, B. R., (1982). A method for calculating synthetic seismograms in laterally varying media, *Geophys. J. Roy. Astr. Soc.*, 69, 339–354.
- Cassidy, J. F., (1992). Numerical experiments in broadband receiver function analysis, *Bull. Seism. Soc. Am.* 82, 1453-1474.

- Célérier, J., Harrison, T. M., Webb, A. A. G. and Yin, A., (2009). The Kumaun and Garhwal Lesser Himalaya, India: Part 1. Structure and stratigraphy: *Geol. Soc. Am. Bull.*, 121, 1262-1280.
- Cěrvený, V., (1987). Ray tracing algorithms in three-dimensional laterally varying layered structures, In: Nolet, G. (Ed.), *Seismic tomography: With applications in global seismology and exploration geophysics*, D. Reidel, Dordrecht, pp. 99–133.
- Cěrvený, V., (2001). *Seismic Ray Theory*, Cambridge Univ. Press, Cambridge.
- Chander, R., Sarkar, I., Khattri, K. N. and Gaur, V. K., (1986). Upper crustal compressional wave velocity in the Garhwal Himalaya, *Tectonophysics*, 124, 133-140.
- Chapman, C. H. and Drummond, R., (1982). Body-wave seismograms in inhomogeneous media using Maslov asymptotic theory, *Bull. Seism. Soc. Am.*, 72, S277–S317.
- Chauhan, P. K. S. and Singh, V. N., (1996). Shear Wave Velocity Structure of China Region from Rayleigh Wave Dispersion, In: *Proceedings of International Seminar and Exhibition Geophysics Beyond 2000*, Nov. 15-20, Hyderabad.
- Chiu, S. K. L., Kanasevich, E. R. and Phadke, S., (1986). Three-dimensional determination of structure and velocity by seismic tomography, *Geophysics*, 51, 1559–1571.
- Chopra, S., Kumar, D. and Rastogi, B. K., (2011). Attenuation of High Frequency P and S Waves in the Gujarat Region, India, *Pure Appl. Geophys.*, 168, 797-813.
- Chopra, S., Kumar, D., Rastogi, B. K., Choudhury, P. and Yadav, R. B. S., (2013a). Estimation of site amplification functions in Gujarat region, India, *Nat. Hazards*, 65, 1135-1155.
- Chopra, S., Kumar, D., Rastogi, B. K., Choudhury, P. and Yadav, R. B. S., (2013b). Estimation of seismic hazard in Gujarat region, India, *Nat. Hazards*, 65, 1157-1178.
- Claerbout, J. F. and Muir, F., (1973). Robust modeling with erratic data, *Geophysics*, 38, 826– 844, doi: 10.1190/1.1440378.
- Constable, S. C., Parker, R. L. and Constable, C. G., (1987). Occam's inversion: A practical algorithm for generating smooth models from electromagnetic sounding data, *Geophysics*, 52, 289–300.

- Critelli, S. and Garzanti, E., (1994). Provenience of the lower Tertiary Murree red beds (Hazara-Kashmir syntax, Pakistan) and the initial rising of the Himalayas, *Sedimentary Geology*, 89, 265-284.
- Cruz-Atienza, V. M., Pacheco, J. F., Singh, S. K., Shapiro, N. M., Valdes, C. and Iglesias, A., (2001). Size of Popocatepetl volcano explosions (1997-2001) from waveform inversion, *Geophys. Res. Lett.*, 28, 4027-4030.
- Danielsson, P. E., Lin, Q., (2003). A Modified Fast Marching Method, In: *Proceedings of Scandinavian Conference on Image Analysis*, June 29-July 2, 2003, Halmstad, Sweden, pp. 1154-1161.
- Dasgupta, S., Pande, P., Ganguly, D., Iqbal, Z., Sanyal, K., Venkatraman, N.V., Dasgupta, S., Sural, B., Harendranath, L., Mazumdar, K., Sanyal, S., Roy, A., Das, L.K., Misra, P.S. and Gupta, H. (2000). *Seismotectonic Atlas of India and Its Environs*, Geological Survey of India, Kolkata.
- Davis, P. M., (1991). Continental rift structures and dynamics with reference to teleseismic studies of the Rio Grande and East African rifts, *Tectonophysics*, 197, 309–325.
- Day, A. J., Peirce, C. and Sinha, M. C., (2001). Three-dimensional crustal structure and magma chamber geometry at the intermediate-spreading, back-arc Valu Fa Ridge, Lau Basin - results of a wide-angle seismic tomographic inversion, *Geophys. J. Int.*, 146, 31–52.
- DeCelles, P. G., Robinson, D. M., Quade, J., Ojha, T. P., Garzione, C. N., Copeland, P. and Upreti, B. N., (2001). Stratigraphy, structure and tectonic evolution the Himalayan fold-thrust belt in western Nepal, *Tectonics*, 20, 487-509.
- Del Pezzo, E., Ibañez, J., Morales, J., Akinci, A. and Maresca, R., (1995). Measurements of intrinsic and scattering seismic attenuation in the crust, *Bull. Seism. Soc. Am.*, 85, 1373–1380.
- DiPietro, J. A. and Pogue, K. R., (2004). Tecnostratigraphic subdivisions of the Himalaya: a view from the west, *Tectonics*, 23, TC5001, doi: 10.1029/2003TC001554.
- Doornbos, D. J. and Husebye, E. S., (1972). Array analysis of PKP phases and their precursors, *Phys. Earth Planet. Inter.*, 6, 387–399.

- Dorbath, C. and Paul, A., (1996). Tomography of the Andean crust and mantle at 20S: First results of the Lithoscope experiment, *Phys. Earth Planet. Int.*, 97, 133–144.
- Dziewonski, A. M., (1984). Mapping the lower mantle: determination of lateral heterogeneity in P velocity up to degree and order 6, *J. Geophys. Res.*, 89, 5929–5952.
- Dziewonski, A. M. and Anderson, D. L., (1981). Preliminary reference Earth model, *Phys. Earth Planet. Int.*, 25, 297–356.
- Eberhart-Phillips, D. and Reyners, M., (1997). Continental subduction and three-dimensional crustal structure: The northern South Island, New Zealand, *J. Geophys. Res.*, 102, 11848–11861.
- Eberhart-Phillips, D., (1990). Three-dimensional P and S velocity structure in the Coalinga Region, California, *J. Geophys. Res.*, 95, 15343–15363.
- Evans, J. R., Eberhart-Phillips, D. and Thurber, C. H., (1994). User's manual for SIMULPS12 for imaging Vp and Vp/Vs: A derivative of the "Thurber" tomographic inversion SIMUL3 for local earthquakes and explosions, Open File Report, U.S. Geological Survey, 94–431.
- Farra, V. and Madariaga, R., (1988). Non-linear reflection tomography, *Geophys. J.*, 95, 135–147. doi: 10.1111/j.1365-246X.1988.tb00456.x
- Fréchet, M. R., (1941). Sur la loi de répartition de certaines grandeurs géographiques, *Journal de la Société de Statistiques de Paris* (in French), 82, 114–122.
- Gansser, A., (1964). *Geology of the Himalaya Interscience*, New York, N.Y., pp. 287.
- Gansser, A., (1981). The geodynamic history of the Himalaya, *Am. Geophys. Unin. Washington, Geod. Ser.*, 3, 111-121.
- Garzanti, E., (1999). Stratigraphy and sedimentary history of the Nepal Tethys Himalaya passive margin. *J. Asian Earth Sci.*, 17, 805-827.
- Gibbons, S. J., Sørensen, M. B., Harris, D. B. and Ringdal, F., (2007). The detection and location of low magnitude earthquakes in northern Norway using multi-channel waveform correlation at regional distances, *Phys. Earth Planet. Int.*, 160, 285-309.

- Gjøystdal, H., Reinhardsen, J. E. and Ursin, B., (1984). Travelttime and wavefront curvature calculations in three-dimensional inhomogeneous layered media with curved interfaces, *Geophysics*, 49, 1466–1494.
- Graeber, F. M. and Asch, G., (1999). Three-dimensional models of P wave velocity and P-to-S velocity ratio in the southern central Andes by simultaneous inversion of local earthquake data, *J. Geophys. Res.*, 104, 20237–20256.
- Gubbins, D., (1992). *Seismology and plate tectonics*, Cambridge University Press, Cambridge.
- Guiziuo, J. L., Mallet, J. L. and Madariaga, R., (1996). 3-D seismic reflection tomography on top of the GOCAD depth modeler, *Geophysics*, 61, 1499–1510.
- Gupta, S. C. and Kumar, A., (1998). Q_c and Q_b Estimates in the Garhwal Himalaya Using Strong Motion Records of Uttarkashi Earthquake, In: *Proceedings of 11th Symp on Earthquake Engineering*, 75–83.
- Gupta, S. C., Singh, V. N. and Kumar, A., (1995). Attenuation of coda waves in the Garhwal Himalaya, India, *Phys. Earth Planet. Int.*, 87, 247-253.
- Gupta, S. C., Kumar, A., Singh, V. N. and Basu, S., (1996). Lapse-time dependence of Q_c in Garhwal Himalaya, *Bull. Ind. Soc. Earth.*, 33, 147-159.
- Gupta, Y., Mohanty, W. K., Chauhan, P. K. S., Verma, R. K. and Roonwal, G. S., (1996). P_g and S_g wave velocities in Delhi and the surrounding region from microseismicity data, *Bull. Ind. Soc. Earth. Tech.*, 33, 229-239.
- Gusev, A. A., (1995). Vertical profile of turbidity and coda Q , *Geophys. J. Int.*, 123, 665–672.
- Hagen, T., (1969). Report on the geological survey of Nepal. 1. Preliminary reconnaissance. 86, pp. 185.
- Hashida, T. and Shimazaki, K., (1984). Determination of seismic attenuation structure and source strength by inversion of seismic intensity data: Method and numerical experiment, *J. Phys. Earth.*, 32, 299-316.

Haslinger, F., Kissling, E., Ansorge, J., Hatzfeld, D., Papadimitriou, E., Karakostas, V., Makropoulos, K., Kahle, H. G. and Peter, Y., (1999). 3D crustal structure from local earthquake tomography around the Gulf of Arta (Ionian region, NW Greece), *Tectonophysics*, 304, 201–218.

Hassouna, M. S. Abdel-Hakim, A. E. and Farag, A., (2005). Robust robotic path planning using level sets, In: *Proceedings of IEEE International Conference on Image Processing*, pp. 473-476.

Hassouna, M. S. and Farag, A. A., (2007). Multistencils Fast Marching Methods: A highly accurate solution to the eikonal equation on Cartesian domains, *IEEE Trans. Pattern Analysis and Machine Intelligence*, 29, 1563-1574.

Havskov, J., Malone, S., McClurg, D. and Crosson, R., (1989). Coda Q for the State of Washington. *Bull. Seism. Soc. Am.*, 79, 1024-1038.

Hazarika, D., Baruah, S. and Gogoi, N. K., (2009). Attenuation of coda waves in the northeastern region of India, 13, 141-160.

Hazarika, D., Kumar, N. and Yadav, D., (2013). Crustal thickness and Poisson's ratio variations across the Northwest Himalaya and Eastern Ladakh, *Acta Geophysica*, 61, 905–922.

Hazler, S. E., Sheehan, A. F., McNamara, D. E. and Walter, W. R., (2001). One-dimensional shear velocity structure of Northern Africa from Rayleigh wave group velocity dispersion, *Pure Appl. Geophys.*, 158, 1475-1493.

Heim, A. and Gansser, A., (1939). Central Himalaya geological observations of Swiss, pp. 1-246.

Herraiz, M. and Espinosa, A. F., (1987). Coda Waves: A Review, *Pure Appl. Geophys.*, 125, 499–577.

Herren, E., (1987). Zaskar shear zone: northeast–southwest extension within the Higher Himalayan (Ladakh, India), *Geology*, 15, 409–413.

Hildebrand, J. A., Dorman, L. M., Hammer, P. T. C., Schreiner, A. E. and Cornuelle, B. D., (1989). Seismic tomography of Jasper Seamount, *Geophys. Res. Lett.*, 16, 1355–1358.

- Hole, J. A., (1992). Nonlinear high-resolution three-dimensional travel-time tomography, *J. Geophys. Res.*, 97, 6553–6562.
- Honegger, K., Dietrich, V., Frank, W., Gansser, A., Thoni, M. and Trommsdorff, V., (1982). Magnetism and metamorphism in the Ladakh Himalayas (the Indus-Tsangpo suture Zone), *Earth Planet. Sci. Lett.*, 60, 253-292.
- Hoshiaba, M., (1993). Separation of scattering attenuation and intrinsic absorption in Japan using the multiple lapse time window analysis of full seismogram envelope, *J. Geophys. Res.*, 98, 15809-15824.
- Hsu, T. Y., Huang, S. K., Chang, Y. W., Kuo, C. H., Lin, C. M., Chang, T. M., Wen, K. L. and Loh, C. H., (2013). Rapid on-site peak ground acceleration estimation based on support vector regression and P-wave features in Taiwan, *Soil Dyn. Earthq. Eng.*, 49, 210-217.
- Huang, M. W., Wang, J. H., Ma, K. F., Wang, C. Y., Hung, J. H. and Wen, K. L., (2007). Frequency-dependent site amplifications with $f \geq 0.01$ Hz evaluated from velocity and density models in central Taiwan, *Bull. Seism. Soc. Am.*, 97, 624-637.
- Hubbard, M. S. and Harrison, T. M., (1989). $^{40}\text{Ar}/^{39}\text{Ar}$ age constraints on deformation and metamorphism in the MCT Zone and the Tibetan Slab, eastern Nepal Himalaya, *Tectonics*, 8, 865-880.
- Humphreys, E. and Clayton, R. W., (1988). Adaption of back projection tomography to seismic travel time problems, *J. Geophys. Res.*, 93, 1073–1085.
- Humphreys, E. D. and Clayton, R. W., (1990). Tomographic image of the Southern California Mantle, *J. Geophys. Res.*, 95, 19725–19746.
- Husebye, E. S. and Ruud, B. O., (1989). Array seismology — Past, present and future developments, In: Litehiser, J. J. (Eds.), *Observatory Seismology*, Univ. of Calif. Press, Berkeley, pp. 123–153.
- Jean, W. Y., Chang, Y. W., Wen, K. L. and Loh, C. H., (2006). Early Estimation of Seismic Hazard for Strong Earthquakes in Taiwan, *Nat. Hazards*, 37, 39-53.
- Jones, R., (1955). A vibration method for measuring the thickness of concrete road slabs in situ, *Mag. Concrete Res.*, 7, 97-102.

Joshi, A., (2006). Analysis of strong motion data of the Uttarkashi earthquake of 20th October 1991 and the Chamoli earthquake of 28th march 1999 for determining the Q value and source parameters, *J. Earthq. Tech.*, 43, 11-19.

Joshi, A., Mohanty, M., Bansal, A. R., Dimri, V. P. and Chadha, R. K., (2010). Use of spectral acceleration data for determination of three-dimensional attenuation structure in the Pithoragarh region of Kumaon Himalaya, *J. Seismol.*, 14, 247-272.

Joshi, A., Mohanty, M., Bansal, A. R., Dimri, V. P. and Chadha, R. K., (2006). Use of strong-motion data for frequency-dependent shear wave attenuation studies in the Pithoragarh region of kumaon Himalaya, *ISSET J. Earthq. Tech.*, 47, 25-46.

Joshi, A., Mohanty, M., Bansal, A. R., Dimri, V. P. and Chadha, R. K., (2008). Heterogeneous Himalayan crust using shear wave attenuation in the Pithoragarh region of Kumaon, In: *Extended Abstracts: 23rd Himalayan-Karakoram-Tibet Workshop, 2008, India.*

Julia, J., Ammon, C. J., Herrmann, R. B. and Correig, A. M., (2000). Joint inversion of receiver functions and surface wave dispersion observations, *Geophys. J. Int.*, 143, 99–112.

Julian, B. R. and Gubbins, D., (1977). Three-dimensional seismic ray tracing, *J. Geophys.*, 43, 95–113.

Kamble, V. P., Verma, R. K. and Chaudhury, H. M., (1974). Crustal structure in Dalhousie-Mandi section of the Himalayan foothills, Part I, *Ind. J. Met. Geophys.*, 25, 229–236.

Kanasewich, E., Burianyk, M. J. A., Ellis, R. M., Clowes, R. M., White, D. J., Lôté, T., Forsyth, D. A., Luetgert, J. A. and Spence, G. D., (1994). Crustal velocity structure of the Omineca Belt, southwestern Canadian Cordillera, *J. Geophys. Res.*, 99, 2653–2670.

Kanaujia, J., Kumar, A. and Gupta, S. C., (2012). 1-D crustal model of the Garhwal Lesser Himalaya from local earthquake observations, *ISSET Golden Jubilee Symposium, Indian Society of Earthquake Technology, Department of Earthquake Engineering Building, IIT Roorkee, Roorkee, October 20-21, No. A003.*

Kao, H. and Rau, R. J., (1999). Detailed structures of the subducted Philippine Sea plate beneath northeast Taiwan: A new type of double seismic zone, *J. Geophys. Res.*, 104, 1015–1033.

- Khattri, K. N. and Tyagi, A. K., (1983). Seismicity patterns in the Himalayan plate boundary and identification of the areas of high seismic potential. *Tectonophysics*, 96, 281-297.
- Khattri, K. N., (1987). Great earthquakes, seismicity gaps and potential for earthquake disaster along the Himalaya Plate boundary. *Tectonophysics*, 138, pp. 79-92.
- Khattri, K. N., Chander, R., Gaur, V. K., Sarkar, I. and Kumar, S., (1989). New seismological results on the tectonics of the Garhwal Himalaya, In: *Proceedings of Indian Academy Sciences, Earth Planet. Sci.*, 98, 91-109.
- Kim, S., (2001). An $O(n)$ level set method for Eikonal equations, *SIAM J. Sci. Comput.*, 22, 2178-2193.
- Kim, S. and Cook, R., (1999). 3D travelttime computation using second-order ENO scheme, *Geophysics*, 64, 1867–1876.
- Kim, W., Rowe, C. A. and Hahm, In-Kyeong, (2012). Detailed one-dimensional seismic velocity profiles beneath the Himalayan collision zone: evidence for a double Moho? *Geosci. J.*, 16, 59-64.
- Kissling, E., Ellsworth, W. L., Eberhart-Phillips, D. and Kradolfer, U., (1994). Initial reference models in local earthquake tomography, *J. geophys. Res.*, 99, 19 635–19 646.
- Kohler, M. D. and Davis, P. M., (1997). Crustal thickness variations in southern California from Los Angeles Region Seismic Experiment passive phase teleseismic travel times, *Bull. Seism. Soc. Am.*, 87, 1330–1344.
- Kosloff, D., Sherwood, J., Koren, Z., Machet, E. and Falkovitz, Y., (1996). Velocity and interface depth determination by tomography of depth migrated gathers, *Geophysics*, 61, 1511–1523.
- Kumar, A., Sinvhal, A., Joshi, A., Kumar, D., Sandeep and Kumar, P., (2015). Coda wave attenuation characteristics for Kumaon and Garhwal Himalaya, India, *Nat. Hazards*, 75, 1057-1074.
- Kumar, K. A. P. and Mohan, G., (2014). Crustal velocity structure beneath Saurashtra, NW India, through waveform modeling: Implications for magmatic underplating, *J. Asian Earth Sci.*, 79, 173-181.

- Kumar, S., (2010). Estimation of crustal $Q\beta$ in the NW Himalaya using teleseismic broadband SH waveforms of the 8 October 2005 South Asian earthquake, *Acta Geophysica*, 58, 645–660.
- Kumar, S., (2012). Seismicity in the NW Himalaya, India: Fractal Dimension, b-value mapping and temporal variations for hazard evaluation. *Geoscience Research*, 3, 83-87.
- Kumar, S., Chander, R. and Khattri, K. N., (2007). Upper mantle velocity structure in the NW Himalaya: Hindu Kush to Garhwal region from travel time studies of deep Hindu Kush earthquakes, *Edu. Res. Rev.*, 2, 302-314.
- Kuo, C. H., Cheng, D. S., Hsieh, H. H., Chang, T. M., Chiang, H. J., Lin, C. M. and Wen, K. L., (2009). Comparison of three different methods in investigating shallow shear wave velocity structures in Ilan, Taiwan, *Soil Dyn. Earthq. Eng.*, 29,133-143.
- Langan, R. T., Lerche, I. and Cutler, R. T., (1985). Tracing of rays through heterogeneous media: An accurate and efficient procedure, *Geophysics*, 50, 1456–1465.
- Langston, C. A., (1979). Structure under Mount Rainier, Washington, inferred from teleseismic body waves, *J. Geophys. Res.* 84, 4749-4762.
- Last, R. J., Nyblade, A. A. and Langston, C. A., (1997). Crustal structure of the East African plateau from receiver functions and Rayleigh wave phase velocities, *J. Geophys. Res.*, 102, 24469-24483.
- Lawrence, J. F. and Wiens, D. A., (2004). Combine receiver-function and surface wave phase-velocity inversion using a niching genetic algorithm: Application to Patagonia, *Bull. Seism. Soc. Am.*, 94, 977–987.
- Lee, W. H. K. and Pereyra, V., (1993). Mathematical introduction to seismic tomography, In: H. M. Iyerand, H. M. and Hirahara, K. (Eds.), *Seismic tomography: theory and practice*, Chapman and Hall, London, pp. 9–22.
- LeForte, P., (1975). Himalayas - the collided range - present knowledge of the continent arc, *Am. J. Sci*, 275, 7-44.
- Lekien, F. and Marsden, J., (2005). Tricubic interpolation in three dimensions, *Int. J. Numer. Math. Engng.*, 63, 455-471.

- Levenberg, K., (1944). A method for the solution of certain nonlinear problems in least squares, *Quart. Appl. Math.*, 2, 164– 168.
- Lévêque, J. J., Rivern, L. and Wittlinger, G., (1993). On the use of the checker-board test to assess the resolution of tomographic inversions, *Geophys. J. Int.*, 115, 313-318.
- Li, C., van der Hilst, R. D., Meltzer, A. S. and Engdahl, E. R., (2008). Subduction of the Indian lithosphere beneath the Tibetan Plateau and Burma, *Earth Planet. Sci. Lett.*, 274, 157-168.
- Lin, C. M., Chang, T. M., Huang, Y. C., Chiang, H. J., Kuo, C. H. and Wen, K. L., (2009). Shallow S-wave velocity structures in the western coastal plain of Taiwan, *Terr. Atmos. Ocean Sci.* 20. doi:10.3319/TAO.2007.12.10.01(T)
- Lutter, W. J. and Nowack, R. L., (1990). Inversion for crustal structure using reflections from the PASSCAL Ouachita experiment, *J. Geophys. Res.*, 95, 4633–4646.
- Lutter, W. J., Nowack, R. L. and Braile, L., (1990). Seismic imaging of upper crustal structure using travel times from the PASSCAL Ouachita experiment, *J. Geophys. Res.*, 95, 4621–4631.
- Hassouna, M. S., Abdel-Hakim, A. E. and Farag, A. (2005). Robust robotic path planning using level sets, In: *Proceedings of IEEE International Conference. Image Processing*, pp. 473-476.
- Ma'hood, M. and Hamzehloo, H., (2009). Attenuation of high frequency P and S waves in the crust of the East-Central Iran, *Geophys. J. Int.*, 179, 1669 -1678.
- Ma'hood, M. and Hamzehloo, H., (2011). Variation of intrinsic and scattering attenuation of seismic waves with depth in the Bam region, East-Central Iran, *Soil Dyn. Earthq. Eng.*, 31, 1338–1346.
- Mahesh, P., Rai, S. S., Sivaram, K., Paul, A., Gupta, S., Sarma, R. and Gaur, V. K., (2013). One-Dimensional reference velocity model and precise locations of earthquake hypocenters in the Kumaon–Garhwal Himalaya, *Bull. Seism. Soc. Am.*, 103, 328-339.
- Malik, S., (2009). 3D Crustal structure modeling of Garhwal Himalayas, Ph.D. Thesis, IIT Roorkee.

- Mandal, P., Padhy, S., Rastogi, B. K., Satyanarayana, H. V. S., Kousalya, M., Vijayraghavan, R. and Srinivasan, A., (2001). Aftershock activity and frequency-dependent low coda Q_c in the epicentral region of the 1999 Chamoli Earthquake of Mw 6.4, *Pure Appl. Geophys.*, 158, 1719-1735.
- Mao, W. J. and Suhadolc, P., (1992). Simultaneous inversion of velocity structures and hypocentral locations: application to the Friuli seismic area NE Italy, *Geophys. J. Int.*, 138, 267-285.
- Matthews, D. L., Ruohoniemi, J. M., Dudeney, J. R., Farrugia, C. F., Lanzerotti, L. J. and Friis-Christensen, E., (1996). Conjugate cusp-region ULF pulsation responses to the solar wind event of May 23, 1989, *J. Geophys. Res.*, 101, 7829–7841.
- McCaughey, M. and Singh, S. C., (1997). Simultaneous velocity and interface tomography of normal incidence and wide-aperture seismic traveltime data, *Geophys. J. Int.*, 131, 87–99.
- Meier, T., Dietrich, K., Stöckhert, B. and Harjes, H.-P., (2004). One-dimensional models of shear wave velocity for the eastern Mediterranean obtained from the inversion of Rayleigh wave phase velocities and tectonic implications, *Geophys. J. Int.*, 156, 45-58
- Meigs, A. J., Burbank, D.W. and Beck, R. A., (1995). Middle-late Miocene (>10 Ma) formation of the Main Boundary Thrust in the western Himalaya. *Geology* 23, 423-426.
- Menke, W., (1989). *Geophysical data analysis: Discrete inverse theory*, Academic Press, New York.
- Miller, C., Thoni, M., Frank, W., Grasemann, B., Klotzli, U., Guntli, P. and Draganitis, E., (2001). The early Paleozoic magmatic event in the northwest Himalaya, India: Source, Tectonic setting and age of emplacement. *Geological magazine*, 138, 237-251.
- Mohan, G., Rai, S. S. and Panza, G. F., (1997). Shear velocity structure of the laterally heterogeneous crust and uppermost mantle beneath the Indian region, *Tectonophysics*, 277, 259-270.
- Mohan, G., Rai, S. S. and Panza, G. F., (1992). Seismic heterogeneities in the Indian lithosphere, *Phys. Earth Planet. In.*, 73, 189-198.
- Mohan, G. and Rai, S. S., (1995). Large-scale three dimensional seismic tomography of the Zagros and Pamir-Hindukush Regions, *Tectonophysics*, 242, 255-265.

- Molnar, P., (1990). A review of the seismicity and the rates of active underthrusting and deformation at the Himalaya. *J. Himalayan Geol.*, 1, 131-154.
- Monsalve, G., Sheehan, A., Rowe, C. and Rajaure, S., (2008). Seismic structure of the crust and the upper mantle beneath the Himalayas: evidence for eclogitization of lower crustal rocks in the Indian Plate, *J. geophys. Res.*, 113, B08315– B08330.
- Monsalve, G., Sheehan, A., Schulte-Pelkum, V., Rajaure, S., Pandey, M. and Wu, F., (2006). Seismicity and 1-D velocity structure of the Himalayan collision zone: Earthquakes in the crust and upper mantle, *J. Geophys. Res.*, 111, B10301, doi:10.1029/2005JB004062.
- Mukhopadhyay, S. and Kayal, J. R., (2003). Seismic tomography structure of the 1999 Chamoli earthquake source area in the Garhwal Himalaya, *Bull. Seismol. Soc. Am.*, 93, 1854-1861.
- Mukhopadhyay, S. and Sharma, J., (2010a). Crustal scale detachment in the Himalayas: a reappraisal, *Geophys. J. Int.*, 183, 850–60.
- Mukhopadhyay, S. and Sharma, J., (2010b). Attenuation Characteristics of Garhwal–Kumaun Himalayas from Analysis of Coda of Local Earthquakes, *J. Seismol.*, 14, 693–713, doi:10.1007/s10950-010-9192-9.
- Mukhopadhyay, S. and Tyagi, C., (2007). Lapse time and frequency-dependent attenuation characteristics of coda waves in the Northwestern Himalayas, *J. Seismol.*, 11, 149-158.
- Mukhopadhyay, S. and Tyagi, C., (2008). Variation of intrinsic and scattering attenuation with depth in NW Himalayas, *Geophys. J. Int.*, 172, 1055-1065.
- Mukhopadhyay, S., Sharma, J. and Arora., B. R., (2008). Seismic Tomography of Garhwal-Kumaun Himalayas: Is the Basal Detachment a Wistful Thinking?, *Himalayan J. Sci.*, 7, 128.
- Mukhopadhyay, S., Sharma, J., Massey, R. and Kayal, J. R., (2008). Lapse time dependence of coda Q in the source region of the 1999 Chamoli Earthquake, *Bull. Seismol. Soc. Am.*, 98, 2080-2086.
- Mukhopadhyay, S., Tyagi, C. and Rai, S. S., (2006). The attenuation mechanism of seismic waves in northwestern Himalayas, *Geophys. J. Int.*, 167, 354-360.

- Nakanishi, I. and Anderson, D. L., (1982). Worldwide distribution of group velocity of mantle Rayleigh waves as determined by spherical harmonic inversion, *Bull. Seism. Soc. Am.*, 72, 1185-1194.
- Nakanishi, I., (1985). Three-dimensional structure beneath the Hokkaido-Tohoku region as derived from a tomographic inversion of P-arrival times, *J. Phys. Earth*, 33, 241–256.
- Nakata T., (1989). Active Faults of Himalaya of India and Nepal, *Geol. Soc. Am.*, 332, 243–264.
- Nasser-Moghaddam, A., (2006). Study of the effect of lateral inhomogeneities on the propagation of Rayleigh waves in an elastic medium: PhD thesis, Univ. of Waterloo, Waterloo, Ontario, Canada.
- Nath, S., K., Khemraj, S. and Vyas, M., (2008). Seismic Hazard Scenario and Attenuation Model of the Garhwal Himalaya Using near-Field Synthesis from Weak Motion Seismometry, *J. Earth Syst. Sci.*, 117, 649–670, doi:10.1007/s12040-008-0062-6.
- Navin, D. A., Peirce, C. and Sinha, M. C., (1998). The RAMESSES experiment –II, Evidence for accumulated melt beneath a slow spreading ridge from wide-angle refraction and multichannel reflection seismic profiles, *Geophys. J. Int.*, 135, 746–772.
- Neele, F., VanDecar, J. and Snieder, R., (1993). The use of P wave amplitude data in a joint inversion with travel times for upper mantle velocity structure, *J. Geophys. Res.*, 98, 12033–12054.
- Negi, S. S., Paul, A., Joshi, A. and Kamal, (2015). Body wave crustal attenuation characteristics in the Garhwal Himalaya, India, *Pure Appl. Geophys.*, 172, 1451-1469.
- Ni, J. and Barazangi, M., (1984). Seismotectonics of the Himalayan collision zone: Geometry of the underthrusting Indian plate beneath the Himalaya, *J. Geophys. Res.*, 89, 1147-1163.
- Oncescu, M. C., Burlacu, V., Anghel, M. and Smalbergheer, V., (1984). Three-dimensional P-wave velocity image under the Carpathian Arc, *Tectonophysics*, 106, 305–319.
- Oreshin, S., Kiselev, S., Vinnik, L., Prakasam, K. S., Rai, S. S., Makeyeva, L. and Savvin, Y., (2008). Crust and mantle beneath western Himalaya, Ladakh and western Tibet from

integrated seismic data, *Earth Planet. Sci. Lett.* 271, 1-4, 75-87, doi: 10.1016/j.epsl.2008.03.048.

Osher, S. and Sethian, J., (1988). Fronts propagating with curvature dependent speed: Algorithms based on hamilton-jacobi formulations, *J. Comp. Phys.*, 79, 12–49.

Padhy, S. and Subhadra, N., (2010). Attenuation of High-Frequency Seismic Waves in Northeast India, *Geophys. J. Int.*, 181, 453–67.

Pandey, I. C., (1950). A geological note on Ramgarh area, Distt. Nainital. *Himalayan Geol.*, v.3, pp.15-28

Papazachos, C. and Nolet, G., (1997). P and S deep velocity structure of the Hellenic area obtained by robust nonlinear inversion of travel times, *J. Geophys. Res.*, 102, 8349–8367.

Park, C. B., Miller, R. D. and Xia, J., (1998). Imaging dispersion curves of surface waves on multi-channel records: Technical Program with biographies, In: 68th SEG Annual Meeting, New Orleans, Louisiana, 1377-1380.

Park, C. B. and Ryden, N., (2007). Historical Overview of the Surface Wave Method, In: Proceedings of the 20th EEGS Symposium on the Application of Geophysics to Engineering and Environmental Problems, April 1-5, 2007, Denver, Colorado.

Park, J. and Levin, V., (2000). Receiver functions from multiple-taper spectral correlation estimates, *Bull. Seism. Soc. Am.*, 90, 1507–1520.

Parrish, R. P. and Hodges, K. V., (1996). Isotopic constraints on the age and provenance of the Lesser and Greater Himalayan sequences, Nepalese Himalaya, *Geol. Soc. Am. Bull.*, 108, 904-911.

Parvez, I. A., Yadav, P. and Nagaraj, K., (2012). Attenuation of P, S and Coda Waves in the NW-Himalayas, India, *Int. J. Geosci.*, 3, 179, doi:10.4236/ijg.2012.31020.

Paul, A., (2010). Evaluation and implications of seismic events in Garhwal-Kumaon region of Himalaya, *J. Geol. Soc. India*, 414-418.

Paul, A., Bhakuni, S. S., Pant, Charu, C., Darmwal, G. S. and Pathak, V., (2010). Microseismicity in central part of Inner Kumaon Lesser Himalaya: Implication to active seismotectonics, *Himalayan Geology*, 31, 107-115.

- Paul, A., Gupta, S. C. and Pant, C. C., (2003). CODA Q estimates for Kumaun Himalaya, In: Proceedings of Indian Academy of Sciences, Earth Planet. Sci., 112, 569-576.
- Pedersen, R. B., Searle, M. P. and Corfield, R. I., (2001). U-Pb zircon ages from the Spang Ophiolite. *J. Geol. Soc. London*, 158, 513-520.
- Pereyra, V., Lee, W. H. K. and Keller, H. B., (1980). Solving two-point seismic-ray tracing problems in a heterogeneous medium, *Bull. Seism. Soc. Am.*, 70, 79–99.
- Phillips, C., Cascante, G. and Hutchins, D. J., (2004). Evaluation of horizontal homogeneity of geomaterials with the distance analysis of surface waves, *Can. Geotech. J.*, 41, 212-226.
- Podvin, P. and Lecomte, I., (1991). Finite difference computation of traveltimes in very contrasted velocity models: a massively parallel approach and its associated tools, *Geophys. J. Int.*, 105, 271–284.
- Prenter, P. M. (1975). *Splines and variational methods*, John Wiley and Sons, Inc. New York.
- Priestley, K., Jackson, J., and McKenzie, D., (2008). Lithospheric structure and deep earthquakes beneath India, the Himalaya and southern Tibet, *Geophys. J. Int.*, 172, 345–362.
- Pulli, J. J., (1984). Attenuation of coda waves in New England, *Bull. Seism. Soc. Am.*, 74, 1149-1166.
- Qin, F., Luo, Y., Olsen, K. B., Cai, W. and Schuster, G. T., (1992). Finite-difference solution of the eikonal equation along expanding wavefronts, *Geophysics*, 57, 478–487.
- Rahimi, H., Hamzehloo, H., Vaccari, F. and Panza, G. F., (2014). Shear-wave velocity tomography of the Lithosphere–Asthenosphere System beneath the Iranian Plateau, *Bull. Seism. Soc. Am.*, 104, 2782-2798.
- Rai, S. S., Priestley, K., Gaur, V. K., Mitra, S., Singh, M. P. and Searle, M., (2006). Configuration of the Indian Moho beneath the NW Himalaya and Ladakh, *Geophys. Res. Lett.*, 33, L15308. doi: 10.1029/2006GL026076
- Raina, B. N. and Dungrakoti, B. D., (1975). Geology of the area between Nainital and Champawat, Kumaon Himalaya, *U. P. Himalayan Geol.*, 5, 1-25.
- Rawlinson, N. and Houseman, G. A., (1998). Inversion for interface structure using teleseismic traveltimes residuals, *Geophys. J. Int.*, 133, 756–772.

- Rawlinson, N. and Kennett, B. L. N., (2008). Telesismic tomography of the upper mantle beneath the southern Lachlan Orogen, Australia, *Phys. Earth Planet. Inter.*, 167, 84-97.
- Rawlinson, N. and Sambridge, M., (2003). Seismic Traveltime Tomography of the Crust and Lithosphere, *Adv. Geophys.*, 46, 81–198.
- Rawlinson, N., Houseman, G. A. and Collins, C. D. N., (2001). Inversion of seismic refraction and wide-angle reflection traveltimes for 3-D layered crustal structure, *Geophys. J. Int.*, 145, 381–401.
- Rawlinson, N. and Sambridge, M., (2004). Multiple reflection and transmission phases in complex layered media using a multistage fast marching method, *Geophysics*, 69, 1338–1350.
- Rix, G. J. and Lai, C. G., (1998). Simultaneous inversion of surface wave velocity and attenuation, In: Robertson, P. K. and Mayne, P. W. (Eds.), *Geotechnical Site Characterization*, Rotterdam, Balkema, pp. 503-508.
- Rix, G. J., Lai, C. G., Orozco, M. C. Hebel, G. L. and Roma, V., (2001), Recent advances in surface wave methods for geotechnical site characterization, In: *Proceedings of 15th International Conference on Soil Mechanics and Geotechnical Engineering*, Aug. 28-31, Istanbul.
- Saltzer, R. L. and Humphreys, E. D., (1997). Upper mantle P wave velocity structure of the eastern Snake River Plain and its relationship to geodynamic models of the region, *J. Geophys. Res.*, 102, 11829–11841.
- Sambridge, M. S. and Kennett, B. L. N., (1990). Boundary value ray tracing in a heterogeneous medium: A simple and versatile algorithm, *Geophys. J. Int.*, 101, 157–168.
- Sambridge, M. S., (1990). Non-linear arrival time inversion: Constraining velocity anomalies by seeking smooth models in 3-D, *Geophys. J. Int.*, 102, 653–677.
- Sambridge, M., (1999). Geophysical inversion with a neighbourhood algorithm—I. Searching a parameter space, *Geophys. J. Int.*, 138, 479-494.
- Sato, H. and Fehler, M., (1998). *Seismic Wave Propagation and Scattering in the Heterogeneous Earth*. AIP Press, Springer Verlag, New York, pp. 308.

- Saxena, S. P. and Rao, P. N., (1975) Does Almora Nappe exist? *Himalayan Geol.*, 5, 169-184.
- Scales, J. A. and Snieder, R., (1997). To Bayes or not to Bayes, *Geophysics*, 62, 1045–1046.
- Schneider, W. A., Jr., (1995). Robust and efficient upwind finite- difference travetime calculations in three dimensions, *Geophysics*, 60, 1108-1117.
- Scott, J. S., Masters, T. G. and Vernon, F. L., (1994). 3-D velocity structure of the San Jacinto fault zone near Anza, California-I. P waves, *Geophys. J. Int.*, 119, 611–626.
- Searle, M. P. and Godin, L., (2003). The South Tibetan Detachment system and the Manasluleucogranite: a structural re-interpretation and restoration of the Annapurna–Manaslu Himalaya, *Nepal J. Geol.*, 111, 505–523.
- Searle, M. P., (1991). *Geology and tectonics of the Karakoram Mountains*, Chichester, John Wiley and Sons Ltd., pp.358.
- Seber, D., Barazangi, M., Tadili, B. A., Ramdani, M., Ibenbrahim, A. and Sari, D. B., (1996). Three dimensional upper mantle structure beneath the intraplate Atlas and interplate Rif mountains of Morocco, *J. Geophys. Res.*, 101, 3125–3138.
- Seeber, L. and Armbruster, J. G., (1981). Great detachment earthquakes along the Himalayan arc and the long-term forecasting, In: Simpson, D. E. and Richards, P.G. (Eds.), *earthquake prediction-an international review*, Maurice Ewing Series 4, AGU, pp. 259-277.
- Sethian, J. A., (1982). *An analysis of flame propagation*: Ph.D. Dissertation, Univ. of California, Berkeley.
- Sethian, J. A., (1987). Numerical methods for propagating fronts, In: Concus, P., and Finn, R. (Eds.), *Variational methods for free surface interfaces*, Springer- Verlag, New York, Inc.
- Sethian, J. A., (1996). A fast marching level set method for monotonically advancing fronts. *Prac. Natl. Acad. Sci. U.S.A.*, 93, 1591-1595.
- Sethian, J. A. and Popovici, A. M., (1999). 3-D travelttime computation using the fast marching method, *Geophysics*, 64, 516-523.

- Shapiro, N. M., Singh, S. K., Iglesias-Mendoza, A., Cruz-Atienza, V. M. and Pacheco, J. F., (2000). Evidence of low Q value below Popocatepetl volcano, and its implication to seismic hazard in Mexico City, *Geophys. Res. Lett.*, 27, 2753-2756.
- Sharma B., Teotia, S. S., Kumar, D. and Raju, P. S., (2009). Attenuation of P- and S-Waves in the Chamoli Region, Himalaya, India, *Pure Appl. Geophys.*, 166, 1949–1966, doi:10.1007/s00024-009-0527-9.
- Shearer, P. M., (2009). *Introduction to Seismology*, 2nd edn., Cambridge University press, Cambridge, New York.
- Shibutani, T., Sambridge, M. and Kennett, B. L. N., (1996). Genetic algorithm inversion for receiver functions with application to crust and uppermost mantle structure beneath eastern Australia, *Geophys. Res. Lett.*, 23, 1829-1832.
- Singh, A. P., Mishra, O. P., Rastogi, B. K. and Kumar, D., (2011). 3-D seismic structure of the Kachchh, Gujarat, and its implications for the earthquake hazard mitigation, *Nat. Hazards*, 57, 83-105.
- Singh, S. K., Dattatrayam, R. S., Shapiro, N. M., Mandal, P., Pacheco, J. F. and Midha, R. K., (1999). Crustal and upper mantle structure of Peninsular India and source parameters of the 21 May 1997, Jabalpur earthquake ($M_w = 5.8$): Results from a new regional broadband network, *Bull. Seism. Soc. Am.*, 89, 1631-1641.
- Sinha. A. K., (1989). *Geology of the Higher Central Himalaya*. John Wiley and Sons, pp 219.
- Snieder, R. and Romanowicz, B., (1988). A new formalism for the effect of lateral heterogeneity on normal modes and surface waves: I Isotropic perturbations, perturbations of interfaces and gravitational perturbations, *Geophys. J. Roy. Astr. Soc.*, 92, 207–222.
- Sørensen, M. B, Atkan, K. and Pulido, N., (2007). Simulated strong ground motions for the Great M 9.3 Sumatra-Andaman Earthquake of 26 December 2004, *Bull. Seism. Soc. Am.*, 97, 139-151.
- Sørensen, M. B., Oprsal, I., Bonnefoy-Claudet, S., Atakan, K., Mai, P. M., Pulido, N. and Yalciner, C., (2006). Local site effects in Ataköy, Istanbul, Turkey, due to a future large earthquake in the Marmara Sea, *Geophys. J. Int.*, 167, 1413-1424.

Sorkhabi, R. B., Stump, E., Foland, K. and Jain, A. K., (1999). Tectonic and cooling history of the Garhwal higher Himalaya (Bhagirathi valley): constraints from thermochronological data. In: Jain , A. K and Manickavasagam, R.M (Eds.), *Geodynamics of the NW Himalaya*, Gondwana Research group Memoir. vol 6, pp 217-235.

Srivastava, P. and Mitra, G., (1994). Thrust geometries and deep structure of the outer and lesser Himalaya, Kumaon and Garhwal (India): implications for evolution of the Himalayan fold-and-thrust-belt, *Tectonics*, 13, 89-109.

Staples, R. K., White, R. S., Brandsdóttir, Menke, W., Maguire, P. K. H. and McBride, J. H., (1997). Färoe-Iceland Ridge experiment 1. Crustal structure of northeastern Iceland, *J. Geophys. Res.*, 102, 7849–7866.

Steck, A., Epard, J. L., Vannay, J. C., Hunziker, J., Girard, M., Morard, A. and Robyr, M., (1998). Geological transect across the Tso Morari and Spiti areas: The nappe structures of the Tethys Himalaya, *Eclogae Geol. Helv.*, 91, 103-121.

Steck, A., Spring, L., Vannay, J. C., Masson, H., Bucher, H., Stutz, E., Marchant, R. and Tiede, J. C., (1993). Geological transect across the North-Western Himalaya Eastern Ladakh and Lahul (A Model for the continental collision of India and Asia), *Eclogae Geol. Helv.* 86, 219-263.

Steck, L. K., Thurber, C. H., Fehler, M., Lutter, W. J., Roberts, P. M., Baldrige, W. S., Stafford, D. G. and Sessions, R., (1998). Crust and upper mantle P wave velocity structure beneath Valles caldera, New Mexico: Results from the Jemez teleseismic tomography experiment, *J. Geophys. Res.*, 103, 24,301–24,320.

Stöcklin, J., (1980). *Geology of Nepal and its regional frame*, *J. Geol. Soc. London*, 137, 1-34.

Tarantola, A. and Valette, B., (1982). Generalized Nonlinear Inverse Problems Solved Using the Least Squares Criterion, *Reviews of Geophysics and Space Physics* 20, 219–232. doi:10.1029/RG020i002p00219

Tarantola, A., (1987). *Inverse problem theory, methods for data fitting and model parameter estimation*, Elsevier, Amsterdam.

Tarantola, A., (2005). *Inverse problem theory and methods for model parameter estimation*, Society for Industrial and Applied Mathematics.

- Telea, A., (2004), An Image Inpainting Technique Based on the Fast Marching Method, *J. Graphics. Tools*, 9, 23-34.
- Telford, W. M., Geldart, L. P., Sheriff, R. E. and Keys, D. A., (1976). *Applied Geophysics*, Cambridge University Press, Cambridge.
- Thakur, V. C., (1992). *Geology of Western Himalaya*, Pergamon Press, Oxford, pp. 363.
- Thakur, V. C., (2004). Active tectonics of Himalayan Frontal Thrust and Seismic hazard to Ganga plain, *Curr. Sci.*, 86 , 1554-1560.
- Thomson, C. J. and Gubbins, D., (1982). Three-dimensional lithospheric modelling at NORSAR: linearity of the method and amplitude variations from the anomalies, *Geophys. J. Roy. Astr. Soc.*, 71, 1–36.
- Thurber, C. H., (1983). Earthquake locations and three-dimensional crustal structure in the Coyote Lake area, central California, *J. Geophys. Res.*, 88, 8226–8236.
- Thurber, C. H. (2003). Seismic Tomography of the Lithosphere with Body Waves, *Pure Appl. Geophys.*, 160, 717-737.
- Tian, Y. and Chen, X.-F. (2006), Simultaneous Inversion of Hypocenters and Velocity Structure using the Quasi-Newton Method and Trust-Region Method, *Chinese J. Geophys.*, 49, 740–750.
- Tripathi, J., Singh, P. and Sharma, M. L., (2014). Attenuation of high-frequency P and S waves in Garhwal Himalaya, India, *Tectonophysics*, 636, 216-227.
- Tsitsiklis, J., (1995). Efficient Algorithms for Globally Optimal Trajectories, *IEEE Trans. Automatic Control*, 40,1528-1538,
- Um, J. and Thurber, C., (1987). A fast algorithm for two-point seismic ray tracing, *Bull. Seism. Soc. Am.*, 77, 972–986.
- Valdiya, K. S., (1978). The extension and analogue of the Chail Nappe in the Kumaun Himalaya, *Indian J. Earth Sci.*, 5, 1–19.
- Valdiya, K. S., (1980). *Geology of the Kumaon Lesser Himalaya*. Wadia institute of Himalaya, Dehradun, India, pp. 291.

- Van der Poel, C., (1951). Dynamic testing of road constructions, *J. Appl. Chem.*, 1, 281-290.
- Van Trier, J. and Symes, W. W., (1991). Upwind finite-difference calculation of traveltimes, *Geophysics*, 56, 812–821.
- VanDecar, J. C., James, D. E. and Assumpcao, M., (1995). Seismic evidence for a fossil mantle plume beneath South America and implications for plate driving forces, *Nature*, 378, 25–31.
- Vashi, N. M. and Merh, S. S., (1975), Structural elements of the rocks in the vicinity of South Almora Thrust near Upradi (Almora District, U.P.) *J. M. S. Univ. Baroda*, 14, 27-32.
- Verma, R. K., Chauhan, P. K. S. and Mohanty, W. K., (1998). Seismic Hazard assessment in NW Himalaya and Kumaon-Garhwal Himalaya region, In: *Proceedings of International Conference on Hydro Power Development in Himalaya*, Shimla, India, April 20-22, 1998, pp. 248-259.
- Vidale, J. E., (1988). Finite-difference calculations of traveltimes, *Bull. Seism. Soc. Am.*, 78, 2062– 2076.
- Vidale, J. E., (1990). Finite-difference calculations of traveltimes in three dimensions, *Geophysics*, 55, 521–526.
- Virieux, J. and Farra, F., (1991). Ray tracing in 3-d complex isotropic media: An analysis of the problem, *Geophysics*, 56, 2057–2069.
- Wang, W. and Houseman, G. A., (1994). Inversion of reflection seismic amplitude data for interface geometry, *Geophys. J. Int.*, 117, 92–110.
- Weber, M., Davis, J. P., Thomas, C., Krüger, F., Scherbaum, F., Schlittenhardt, J. and Körnig, M., (1996). The structure of the lowermost mantle as determined from using seismic arrays, In: E. Boschi, E., Ekstrom, G. and Morelli, A. (Eds.), *Seismic Modeling of the Earth's Structure*, Instit. Naz. Di Geophys., Rome, pp. 399–442.
- White, D. J., (1989). Two-dimensional seismic refraction tomography, *Geophys. J. Int.*, 97, 223–245.
- Whiteway, F. E., (1966). The use of arrays for earthquake seismology, *Proc. R. Soc. London, Ser. A*, 290, 328 – 342.

- Williamson, P. R., (1990). Tomographic inversion in reflection seismology, *Geophys. J. Int.*, 100, 255–274.
- Windley, B. F., (1995). *The evolving continents*, 3rd edn., John Wiley and Sons, Chichester.
- Woodhouse, J. H., (1974). Surfacewaves in a laterally varying layered structure, *Geophys. J. Roy. Astr. Soc.*, 37, 461–490.
- Woodhouse, J. H., (1981). A note on the calculation of travel times in a transversely isotropic Earth model. *Phys. Earth Planet. Int.*, 25, 357–359.
- Woodhouse, J. H. and Dziewonski, A. M., (1984). Mapping the upper mantle: three-dimensional modeling of earth structure by inversion of seismic waveforms, *J. Geophys. Res.* 89, 5953–5986.
- Wright, C., (1972). Array studies of seismic waves arriving between P and PP in the distance range 90 to 115, *Bull. Seism. Soc. Am.*, 62, 385–400.
- Xavier, C., (1994). *Fortran 77 and Numerical Methods*, New Age International, New Delhi.
- Xia, J., (2014). Estimation of near-surface shear-wave velocities and quality factors using multichannel analysis of surface-wave methods, *J. Appl. Geophys.*, 103, 140-151.
- Xia, J., Miller, R. D. and Park, C. B., (1999). Estimation of near-surface shear-wave velocity by inversion of Rayleigh waves. *Geophysics*, 64, 691-700.
- Yatziv, L., Bartesaghi, A. and Sapiro, G., (2006). O(N) Implementation of the Fast Marching Algorithm, *J. Comput. Phys.*, 212, 393-399.
- Yin, A., (2006). Cenozoic tectonic evolution of the Himalayan orogeny as constrained by along-strike variation of structural geometry, exhumation history, and foreland sedimentation, *Earth Sci. Rev.*, 76, 1-131.
- Yoshimoto, K., Sato, H. and Ohtake, M., (1993). Frequency-dependent Attenuation of P and S Waves in the Kanto Area, Japan, Based on the Coda-normalization Method, *Geophys. J. Int.*, 114, 165–174.
- Yu, G., Khattri, K. N., Anderson, J. G., Brune, J. N. and Zeng, Y. (1995). Strong ground motion from the Uttarkashi, Himalaya, India, earthquake: Comparison of observations with synthetics using the composite source model, 85, 31-50.

Zelt, B. C., Ellis, R. M., Zelt, C. A., Hyndman, R. D., Lowe, C., Spence, G. D. and Fisher, M. A., (2001). Three-dimensional crustal velocity structure beneath the Strait of Georgia, British Columbia, *Geophys. J. Int.*, 144, 695–712.

Zelt, C. A. and Smith, R. B., (1992). Seismic travelt ime inversion for 2-D crustal velocity structure, *Geophys. J. Int.*, 108, 16–34.

Zelt, C. A., Hojka, A. M., Flueh, E. R. and McIntosh, K. D., (1999). 3D simultaneous seismic refraction and reflection tomography of wide-angle data from the central Chilean margin, *Geophys. Res. Lett.*, 26, 2577–2580.

Zhang, J. and Toksöz, M. N., (1998). Nonlinear refraction travelt ime tomography, *Geophysics*, 63, 1726–1737.

Zhao, D., Hasegawa, A. and Horiuchi, S., (1992). Tomographic imaging of P and S wave velocity structure beneath Northeastern Japan, *J. Geophys. Res.*, 97, 19909–19928.

Zhao, D., Hasegawa, A. and Kanamori, H., (1994). Deep structure of Japan subduction zone as derived from local, regional, and teleseismic events, *J. Geophys. Res.*, 99, 22313–22329.

Zhao, D., Kanamori, H. and Humphreys, E., (1996). Simultaneous inversion of local and teleseismic data for the crust and mantle structure of southern California, *Phys. Earth Planet. Int.*, 93, 191–214.

Zhu, H. and Ebel, J. E., (1994). Tomographic inversion for the seismic velocity structure beneath northern New England using seismic refraction data, *J. Geophys. Res.*, 99, 15331–15357.

